

A Study of the Reactions $\pi^{\pm} p \rightarrow \pi^{\pm} \pi^{+} \pi^{-} \pi^{0} p$ and $\pi^{\pm} p \rightarrow \pi^{\pm} \pi^{+} \pi^{+} \pi^{-} n$
at $p_{\text{lab}} = 14 \text{ GeV}/c$ Using a Triggered Hybrid Bubble Chamber

Thesis by
Frank Joseph Nagy

In Partial Fullfilment of the Requirements
for the Degree of
Doctor of Philosophy

California Institute of Technology
Pasadena, California

1980

(Submitted December 20, 1979)

"Any sufficiently advanced technology is
indistinguishable from magic."

- Arthur C. Clarke

"When the end of the world is near, spend the
remaining time in a bar."

- Jack L. Chalker
from
And the Devil Will Drag You
Under

Acknowledgements

Foremost I must acknowledge the help and guidance of my thesis advisor, Dr. Charles W. Peck, whose leadership was crucial in performing this demanding experiment and whose encouragement helped to bring my thesis work to its completion. I also wish to thank my collaborators from the three institutions involved in this experiment:

California Institute of Technology (Cal Tech), Lawrence Berkeley Laboratory (LBL), and Stanford Linear Accelerator Center (SLAC).

Thanks must also be extended to the scanners and measurers of the bubble chamber data analysis staffs of these institutions and to the accelerator and bubble chamber operations crews of SLAC without whose efforts this experiment could not have been done.

I would like to extend special thanks to the following physicists for their efforts on the experiment and their guidance during my stays at the various institutions: V. Davidson, A. Dzierba, A. Firestone, L. C. Rosenfeld, and A. Sheng of Cal Tech, R. Ely, D. Grether, and P. Oddone of LBL, and J. Ballam, J. T. Carroll, G. B. Chadwick, V. Chaloupka, D. Linglin, and K. C. Moffeit of SLAC. I also wish to thank G. C. Fox and R. D. Field of Cal Tech for their support and help.

To my many friends at Cal Tech, I wish to extend my thanks for enriching my life. To a special group, my appreciation for their love and understanding. For "entertaining" me with their endless questions and problems concerning computers, I wish the terminal users the best of luck in the future (they will need it). I must also express my

appreciation of the efforts of the Zeta plotter and the unnamed author of the PLOT plotting program without whom this thesis could not be written. I also extend thanks to Louise Sartain for putting up with me for all these years.

Finally, I want to thank the U. S. Department of Energy for their support of this research.

Abstract

We have studied the reactions $\pi^{\pm}p \rightarrow \pi^{\pm}\pi^{+}\pi^{-}\pi^{0}p$ and $\pi^{\pm}p \rightarrow \pi^{\pm}\pi^{+}\pi^{+}\pi^{-}n$ at a beam momentum of 14 GeV/c. A bubble chamber with a downstream wire spark chamber spectrometer was used to record the data. The bubble chamber camera was triggered by identifying inelastic events in an online computer using data from the downstream spectrometer. The film taken represents an exposure of about 80 events/microbarn for the π^{+} data and 70 events/microbarn for the π^{-} data.

We find these reactions to be very rich in subprocesses involving baryon and meson resonances. The invariant mass spectra are presented and estimates of the cross sections for the production of known baryon and meson resonances are given.

The reactions $\pi^{\pm}p \rightarrow \pi^{\pm}\omega^{0}p$ provided more evidence for the existence of an N^{*} resonance with mass 1789 ± 5 MeV and width 81 ± 9 MeV which decays into $\omega^{0}p$. Using previously published data along with our results, we find that the production cross section of this N^{*} is independent of s . Studies of the angular distributions raise questions about the validity of the spin-parity analyses of this N^{*} done so far.

We have studied the processes $\pi^{\pm}p \rightarrow \pi^{\pm}\eta^{0}p$ in the relatively unexplored region of low $|t_{\pi\pi}|$ and small $\eta^{0}p$ mass. We found that the $\pi^{+}\eta^{0}p$ cross section is about twice the $\pi^{-}\eta^{0}p$ cross section in this region. The $\eta^{0}p$ mass spectrum for the π^{+} data shows an enhancement at about 1600 MeV while the π^{-} data show no evidence of a peak in the $\eta^{0}p$ mass spectrum.

Contents

	<u>Page</u>
Acknowledgements	iii
Abstract	v
Chapter I. Introduction	
1. Diffraction Dissociation	1
2. This Experiment	2
3. Five-body Final States: $\pi p \rightarrow \pi \pi \pi \pi N$	5
4. $\pi^\pm p \rightarrow \pi^\pm \omega^0 p$ and $\pi^\pm p \rightarrow \pi^\pm \eta^0 p$	10
5. Summary of the Results	16
Chapter II. Experimental Method	
1. Overview	19
2. Beam	19
3. Bubble Chamber	22
4. Spectrometer	23
5. Online Trigger and Data Collection Computer and Programs	29
Chapter III. Data Reduction	
1. Overview	33
2. Spark Chamber Data	33
3. Bubble Chamber Data	40
4. Merging the Spark Chamber and Bubble Chamber Data	44
5. Kinematic Fitting	46
6. Fit Selection	49
Chapter IV. Cross Section Determination	
1. Overview	56

	<u>Page</u>
2. Elastics Normalization	57
3. Beam Contamination	63
4. Geometrical Acceptance Correction	66
5. Computer Trigger Efficiency Correction	70
6. Channel Corrections and Background Estimates	77
Chapter V. Results of the Five-body Channels	
1. Overview	102
2. The $d\sigma/dt_{pN}$ Distributions	109
3. Invariant Masses Involving the Fast Pion	113
4. Fast Invariant Masses Selected on a Fast ρ Meson	126
5. Invariant Masses Involving the Slow System Particles	133
6. Associated Fast Meson and Slow System Resonance Production	159
7. Double Slow Resonance Production and Sequential Decays	205
Chapter VI. Production of the η^0 and ω^0 Mesons	
1. Introduction	237
2. $\pi^\pm \eta^0 p$ Final State	240
3. $\pi^\pm \omega^0 p$ Final State	251
4. Angular Distributions of the $\omega^0 p$ System	273
a) Phenomenology of Angular Distributions	273
b) Observed Angular Distributions	282
5. Discussion of the $\omega^0 p$ Resonance Spin-parity Analyses	324
Appendix A. Fast Algorithm	330

	<u>Page</u>
Appendix B. TORTIS Track Finding and Spark Chamber Calibration	
1. Track Finding	342
2. Calibration Test Quantities	347
3. Initial Calibration	350
4. Tracking the Calibration with Data Runs	351
Appendix C. Computer Trigger Efficiency Determination	355
List of References	360

List of Tables

<u>Table</u>		<u>Page</u>
I.1	$\pi^+ p \rightarrow \pi^+ \pi \pi \pi N$ cross sections	6
I.2	$\pi^- p \rightarrow \pi^- \pi \pi \pi N$ cross sections	7
I.3	Predicted maximum cross section estimates	9
I.4	$\pi^+ p \rightarrow \pi^+ p \omega^0$ and $\pi^+ p \rightarrow \pi^+ p \eta^0$ cross sections	11
I.5	$\pi^- p \rightarrow \pi^- p \omega^0$ and $\pi^- p \rightarrow \pi^- p \eta^0$ cross section	12
I.6	Predicted ω^0 and η^0 cross sections	12
I.7	A compilation of the observations of the $p \omega^0$ enhancement	15
II.1	Beam shape and momentum at bubble chamber	22
III.1	Results of the data collection and reduction for each experiment	35
III.2	Estimate of the fraction of 1C events assigned to the wrong channel	54
IV.1	Lost picture fractions	61
IV.2	Elastic Normalization quantities	62
IV.3	Four prong exposures	62
IV.4	Beam fractions	64
IV.5	Lost and background event counts in 1C 4-prong channels	80
IV.6	Normalizations and background fractions for the 1C 4-prong channels	101
V.1	Cuts used to define the 1C data sample	104
V.2	Observed channel cross sections	105
V.3	Results of the fits to $d\sigma/dt_{\pi\pi} = A \exp(B t_{\pi\pi})$	106
V.4	Results of the fits to $d\sigma/dt_{pN} = A \exp(B t_{pN} + Ct_{pN}^2)$	110

<u>Table</u>	<u>Page</u>	
V.5	Resonance masses and widths used in the fits	114
V.6	Major fast resonance production estimates	115
V.7	Additional fast resonance production estimates	116
V.8	Channel cross sections with fast resonance production removed	118
V.9	Background fractions and total events within fast ρ cuts	119
V.10	Estimated slow system resonance production	136-137
V.11	Background fractions and total events within slow Δ and ρ cuts	161
V.12	Estimated slow system resonance production for the fast ρ cuts	164-165
V.13	Estimated fast meson resonance production for slow system resonance cuts	186-187
V.14	Estimated slow system double resonance production	207
V.15	Estimated slow system resonance production with cascade decay	208
VI.1	Fitted parameters for $\eta^0 \rightarrow \pi^+ \pi^- \pi^0$ peak	240
VI.2	Fitted parameters for $\omega^0 \rightarrow \pi^+ \pi^- \pi^0$ peak	253
VI.3	Fitted parameters for the $\omega^0 p$ peak	265
VI.4	$d\sigma/dt_{\pi\pi}$ slopes for $\omega^0 p$ mass bands	269
VI.5	c_1 values from $1+c_1 \cos\phi_{pp}$ fits to the $d\sigma/d\phi_{pp}$ distributions	293
VI.6	Results of the $1+a_1 \cos\theta_{pp} + a_2 \cos^2\theta_{pp}$ fits to the $d\sigma/d\cos\theta_{pp}$ distributions	294
VI.7	Asymmetry of the $d\sigma/d\cos\theta_{pp}$ distributions	295

<u>Table</u>		<u>Page</u>
VI.8	a_2 values from fits of $1+a_2\cos^2\theta_{pn}$ to the $d\sigma/d\cos\theta_{pn}$ distributions	305
VI.9	Results of $1+c_1\cos\phi_{pn}+c_2\cos2\phi_{pn}$ fits to the $d\sigma/d\phi_{pn}$ distributions	306
VI.10	ω^0 Gottfried-Jackson frame ρ_{00} density matrix element	307
VI.11	a_2 values from $1+a_2\cos^2\theta_{n\omega}$ fits to the $d\sigma/d\cos\theta_{n\omega}$ distributions	309
VI.12	ω^0 helicity frame ρ_{00} density matrix element	318
VI.13	c_2 values from $1+c_2\cos2\phi_{n\omega}$ fits to the $d\sigma/d\phi_{n\omega}$ distributions	319
VI.14	ω^0 helicity frame ρ_{1-1} density matrix element	319
VI.15	$\cos\theta_{pp}$ versus $\cos\theta_{n\omega}$ correlation results for ω^0 peak events	321
VI.16	$\cos\theta_{pp}$ versus $\cos\theta_{n\omega}$ correlation results for ω^0 wings events	322
VI.17	$\cos\theta_{pp}$ versus $\cos\theta_{pn}$ correlation results for ω^0 peak events	323
VI.18	Predicted $\cos\theta_{pp}$ versus $\cos\theta_{n\omega}$ correlation pattern for $J^P=3/2^-$	326
VI.19	Combined $\cos\theta_{pp}$ versus $\cos\theta_{n\omega}$ correlation fractions	327
A.1	Definition of quantities in Appendix A	340
B.1	Constants correction formulae	353
B.2	R.M.S. run-to-run changes in the spark chamber constant constants (in inches)	354
C.1	$\vec{m}(p)$ coefficients	357
C.2	Elastic roll elastic mis-trigger fraction	359

List of Figures

<u>Fig.</u>		<u>Page</u>
I.1	Plots of the Tables I.1 and I.2 cross sections	8
I.2	Plots of the Tables I.4 and I.5 cross sections	13
II.1	Elevation view of the secondary beam line	21
II.2	Plan view of the bubble chamber and spectrometer	24
II.3	Schematic of the trigger, spark digitization, and computer input electronics	27
II.4	Flowchart of the online computer program	30
III.1	Flowchart of the data reduction process	34
IV.1	Contour plot of $\bar{\epsilon}(p, \cos\theta)$	69
IV.2	$\langle \epsilon_f \rangle$ versus recoil (N^*) mass	74
IV.3	$\langle \epsilon_f \rangle / \epsilon_{lin}(m_{N^*})$ versus recoil mass	75
IV.4	Corrected and uncorrected π^- recoil mass distributions	76
IV.5	Kinematic fit confidence level distributions for the 1C channels	78
IV.6a-d	Missing-mass-squared (mm^2) distributions ($dN/d\text{mm}^2$)	81-85
IV.7a-d	$dN/d\text{mm}^2$ for 1C events with $\text{CL} < 5\%$	87-89
IV.8a-b	$dN/d\text{mm}^2$ for 1C events rejected by ionization	92-93
IV.9a-b	$dN/d\text{mm}^2$ for 1C events with a rejected ambiguous 1C fit	94-95
IV.10a-d	$dN/d\text{mm}^2$ for 1C events with an ambiguous 1C fit	96-98
V.1	General Feynman diagrams representing our data	103
V.2	$d\sigma/dt_{\pi\pi}$ for the 1C reactions	108
V.3	$d\sigma/dt_{pN}$ for the 1C reactions	111

<u>Fig.</u>		<u>Page</u>
V.4	$d\sigma/dt_{pp}$ for the 4C reactions	112
V.5a-l	dN/dm for fast invariant masses	120-125
V.6a-k	dN/dm for fast invariant masses cut on ρ_f^0 or ρ_f^\pm	128-132
V.7a-k	$d\sigma/dm$ for π^0 channel slow system invariant masses	138-149
V.8a-h	$d\sigma/dm$ for n channel slow system invariant masses	150-158
V.9a-g	dN/dm for π^0 channel slow system invariant masses cut on ρ_f^0	166-173
V.10a-f	dN/dm for n channel slow system invariant masses cut on ρ_f^0	174-180
V.11a-d	dN/dm for π^0 channel slow system invariant masses cut on ρ_f^\pm	181-185
V.12a-j	dN/dm for fast invariant masses cut on Δ^{++} or Δ^-	188-192
V.13a-l	dN/dm for fast invariant masses cut on slow ρ^0	193-198
V.14a-n	dN/dm for fast invariant masses cut on slow ρ^\pm	199-204
V.15a-d	$d\sigma/dm$ for π^0 channel slow system invariant masses cut on Δ^{++}	209-213
V.16a-b	$d\sigma/dm$ for n channel slow system invariant masses cut on Δ^-	214-216
V.17a-d	$d\sigma/dm$ for π^0 channel slow system invariant masses cut on slow ρ^0	217-221
V.18a-d	$d\sigma/dm$ for n channel slow system invariant masses cut on slow ρ^0	222-226
V.19a-d	$d\sigma/dm$ for π^0 channel slow system invariant masses cut on slow ρ^+	227-231
V.20a-d	$d\sigma/dm$ for π^0 channel slow system invariant masses cut on slow ρ^-	232-236

<u>Fig.</u>		<u>Page</u>
VI.1	dN/dm for $\pi_F^\pm \eta^0$ mass showing A_2^\pm exclusion cut	239
VI.2	$d\sigma/dm$ for $\pi^+ \pi^- \pi^0$ mass in η^0 region	241-242
VI.3	$d\sigma/dm$ for $\eta^0 p$ mass	245
VI.4	Feynman diagrams for η^0 production	247
VI.5a-b	Scatterplots of $\pi^+ \pi^- \pi^0$ mass versus $\pi^+ \pi^- \pi^0 p$ mass	249-250
VI.6	$d\sigma/dm$ for $\pi^+ \pi^- \pi^0$ mass in ω^0 region	252
VI.7a-b	$dN/d\lambda$ for events in ω^0 peak and in ω^0 wings	254-256
VI.8	$d\sigma/dt_{\pi\pi}$ for events in ω^0 peak	258-259
VI.9	$d\sigma/dm$ for $\omega^0 p$ mass	261
VI.10	Scatterplot of $\pi_F^+ \omega^0$ mass versus $\omega^0 p$ mass	262
VI.11a	Scatterplot of $\pi^+ p$ mass versus $\omega^0 p$ mass	263
VI.11b	Scatterplot of $\pi^+ p$ mass versus $\pi^+ \pi^- \pi^0 p$ mass	264
VI.12a-b	$d\sigma/dt_{\pi\pi}$ for separate $\omega^0 p$ mass regions	266-268
VI.13	s dependence of $N^* \rightarrow \omega^0 p$ production cross section	270
VI.14	Definition of $\omega^0 p$ Gottfried-Jackson frame and the (θ_{pp}, ϕ_{pp}) angles	279
VI.15a	Definition of ω^0 Gottfried-Jackson frame and the (θ_{pn}, ϕ_{pn}) angles	280
VI.15b	Definition of ω^0 helicity frame and the $(\theta_{n\omega}, \phi_{n\omega})$ angles	281
VI.16a	$\langle Y_\ell^m \rangle$ versus $\omega^0 p$ mass	284
VI.16b	$\langle Y_\ell^m \rangle$ versus $\pi^+ \pi^- \pi^0 p$ mass (ω^0 wings)	285
VI.17a-b	$d\sigma/d\cos\theta_{pp}$ for low masses	287-288
VI.18a-b	$d\sigma/d\phi_{pp}$ for low masses	289-290
VI.19a-b	$d\sigma/d\cos\theta_{pp}$ for high masses	291-292

<u>Fig.</u>		<u>Page</u>
VI.20	$\cos\theta_{pp}$ asymmetry versus $\omega^0 p$ mass	296
VI.21a-b	$d\sigma/d\cos\theta_{pn}$ for low masses	297-298
VI.22a-b	$d\sigma/d\phi_{pn}$ for low masses	299-300
VI.23a-b	$d\sigma/d\cos\theta_{pn}$ for high masses	301-302
VI.24a-b	$d\sigma/d\phi_{pn}$ for high masses	303-304
VI.25	ω^0 Gottfried-Jackson frame ρ_{00} versus $\omega^0 p$ mass	308
VI.26a-b	$d\sigma/d\cos\theta_{n\omega}$ for low masses	310-311
VI.27a-b	$d\sigma/d\phi_{n\omega}$ for low masses	312-313
VI.28a-b	$d\sigma/d\cos\theta_{n\omega}$ for high masses	314-315
VI.29a-b	$d\sigma/d\phi_{n\omega}$ for high masses	316-317
A.1	Schematic of FAST track analysis algorithm	341

Chapter I

Introduction

1. Diffractive Dissociation

The major single component of the total cross section ($\sim 30\%-50\%$) for hadron-hadron scattering is forward diffractive scattering. This type of scattering consists of two similar parts: elastic scattering and inelastic diffractive dissociation. Diffractive dissociation reactions are similar to elastic scattering except that one of the particles involved in the reaction is transformed into several final state particles. As was first pointed out by Good and Walker [1960], this process is analogous to the diffraction of polarized light by a polarizer in which the incoming internal state (polarization) is transformed into a new outgoing internal state.

Hadronic diffraction has been extensively studied in many experiments (see the reviews by Leith [1975] for instance). In general, diffractive dissociation has properties similar to those of elastic scattering. Compared to other inelastic processes, both have very little energy dependence, are independent of the non-diffracting incoming particle (factorizable), and are sharply forward-peaked [Leith 1975]. Theoretical ideas on diffractive dissociation stress this similarity; exchange of the Pomeron Regge pole is used to explain both elastic scattering and inelastic diffractive dissociation. Other theoretical models, such as that of Drell, Hiida, and Deck [Drell and Hiida 1961 and Deck 1964], have been put forward to explain non-resonant

diffractive dissociation in which the final state particles do not come from a diffractively produced excited state. Much experimental work has been invested in studying these non-resonant states as in the diffraction of beam pions into a low mass 3π system, in particular the A_1 and A_3 effects. At the same time, studies of the diffractive production of the A_2 meson from beam pions have shown that excited states can be diffractively produced.

2. This Experiment

As mentioned above, pion dissociation has been very extensively studied in many experiments. Nucleon dissociation, unlike pion dissociation, has yet to be examined by any experiment with comparable statistics. Our experiment was conceived to provide a high statistics body of data on nucleon diffractive dissociation by pion beams. This experiment also had to cover most of the 4π solid angle so that the particle angular distributions resulting from the fragmentation of the nucleon would be unbiased. The necessity of a laboratory frame 4π detector can be gotten around by using a nucleon beam where the products of nucleon dissociation appear as a system of fast forward particles. Such an experiment still requires a large forward detector system to cover most of the 4π solid angle in the beam nucleon rest frame. In addition there is the added complication of the veto system for the nucleon target to insure that only the beam particle dissociates. This veto system introduces further inefficiencies, particularly in the region of low momentum transfer where the target recoil

particles may not have enough momenta to reach the veto detectors due to energy loss in the target and its container. Finally, with a pion beam it is very easy to change from a particle to an anti-particle beam (π^+ to π^-) to test factorization while antiproton targets do not exist.

By using a liquid hydrogen bubble chamber as the target and detector, nearly complete coverage of the laboratory 4π solid angle is possible. However, a standard bubble chamber experiment designed to gather large numbers of events in the proton diffractive dissociation region would require an unmanageably large number of pictures, most of which would be of elastic scattering, pion diffraction, or non-diffractive events. The film processing load can be reduced to a workable size if only those events of interest are recorded by somehow triggering the bubble chamber. Since the bubble chamber must be made track-sensitive before each beam pulse (by sharply reducing the pressure, a process with a millisecond time scale), this trigger must operate between the time of the beam pulse and the time (1-2 milliseconds later) when the camera flash lamps would normally be fired. Thus the trigger for the bubble chamber is of the camera flash lamps, not the bubble chamber expansion mechanism.

Our experiment used as a trigger the requirement that the mass recoiling against a fast forward particle be within preset limits (the lower limit was just above the elastic peak). We detected and measured the fast forward particle in a magnetic spectrometer just downstream of the bubble chamber. The trigger calculations were done by

an online computer. Since a triggered bubble chamber does not take a picture with every beam pulse, a rapid cycling bubble chamber allows for a modest real event rate even if the trigger conditions are met for only a few percent of the pulses. The SLAC 40 inch rapid cycling bubble chamber (4-10 pps) was chosen for this experiment. This chamber also had a beam exit window through the magnetic flux return, a necessary condition for this experiment. A pion beam with a momentum of 14 GeV/c was used. At this momentum we had sufficient beam intensity to have about 10 beam tracks per pulse in the bubble chamber in a very small momentum bite (about $\pm 0.3\%$).

The experimental apparatus and data reduction procedures are discussed further in later chapters. More details of the experimental apparatus and the data reduction procedures (especially concerning hybridization) are to be found in the thesis of L. C. Rosenfeld [Rosenfeld 1977]. A discussion of diffractive dissociation in the reactions:

$$\pi^{\pm} p \rightarrow \pi^{\pm} p \pi^0 \quad (1a)$$

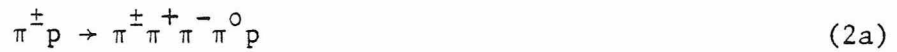
$$\pi^{\pm} p \rightarrow \pi^{\pm} \pi^+ n \quad (1b)$$

$$\pi^{\pm} p \rightarrow \pi^{\pm} \pi^+ \pi^- p \quad (1c)$$

observed in this experiment has been published elsewhere [Chadwick 1978].

3. Five-body Final States: $\pi p \rightarrow \pi\pi\pi\pi N$

The 5-body final states produced by pion beams:



are examined in this thesis. These reactions have been studied by several other bubble chamber experiments. Tables I.1 and I.2 list several of these experiments giving the beam momenta and cross sections observed for these reactions. These final states have been found to be very rich with many sub-reactions involving one or more resonances. The extent to which diffractive dissociation contributes to these final states is unclear and buried beneath the contributions of many other processes.

The cross sections given in Tables I.1 and I.2 were fit with the form ap^{-n} (p is the laboratory beam momentum) to obtain estimates of the cross sections at our beam momenta. These estimates of the total 5-body cross sections are given in Table I.3. The cross sections observed in our experiment are expected to be smaller than those in Table I.3 as some unknown fraction of the total cross section is excluded by the trigger condition. We can expect that our trigger will exclude all or part of those reactions in which the fastest pion is one of the decay products of a resonance. The arrangement of our apparatus is such that only very fast pions (with more than half the beam momentum) of the same charge as the beam can trigger the experiment. Slower pions and oppositely charged pions are bent into the sides of the

Table I.1

$\pi^+ p \rightarrow \pi^+ \pi \pi \pi N$ cross sections

Reference	P_{beam} (GeV/c)	σ (μb)	
		$\pi^+ p \rightarrow \pi^+ \pi^+ \pi^- \pi^0 p$	$\pi^+ p \rightarrow \pi^+ \pi^+ \pi^+ \pi^- n$
Aderholz 1965	4		930±330
Otter 1975	4	3430±690	
Brown 1970	4.08	3780±360	970±100
Pols 1971	5	2880±40	850±20
Prentice 1971	5.5	1940±190	
Slattery 1967	7	2200±200	
Wagner 1975	7.1	2160±90	
Deutschmann 1964	8	2100±200	900±100
Aderholz 1968	8.04	1910±80	740±70
Kung 1969	8.5	2120±327	
Kennedy 1978	10.3	1654±100	503±38
Baltay 1978	15	1005±77	
Ballam 1971	16	1280±170	
Ballam 1967	16		350±100
Grassler 1974	16	1050±100	360±60
Hones 1974	18.5	1200±150	

Table I.2

$\pi^- p \rightarrow \pi^- \pi \pi \pi N$ cross sections

<u>Reference</u>	<u>P_{beam}</u> <u>(GeV/c)</u>	<u>σ (μb)</u>	
		<u>$\pi^- p \rightarrow \pi^- \pi^+ \pi^- \pi^0 p$</u>	<u>$\pi^- p \rightarrow \pi^- \pi^+ \pi^+ \pi^- n$</u>
Bondar 1964	4	2110±90	1100±60
Chung 1968	4.2	2180±110	1160±60
Miyashita 1970	6.7	1720±200	1170±100
Milgram 1970	6.9	1600±120	
Cason 1970	8	1390±90	530±40
Biswas 1964	10.25	1770±350	1030±340
Caso 1967	11	1200±200	650±100
Kittel 1971	11	1240±110	680±50
Brandenburg 1970	13	840±80	
Ballam 1971	16	1240±150	
Ballam 1967	16		650±100
Kittel 1971	16	820±100	450±50
Cason 1973	18.5	860±70	
Sisterson 1972	20	780±100	

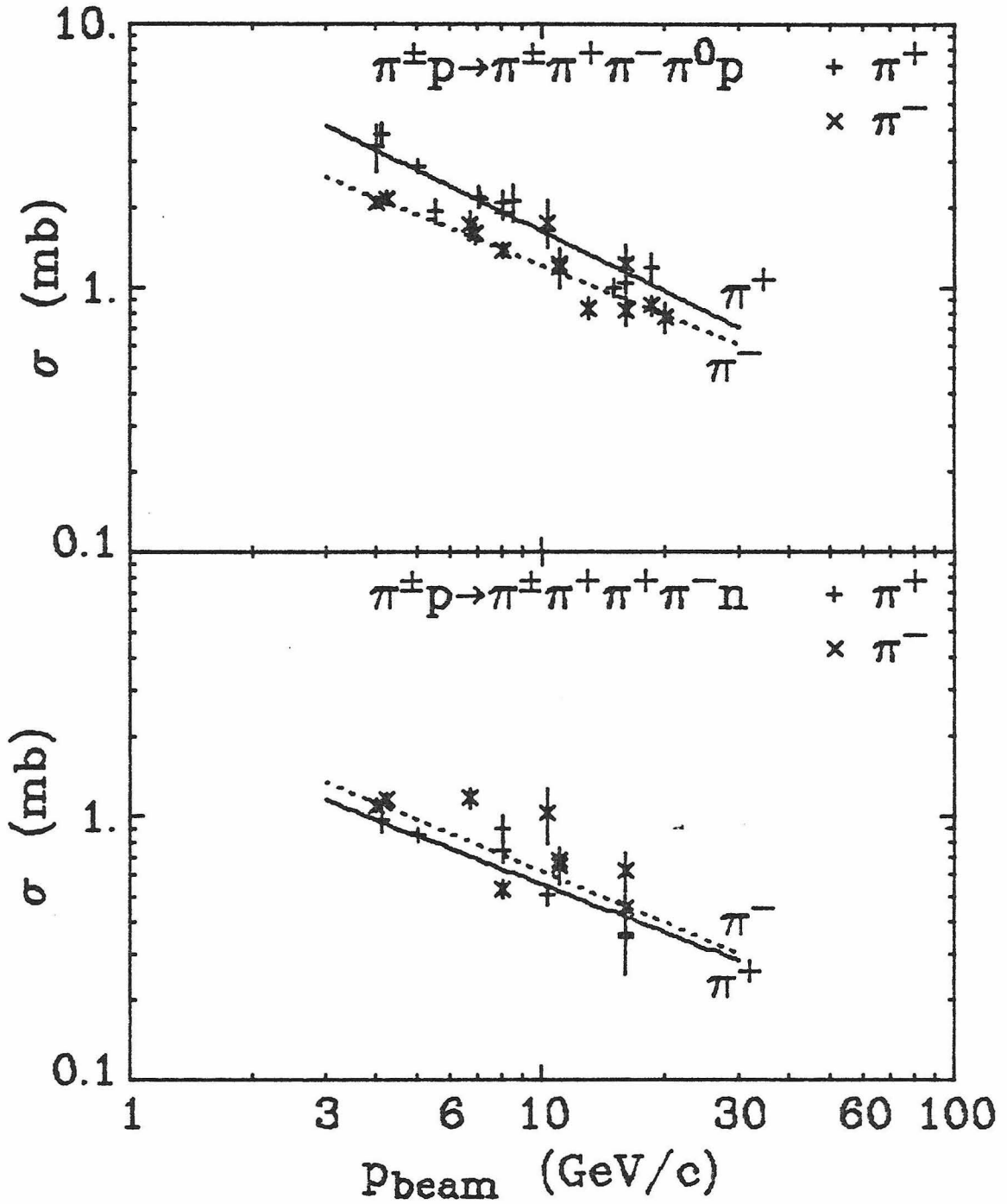


Figure I.1

Plots of the cross sections listed in Tables I.1 and I.2. The lines are from the ap^{-n} fits used to interpolate to our beam momenta.

apertures of the magnets. At least half of the events with a neutral fast meson (such as a ρ^0) will be lost due to decays in which the pion going forward has the opposite charge relative to the beam. Also, since the software trigger places a modest upper limit on the mass recoiling against the fast pion, the fraction of such resonance decays lost will be greater than one half. From an examination of the quasi-2-body and quasi-3-body cross sections measured in other experiments, we expect that this experiment will observe between 25% and 50% of the cross sections given in Table I.3.

Table I.3

Predicted maximum cross section estimates

<u>Final State</u>	<u>σ (μb)</u>
$\pi^+ \pi^+ \pi^- \pi^0 \text{p}$	1290 ± 70
$\pi^- \pi^+ \pi^- \pi^0 \text{p}$	980 ± 130
$\pi^+ \pi^+ \pi^+ \pi^- \text{n}$	460 ± 100
$\pi^- \pi^+ \pi^+ \pi^- \text{n}$	450 ± 70

The previous works on the final states listed above have concentrated on meson resonances such as:

$$\pi^\pm \text{p} \rightarrow \text{g}^\pm (1680) \text{p} \quad (3\text{a})$$

$$\pi^\pm \text{p} \rightarrow \text{B}^\pm (1235) \text{p} \quad (3\text{b})$$

$$\pi^\pm \text{p} \rightarrow \text{A}_2^\pm (1310) \text{p} \quad (3\text{c})$$

and quasi-2-body reactions including:

$$\pi^+ p \rightarrow \omega^0 \Delta^{++} \quad (4a)$$

$$\pi^- p \rightarrow \omega^0 \Delta^0 \quad (4b)$$

among others. In these works, the more detailed studies were in addition to the measurements of semi-inclusive resonance production in these explicit final states (reactions (2a) and (2b)). Thus there is no body of data to which we can directly compare our results in detail for the 5-body final states because reactions such as those given in (3) and (4) are mostly excluded by our geometrical and trigger acceptances. However, there are some quasi-3-body reactions that have been studied by other experiments in kinematic regions that overlap ours.

4. $\pi^\pm p \rightarrow \pi^\pm \omega^0 p$ and $\pi^\pm p \rightarrow \pi^\pm \eta^0 p$

The quasi-3-body reactions:

$$\pi^\pm p \rightarrow \pi^\pm \omega^0 p \quad (5a)$$

$$\pi^\pm p \rightarrow \pi^\pm \eta^0 p \quad (5b)$$

have been investigated in bubble chamber experiments as sub-reactions of the final states in (2) by virtue of the $\pi^+ \pi^- \pi^0$ decays of the ω^0 and η^0 mesons. Tables I.4 and I.5 list some of these experiments giving the beam momenta and observed cross sections for these reactions. The cross sections have been corrected for the unseen decay modes of the ω^0 and η^0 mesons. As in the previous section, these cross sections were fitted by ap^{-n} and the total reaction cross sections at our beam momenta were estimated (see Table I.6). However,

Table I.4

$\pi^+ p \rightarrow \pi^+ p \omega^0$ and $\pi^+ p \rightarrow \pi^+ p \eta^0$ cross sections

<u>Reference</u>	<u>P_{beam} (GeV/c)</u>	<u>σ (μb)</u>	
		<u>$\pi^+ p \rightarrow \pi^+ p \omega^0$</u>	<u>$\pi^+ p \rightarrow \pi^+ p \eta^0$</u>
Otter 1975	4	901±222	
Otter 1975	5	545±23	
Prentice 1971	5.5	510±71	162±33
Otter 1975	8	245±22	
Kennedy 1978	10.3	137±13	76±13
Baltay 1978	15	51.5±5.5	31±5
Bartke 1977	16	117±12	35±5
Otter 1975	16	70±7	
Hones 1970	18.5	101±14	34±9

Table I.5

$\pi^- p \rightarrow \pi^- p \omega^0$ and $\pi^- p \rightarrow \pi^- p \eta^0$ cross sections

<u>Reference</u>	<u>P_{beam}</u> <u>(GeV/c)</u>	<u>σ (μb)</u>	
		<u>$\pi^- p \rightarrow \pi^- p \omega^0$</u>	<u>$\pi^- p \rightarrow \pi^- p \eta^0$</u>
Bondar 1964	4	289±45	
Chung 1968	4.2	206±28	89±30
Gordon 1975	6	482±47	
Miyashita 1970	6.7	178±24	
Armenise 1973	9.1	137±24	
Biswas 1964	10.25	133±56	
Caso 1967	11	78±33	85±42
Bartke 1977	16	82±11	17±5
Cason 1973	18.5	39±5	31±7
Sisterson 1972	20	48±10	
Gordon 1975	22	31±8	19.5±6.6

Table I.6

Predicted ω^0 and η^0 cross section estimates

<u>Reaction</u>	<u>Total_†</u> <u>σ (μb)</u>	<u>Observable</u> <u>σ (μb)</u>
$\pi^+ p \omega^0$	92±14	39±8
$\pi^- p \omega^0$	63±10	20±10
$\pi^+ p \eta^0$	38±9	3±2
$\pi^- p \eta^0$	22±11	6±5

(† corrected for unseen decays)

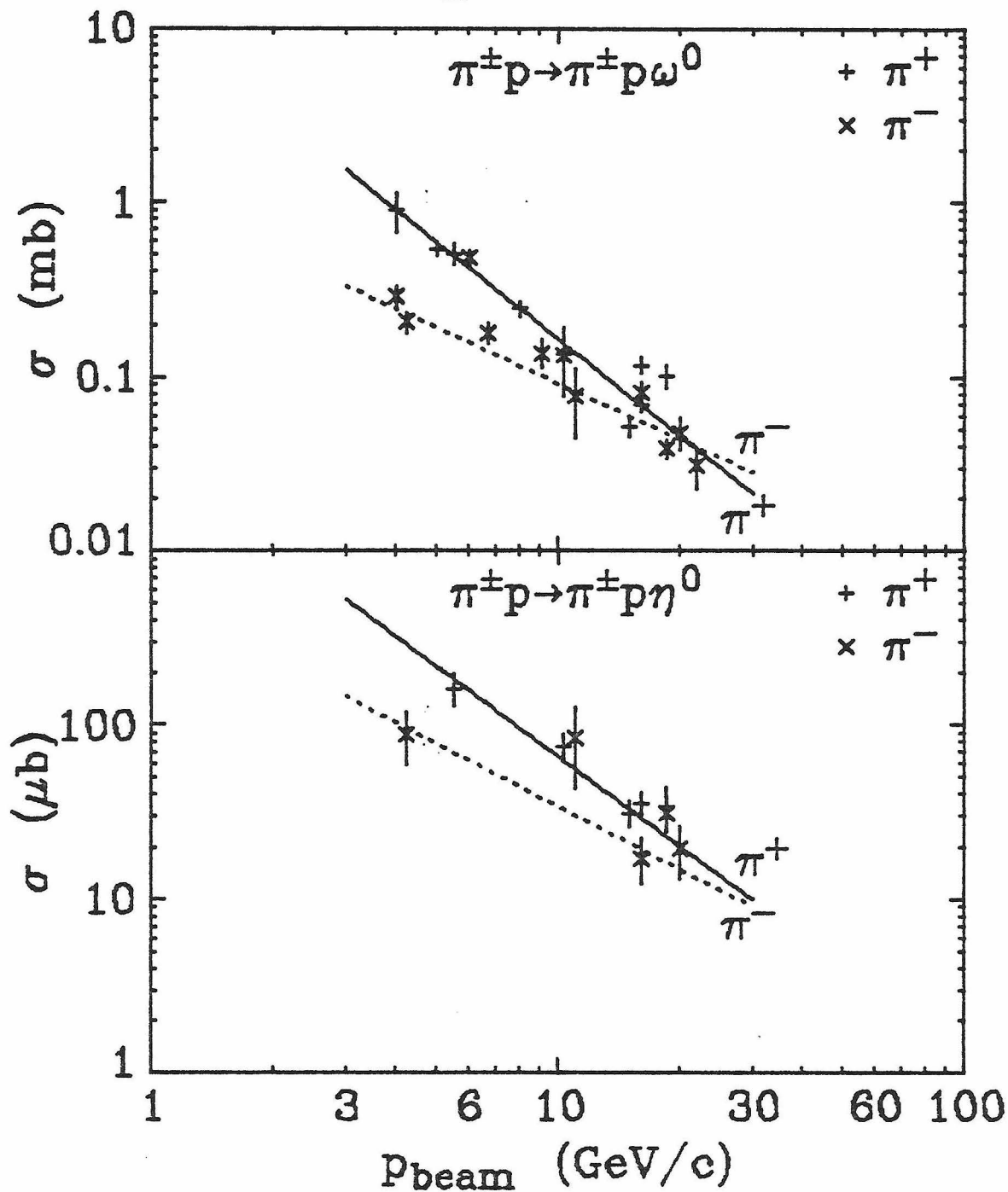


Figure I.2

Plots of the cross sections listed in Tables I.4 and I.5. The lines are from ap^{-n} fits used to interpolate to our beam momenta.

once again our experiment cannot observe the full kinematic range of reactions (5). Previous experiments have concentrated on investigations of the B meson (reactions (3b) via $B^{\pm} \rightarrow \pi^{\pm} \omega^0$), the A_2 meson (reactions (3c) via $A_2^{\pm} \rightarrow \pi^{\pm} \eta^0$), and the quasi-2-body reactions in (4). It is precisely these reactions that our trigger rejects in whole or part. Some data does exist [Baltay 1978, Caso 1967, Cason 1973, and Kennedy 1978] that allows us to make rough estimates of the cross sections we should observe for reactions (5). These estimates are also given in Table I.6 (in the "Observable" column, uncorrected for unseen decays). These estimates are made by subtracting the $B^{\pm} p$ and $\omega^0 \Delta^{++}$ or $\omega^0 \Delta^0$ cross sections from the total $\pi^{\pm} \omega^0 p$ cross section and subtracting the $A_2^{\pm} p$ ($A_2^{\pm} \rightarrow \pi^{\pm} \eta^0$) cross section from the total $\pi^{\pm} \eta^0 p$ cross section (the error on the $\pi^{\pm} \eta^0 p$ estimate is due to the scantiness of the data).

Several experiments, including ours in preliminary results, have reported observation of a $\rho\omega^0$ enhancement at about 1800 MeV. All these experiments were bubble chamber experiments and their results are based on relatively few events (exposures on the order of a few events per microbarn). A collection of the observations are given in Table I.7. Preliminary results reported for our experiment [Davidson 1974 and Linglin 1974] are included for completeness. For many of the experiments (as noted in the table) the cross section of the enhancement was estimated by us from data and figures given in the reference.

Given the observation of this $\rho\omega^0$ enhancement in several beams at many energies, this effect seems to be an N^* which couples strongly to $\rho\omega^0$. The narrow width seen for the enhancement seems to support this

Table I.7

A compilation of the observations of the $p\omega^0$ enhancement

<u>Reference</u>	<u>Beam</u>	<u>P_{beam} (GeV/c)</u>	<u>Mass (MeV)</u>	<u>Width (MeV)</u>	<u>σ (μb)</u> ^{a)}
Atherton 1975	\bar{p}	5.7	1810 \pm 15	87 \pm 20	14 \pm 3 ^{c)}
Davidson 1974	π^-	4.5 6 14.2 ^{b)}	1820	120	9 \pm 1.9 10.6 \pm 2.7 5.2 \pm 1.2
Guyader 1971	p	13.1	1750 \pm 25	100 \pm 25	16 \pm 4 ^{c)}
Juhala 1969	K^-	4.6-5	1780		9 \pm 3 ^{d)}
Linglin 1974	π^+	7 13.7 ^{b)}	1800 \pm 15	110 \pm 20	7.2 \pm 2 6 \pm 1
Milgram 1970	π^-	3 7	1764 \pm 18	115 \pm 50	9.2 \pm 2 8.1 \pm 1.5
Chien 1976	K^+	6.8			15 \pm 5 ^{d)}
Colton 1970	p	6.6			18 \pm 5 ^{c,d)}
Davis 1972	K^+	12			2.5 \pm 0.8 ^{d)}
Sisterson 1970	π^-	20			8 \pm 2 ^{d)}
Theocharopoulos 1974	K^-	8.25			5 \pm 2 ^{d)}
Wohl 1978	K^-	14.3			3 \pm 2 ^{d)}

a) cross section is for $\omega^0 \rightarrow \pi^+ \pi^- \pi^0$ decay mode.

b) preliminary results of this experiment.

c) cross section is one half that quoted in or estimated from reference for comparison to πp or Kp data.

d) cross section estimated from data and figures in reference.

view. This interpretation has been pointed out in other papers as well [Atherton 1975 and Milgram 1970]. Some experiments have attempted to explain the enhancement with a Double Regge Pole Model (DRPM) with varying degrees of success [Sisterson 1970, Milgram 1970, and Juhala 1969]. For the most part, however, this effect seems as well established as an N^* as some of the other resonances listed in the Particle Data Tables [Particle Data Group 1978]. With our large statistics, we can investigate this effect in more depth, including more detailed studies of the $\omega^0 p$ angular distributions than done previously.

5. Summary of the Results

We present plots of the invariant mass distributions for the reactions:

$$\pi^\pm p \rightarrow \pi_f^\pm \pi^+ \pi^- \pi^0 p \quad (6a)$$

$$\pi^\pm p \rightarrow \pi_f^\pm \pi^+ \pi^+ \pi^- n \quad (6b)$$

where the fast pion (π_f^\pm) was used to trigger the experiment. Our experiment separates these reactions into a fast pion with a momentum above 8 GeV/c and a slow system of three pions and a nucleon. The slow system particles have momenta below 1 GeV/c for the majority of the events. The fast invariant masses (involving the π_f^\pm) show strong ρ_f^0 and ρ_f^\pm peaks. These fast mesons are correlated to some extent with the production of resonances (Δ or ρ) in the slow system. By subtracting the estimated contributions of the fast meson resonances, the resulting reduced channel cross sections are nearly independent of the

sign of the beam as would be expected for diffractive dissociation.

The reduced $\pi^+ \pi^- \pi^0 p$ channel cross sections are approximately twice the $\pi^+ \pi^+ \pi^- n$ channel cross sections.

Examination of the slow system mass distributions reveals that they are very rich in resonance production. The Δ^{++} and Δ^- are particularly strong with about one half of the $\pi_f^+ \pi^+ \pi^- \pi^0 p$ channel events being from $\pi_f^+ \pi^- \pi^0 \Delta^{++}$. Some double resonance production in the slow system is seen, in particular the reaction:



has a fairly large signal. The quasi-3-body reactions (including (7), $\rho_f \Delta \pi$, and $\rho_f \rho N$) are very prolific while the quasi-2-body reactions are relatively weak. The most prominent quasi-2-body reactions are:



A peak in the $\pi^+ \pi^+ \pi^- n$ mass spectra at about 1700 MeV appears to be a new decay mode of a known N^* . The decay scheme seems to be:



A second peak, this one in the $\pi^+ \pi^- \omega^0 p$ mass spectra, was found to be the ω^0 resonance discussed in the previous section. This N^* was found to have a mass of 1790 ± 5 MeV and a very narrow width of 81 ± 9 MeV (narrow relative to the known N^* 's). Studies of the angular distributions of the $\omega^0 p$ system were made in an effort to determine the spin-parity of the N^* . Though our results are in good agreement with other experiments from which Lednicky [1975] found a J^P of $3/2^-$ for the $\omega^0 p$ resonance, the failure of some of the predictions using this result when compared to our data raises questions about the validity of the assumptions underlying the spin-parity analysis.

We have also studied the η^0 production in the relatively unexplored kinematic region of low $|t_{\pi\pi}|$ and small $\eta^0 p$ mass. We found that the $\pi^+ \eta^0 p$ cross section was about twice the $\pi^- \eta^0 p$ cross section in this kinematic region. We interpret this difference in the cross sections due to the change in the sign of the beam as evidence for the importance of negative signature Regge trajectory exchange (such as the ρ) in this reaction at our energy. This interpretation can also explain the presence of a 1600 MeV peak in the $\eta^0 p$ mass spectrum of the π^+ data while the π^- data has no indications of such a peak.

Chapter II

Experimental Method

1. Overview

In this experiment, we have merged a missing mass technique with a bubble chamber to study nucleon diffraction-like processes. A magnetic spectrometer equipped with wire spark chambers was placed downstream of the bubble chamber to measure the momentum and angles of the pion scattered out of the beam. This measurement allowed an online computer program to calculate the missing mass of the nucleon system recoiling against this fast forward particle. We then used this online missing mass measurement to trigger the bubble chamber flash lamps in order to enhance the number of inelastic nucleon excitations observed on the film. The spectrometer information was also used in the offline data reduction to improve the measurement of the momentum of the fast forward particle.

2. Beam

The experiment was done in beam line 14 of the Stanford Linear Accelerator Center. A schematic of the beam line is shown in Fig. II.1. A 19 GeV/c electron beam from the accelerator was targeted on a 1 radiation length beryllium target to produce the secondary pion beam at a 1° production angle. The pions produced in the target were transported to the bubble chamber (BC) by a series of bends in the vertical plane. The beam was brought to a focus at two positions before reaching the BC. The first focus (F1) provided preliminary

momentum definition for the beam. The slits at F1 were preceded by 1.1 radiation lengths of lead to reduce the electron and positron beam fractions. Though the F1 slits were moveable, they were left in fixed positions during the data taking. We varied the secondary beam intensity by changing the intensity of the primary electron beam.

The second focus (F2) came after the main vertical bend so that the collimator located there served as the momentum defining slit (fixed position and size). For both the π^+ and π^- beams, the F2 slit was followed by a pair of scintillation counters (B1 and B2) that were primarily used in beam tuning and monitoring. During part of the π^+ running we also had a scintillator (B0) and a set of proportional wire chambers (PWC's) before the momentum slit as aids in beam tuning.

Immediately before the BC vacuum tank, we placed another scintillator (B3). The computer trigger software used B3 to prevent a BC picture from being taken if too many or no beam particles passed through B3. For the π^+ running, another set of PWC's were added upstream of B3. These two chambers were arranged with their wires at right angles and then rotated about the beam as a unit through an angle of 45° (see the discussion of the spectrometer's XY and UV coordinate systems below). This orientation was used because the beam had a very narrow horizontal width. These PWC's were used to define the beam profiles during tuning and were used for part of the π^+ data reduction to reduce the uncertainty in the beam particle's momentum vector.

The nominal beam shape and momenta are given below in Table II.1.

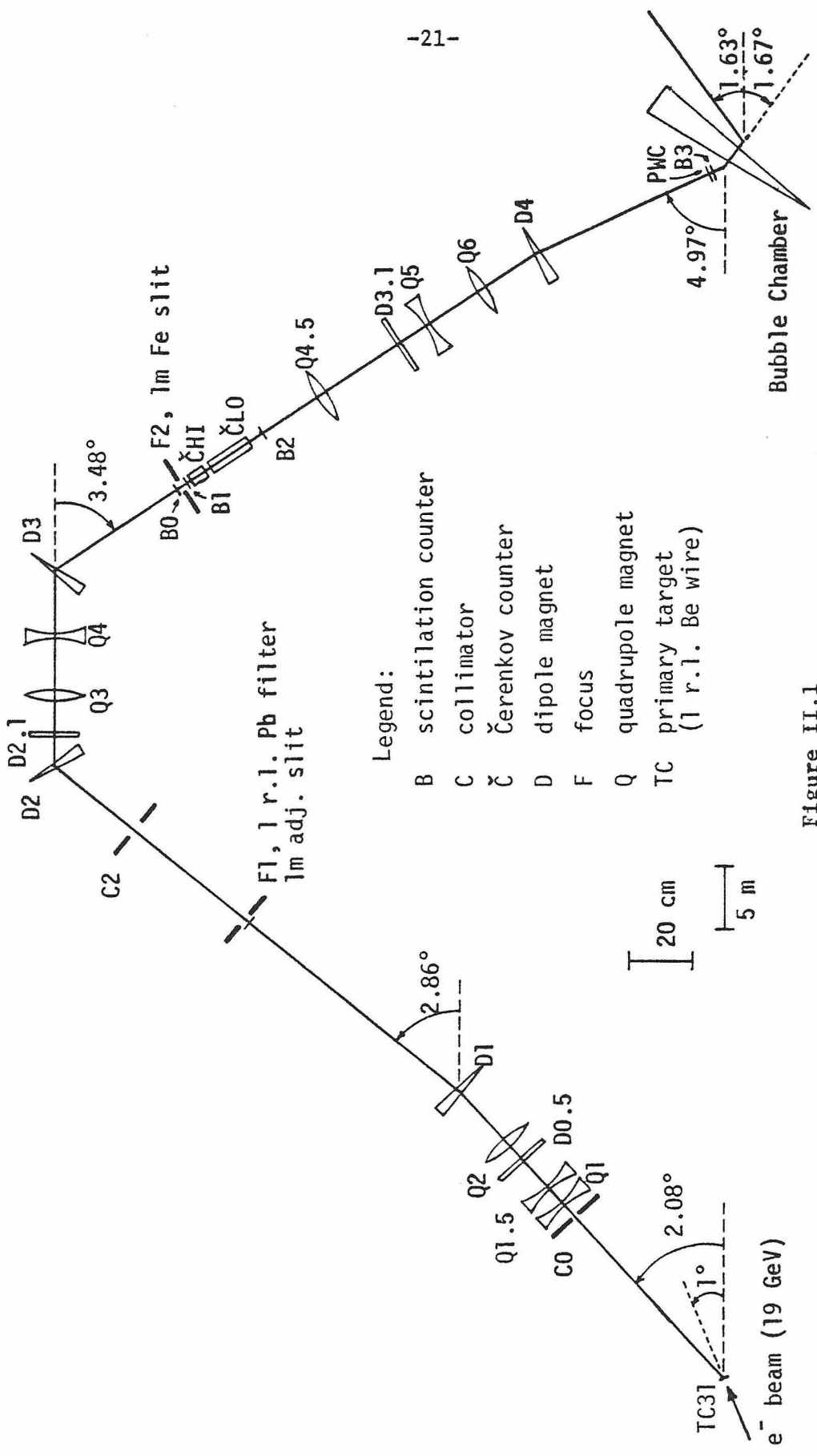


Figure II.1

Elevation view of the secondary beam line. This beam line was used to form the 14 GeV/c π^\pm beam and transport it to the bubble chamber. All major bends were in the vertical plane. The horizontal trim magnets (D0.5, D2.1, and D3.1) were normally off (zero bend).

Table II.1

Beam shape at the bubble chamber

Vertical FWHM	15 cm
Horizontal FWHM	0.8 cm
Azimuthal angular FWHM	1.5 mrad
Horizontal (dip) angular FWHM	2.2 mrad

Beam momentum at the bubble chamber

	<u>p (GeV/c)</u>	<u>σ (MeV/c)</u>	<u>$\delta p/p$</u>
π^-	14.20	36	0.22%
π^+	13.72	55	0.40%

3. Bubble Chamber

The SLAC 40" liquid hydrogen bubble chamber was used as the target for this experiment. The beam was brought to a horizontal focus and dispersed to an approximately parallel beam in the vertical plane as seen from the observed beam dimensions in Table II.1. The 40" bubble chamber can be run at a rate of 2 to 12 expansions per second; we took most of the π^- beam data at 4 pps while much of the π^+ data was taken at 8.6 pps. Although the bubble chamber can be expanded and made track sensitive at these rates, its camera can only take 2 pictures per second.

The magnetic field of the 40" bubble chamber was set to bend the beam upwards in a vertical plane so the non-interacting beam particles and the fast forward scattered pion passed through the bubble chamber's vacuum tank exit window (8 inch diameter). The field value was set to

26 kilogauss to bend a 14 GeV/c beam through about 6.6° . The exact field values were determined from the data by the standard method of measuring the apparent invariant mass of neutral vees. For those vees that fit the hypothesis $K_S^0 \rightarrow \pi^+ \pi^-$, the field scale was adjusted until the $\pi^+ \pi^-$ invariant mass was centered on the K^0 mass. The position dependent values of the field were determined from this scale value and a separately measured field map made by the SLAC technical staff. In addition to the main field map, we also used a map of the fringe field in HYBRID, the program used to connect the bubble chamber and spark chamber measurements.

4. Spectrometer

Unscattered beam particles and fast forward scattered pions left the bubble chamber through the 8 inch (diameter) exit window of the BC vacuum tank. This aperture limited the maximum angle acceptance of our magnetic spectrometer. The spectrometer consisted of four stations of magnetostrictive readout wire spark chambers, two on either side of the magnet (see Fig. II.2). The magnet was a 40D48 with an $\int B d\ell$ of 28.56 Kg-m, thus bending a 14 GeV/c particle through an angle of 61.2 milliradians. The 15 inch vertical aperture of the magnet limited our low momentum acceptance because low momentum particles left the bubble chamber at larger vertical angles than the high momentum particles due to being bent more in the bubble chamber magnetic field. Thus low momentum particles that made it through the BC vacuum exit window generally hit the spectrometer magnet above its

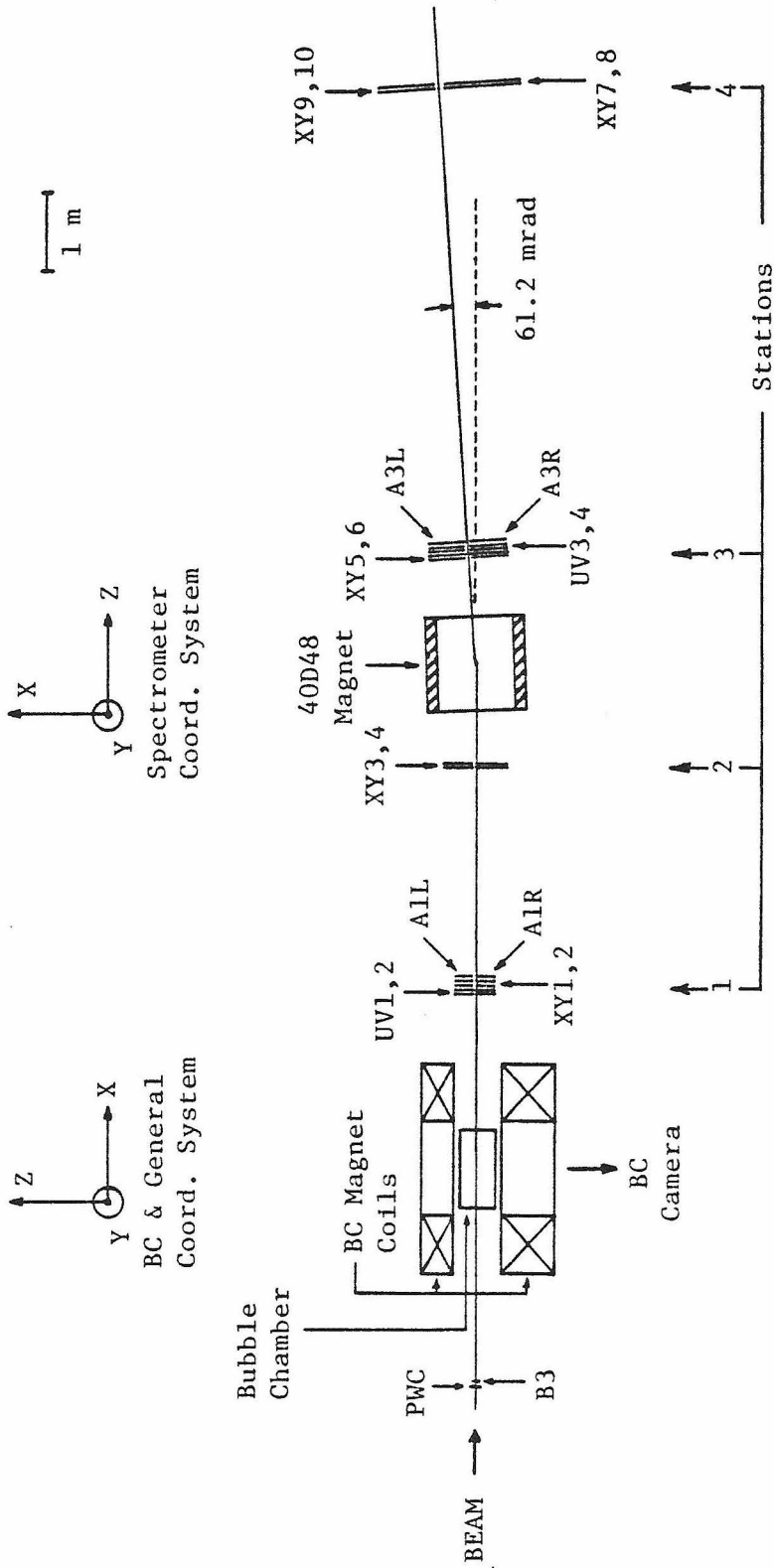


Figure II.2

Plan view of the bubble chamber and spectrometer. XY1-10 and UV1-4 are the wire spark chambers. B3, A1R, A1L, A3R, and A3L are scintillation counters. PWC is the beam proportional wire chambers used in the π^+ experiment. Not shown are the bubble chamber vacuum tank or the iron flux return yokes of the magnets.

aperture. The spectrometer magnet bent particles in the horizontal plane to facilitate physical construction of the final (wide angle) spark chamber station.

Our spectrometer coordinate system was such that the Z direction was defined to be downstream along the beam, Y was in the vertical (opposite gravity) direction, and X was the horizontal direction such that the coordinate system was right handed. Each spark chamber station then consisted of at least two XY spark chambers. Each spark chamber contained two perpendicular magnetostrictive wands to provide a readout of the spark position in two dimensions. Stations 1 (nearest to the bubble chamber) and 3 (immediately downstream of the magnet) contained an extra pair of UV spark chambers. These UV chambers were rotated 45° about the Z-axis so the UV position measurements would allow the separation of the XY measurements of two or more tracks into their correct (X,Y) pairs. The final station (4) was really two pairs of chambers (or sub-stations, called 4R and 4L for right and left halves) situated side by side; this was done to allow measurement of widely bent (lower momentum) particles.

All the chambers were similar. They consisted of two 1 meter by 1 meter areas of wire and nylon mesh (wires in one direction, nylon fibers in the other) separated by 1 cm. The wires of the two sides were oriented at right angles to one another to provide for the simultaneous XY (or UV) measurements. The wires in the mesh were separated by 0.5 mm, but by using two sets of chambers and the pulse-center finding circuitry in the electronic readout system, we were able to achieve

a resolution of about 0.3 mm. The chambers were filled with 80% Ne/20% He gas at atmospheric pressure and the high voltage pulse was controlled by a triggered thyatron switch.

The unscattered beam particles passed through the center of the spark chambers in stations 1, 2, and 3 and between the two halves (4R and 4L) of station 4. The spark chambers were made inactive (dead) in the regions normally traversed by the beam, since otherwise one or more beam tracks would frequently appear in the spectrometer along with the trigger candidate track. For the XY chambers this was done by not providing high voltage on the HV plane in a narrow (in the X direction) stripe. For the UV chambers, a foam block was inserted between the HV and ground planes to prevent the formation of sparks in the beam region. These dead regions provided the lower limit to the scattering angles accepted in the spectrometer. To reduce multiple scattering effects, helium filled bags were placed between the stations (including inside the magnet gap).

Stations 1 and 3 also included the A1 and A3 trigger counters. These were plastic scintillator paddle counters, a pair at each station (an R or right and an L or left counter) with a gap between them to pass the beam. At each station, the scintillators covered the active area of the spark chambers at that station. The A counters were used to form the (single track) trigger by the coincidence of any pair with one counter at each station:

$$RR = A1R \cdot A3R \quad (1a)$$

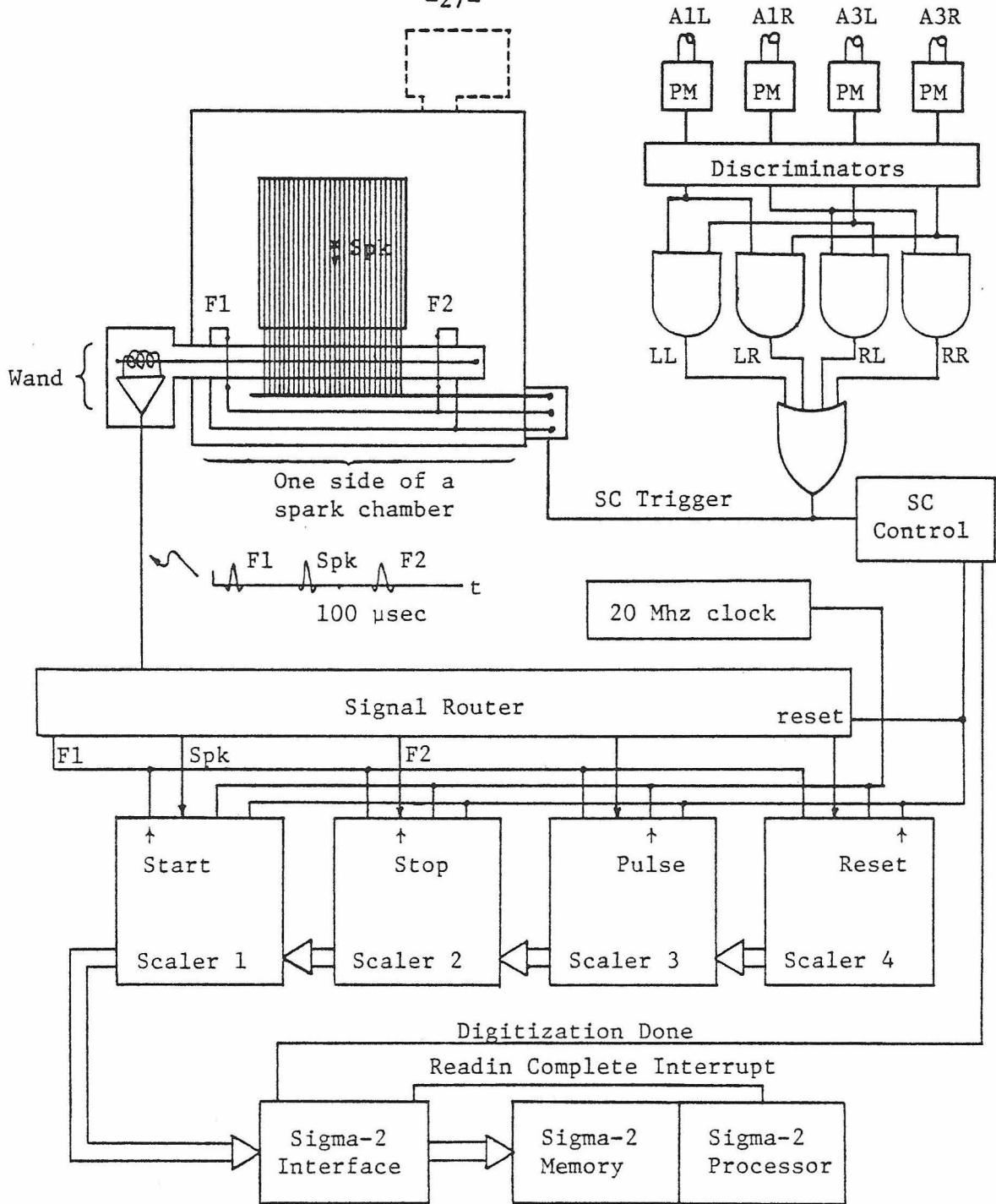


Figure II.3

Schematic of the triggering, spark digitization, and computer input electronics. F1 and F2 are fiducial pulses, and Spk is a spark pulse.

$$RL = A1R \cdot A3L \quad (1b)$$

$$LR = A1L \cdot A3R \quad (1c)$$

$$LL = A1L \cdot A3L \quad (1d)$$

$$SCTRIG = RR + RL + LR + LL \quad (2)$$

This logic is also shown in the diagram in Fig. II.3. This fast trigger fired the spark chambers and initiated the digitizing of the spark positions. These and other signals were accumulated in a set of computer read scalers which were reset before each beam pulse (see Fig. II.3). After a delay of 300 μ sec to allow all the sparks to be digitized, the computer DMA (Direct Memory Access) began to read the counter scalers (not shown in Fig. II.3) and SC (spark chamber) scalers into memory. When this operation was complete, the computer was interrupted and control transferred to the BC trigger program (called FAST).

Each spark chamber wand included two fiducial wires that bounded the active area of the spark chamber (the fiducials were separated by 37 to 41 inches, depending on the particular chamber). The fiducial and spark signals were detected and amplified by a pre-amplifier built into the wand. The amplified signals were sent to the digitization/scaler box for further amplification and digitization. The time between the first fiducial signal and up to 4 additional signals (either sparks or the second fiducial) were converted into counts of the 20 MHz internal clock and stored in the four scaler registers associated with each wand. The scaler system included an adjustable discriminator (so low level noise was ignored) and center-finding for each signal but the

first. A separate unit provided the control for this system (reset, begin digitization, and begin readout).

5. Online Trigger and Data Collection Computer and Programs

The data logging and bubble chamber trigger decision were done with an online computer. For this purpose we used a 16-bit Sigma-2 computer (made by Xerox Data Systems) equipped with 32K words of core and a foreground/background operating system. The foreground programs did the data logging, performed the calculations necessary to generate the bubble chamber trigger, and accumulated run statistics. The background program was used for software development or to run a more complete analysis on a fraction (about 10% in practice) of the data being taken by the foreground. The computer controlled the data collection and trigger electronics by generating pulses or logic levels on a set of output lines. The two most important of these controlled the BC camera flash lamps and the beam gate respectively. The computer also read the BC roll and frame numbers and ready-condition signal from input lines. The BC roll and frame numbers were recorded on the spark chamber data tape so the BC and SC data for a particular event could be located and matched. By checking the BC status line, the computer could automatically pause data collecting (via its control of the beam gate) when the BC went offline for any reason. The experimenter controlled the trigger conditions, began and ended data runs, and monitored the performance of the equipment with the computer. A special part of the foreground program monitored and displayed (on a

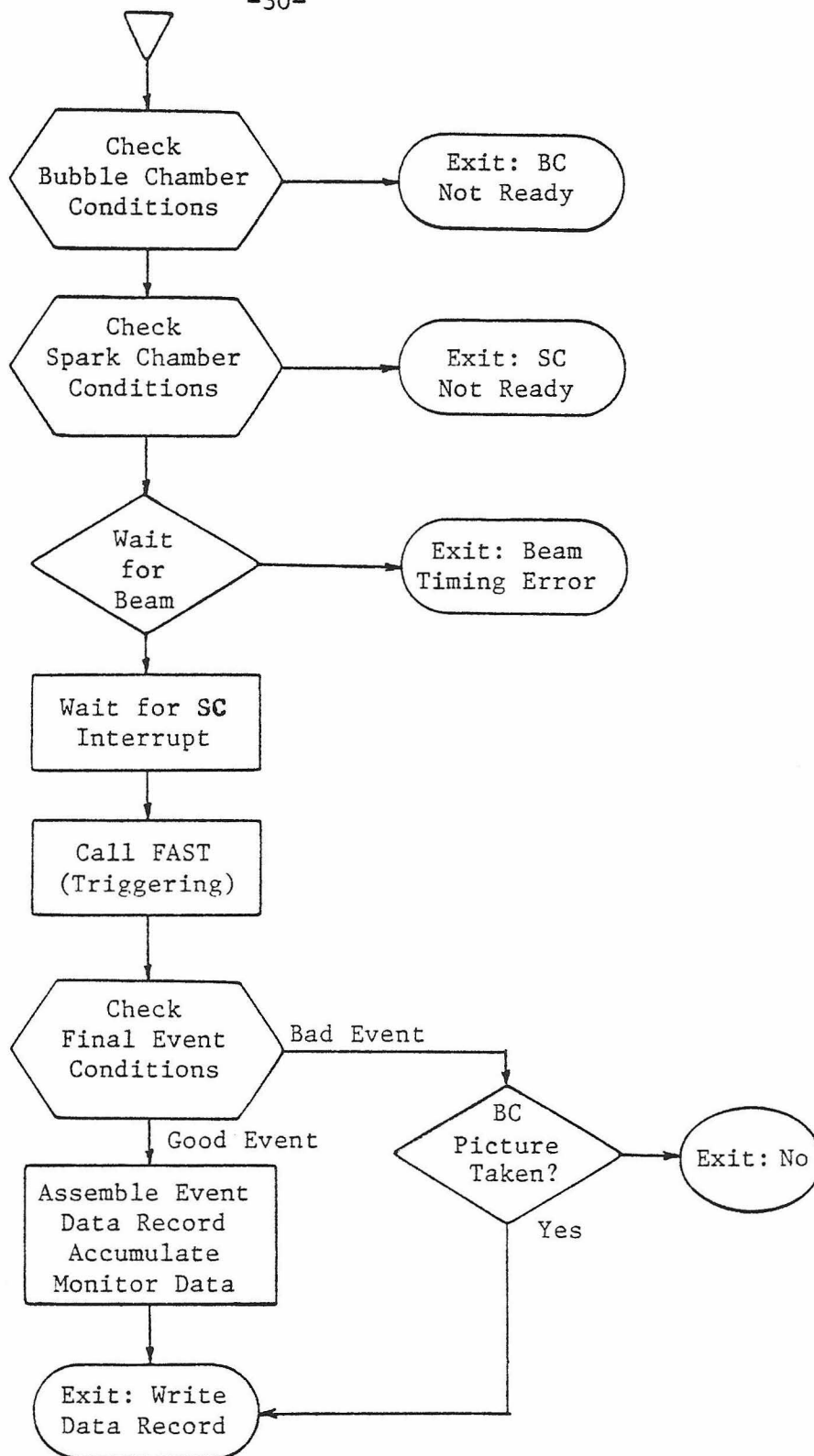


Figure II.4

Flow of control in the online trigger and data collection computer programs.

set of Nixie tubes) the beam intensity in real time to allow the beam line operator to maintain a stable beam. The background program provided us with histograms of relevant quantities which were used to monitor and re-calibrate constants used in the trigger program.

Fig. II.4 gives a flow chart sketching the control flow of the foreground program. The foreground program was initiated a few milliseconds before each beam pulse to allow time for initialization. At this time the status of the equipment was checked to insure that the beam pulse could be used. Once the beam pulse had occurred and the spark chambers were fired, the readin-completion interrupt from the spark chamber electronics initiated the BC trigger program (FAST). Before examining the spark chamber data, FAST used the data in the counter scalers to check the following event conditions:

- (1) a beam gate did occur,
- (2) the beam counter B3 recorded the passage of between 1 and 12 particles,
- (3) and the spark chambers had been fired.

In addition to these software conditions, FAST also imposed the mass cut of $m_\ell < m_x < m_u$ where m_ℓ and m_u were the lower and upper limits on the mass (m_x) recoiling against the fast forward pion. Typically m_ℓ and m_u were set to 1.1 and 3.8 GeV respectively. The lower limit eliminated the majority of elastic events and the upper limit removed a large fraction of the pion diffraction events. The approximations and track-finding algorithm used by FAST are discussed in more detail in Appendix A. FAST was required to make its decision within the bubble

chamber flash lamp delay time (usually set to 2 milliseconds). If FAST determined a picture was not required, the BC camera control was inhibited from taking a picture. After FAST was completed, the foreground program checked to see if the event data was to be recorded on magnetic tape. The event data was written whenever a picture was taken or, if no picture, when the software conditions listed above were met. Finally, the foreground program accumulated statistics (printed at the end of each run) used to monitor the performance of the spark and proportional chambers.

As the background program we normally ran TORTIS which was the complete (both X and Y-view track finding and matching plus corrections) spark chamber analysis program. TORTIS is described in more detail in Chapter III on the data reduction methods. The TORTIS used on the Sigma-2 provided us with a sampling of our data as it was being collected. This was done by providing a facility for the foreground program to transfer an event data block directly to the background program. We used TORTIS to prepare histograms of various quantities to provide us with checks on the performance of the spectrometer and trigger software. We also used TORTIS to determine the calibration constants of the spectrometer and the shape and momentum of the beam (needed by FAST).

Chapter III

Data Reduction

1. Overview

After the data had been collected in the form of bubble chamber film and magnetic tape records of spark chamber data, there ensued the task of reducing the data to a useable form. This involved locating and measuring the events on the film, merging the spark chamber data with the bubble chamber data, and producing data summary tapes containing four momenta for the particles involved in each event. These final tapes were then used to prepare histograms of interesting quantities and as the data input to physics analysis programs. Fig. III.1 gives a flow chart of the steps (including computer program names in all capital letters) involved in the data reduction process as detailed in this chapter. Table III.1 gives the statistics of these experiments from the number of beam pulses through to the resulting numbers of events for specific final states resulting from the data reduction process.

2. Spark Chamber Data

This experiment produced raw data in two forms: pictures of tracks in the bubble chamber and digitized spark chamber and counter data on magnetic tapes. This information had to be further analyzed and merged together into a single set of data before yielding information from which the desired physics results were extracted. For the spark chamber data, this further analysis was handled by a program called TORTIS.

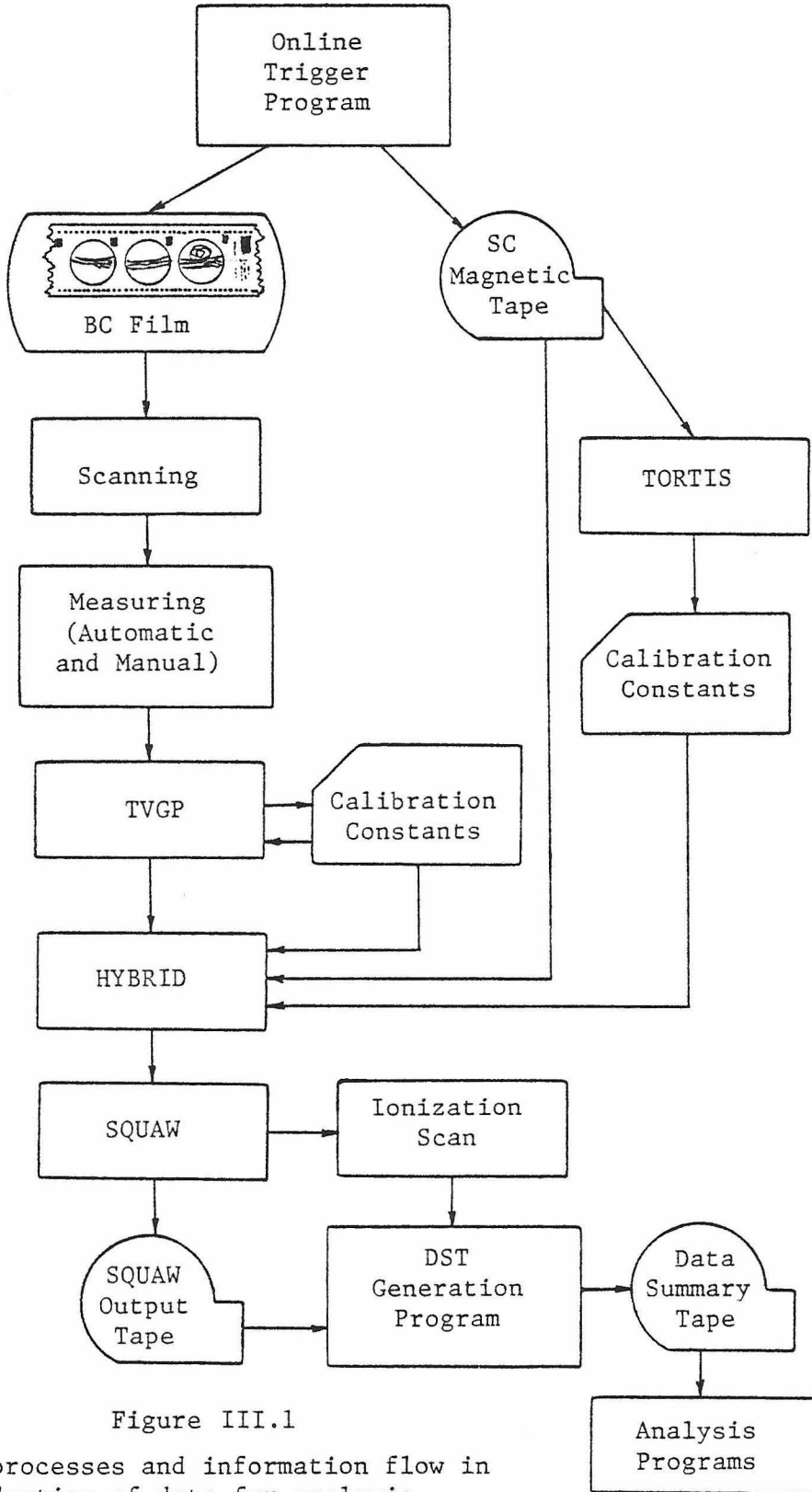


Figure III.1

Major processes and information flow in the reduction of data for analysis.

Table III.1

Results of the data collection and reduction
for each experiment

	π^-	π^+
Beam pulses	6.8×10^6	8.7×10^6
Spark Chamber triggers	2.9×10^6	2.9×10^6
SC triggers/beam pulse	0.422	0.333
BC picture triggers	3.7×10^5	5.7×10^5
BC pictures lost due to late trigger	1.0×10^4	3.2×10^4
Fraction of pictures lost	2.62%	5.60%
BC events	1.21×10^5	1.89×10^5
Elastic scatter events	4.4×10^4	7.5×10^4
Inelastic 2-prong events	4.5×10^4	3.3×10^4
4-prong events	36793	66894
$\pi^\pm p \rightarrow \pi^\pm \pi^+ \pi^- p$ events	17203	27102
$\pi^\pm p \rightarrow \pi^\pm \pi^+ \pi^- \pi^0 p$ events	7542	10792
$\pi^\pm p \rightarrow \pi^\pm \pi^+ \pi^- \pi^0 n$ events	4234	4839

TORTIS was actually used in three versions in this experiment. All three versions used the same spark processing and track finding algorithms; the only differences were in the auxiliary routines and the use of the program. One TORTIS was the background task in the experiment's online computer and was used for calibration and monitoring the performance of the equipment and software. Another TORTIS was built into the HYBRID (or MATCH at SLAC) program that merged the bubble chamber film measurements and the spark chamber measurements. HYBRID will be described more fully in a later section of this chapter. The third TORTIS was a stand-alone program on the CDC 7600 computer at LBL. This TORTIS was used to fine tune the spark chamber and beam calibration constants. These constants were then used in HYBRID (or MATCH) to calculate the parameters of the spark chamber track for each event.

TORTIS accepted as input the raw spark chamber data for an event. This consisted of the digitized counts of a 20 MHz clock for the sparks and fiducials. Also included in the event data record were some computer generated numbers and counts from scintillation counters as auxiliary data. TORTIS first scanned the raw spark chamber data to remove obvious bad sparks and the fiducial counts. The fiducials were recognized and used to form a running average for each wand. Next, the spark values were converted from clock counts to positions in the spectrometer coordinate system. The averaged fiducials were used in this conversion since they measured the distance between the fixed fiducial wires in terms of time (as clock counts). After converting the spark data, TORTIS merged the data from the spark pairs at each

station. This was done by searching for spark pairs (one in each chamber) whose positions differed by an amount less than a preset value. The average of these two positions was then used as the position of a single spark in the spark chamber station. Thus we ended up with a set of unique spark positions at each station and in each plane (X, Y, U, and V) at that station. Here also, the sparks from the two halves of station 4 were concatenated so station 4 could be logically treated as a single station.

Track finding was done by finding projections of tracks in the X and Y-planes separately. In finding these projected tracks, TORTIS used the constraint that the track halves (before and after the magnet) must meet at the magnet center in both views, and that the Y-track had a very small bend angle in the magnet. No constraint could be made on the bend in the X-view since that bend is proportional to the momentum. However, a weak constraint that the X-track intersected the bubble chamber fiducial region was applied to eliminate track testing with extraneous sparks. The X and Y-track views were matched into single tracks by using the information from the UV spark chambers at stations 1 and 3. Each XY combination was used to predict the expected UV spark positions. If a spark was found in the correct position (within a preset cut) in either set of UV chambers, then that XY combination was taken to be a good matched track. In addition, if only a single XY combination existed (only 1 X-track and 1 Y-track), that track was also taken to be a good match provided that the X and Y-sparks in station 4 came from the same half of the station. The TORTIS track-finding

algorithm is discussed in more detail in Appendix B.

TORTIS also calculated a four or six component χ^2 statistic for each track. This χ^2 was useful in selecting the best track match from a set of ambiguous tracks (which had common sparks among them) and in determining the match χ^2 in HYBRID. The components of the χ^2 were:

- (1) DXM, the difference in the spectrometer X-plane at the magnet midplane between the projections of stations 1 and 2 sparks and the stations 3 and 4 sparks.
- (2) DYM, the same as in (1) above, but now in the spectrometer Y-plane.
- (3) DU1 and DV1, the differences in the positions of the spark in the UV1 chambers (if any) and the position calculated from the XY measurements of the track.
- (4) DU3 and DV3, same as in (3) for the UV3 chambers.

The last two components could appear independently depending upon the presence of sparks in the UV chambers, thus changing the number of components in the χ^2 . In particular, the UV3 chambers were not used in the π^- run of the experiment. The distributions of these quantities (the components of the χ^2) had widths of approximately 1.5 mm (FWHM). The errors governing these widths (and used a priori in the χ^2) were the spark chamber setting errors ($\sigma \sim 0.3\text{mm}$) and errors arising from multiple coulomb scattering (contribution about the same as the spark chamber setting error).

Both TORTIS and FAST (the online trigger program) required a set of parameters which described the position and size of the spark cham-

bers and described the beam. Some of these constants were determined by the design of the spectrometer and spark chambers, such as the spectrometer design momentum and bend angle and the actual spark chamber fiducial separations. The spark chamber fiducial separation was also measured by the digitization system in terms of 20 MHz clock counts. This time measurement was thus a direct measurement of the speed of sound in the magnetostrictive wands. Since the speed of sound was very sensitive to the temperature, a running average of the fiducial time separation was kept. Thus the fiducial separation was an example of a parameter that varied with time but was treated as a constant for any one particular event. The beam parameters (momentum, angles, and shape) were also taken as constants that changed when the beam was retuned. Finally there were the spark chamber spatial position parameters that located the zero point of each chamber relative to the entire spectrometer. The Z-positions (along the beam) were fixed by the emplacement of the chambers. The transverse (X and Y) positions were initially measured by a survey, but the values actually used by TORTIS and FAST were slightly different (by a small fraction of an inch) from these survey values. The adjustments to the survey values were made by using TORTIS to calculate the new parameters using special runs in which we steered the beam into the active area of the spark chambers. TORTIS was also used to recalculate these constants for each data run to remove the effects of small random drifts in the values. The beam calibration runs also permitted us to determine the beam parameters we needed. The beam runs were repeated at several

points during the course of the experiment and most particularly after the beam conditions were changed. The procedures used in these calibrations are discussed in more detail in Appendix B.

3. Bubble Chamber Data

In contrast to the spark chamber data, the bubble chamber results required much more processing to get them to the point at which they could be merged with the spark chamber results. The film processing was divided up among the three laboratories participating in this experiment. Cal Tech was responsible for 24% of the π^- film, LBL for 76% of the π^- and 22% of the π^+ film while SLAC did the remainder of the π^+ film. A portion of the SLAC π^+ film (19% of the total) was actually scanned and measured (first pass) at LBL with the remaining processing done at SLAC.

A normal roll of film consisted of 1000 frames which contained about 400 events within the bubble chamber fiducial volume (only 350 for the π^- film due to a different fiducial volume and the ignoring of some event types). The remainder of the frames contained events outside the fiducial volume (in invisible hydrogen and the beam entrance and exit windows). In addition, each roll contained an approximately equal number of events in the fiducial volume which were not associated with the computer trigger and so had no track in the spectrometer. Human scanners were used to locate visible events (according to roll, frame, position on the film, and event type). At SLAC and Cal Tech, directed scans were done by using the tracks found by TORTIS to predict

the location of the outgoing fast track on the film. At LBL, an unassisted scan was done with a special program used to filter out events that were not associated with spectrometer tracks.

The events selected by the scanners were then measured. As with the scanning, different measurement schemes were pursued by each of the involved groups. All the Cal Tech data (including remeasures) were done on the automatic POLLY film measuring system [Allion 1969]. POLLY was operated by a PDP-10 computer with the human operator directing its operation and verifying its actions. One of the major functions of the operator was to manually guide POLLY when measuring tracks where confusion with other tracks or obstructions (i.e., flash lamp reflections, δ -ray spirals, etc.) made automatic measuring difficult. The SLAC spiral reader measured most of the SLAC film sample [Lloyd 1965]. The spiral reader is an automatic machine which does, however, allow the operator to manually measure otherwise difficult tracks. Special event classes (more than 4 prongs or a neutral or charged decay) and certain events judged to be hard to measure on the spiral reader were measured on the SLAC manual measuring machines. The remeasures were handled in the same style as the original measurement pass by dividing the load between the spiral reader and the manual machines. All the other measurement passes were done on the SLAC manual machines. At LBL, two measurement systems were also used. The film was first processed by a flying spot digitizer (FSD, also known as an HPD or Hough-Powell Device). The FSD is fully automatic with no provision for operator assistance and was controlled by the DAPR pro-

gram running on an IBM 7094 computer [White 1968]. Those events that the FSD could not measure were measured on the COBWEB system [Albrecht 1968]. About 55% of the LBL π^- film had to be measured on COBWEB. After improving the performance of the FSD by using the spark chamber data in the pattern recognition process, only 20% of the LBL π^+ film was measured on COBWEB. COBWEB consisted of several Frankenstein film plane digitizers being run in semi-automatic mode under the control of an IBM 7044 computer. The semi-automatic operator allowed the machine to follow tracks with the operator's help and to automatically digitize at intervals along the track. Basically, the computer control was used to speedup the measurement process. In addition to FSD failures, COBWEB also made all the second pass measurements.

Although the three labs used different measuring systems, their outputs were similar. The data for an event included identification information plus several (minimum of two) pairs of film plane digitizations for each track in each of three views. The data were used as input to the standard geometrical reconstruction program TVGP (for Three View Geometry Program) [Solmitz 1966]. TVGP has been used on many other bubble chamber experiments and is structured such that the parameters to describe a particular experiment appear as sets of constants. These constants describe such things as the optical path (from the liquid to the camera), characteristics of the measuring engine (optical characteristics and measuring error) and the bubble chamber operating conditions (magnetic field and liquid type and density). Some of these were set a priori, some (the optical constants)

from measurements of the fiducials as recorded on the film (their spatial positions were known by surveying), and some from measurements of particular events. The latter allowed the magnetic field to be determined by measuring the K^0 mass in neutral decays ($K^0 \rightarrow \pi^+ \pi^-$) and the liquid hydrogen density to be gotten from measurements of the muon range in stopped pion decays ($\pi^+ \rightarrow \mu^+ \nu_\mu$ at rest, followed by $\mu^+ \rightarrow e^+ \nu_e \bar{\nu}_\mu$ also at rest).

With these constants providing needed parameters, TVGP produced a five parameter description (with an associated 5×5 error matrix of the parameters) for each track of an event. This was done by using the film plane digitizations gotten from the measurement tape to calculate the particle's trajectory in three dimensions. The five parameters thus deduced are the polar (with respect to the camera axis) and azimuthal (about the camera axis) angles at the beginning and end of the track, and the track's initial curvature. However, due to energy loss by ionization of the liquid hydrogen, the particle's trajectory depends on its mass as well as its momentum, especially for lower momentum particles. Thus TVGP provides for a number of different mass interpretations to be made for each track. The mass interpretations we used for this experiment were π^+ and proton for positive tracks and π^- for negative tracks. The SLAC data also included the interpretations K^\pm , \bar{p} , and various strange particles for events with decays to include the small number of events coming from rarer reactions. The vast bulk of our data, however, only involved pion and proton tracks.

4. Merging the Spark Chamber and Bubble Chamber Data

The measurement of the fast forward and beam tracks in the bubble chamber had large errors on their momenta ($\delta p/p \sim 5-10\%$ for momenta above 8 GeV/c or so). The standard bubble chamber technique of beam averaging using the very well known central beam momentum ($\delta p/p < 0.5\%$ for our beam) was used to improve the measurements of the beam. A similar process which we called hybridization was done to the bubble chamber measurements of the fast forward track using the better momentum from the spark chamber measurements of the same track. Both these similar operations were carried out by the computer program HYBRID which we wrote for this experiment. HYBRID used the TVGP output tape and a spark chamber data tape as inputs, producing an output tape resembling a TVGP output tape but with averaged beam tracks and hybridized fast tracks.

HYBRID proceeded by first using a portion of the TORTIS computer code to locate spectrometer tracks. The TVGP track banks were then searched for the highest momentum track of the same charge as the beam. The matching process then selected the best TORTIS track that was compatible with the bubble chamber measurement of the fast pion. This matching involved a 9 or 11 component χ^2 . The first 4 (or 6) components were those from the χ^2 for the TORTIS track (see Section III.2). The five new components measured the actual matching of the bubble chamber and spectrometer measurements:

- (1) Difference of the bubble chamber and spectrometer momentum measurements (FWHM ~ 1.5 GeV/c).

- (2) Difference in the polar (or dip) angles at the end of the bubble chamber track (FWHM ~ 7.5 mrad).
- (3) Difference in the azimuthal angles, again at the end of the bubble chamber track (FWHM ~ 3.5 mrad).
- (4) Difference in the transverse coordinates (Y and Z) at the end of the bubble chamber track (Y FWHM ~ 2.5 mm and Z FWHM ~ 3.0 mm).

The χ^2 also included the TVGP correlations (in the error matrix) for all but the position measurements.

After a satisfactory match was found, HYBRID then merged the bubble chamber and spectrometer measurements to form the hybrid fast track measurements. This hybridization was done by taking a weighted average of the momenta (which was dominated by the spectrometer measurement due to its much smaller error) as the hybrid track momentum, using the bubble chamber azimuthal angle, and using the spectrometer polar (or dip) angle without averaging either angle. Details of the HYBRID program and its functioning may be found in L. C. Rosenfeld's thesis [Rosenfeld 1977].

5. Kinematic Fitting

The four-prong events of this experiment are mostly a result of the following five reactions:

$$\pi^{\pm} p \rightarrow \pi_{\text{f}}^{\pm} \pi^{+} \pi^{-} p \quad (1)$$

$$\pi^{\pm} p \rightarrow \pi_{\text{f}}^{\pm} \pi^{+} \pi^{-} \pi^{0} p \quad (2)$$

$$\pi^{\pm} p \rightarrow \pi_{\text{f}}^{\pm} \pi^{+} \pi^{+} \pi^{-} n \quad (3)$$

$$\pi^{\pm} p \rightarrow \pi_{\text{f}}^{\pm} \pi^{+} \pi^{-} \text{(MM)} \quad (4)$$

$$\pi^{\pm} p \rightarrow \pi_{\text{f}}^{\pm} \pi^{+} \pi^{+} \pi^{-} \text{(MM)} \quad (5)$$

where (MM) stands for missing mass consisting of two or more neutral particles (i.e., $\pi^{0}(\pi^{0})^n$ for reaction (4) or $n(\pi^{0})^n$ for reaction (5), both with $n \geq 1$). The leading pion is labeled as the fast pion (π_{f}) that was responsible for triggering the experiment. After hybridization, the data tapes contained measurements of the momentum vectors of all the charged particles of these reactions. Using the principle of conservation of energy and momentum, the mass of the neutral system of reactions (2) through (5) can be calculated.

Events were fitted to the reactions (1) through (3) using as constraining relations the four equations from conservation of energy and momentum (four-momentum):

$$\sum_{\text{initial}} E_i = \sum_{\text{final}} E_i \quad (6a)$$

$$\sum_{\text{initial}} \vec{p}_i = \sum_{\text{final}} \vec{p}_i \quad (6b)$$

These kinematic fits were carried out using the SQUAW computer program [Dahl 1968] which is a companion to TVGP. Since energy-momentum conservation is used to constrain the kinematic fits, the resulting values (after the fit) of the energy and momenta of the particles of the event will exactly conserve energy and momentum. Reactions (2) and (3) involve a missing neutral particle whose four-momentum is not measured, but by assuming a mass for the particle, the kinematic fit determines the unknown momentum vector. Reactions (2) and (3) thus result in one constraint (1C) fits since the four energy-momentum equations must provide for the calculation of the three momentum components of the missing neutral particle. Similarly, reactions (4) and (5) produce zero constraint (0C) "fits" which are really the use of equations (6) to calculate the missing momentum and energy. This is because the missing neutral system (usually consisting of several neutral particles) has an unknown mass. In contrast, reaction (1) results in fully constrained (4C) fits since all the momentum vectors are measured and all the masses are known.

Reactions (1), (2), and (4) may result in more than one fit per event. This can be due to the two slow positive particles being interpreted as π^+p or $p\pi^+$ respectively. Approximately 18% of the 1C four-prong events that fit reaction (2) made the fit twice, the second fit having the mass interpretations (π^+p) of the slow positive tracks interchanged ($p\pi^+$). This was about the same fraction of 0C events which had two "fits" to reaction (4). Only 4% of the 4C events had two fits with interchanged tracks. This fraction is small (compared

to the 1C and 0C cases) because the fits with the wrong mass interpretations were frequently failed by SQUAW which resulted in only one good 4C fit per event. Also, not all events could have had two fits because the initial momentum and rate of energy loss were inconsistent for one mass interpretation of a track or one track was definitely known to be a proton (by being flagged as a stopping proton by the scanner). The ambiguous events (multiple fits) were reduced to a single fit as described in the next section.

All fits to reactions (2) through (4) used the hybrid track for the fast track (π_f^\pm). The 4C fits to reaction (1) were made as HYBRID fits using the hybrid track and as BCONLY fits for which only the bubble chamber measurement was used for the fast track. Thus both a HYBRID and a BCONLY 4C fit were attempted for each event. This was done primarily for the two-prong events to insure that all the elastic events were found. The elastic events on the film were ones that had leaked through the trigger and as such, the spark chamber measurement of the fast track may have been slightly wrong in some way (e.g., a secondary scattering when exiting from the bubble chamber). In fact, about 5% of the two-prong elastic events had just the BCONLY fit with less than 1% having only the HYBRID fit. For the 4C four-prong events, 7% of them made just the HYBRID fit and 4% just the BCONLY fit (the remainder made both types of fit). These numbers were a result of our selection of the bubble chamber fiducial volume. We accepted events very near to the bubble chamber exit windows. These events had very short (10 cm or so) fast tracks visible and so had very poor measure-

ments of the fast particle momentum. This was of no consequence in the HYBRID fits since there the fast track momentum was essentially determined by the spark chamber measurement.

As discussed earlier, the parameters describing the event (momenta and energies of the particles) exactly conserved energy and momentum after kinematic fitting. Since the fits were constrained by energy-momentum conservation, the errors in the parameters were considerably reduced by the kinematic fitting process (relative to the errors from before the fitting). Thus fitting improved the resolution of the experiment. Finally, the chi-square (χ^2) statistic of the fit was useful in selecting between ambiguous fits for a single event as discussed in the following section.

6. Fit Selection

Although kinematic fitting improved the resolution, it did not completely solve the problem of dividing the events into separate channels as given by reactions (1) to (5). Kinematic fitting did provide the χ^2 statistic which was useful in selecting among the ambiguous fits. In addition there was extra information to be gotten from the bubble chamber film. This information was the ionization, or bubble density, of the track. This quantity is nearly proportional to $1/\beta^2$ and so the bubble densities associated with different mass interpretations for the same track go as the mass squared:

$$\frac{1}{\beta^2} = \frac{E^2}{p^2} = 1 + \frac{m^2}{p^2} \quad (7)$$

The bubble density on the film is also proportional to $1/\cos\lambda$ where λ is the dip angle between the track and the plane perpendicular to the camera axis of the bubble chamber. As the dip angle increases, the track is becoming more parallel to the camera axis so the camera is looking along the track to an increasing extent. Thus the apparent bubble density (as projected onto the film) increases with the dip angle.

We used a program to prepare a list of events for which the ionization information was needed. For each slow positive track (two tracks for each four-prong event), the program calculated and printed the projected bubble densities for different mass interpretations. This was done for each view and in units of the bubble density of a minimum ionizing track for which the beam tracks provided a handy reference, thus considerably reducing the effects of the bubble chamber operating conditions. These lists were then given to human scanners who selected the correct mass interpretation having observed the apparent bubble density on the film. These selections were then fed into the DST program (see below) as the ionization data. For some of the SLAC π^+ data, these selections were done by programs using bubble density information collected automatically by the spiral reader.

Not all the events were scanned for ionization information. Some events only made a single kinematic fit in SQUAW and so were unambiguous. Tracks with momenta above 1.2 GeV/c were skipped since the $1/p^2$ decrease of the bubble density overwhelms the increase due to the mass to the point such that the tracks always appear minimum ionizing. In

addition, the scanners marked some events as undecidable because the tracks were obscured or had too high a dip angle. The π^- film was particularly difficult to scan for the ionization as the film quality and bubble chamber operating conditions were not as optimal as those for the π^+ film. In either case, the four-prong events were easier to scan than the two-prong events since the two slow positive tracks could be visually compared to decide which one was the denser in bubbles/cm.

The ionization information plus the output tape from SQUAW containing both the measured and fitted track parameters were used by the DST generator program to produce data summary tapes (DST's). The DST's were then used by all the efficiency calculation and physics analysis programs. In addition to constructing the data record from a pre-specified map, the DST generator program also assigned each event to a particular channel by eliminating ambiguous fits. The algorithm adopted to remove ambiguous fits (leaving one "best" fit per event) used the information from the ionization scan and the kinematic fit χ^2 to effect its choice of the "best" fit. This process was not exact and therefore corrections to the cross sections were calculated by other means as discussed in the final section of Chapter IV. The general scheme of the selection algorithm was to use the ionization data to reject all fits with tracks whose mass interpretations were incompatible with the ionization results. As an exception to this rule, if all the 4C fits of an event were rejected by the ionization results, then the ionization information was ignored so that none of

the 4C fits were rejected (i.e., the 4C fit information was considered to be more reliable than the ionization data for these events). This happened for only 2.5% of the 4C events. About 4% of the 4C events had multiple 4C fits from the $\pi^+p/p\pi^+$ positive track ambiguity. The ionization data eliminated 3/4 (3% of all 4C events) of these ambiguities by rejecting all but one of the 4C fits. Similarly, 18% of the π^0 1C events (reaction (2)) had more than one fit to the π^0 reaction with 2/3 of these ambiguities (12% of the π^0 events) being removed by the ionization. Of the events with 1C fits (reactions (2) and (3)), 34% were ambiguous between the π^0 and n fits, this being reduced to only a 17% ambiguity by the ionization data.

If after using the ionization results an event was still ambiguous with several non-0C fits, then the "best" fit for that event was selected by choosing the fit with the lowest χ^2 value. This procedure cannot give a perfect separation of the channels since the χ^2 value gotten for a fit depends on the exact values of randomly distributed quantities. Thus if the chi-squares associated with ambiguous fits were nearly equal, random fluctuations ensured that the true fit sometimes had a χ^2 greater than that of the ambiguous false fit (and so was rejected).

With a couple of assumptions and the information given above, an estimate (as an approximate upper limit) can be made of the fraction of the 1C events that are misidentified (wrong fit selected). More precise estimates of the losses and backgrounds and the procedure used to obtain them are discussed in the final section of Chapter IV. At

this point, we need to estimate the fraction of times that the ionization and chi-square fit selections pick the wrong fit for an event. We can take the fraction of times the ionization information causes the wrong fit to be selected (the error in the ionization) to be less than 30%, especially as the four-prong ionization scan was significantly easier to perform than that for the two-prongs. This number comes from looking at the scatterplots of the confidence levels of the chi-squares for rejected (by the ionization) fits versus those of non-rejected fits. Similarly, from the scatterplots of the confidence levels for ambiguous fits, a maximum of about 20% of the chi-square selection events were in the region where the chi-squares overlap due to randomness. If we assume that in the overlap band that the worse case is for the two chi-squares to be independently and uniformly distributed so that in half of the overlap band cases the selection process picks the wrong fit, then the chi-square selection failed in about 10% of the events for which it was applied. Table III.2 summarizes the effects of these selection errors as an approximate upper limit for the fraction of the events in the 1C channels that are misidentified.

Table III.2

Estimate of the fraction of 1C events
assigned to the wrong channel

<u>Fraction of</u> <u>1C events in</u>	<u>Ambiguous</u>	<u>Resolved by</u> <u>ionization</u>	<u>Resolved by</u> <u>chi-square</u>	<u>Fraction</u> <u>misidentified</u>
π^0 channel:				
with >1 π^0 fit	18%	12%	6%	5%
with n fit	34%	17%	17%	8%
n channel:				
with π^0 fit	34%	17%	17%	8%

So we see that the selection algorithm misidentifies approximately 10% of the events in a channel. This number represents an upper limit to the errors introduced by the selection process, but does not take into account losses to the 0C channels or backgrounds made up of true 0C events (with multiple neutrals) that made a passing 1C fit. Also, about 10% of the 1C events have had all their 1C fits rejected by the ionization selection and so ended up in the 0C channels. Estimates for the channel losses and backgrounds are given in Chapter IV.

Finally, there is also about a 1% background in the π^- four prongs associated with events from the reaction:

$$\pi^\pm p \rightarrow \pi^\pm K^+ K^- p \quad (8)$$

which were fit as such and separated from the SLAC π^+ data. This is the largest four prong reaction that does not belong to the set of reactions (1) through (5). All other strange particle reactions will

either involve a decay seen in the bubble chamber (and so relegated to a separate class of events) or be considerably below the 1% level.

Chapter IV

Cross Section Determination

1. Overview

Suppose that in this experiment we observe N events for some reaction ($\pi^\pm p \rightarrow \pi^\pm X \rightarrow \pi^\pm \pi \pi \pi N$) in some particular region of phase space. Each event has a weight, w_i , to correct for the effects of our limited geometrical acceptance and inefficiencies in the computer trigger. We then calculate the observed cross section for this reaction with the formula:

$$\sigma = \frac{1}{f_{\text{obs}}} \cdot \frac{1}{e} \cdot \sum_i^N w_i \quad (1)$$

where e is the exposure in events per microbarn. The factor f_{obs} in this formula represents the fraction of the selected reaction which survives the cuts used to select the events. In many cases, f_{obs} will be one, but if in selecting the events a range of masses containing a resonance peak were selected by cuts, f_{obs} would be the fraction of the resonance shape found between the mass cuts. The exposure factor e includes corrections for several other effects that remove events from or add events to the set of events in a channel. Events were lost due to inefficiencies in the spark chambers (e.g., not making sparks) and due to selection cuts in the programs used to find tracks in the spark chambers and to match these tracks to their corresponding bubble chamber tracks. Non-pion contaminants in the beam add events which must be removed before cross sections can be given for $\pi^\pm p$ reactions.

Events were lost due to bubble chamber pictures not being taken when the computer trigger program exceeded the flash lamp delay time. In selecting the events that make up a channel's data sample, some are lost and must be corrected for and similarly background events remaining in the data sample must also be corrected for. A large part of the remainder of this chapter discusses how these various corrections were made.

2. Elastics Normalization

We have normalized our experiment by using published π elastic cross sections to calculate the exposure (e). During the experiment we took elastic trigger rolls for which the lower mass cut used in the computer trigger was set to zero so elastic scatter events were triggered upon. These elastic rolls (about 4% of the π^- film and 5% of the π^+ film) provided us with an unbiased sample of elastic events from which an elastic rolls exposure was found by using the published π elastic cross sections. Since the four prongs were unaffected by this change in the trigger, the ratio of the number of four prongs in the total data sample (elastic and production trigger rolls) to the number of four prongs in the elastic trigger sample was used to scale the elastic rolls exposure to the exposure for the entire data sample. The formula used to calculate the exposure was:

$$e = \epsilon_{ch} e' = (\epsilon_{ch}) \frac{N_{tot}^{4P}}{N_{el}^{4P}} \frac{\epsilon_{bm}^{4P}}{\epsilon_{bm}^{\pi p}} \frac{1-l_{pix}^{4P}}{1-l_{pix}^{\pi p}} \frac{1}{\epsilon_{cuts}^{\pi p}} \frac{N_{\pi p}}{\sigma_{\pi p}} \quad (2)$$

where ϵ_{ch} is the correction resulting from inefficiencies in the final selection of events for a particular channel's data sample. Section 6 of this chapter discusses ϵ_{ch} in more detail and Table IV.8 presents the final values for e for the four channels of interest. At this point we will consider e' which is the four prong exposure uncorrected for channel selection effects. The published elastic cross section we are normalizing to is represented by the $\sigma_{\pi p}$ factor in equation (2). This was gotten by integrating published values for $d\sigma/dt(\pi p \rightarrow \pi p)$ over the interval $0.05 \leq |t| \leq 0.3$ (GeV/c)². This t interval was chosen to remove effects of the geometric acceptance (e.g., loss of events at very low $|t|$). $N_{\pi p}$ is the sum of weights for elastic events (in this same t interval) from our elastic trigger rolls. The fraction of true elastic events that survive the cuts used to define an elastic event is given by $\epsilon_{cuts}^{\pi p}$. This factor serves to correct e' for the small number of elastic events lost in selecting the elastic events. N_{tot}^{4P} is the number of four-prong events found on all the film and N_{el}^{4P} is the number of four prongs found on the elastic rolls; their ratio serves to scale $N_{\pi p}$ from elastic roll elastic events to all the elastic events that occurred during the experiment (including those elastic events excluded from the production film by the computer trigger). We have taken corrections for inefficiencies in making sparks, finding spark chamber (SC) tracks, and matching SC and bubble chamber tracks to be independent of the event type and computer trigger. These corrections then cancel and are left out of equation (2). The ratio of the beam contamination corrections, $\epsilon_{bm}^{4P}/\epsilon_{bm}^{\pi p}$, is also taken to be one.

This correction is discussed in more detail in section 3 of this chapter.

The quantities $\lambda_{\text{pix}}^{4\text{P}}$ and $\lambda_{\text{pix}}^{\pi\text{P}}$ are the fractions of four prong and elastic pictures lost because the computer trigger program processing time exceeded the flash lamp delay time. The factor $\lambda_{\text{pix}}^{4\text{P}}$ was taken to be equal to the fraction of all production (inelastic trigger) pictures lost, $\lambda_{\text{pix}}^{\text{prod}}$. The elastic loss fraction ($\lambda_{\text{pix}}^{\pi\text{P}}$) was determined from the loss fractions for the production and elastic trigger rolls ($\lambda_{\text{pix}}^{\text{elas}}$). We assumed that the reason for a picture being lost was that extra sparks from a second event or a beam particle outside the normal beam area would cause the trigger program to use an excessive amount of time in the track finding due to the larger number of possible spark combinations. To see how changing the trigger conditions gave the different values found for $\lambda_{\text{pix}}^{\text{prod}}$ and $\lambda_{\text{pix}}^{\text{elas}}$ (see Table IV.1), consider the case in which two events occur and leave tracks in the spark chambers. Since elastic events are so prevalent in this experiment, the probability is very good that at least one of these events is an elastic event. If we are taking a production roll, the trigger program must find an inelastic event before deciding to take the picture and so may first find and reject the elastic event track and will use some fraction of the available time to do so. The same situation of an elastic event occurring with an inelastic event then has a smaller probability to lose a picture when an elastic trigger roll is being taken. The probability is smaller than the production case because the finding of either event's spark chamber track by the trigger pro-

gram is sufficient to satisfy the trigger conditions.

For inelastic events, the trigger program and conditions are identical for production and elastic rolls so we have assumed that the probability to lose an inelastic event picture is the same for both these cases. We have also assumed that the probability of losing an inelastic event picture was given by the production roll picture loss fraction ($\lambda_{\text{pix}}^{\text{prod}}$). From Table IV.1 we see that $\lambda_{\text{pix}}^{\text{elas}}$ is approximately one half of $\lambda_{\text{pix}}^{\text{prod}}$. This comes as a result of the small probability to lose an elastic event picture (as discussed above) and the larger number of elastic events on the elastic rolls. The probability of losing an elastic event picture ($\lambda_{\text{pix}}^{\pi\text{P}}$) was determined by:

$$\lambda_{\text{pix}}^{\pi\text{P}} = \frac{\lambda_{\text{pix}}^{\text{elas}} - \lambda_{\text{pix}}^{\text{prod}}(1 - f_e)}{f_e} \quad (3)$$

where f_e is the fraction of elastic roll events that really were elastic events. This fraction was found to be $70.1 \pm 0.7\%$ when averaged over the two experiments (the individual experiment values agreed within their errors). Table IV.1 gives the values of the quantities in equation (3) along with the correction ratio of $(1 - \lambda_{\text{pix}}^{\text{4P}})/(1 - \lambda_{\text{pix}}^{\pi\text{P}})$ for equation (2). The errors in $\lambda_{\text{pix}}^{\pi\text{P}}$ and the correction ratio are dominated by the error in $\lambda_{\text{pix}}^{\text{elas}}$ which is large due to the small number of elastic rolls. However, the error introduced into the normalization by the lost picture correction is small since $\lambda_{\text{pix}}^{\pi\text{P}}$ is a small number (compared to 1).

Table IV.1

	π^-	π^+
$\ell_{\text{pix}}^{\text{prod}} \equiv \ell_{\text{pix}}^{4\text{P}}$	2.62%	5.56%
$\ell_{\text{pix}}^{\text{elas}}$	1.88±0.12%	2.95±0.10%
$\ell_{\text{pix}}^{\pi\text{p}}$	1.56±0.17%	1.81±0.15%
$(1-\ell_{\text{pix}}^{4\text{P}})/(1-\ell_{\text{pix}}^{\pi\text{p}})$	0.989±0.002	0.963±0.001

Table IV.2 lists the values of some of the quantities used in equation (2) [Davidson 1976]. The integrated elastic cross sections were evaluated from published data [Foley 1963 and 1969] for $d\sigma/dt$ integrated over the required interval and interpolated to our beam momenta. The values obtained for $\sigma_{\pi\text{p}}$ are considered to have a 3% systematic error [Foley 1963 and 1969] in addition to the quoted statistical error. During the π^- experiment, the upper trigger mass cut was set at 2.8 GeV until roll 125 after which it was raised to 3.8 GeV (which was used throughout the π^+ experiment). For this reason, only four prongs with N^* masses between 1.3 and 2.7 GeV were used in determining $N_{\text{tot}}^{4\text{P}}$ and $N_{\text{el}}^{4\text{P}}$.

Using the Table IV.2 values (and combining the two parts of the π^+ experiment to get a single number) we found the overall four-prong exposures quoted in Table IV.3. These exposures are the result of calculating e' and do not include the channel detection efficiency (ϵ_{ch}). The errors quoted in Table IV.3 are purely statistical. Both experiments are considered to have systematic errors of approximately 5% which when combined with the 3% systematic error in $\sigma_{\pi\text{p}}$ gives over-

all systematic errors of about 6%.

Table IV.2

	<u>Elastic normalization quantities</u>		
	<u>π^- data</u>	<u>SLAC π^+ data</u>	<u>LBL π^+ data</u>
$1/\epsilon_{\text{cuts}}^{\pi p}$	1.015±0.005	1.003±0.005	1.010±0.005
$\sigma_{\pi p}$ (in mb)	2.17±0.05	2.19±0.05	2.19±0.05
$N_{\pi p}$	4236±82	4082±81	1127±43
N_{tot}^{4P}	24985	20021	13716
N_{e1}^{4P}	632	708	229

Table IV.3

	<u>Four prong exposures</u>	
	<u>π^-</u>	<u>π^+</u>
e' (events/ μb)	77.7±3.9	85.7±3.8
percent error	5%	4.4%
systematic error	6%	6%

3. Beam Contamination

We must also correct the exposure for the events that come from the non-pion components of the beam. The hadronic beam fractions given in Table IV.4 were calculated from the data in the SLAC User's Handbook [Boyarski 1968] while the electron fractions came from the electron-to-pion ratio measured for the π^- experiment. The muon fractions were estimated from π and K decay over the length of the beam (14.88 meters).

Table IV.4

<u>Particle type</u>	<u>π^+ beam</u>	<u>π^- beam</u>
π^\pm	90%	94%
K^\pm	5%	3%
p or \bar{p}	3%	—
e^\pm	—	.4%
μ^\pm	<2%	<2%

The \bar{p} fraction of the π^- beam and the e^+ fraction of the π^+ beam were ignored since they represented less than 0.1% of the beam. The muon fractions were calculated from π and K decay but are given as upper limits only because an unknown fraction of these decay muons will escape from the beam phase space before the bubble chamber is reached. The fractions of positrons and direct muons in the beam were very small compared to the electrons since most of the electrons came from elastic or inelastic scattering of the primary electron beam from the produc-

tion target. In events of the type we are interested in, like elastic scattering or the reaction $\pi p \rightarrow \pi X$, with a beam momentum near 14 GeV/c, we cannot tell the difference between events caused by pions, kaons, or protons in the beam. The electrons and muons in the beam interact much less frequently than the hadrons and so contribute essentially no events. Because the kaons and protons contribute both reaction and elastic events, both the numerator and denominator of equation (1) must be corrected as indicated by the ratio $\epsilon_{bm}^{4P}/\epsilon_{bm}^{\pi p}$ in equation (2). If we combine and rewrite equations (1) and (2) with N_{obs} being the observed weight-sum ($\sum w_i$ from equation (1)) and N_{el} the weight-sum for elastic events (same as $N_{\pi p}$ in equation (2)), we have:

$$\sigma_{obs} = s \sigma_{\pi p} \frac{N_{obs}}{N_{el}} \quad (4)$$

where the other factors have been absorbed into the scaling constant s . Then to get the "true" cross section for the reaction $\pi p \rightarrow \pi X$, we must subtract from N_{obs} and N_{el} the numbers of events due to the beam contaminant of particle type c :

$$\sigma_{\pi X} = s \sigma_{\pi p} \frac{N_{\pi X}}{N_{\pi p}} = s \sigma_{\pi p} \frac{N_{obs} - N_{cX}}{N_{el} - N_{cp}} = \sigma_{obs} \frac{1 - N_{cX}/N_{obs}}{1 - N_{cp}/N_{el}} \quad (5)$$

where N_{cX} and N_{cp} are the weight-sums for events from the contaminant reaction ($cp \rightarrow cX$) and contaminant elastic scattering ($cp \rightarrow cp$) with c standing for K^\pm (either beam) or p (π^+ beam only). Since the contaminants are known to be a small fraction of the beam so that $N_{obs} \gg N_{cX}$ and $N_{el} \gg N_{cp}$ (and taking $N_{el} \approx N_{\pi p}$), we have:

$$\sigma_{\pi X} = \sigma_{\text{obs}} \left(1 - \frac{N_{cX}}{N_{\text{obs}}} \right) \left(1 - \frac{N_{cP}}{N_{\pi P}} \right) \quad (6)$$

Since the cross section for a scattering process is proportional to the number of scattered particles observed divided by the number of beam particles incident on the target, we can rewrite this as:

$$\sigma_{\pi X} \approx \sigma_{\text{obs}} \left(1 - \frac{f_c \sigma_{cX}}{\sigma_{\text{obs}}} \right) \left(1 - \frac{f_c \sigma_{cP}}{\sigma_{\pi P}} \right) \quad (7)$$

where f_c is the fraction of the beam that consists of particle type c and we have used $\sigma_{\text{obs}} \approx \sigma_{\pi X}$ (to lowest order). Now, by ignoring small second order terms and defining the scale factor r by $\sigma_{cX}/\sigma_{\pi X} = r (\sigma_{cP}/\sigma_{\pi P})$, we get:

$$\sigma_{\pi X} \approx \sigma_{\text{obs}} \left(1 - (r - 1) f_c \frac{\sigma_{cP}}{\sigma_{\pi P}} \right) \quad (8)$$

Finally, by using factorization [Leith 1976] we can say that r is 1.0 with a 20% systematic error. Thus we can set the ratio $\epsilon_{\text{bm}}^{4P}/\epsilon_{\text{bm}}^{\pi}$ to 1.0 and include the effect of the beam contamination in the systematic error. Thus the systematic errors due to the beam contaminations are:

$$\pi^+ \text{ beam:} \quad 0.2(f_K \sigma_{Kp} + f_p \sigma_{pp})/\sigma_{\pi p} = 2.3\% \quad (9a)$$

$$\pi^- \text{ beam:} \quad 0.2f_K \sigma_{Kp}/\sigma_{\pi p} = 0.2\% \quad (9b)$$

4. Geometrical Acceptance Correction

By using a hydrogen bubble chamber as target and detector, we have essentially 100% detection efficiency over the entire 4π solid angle for the slow tracks resulting from proton dissociation. However, we must correct for the geometrical biases in the detection of the fast forward pion resulting from the limited bubble chamber exit and spectrometer apertures. These biases occur because the geometry of the apertures precludes detection of all the events; in particular, only those events with a fast track at a given scattering angle (θ) and momentum (p) and in a particular range (or set of ranges) of the azimuthal angle (ϕ) about the beam particle's direction are detected. Since the physics is independent of ϕ , the number of events observed (as a function of p and θ) must be corrected for the number of unobserved events in the ϕ ranges blocked by the apertures. The limited geometrical acceptance is taken into account by weighting each event by the inverse of the probability for the detection of that event (the geometrical efficiency). The geometrical efficiency, $\epsilon(\vec{x}, \vec{x}', \vec{p})$, is in general a function of the vertex position (\vec{x}), the beam angles (\vec{x}'), and the momentum vector of the fast particle (\vec{p}). This efficiency was determined for each event by tracing the fast track through the BC exit and spectrometer for 128 equally spaced azimuthal angles and determining what fraction of these traced rays successfully pass through the spectrometer. This procedure thus corresponds to numerically integrating:

$$\epsilon(\vec{x}, \vec{x}', p, \cos\theta) = \frac{1}{2\pi} \int_0^{2\pi} \epsilon(\vec{x}, \vec{x}', \vec{p}) d\phi \quad (10)$$

The ray tracing was further enhanced to smooth out aperture edge effects by retracing (with multiple scattering taken into account) those fast track rays which passed near an aperture edge for an additional 5 tries. Thus each event was ray traced through the spectrometer about 150 times. This gave sufficient statistical accuracy so that the error in the geometrical efficiency was ignored when calculating the error in a weight-sum.

The ray tracing program was checked by comparing traced rays with observed rays. When processing the data to calculate $\epsilon(\vec{x}, \vec{x}', p, \cos\theta)$ for each event, the traced and observed spark positions at stations 1 and 2 were compared and used to adjust the bubble chamber-to-spectrometer connection parameters. The agreement was better than 0.01 inches (the spark chamber setting error is approximately 0.017 inches). For some 4% of the events, the ray tracing program claimed that the actual ray of the fast track failed to pass through all the apertures.

For some regions of (p, θ) , the efficiency $\epsilon(\vec{x}, \vec{x}', p, \cos\theta)$ is zero for portions of the bubble chamber (\vec{x}) or beam phase space (\vec{x}'). Thus events that actually occur in these regions are not detected and we are formally in the position of dealing with the indeterminate quantity of 0 events divided by a 0 efficiency to correct the cross sections. This difficulty was overcome by averaging the efficiency over the ranges of \vec{x} and \vec{x}' in these cases:

$$\bar{\epsilon}(p, \cos\theta) = \iint_{\vec{x}, \vec{x}'} \epsilon(\vec{x}, \vec{x}', p) \eta(\vec{x}, \vec{x}') d^3\vec{x} d^2\vec{x}' \quad (11)$$

where $\eta(\vec{x}, \vec{x}')$ is the normalized beam distribution which gives the fraction of the beam particles which pass through the volume $d^3\vec{x}$ at \vec{x} in the bubble chamber with beam angles within the range \vec{x}' to $\vec{x}'+d^2\vec{x}'$. These integrals were done by use of a Monte Carlo program which generated events within the (\vec{x}, \vec{x}') space for a fixed (p, θ) . The resulting rays were traced through the spectrometer with the same ray tracing program described above. Besides allowing $\bar{\epsilon}(p, \cos\theta)$ to be calculated, this procedure also allowed the (p, θ) region where $\epsilon(\vec{x}, \vec{x}', p, \cos\theta)$ is never zero to be found. This method had the disadvantage relative to the method discussed earlier (using the data itself to do the numerical integration) that the beam distributions in (\vec{x}, \vec{x}') must be known and adequately parameterized.

As it turned out, most of the events lay within the region of the (p, θ) plane for which $\epsilon(\vec{x}, \vec{x}', p, \cos\theta)$ is always non-zero. For the four prongs, only 14% of the events were outside this region and thus have $\bar{\epsilon}(p, \cos\theta)$ used as their geometrical efficiency. The $\epsilon(\vec{x}, \vec{x}', p, \cos\theta)$ non-zero region corresponds to approximately the area within the 0.3 contour line in Fig. IV.1.

π^+ Experiment Geometric Acceptance

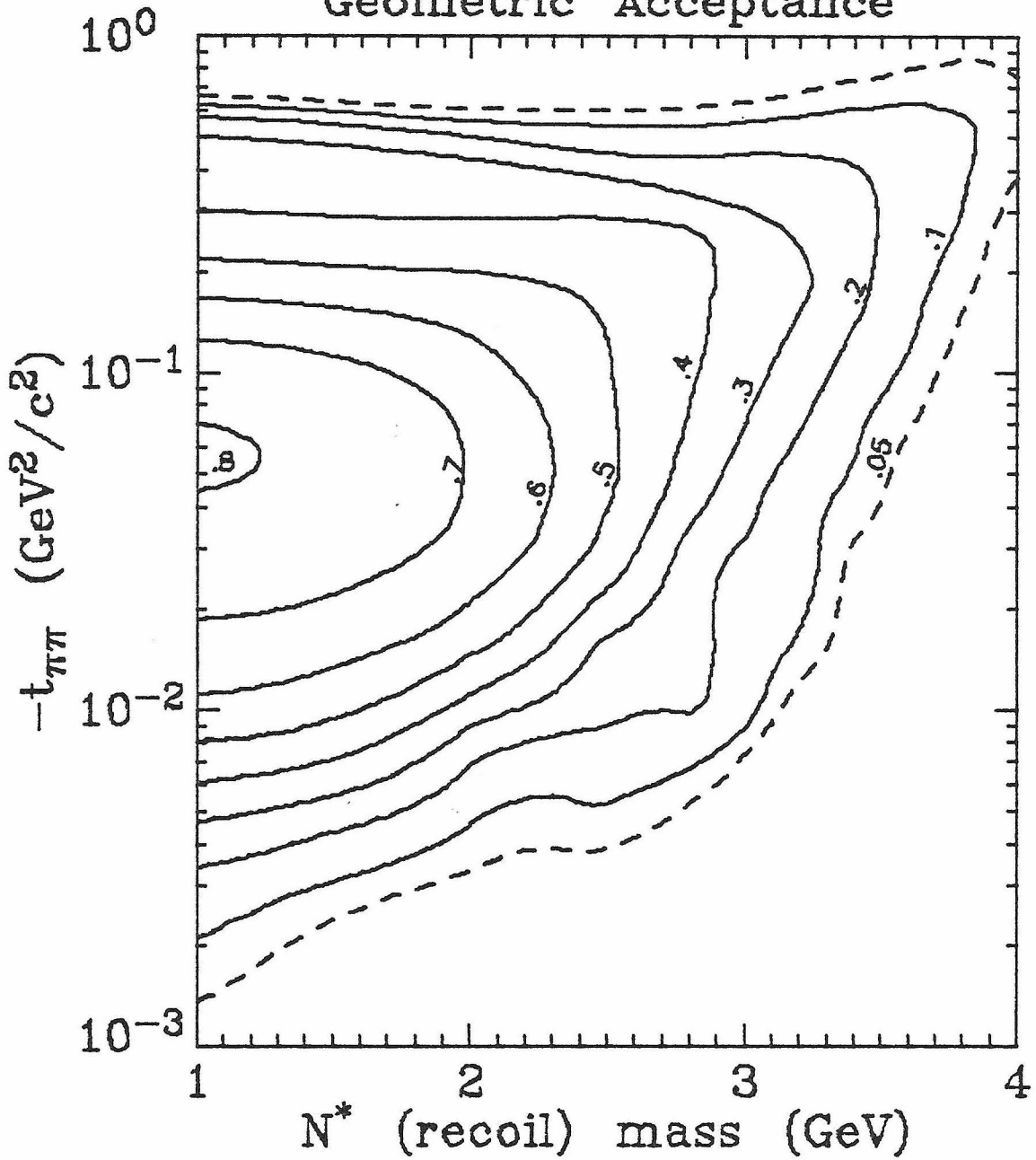


Figure IV.1

Contour plot of $\bar{\epsilon}(p, \cos\theta)$ as a function of the mass of the system recoiling against the fast forward pion (m_X or the N^* mass) and the momentum transfer from the beam to the fast pion ($t_{\pi\pi}$).

5. Computer Trigger Efficiency Correction

We have also weighted each event by the inverse of its computer trigger efficiency. This efficiency reflects the loss of events by the three cuts made by the computer trigger program in selecting inelastic events for bubble chamber pictures:

- (1) the DEL3 cut which corresponds to a high recoil mass cut,
- (2) the RESID cut, which eliminates false spark chamber tracks,
and
- (3) the MMF cut which removes the elastic events (low recoil mass).

The three quantities called DEL3, RESID, and MMF are given in Appendix A as d_3 (equations (8) and (10)), r (equation (31)), and $d_3 - C_t(x_2 - x_1)^2$ (equation (28)) respectively. Similarly the three cuts made by the trigger program are given by equations (11a), (32), and (28) in Appendix A. The total computer trigger efficiency is the probability for an inelastic event to pass all three cuts:

$$\epsilon_f = \epsilon_{\text{RESID}} \cdot \epsilon_{\text{DEL3}} \cdot \epsilon_{\text{MMF}} \quad (12)$$

The resulting computer trigger efficiency for the four prongs is dominated by ϵ_{RESID} since the four prong threshold is considerably above the lower mass cut at 1.1 GeV. There is a large effect from ϵ_{DEL3} beginning at 3.7 GeV (near the upper mass cut), but most of the interesting features of the data occur far below this region. Though the average of ϵ_f shows a very small linear dependence on the recoil mass (see Fig. IV.2), it mostly constitutes an overall constant correction to the four

prong cross section on the order of a few percent.

The computer trigger efficiency, like the geometrical efficiency, is a function of the momentum vector of the fast track (\vec{p}) as is to be expected since the computer trigger program calculates its test quantities from measurements of the fast particle. The computer trigger efficiency is dominated by statistical effects in the beam phase space (especially the beam energy), the spark chamber setting error (resolution), and multiple scattering of the fast particle. This efficiency is also dependent on the values of the program parameters used to describe the apparatus and determine the trigger cuts. The efficiencies due to the individual RESID, DEL3, and MMF cuts were calculated by using the gaussian integrals:

$$\epsilon_{\text{RESID}} = \frac{1}{\sqrt{2\pi} \sigma_R(p, \theta)} \int_{-\text{ITRC}}^{+\text{ITRC}} \exp\{-(r-\bar{r}(p, \theta))^2/2\sigma_R^2(p, \theta)\} dr \quad (13a)$$

$$\epsilon_{\text{DEL3}} = \frac{1}{\sqrt{2\pi} \sigma_D(p, \theta)} \int_{-\infty}^{\text{IDMAX}} \exp\{-(m-\bar{d}(p, \theta))^2/2\sigma_D^2(p, \theta)\} dm \quad (13b)$$

$$\epsilon_{\text{MMF}} = \frac{1}{\sqrt{2\pi} \sigma_M(p, \theta)} \int_{\text{IDMIN}}^{+\infty} \exp\{-(m-\bar{m}(p, \theta))^2/2\sigma_M^2(p, \theta)\} dm \quad (13c)$$

where ITRC, IDMAX, and IDMIN are the values of the parameters used to define the cuts on RESID, DEL3, and MMF respectively. These parameters are called w_r , $d_{3\text{max}}$, and d'_{min} in Appendix A. Monte Carlo studies were used to evaluate the dependence of the means and variances of the test quantities (e.g., $\bar{r}(p, \theta)$ and $\sigma_R(p, \theta)$ in equation (13a)) on the

fast particle's momentum vector. A detailed discussion of this procedure is given in Appendix C. With the test quantity means and variances parameterized as functions of the fast particle's momentum vector, equations (12) and (13a-c) allowed us to calculate the computer trigger efficiency for each event.

The upper trigger mass cut for the π^- experiment was raised from 2.8 GeV to 3.8 GeV at roll 126 (of the BC film). The 3.8 GeV cut was used for the entire π^+ experiment. Shown in Fig. IV.2 is the average trigger efficiency ($\langle \epsilon_f \rangle$ or $\langle \epsilon_{fast} \rangle$) for 4C and 1C four-prong events as a function of the N^* mass for rolls below 126 and rolls above 126 separately. The two different upper mass cuts are clearly evident as rapid drops in $\langle \epsilon_{fast} \rangle$ at 2.8 and 3.8 GeV. Also evident is the weak linear dependence of ϵ_f on the N^* mass for masses below the trigger cut. Fig. IV.3 shows $\langle \epsilon_{fast} \rangle$ with the linear dependence ($\epsilon_{lin}(m_{N^*})$) on the N^* mass removed. For masses below the trigger cut, $\langle \epsilon_{fast} \rangle / \epsilon_{lin}(m_{N^*})$ is a constant with the value 1.0. The curve in Fig. IV.3 that goes from 1 at 2.7 GeV to 0 at 2.9 GeV is an estimate of the shape of ϵ_f (with the linear mass dependence removed) at the mass cut. The data points above 2.8 GeV for rolls below 126 are non-zero and have large error bars because $\langle \epsilon_{fast} \rangle$ was calculated using the actual data which has very few events in the region. This estimate of ϵ_f was combined with the ratio of the number of events from rolls above 126 (and including roll 126) to the number of events from rolls below 126 to yield an extra weight function to correct for the "missing" events above the 2.8 GeV trigger mass cut. This ratio was found to be 2.7

by using the 4C and 1C weighted events (weighted by the geometrical acceptance and trigger efficiency). By weighted events, we mean the weight-sum for the events. Taking either 4C or 1C events separately or using unweighted as opposed to weighted events did not give a significantly different value for the ratio. The resulting corrected N^* mass distribution for the 1C events is shown in Fig. IV.4 along with the uncorrected distribution for all rolls. The corrected distribution now has the same overall shape as the distribution for rolls above or equal to 126.

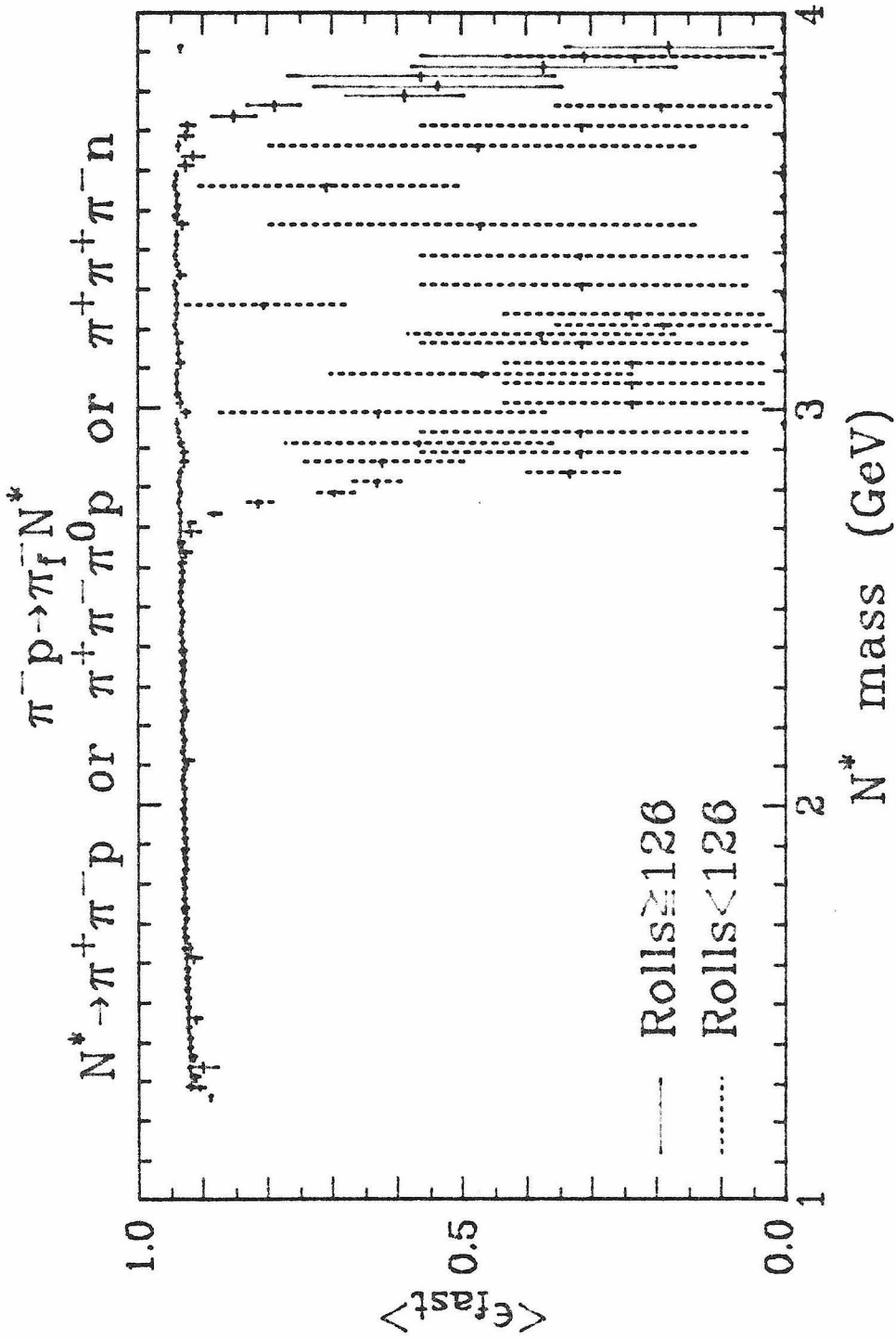


Figure IV.2

Average trigger efficiency ($\langle \epsilon_f \rangle$) as a function of the N^* (recoil system) mass for the two different upper mass cuts used in the π^- experiment.

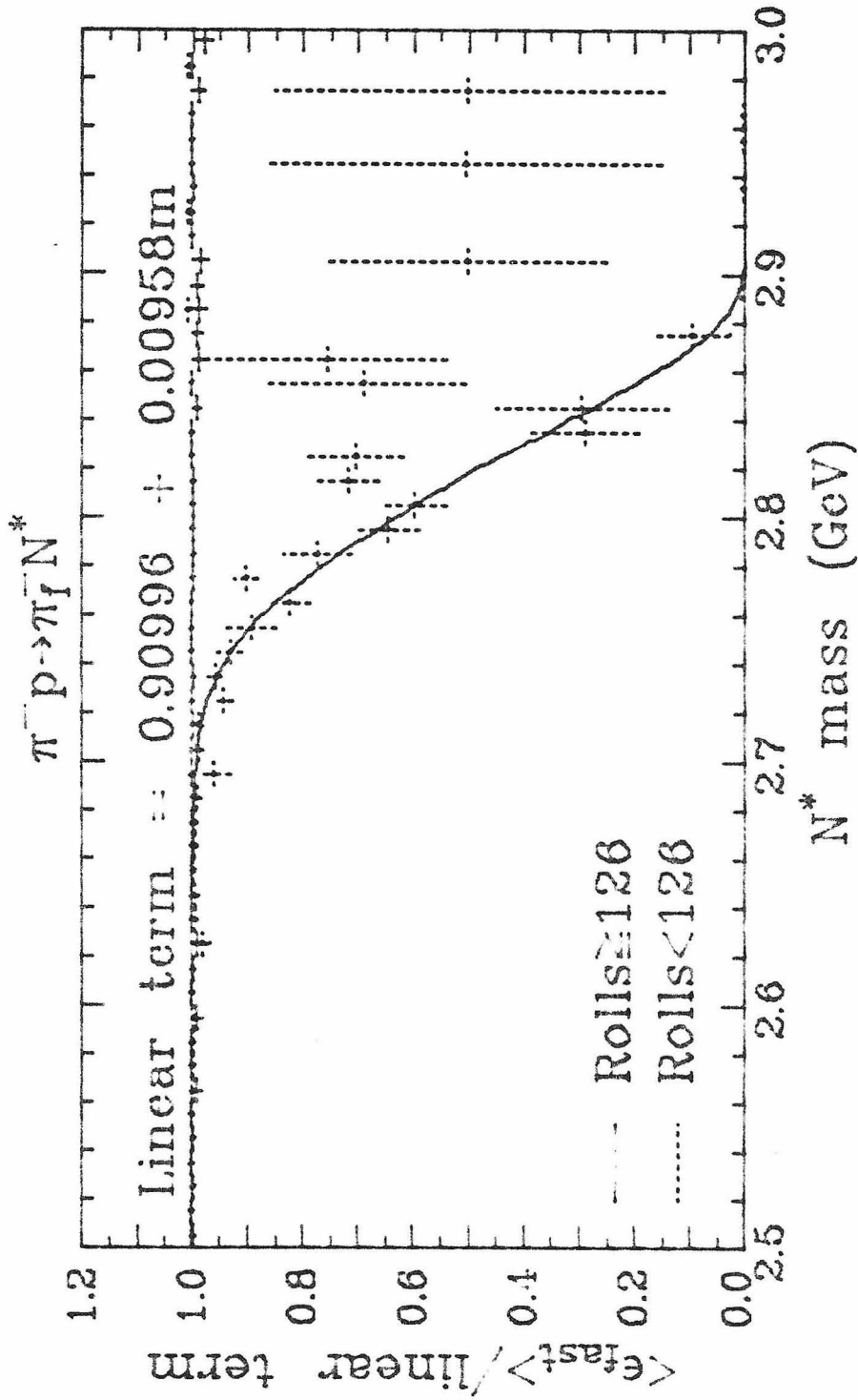


Figure IV.3

The linear dependence in the N^* mass has been divided out of $\langle \epsilon_f \rangle$ which results in a flat curve for rolls above 126. The line through the low roll data is an estimate of the decrease of ϵ_f with mass at the cut.

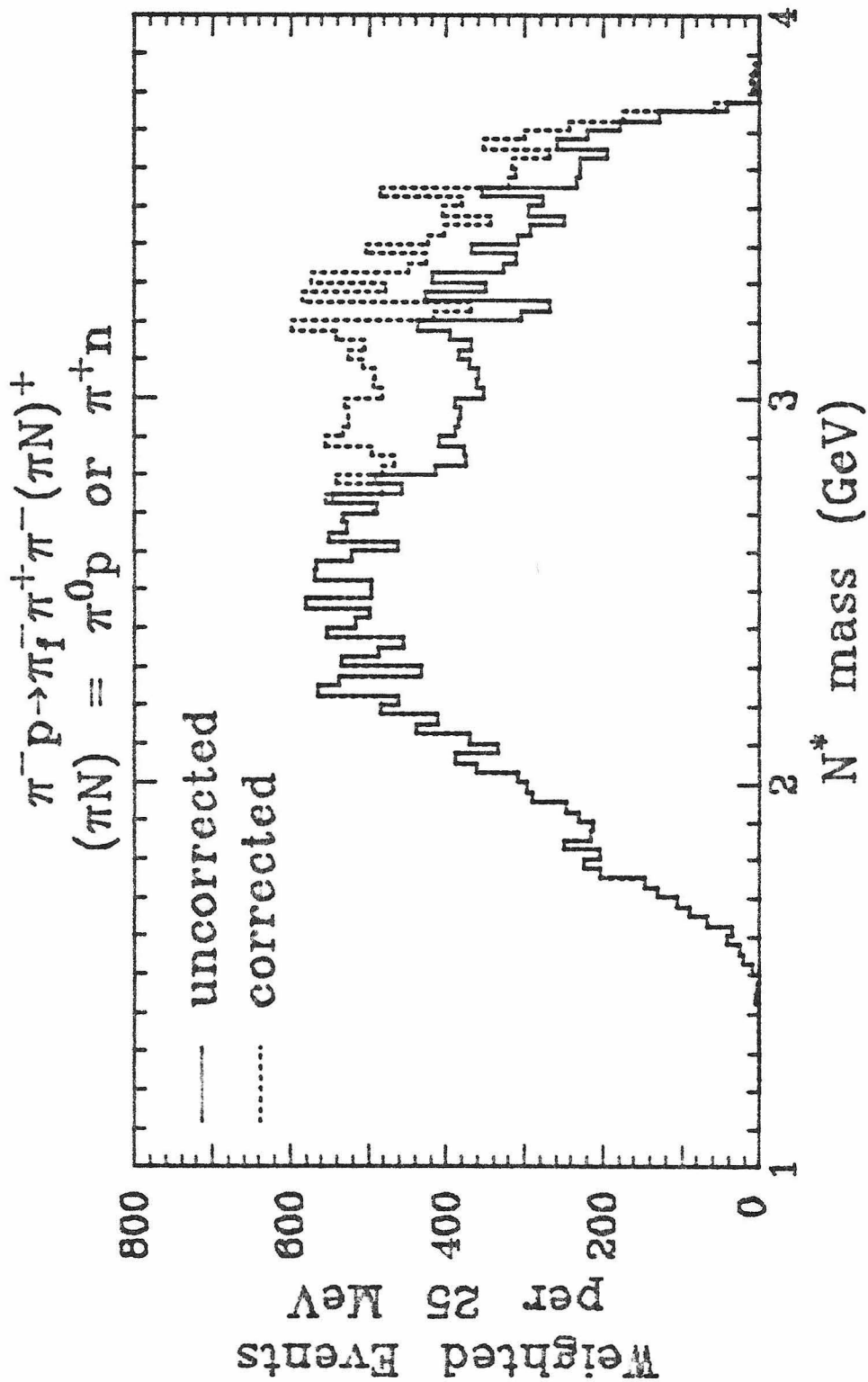


Figure IV.4

Effects of the correction weight function on the $\pi^- N^*$ mass distribution.

6. Channel Corrections and Background Estimates

The procedure adopted to resolve questions of ambiguous fits (multiple kinematic fits for different channel hypotheses) for an event was to select a single fit to describe the event. Thus each event was assigned to one and only one channel. However, this process is not perfect. Some events that belong to a channel are not assigned to it and thus lost. In addition, a background of events lost from the other channels creeps into each channel. The number of events so lost or gained are estimated and used to calculate the correction to the cross section (shown in equation (2) as the factor ϵ_{ch}).

Fig. IV.5 shows the confidence level distributions of the events in the four 1C channels. The confidence level (CL) for an event is the probability of χ^2 values (for the kinematic fit) larger than the particular value observed for that event. The CL distribution is useful in that in a perfect world (errors assigned correctly and residuals distributed as gaussians), it would be a constant distribution so that 5% of the events would have $CL < 5\%$ and so forth. As is seen in Fig. IV.5, considerably more than 5% of the events have $CL < 5\%$. These extra events are from two sources, background events from other channels that were incorrectly identified and good events from the correct channel. There are more than 5% of the events of the channel in the $CL < 5\%$ bin because the residual distributions contain more events in their tails than given by gaussian shapes. These excess tail events also show up as extra events in the CL bins immediately above 5%. The distributions above about 20% are very flat as is to be expected. Thus, after making

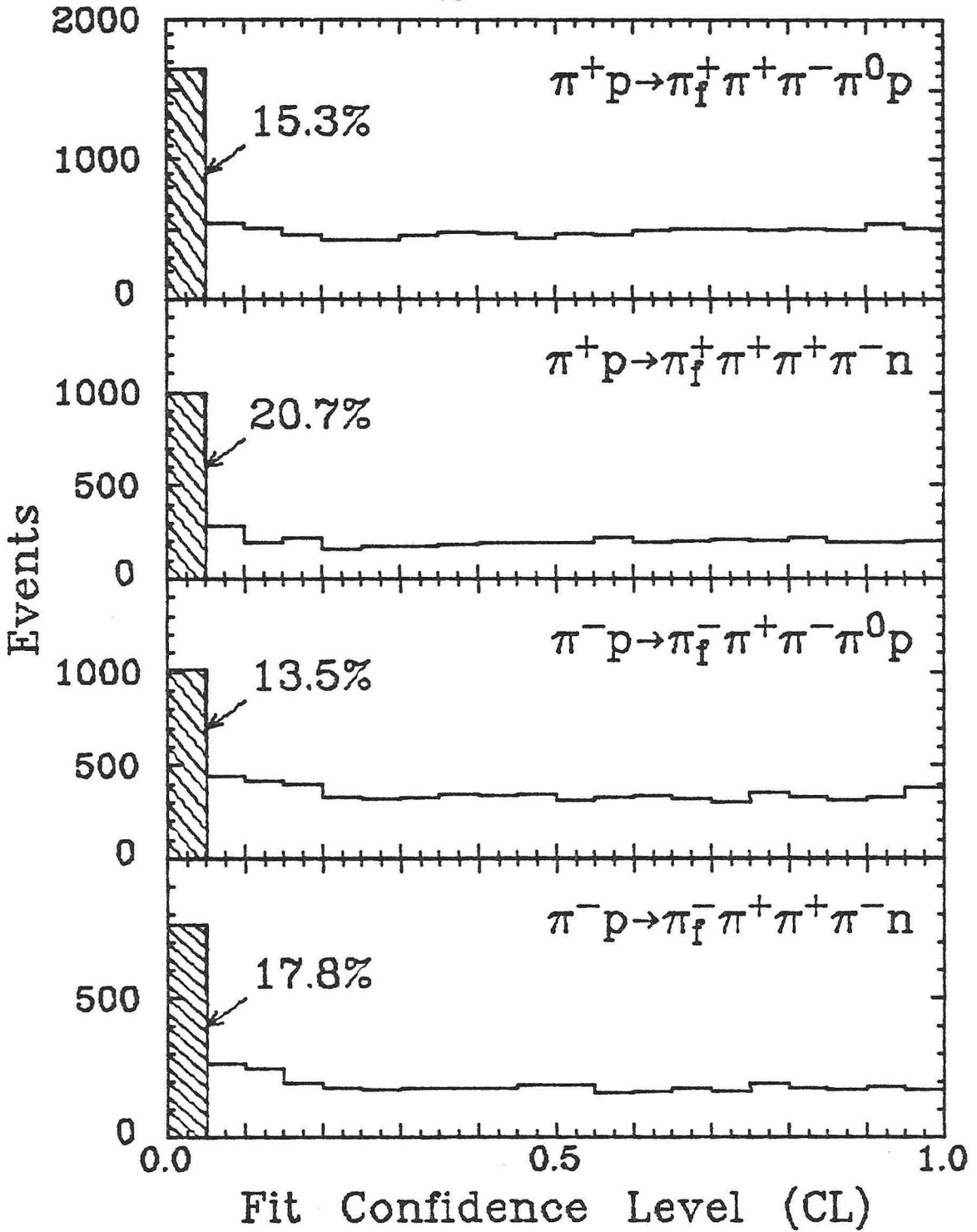


Figure IV.5

Distributions of the kinematic fit confidence level (χ^2 probability) for the four 1C channels. The shaded region shows the events below the 5% CL cut along with the fractions of these events in the channel.

the $CL \geq 5\%$ cut on the data, there remained the problem of estimating the number of background events remaining in the channel and of estimating the number of good events lost from the channel by the CL cut and the fit selection process. Once these numbers were known, the channel efficiency (ϵ_{ch}) and the normalization constant (e from equation (2)) were calculated for each channel individually.

The pertinent numbers of events are given in Table IV.5. The number of events comprising each channel's data sample is given in line 1 of the table. The distributions of the missing-mass-squared (m^2) are shown in Figs. IV.6a-d. One feature of our experiment that can be seen from these figures is that the hybridization to improve the measurement of the fast track has dramatically improved our resolution in the neutral missing mass. The width of the π^0 missing mass peak corresponds to a sigma of about 70 MeV which is less than one half of the π^0 peak sigma of many pure bubble chamber experiments at these energies [Baltay 1978, Cason 1970 and 1973, Hones 1970, Johnson 1976, and Kung 1969]. Similarly, the n missing mass peak in our experiment shows a sigma of about 50 MeV which is also better resolution than that obtained in previous experiments [Cason 1970 and Johnson 1976]. Also shown on the plots are the values of the centroids of the peaks. The π^- experiment was processed through TVGP with a slightly low value for the bubble chamber magnetic field so the peaks are 10 to 15 MeV below the correct values (the π^0 or n mass squared). A similar shift is also to be observed in the invariant masses of the π^- experiment (for instance, the ω^0 peak is about 5 MeV high). This shift was not cor-

Table IV.4

Lost and background event counts in IC 4-prong channels

	π^+ experiment		π^- experiment	
	π^0 channel	n channel	π^0 channel	n channel
1. Events with $CL \geq 5\%$ (channel data sample)	9145	3838	6525	3524
2. Estimate of good channel events removed with $CL < 5\%$	692 \pm 62	426 \pm 30	634 \pm 76	400 \pm 48
3. Events lost to opposite IC channel	0 \pm 15	0 \pm 15	50 \pm 24	50 \pm 15
4. Events lost to 4C channel	0	0	0	0
5. Events lost to 0C channel	29 \pm 11	14 \pm 6	152 \pm 26	65 \pm 17
6. Total events lost from channel	721 \pm 65	440 \pm 34	836 \pm 84	515 \pm 53
7. Background events in channel with $m_0^2 > m_0^2$ (from 0C and IC channels)	865 \pm 96	395 \pm 62	317 \pm 81	335 \pm 59
8. Background in channel from 4C's	0	0	324 \pm 65	36 \pm 20
9. Background events from IC channel with $m_0^2 < m_0^2$	0	0	0	0 \pm 15
10. Total background events in channel	865 \pm 96	395 \pm 62	641 \pm 104	371 \pm 64
11. True number of events in channel	8971 \pm 116	3867 \pm 69	6720 \pm 134	3668 \pm 83

Figures IV.6a-d

Missing-mass-squared distributions for the selected ($CL \geq 5\%$) events of the four 1C channels. The shaded distributions show the estimated background event distributions in each channel. Also given are the approximate mm^2 values of the peak centroids.

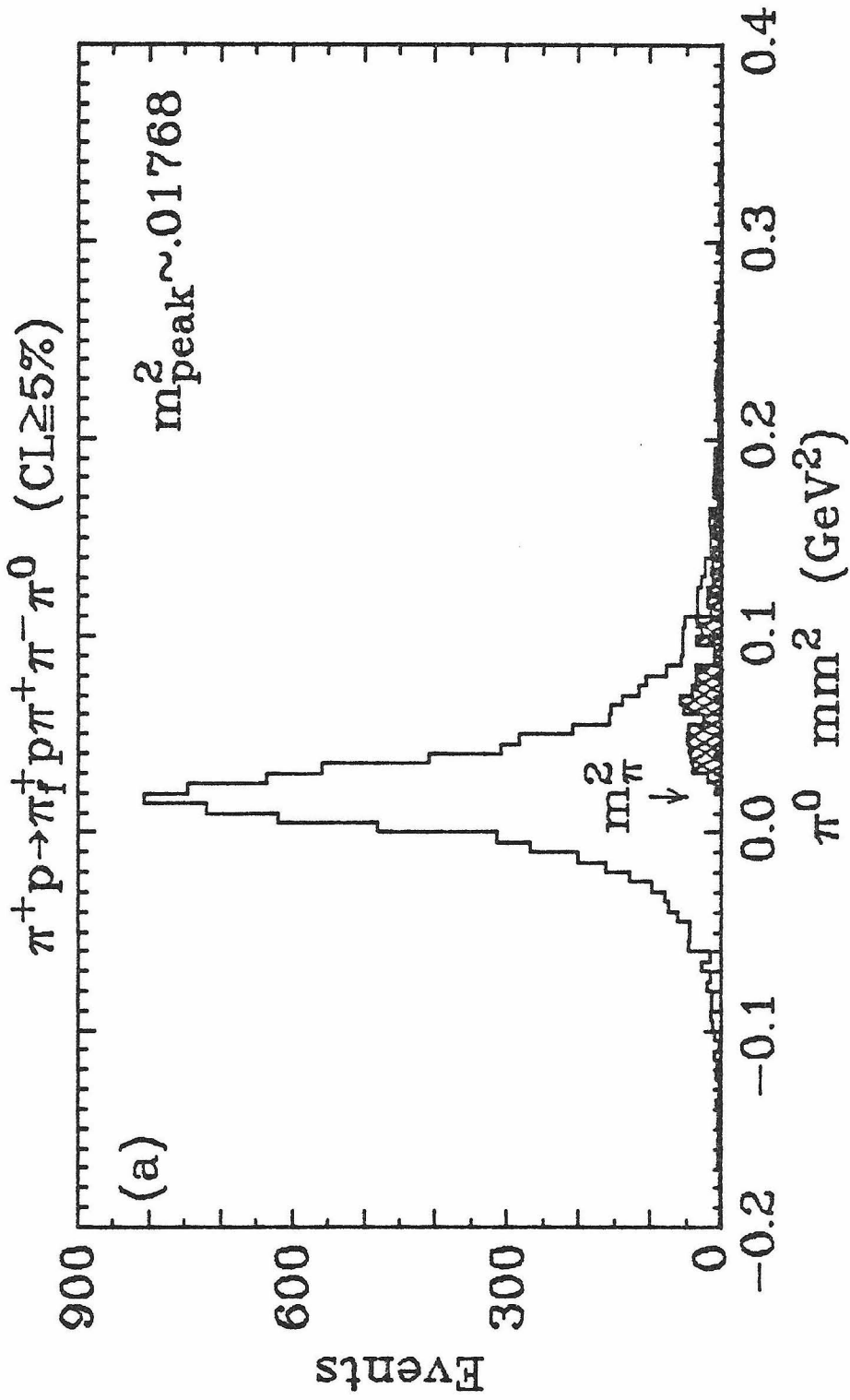


Figure IV.6a

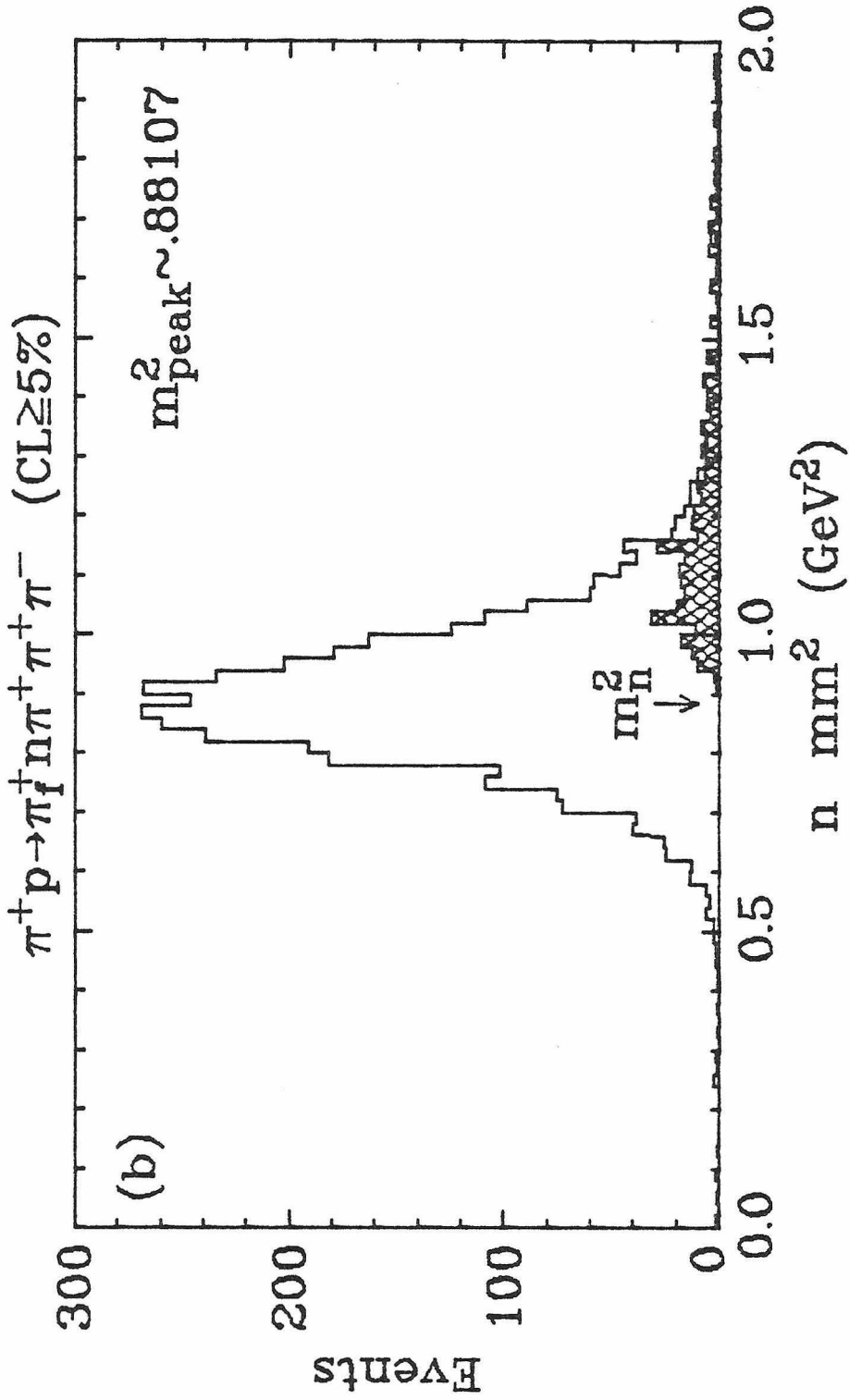


Figure IV.6b

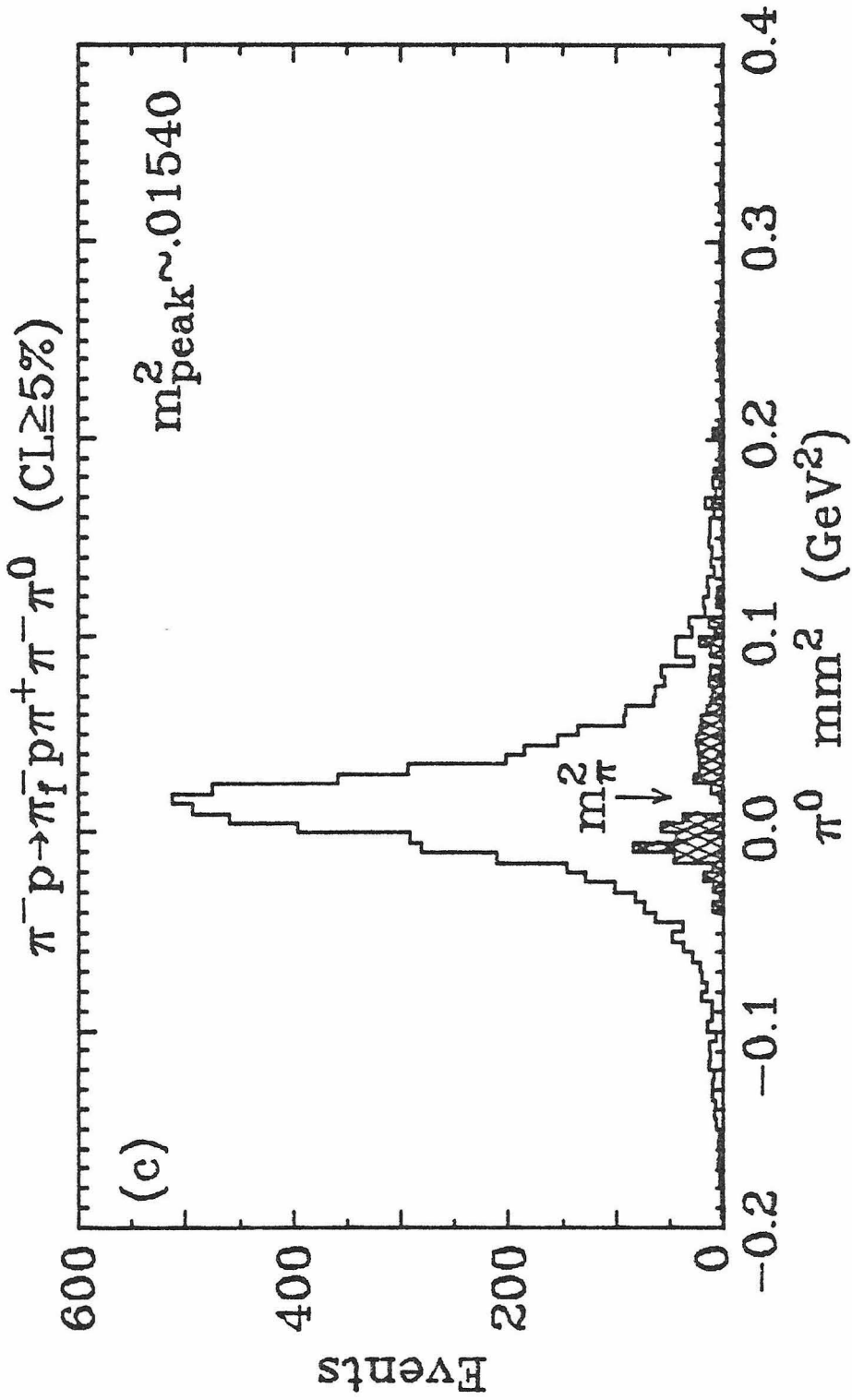


Figure IV.6c

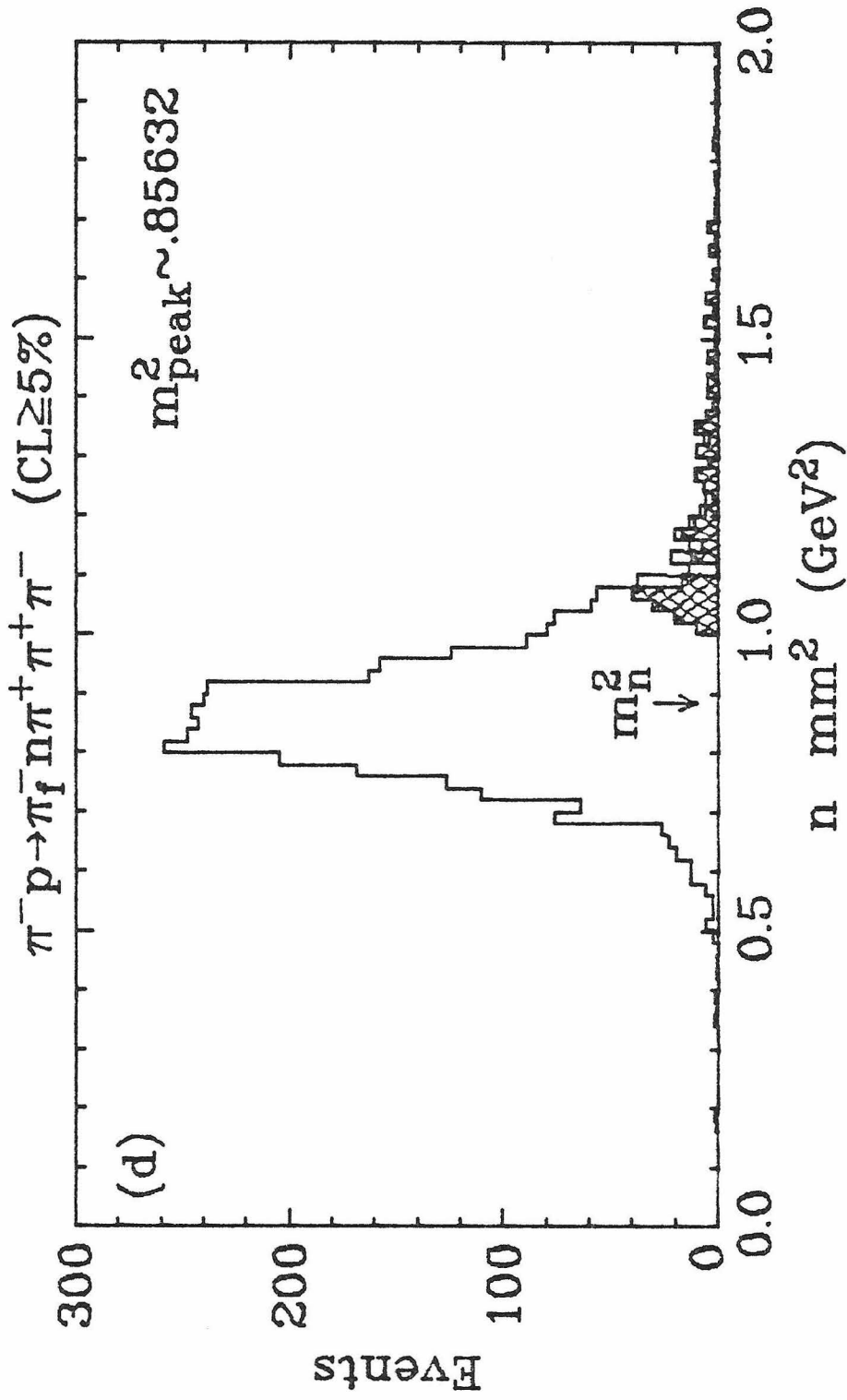


Figure IV.6d

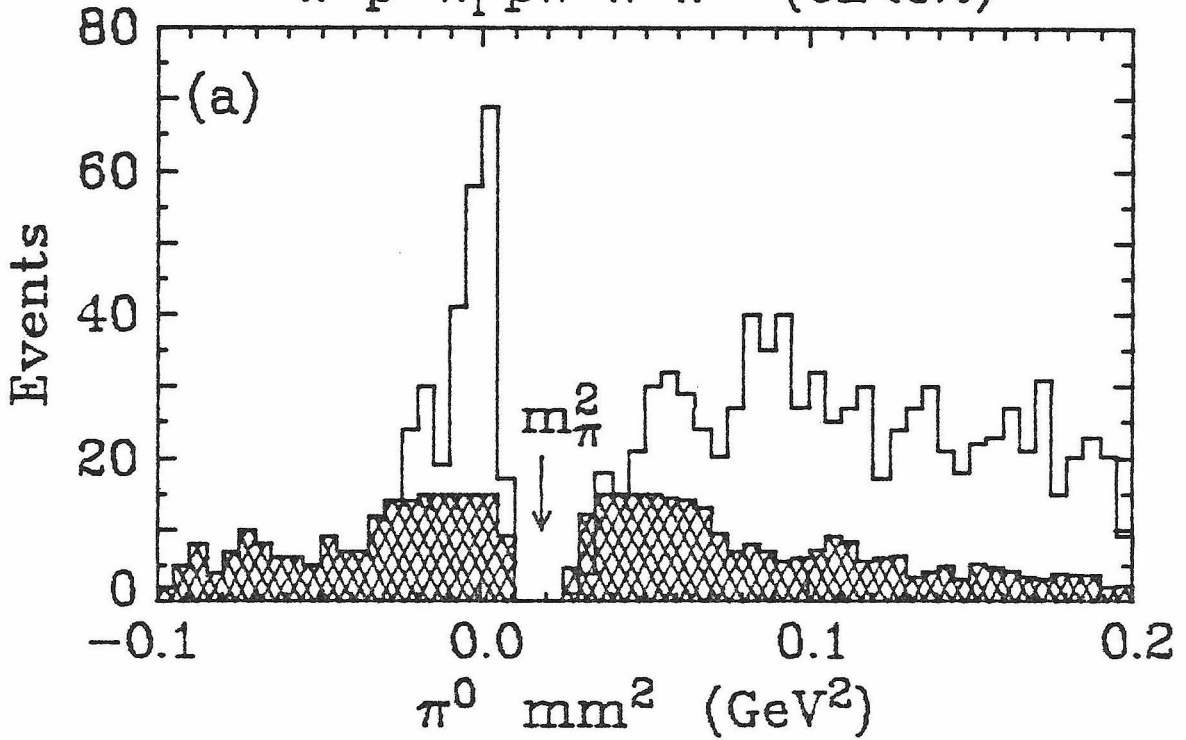
rected for.

The number of events lost from the channel by the confidence level cut (line 2 of Table IV.4) was estimated by using Figs. IV.7a-d. These plots show the missing-mass-squared distributions for the events with a confidence level below the 5% cut used to define the channel data samples. The shaded areas show the estimated distributions of good channel events removed by the CL cut. This estimation relied upon two assumptions about the missing mass distributions. The first assumption was that events belonging to the channel in question have a missing mass distribution that is symmetric about the mass of the channel's neutral particle. The second assumption is that events that do not belong to the channel have a very different missing mass distribution compared to that for the channel's events. Furthermore, these background events should occur in localized regions and be non-symmetric. Thus in Figs. IV.7a-d, the shaded distributions for events with mm^2 above the neutral particle's mass squared (m_0^2 , indicated by the arrow) is a reflection of the same distribution from below m_0^2 . This was done because the background events with mm^2 less than m_0^2 are fewer in number and are confined to a smaller region of the mm^2 distribution. In the case of the π^0 channel (Figs. IV.7a and IV.7c), the excess events peaking near zero are taken to be background leaking into the π^0 channel from the $4C$ channel. In the n channels, the π^- experiment was found to include some events with $mm^2 < m_0^2$ that appeared to be π^0 events (Fig. IV.7d) while no evidence was found for any non-channel events

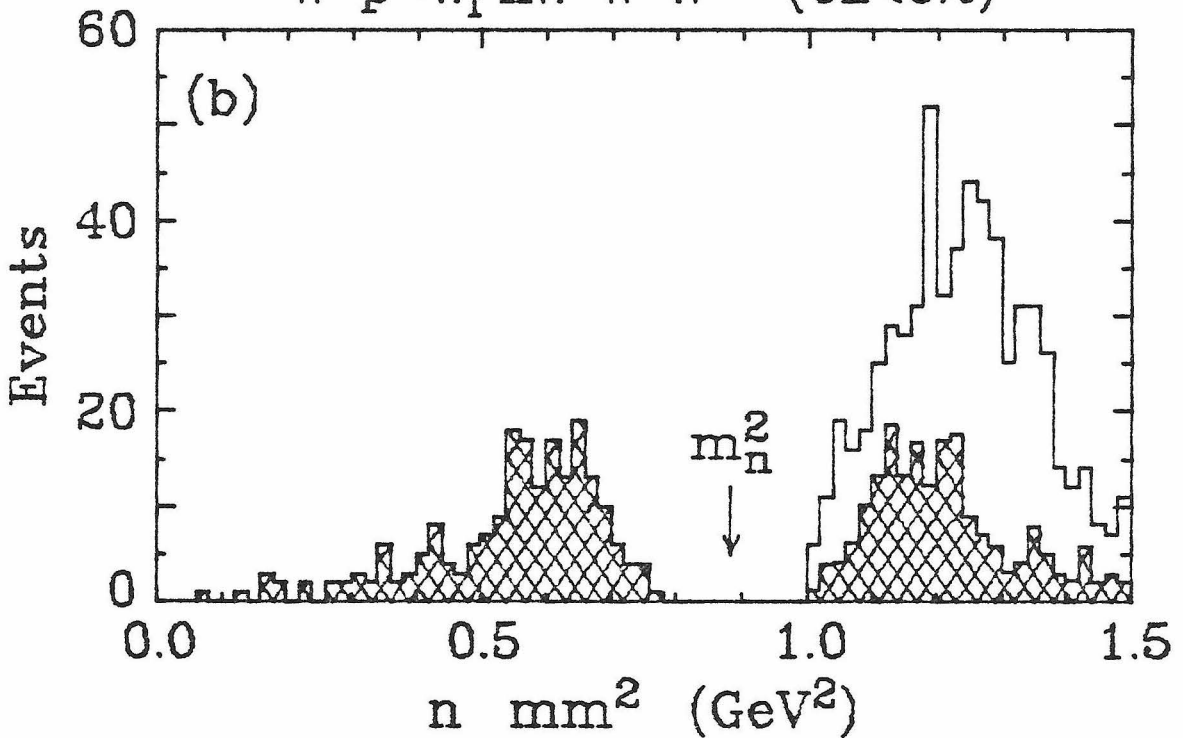
Figures IV.7a-d

Missing-mass-squared distributions for the events removed from the four 1C channels by the confidence level cut ($CL < 5\%$ events). The shaded events show the estimates of the distributions of "true" channel events lost with the CL cut.

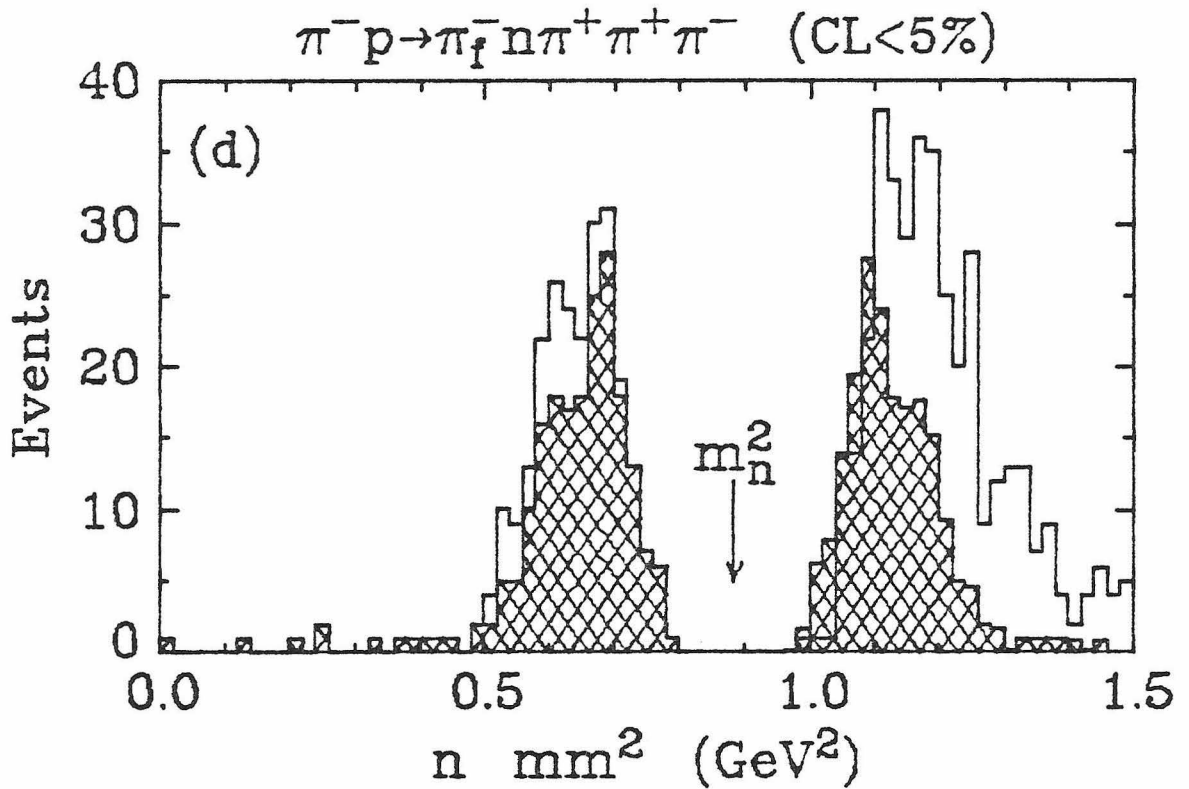
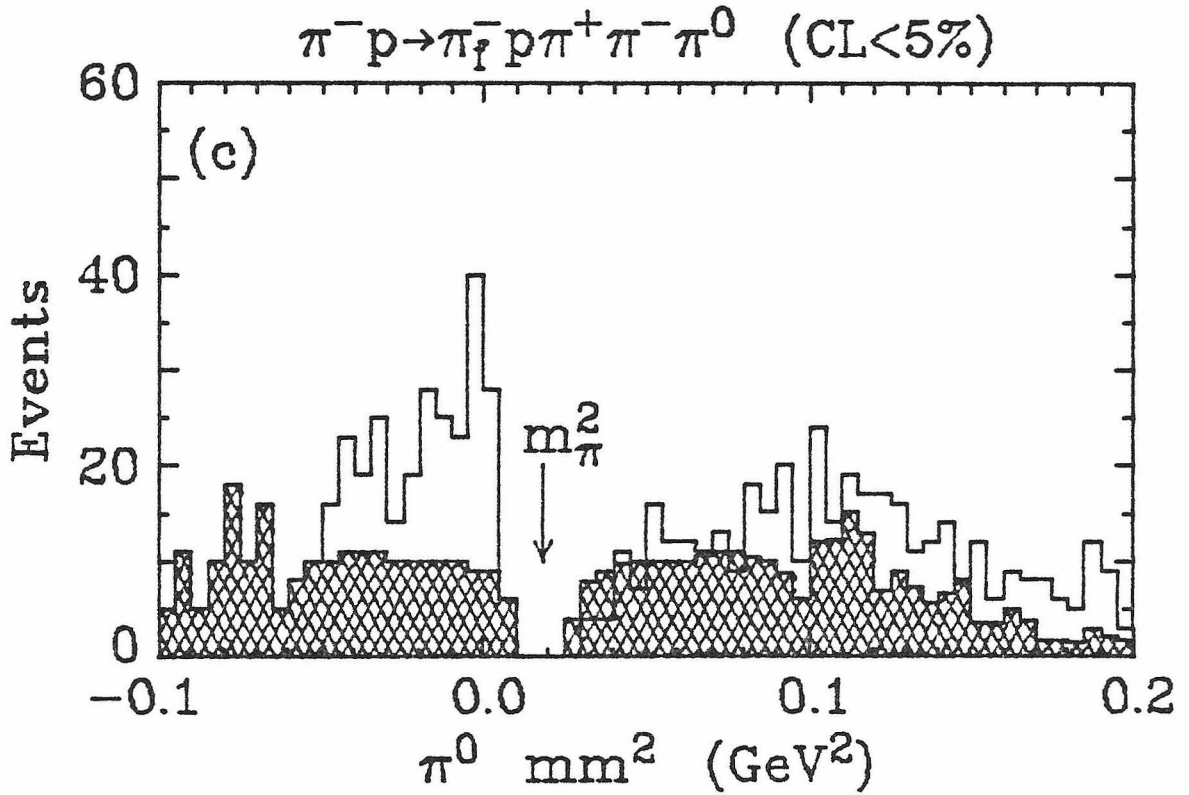
$\pi^+ p \rightarrow \pi_f^+ p \pi^+ \pi^- \pi^0$ (CL<5%)



$\pi^+ p \rightarrow \pi_f^+ n \pi^+ \pi^+ \pi^-$ (CL<5%)



Figures IV.7a and b



Figures IV.7c and d

with $mm^2 < m_0^2$ in the π^+ data (Fig. IV.7b). The errors associated with the estimates in line 2 of Table IV.4 were chosen to encompass the uncertainty in the outlined procedure, particularly with regards to the subtraction of background events with $mm^2 < m_0^2$.

Returning to Figs. IV.6a-d, the shaded regions here show the estimated mm^2 distributions of the background events remaining in the channels. At the same time, the numbers of background events are given on lines 7 through 9 of Table IV.4 (line 10 is the sum of all the events from separate sources of background). The background events are mostly from the 0C channel and possibly the other 1C channel (e.g., from the n channel as background in the π^0 channel and vice versa). They have missing masses that lie above the neutral particle mass (for the most part) and are consistent with their distributions starting near the multineutral threshold ($\pi^0\pi^0$ at $4m_\pi^2$ for the π^0 channel and $n\pi^0$ at $(m_n + m_\pi)^2$ for the n channel). In addition, the π^0 channel mm^2 distribution for the π^- experiment (Fig. IV.6c) shows a considerable number of background events from the 4C channel (the small shaded peak at about 0 in the figure).

These estimated distributions were made by explicit use of the assumptions stated above. It was assumed that most of the background events had $mm^2 > m_0^2$ and that, except for any 4C background, the events with $mm^2 < m_0^2$ were relatively free of background. Symmetry was used to then subtract away all but the background events. This was done by constructing a histogram in which events with $mm^2 > m_0^2$ were accumulated with a weight of +1 (as in a normal histogram) and events with $mm^2 < m_0^2$

were accumulated with a weight of -1 and shifted to a new mm^2 value given by:

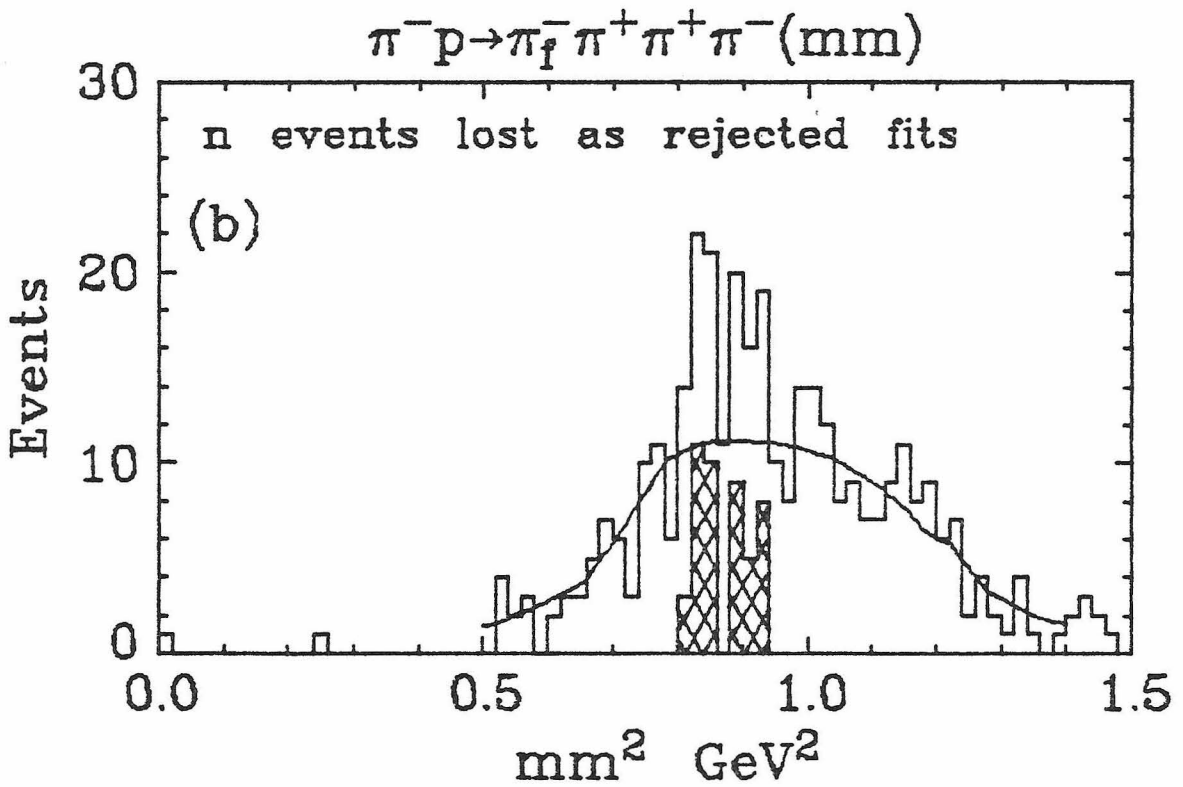
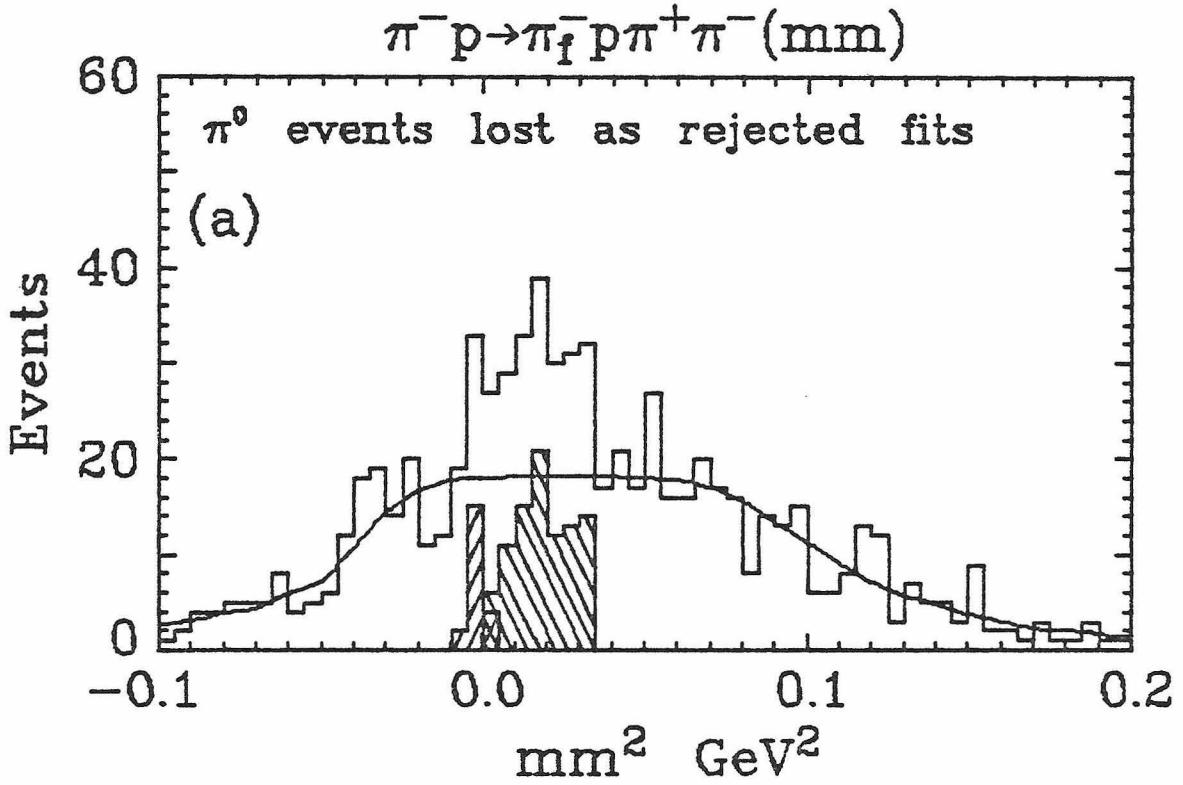
$$(mm^2)_{\text{new}} = 2m_0^2 - (mm^2)_{\text{old}} \quad (14)$$

Thus all the events appear to have $mm^2 > m_0^2$ in the histogram, but slightly less than half have a negative weight. This accomplishes the desired purpose of reflecting the $mm^2 < m_0^2$ part of the distribution about the centroid and subtracting it from the original $mm^2 > m_0^2$ part. This was done on an event-by-event basis to suppress a false signal from a mismatch in the relative mm^2 positions of the steep side of the mass peak. Even so, large statistical fluctuations appeared at the leading edge of the mm^2 background distribution and were removed by a hand smoothing approximation. The error in the estimated number of background events is the square root of the number of events in the channel's data sample. This error represents an error of about 15% to 30% in the estimate of the background and is considered adequate to cover any systematic errors in the procedure used to make the background estimate. Finally, for the π^- experiment π^0 channel data, the 4C background was arrived at by inverting the process and subtracting the upper portion ($mm^2 > m_0^2$) of the distribution from the lower portion. The procedure outlined above was checked by hand-drawing a smooth symmetric curve through the mm^2 distribution and estimating the background from the excess above the curve (in the 4C and multineutral mm^2 regions).

Besides losing events by the CL cut, 1C events were also lost by

Figures IV.8a and b

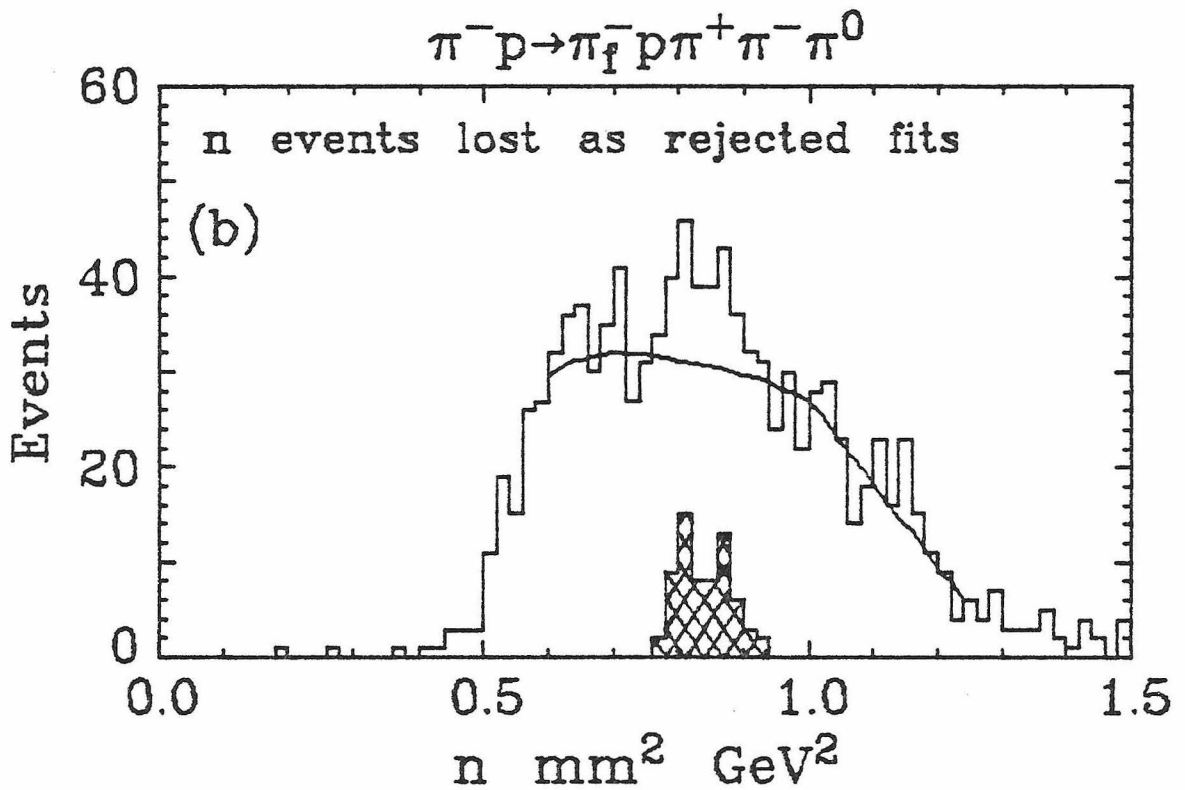
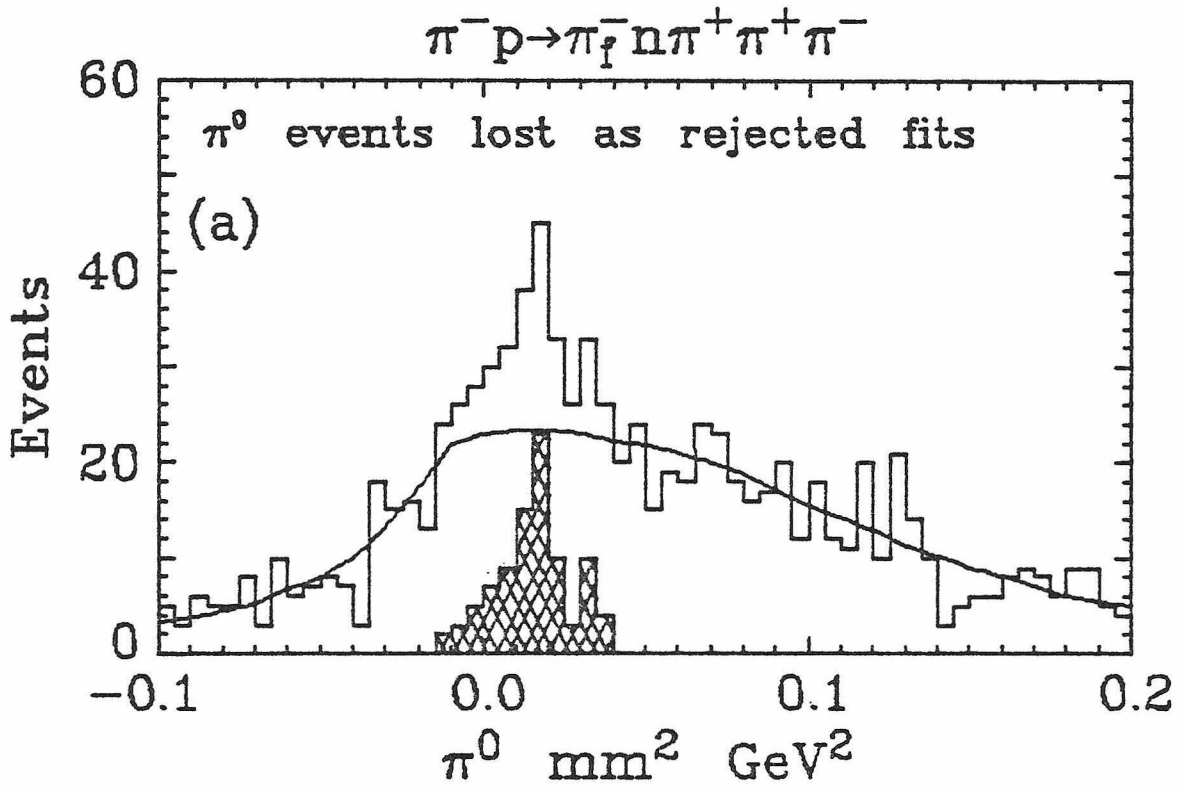
Missing-mass-squared distributions for events with 1C fits rejected by the ionization selection (and so becoming events in the 0C channels). The shaded regions show the estimated distributions of 1C events incorrectly rejected by the ionization selection. The small shaded peak in Fig. IV.8a near a m^2 of 0 represents 4C events that were incorrectly rejected by the ionization selection.



Figures IV.8a and b

Figures IV.9a and b

Missing-mass-squared distributions for 1C events with a second ambiguous 1C fit that was rejected by the ionization selection (the mm^2 distribution shown is that for the rejected fits). The shaded regions show the estimated mm^2 distributions of the 1C fits that were incorrectly rejected by the ionization selection.

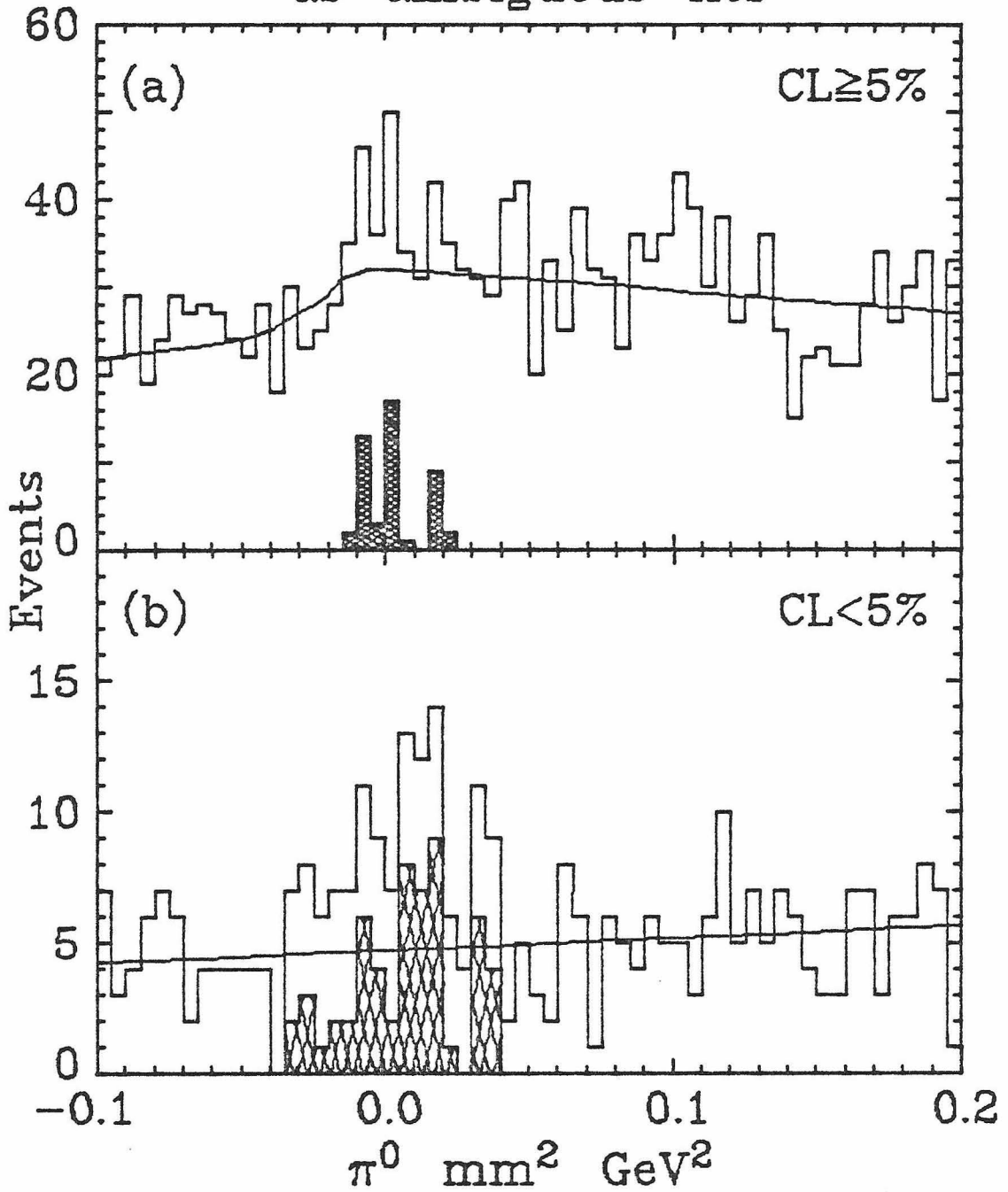


Figures IV.9a and b

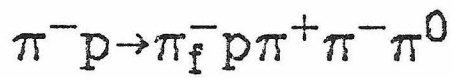
Figures IV.10a-d

Missing-mass-squared distributions for 1C events with a second ambiguous 1C fit. The shaded regions show the estimated m^2 distributions for 1C fits that should have been chosen as the correct fit.

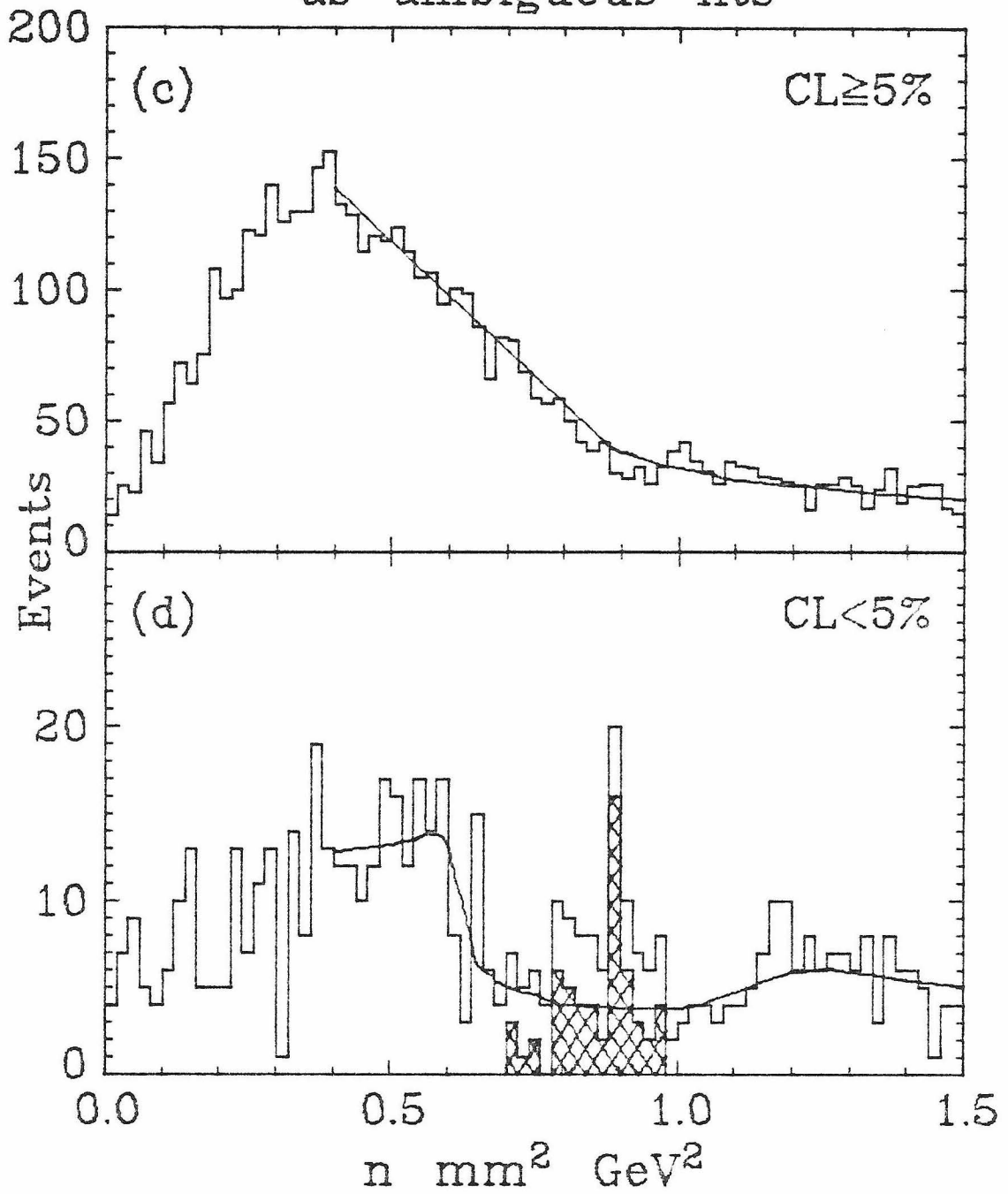
$\pi^- p \rightarrow \pi^- n \pi^+ \pi^+ \pi^-$
Lost π^0 events
as ambiguous fits



Figures IV.10a and b



Lost n events
as ambiguous fits



Figures IV.10c and d

the procedures used to select the best fit and assign each event to a single channel. The ionization selection caused some 1C events to be lost to the 0C channels (Figs. IV.8a and b) or selected the wrong 1C fit from among a set of ambiguous fits (Figs. IV.9a-b and IV.10a-d). The basic procedure used to estimate the number of events lost in these ways was to look at the mm^2 distributions for various classes of events. The results of these estimates are given in lines 3, 4, and 5 of Table IV.4. In all of these cases, the number of events was estimated by the excess events above a hand-drawn curve used to approximate the smooth mm^2 distribution from the correctly rejected fits. The errors assigned to these estimates also included the uncertainty in the choosing of the correct hand-drawn curve. Figs. IV.8a and b show the mm^2 distributions for the 1C fits of events for which the 1C fits were rejected by the ionization selection so the events were assigned to a 0C channel. Figs. IV.9a and b show the mm^2 distributions for 1C fits rejected by the ionization selection in favor of other 1C fits (of the opposite channel). The estimates from these figures (Figs. IV.9a-b) provided a check on the estimates obtained from Figs. IV.10a-d which show the mm^2 distributions for 1C fits ambiguous to the 1C fit used to assign the event to a channel. All of these figures (IV.8a-IV.10d) show mm^2 distributions for the π^- experiment only as that experiment suffered much larger fit selection losses than the π^+ experiment.

The results of estimating the losses from the channel data sample and the background remaining in the data are summarized in Table IV.5. Given there is the fraction of the data sample of each channel due to

the background events (about 10% of each channel) and the fraction of the channel's events that were lost by the fit selection process and the CL cut (again about 10% for each channel). The channel correction factor (ϵ_{ch} in equation (2)) was taken as 1 minus the channel loss fraction. The background estimate was not included in the correction factor so that the cross section for production of a resonance would be the corrected normalization divided into the number of events in the resonance. The background events left by the fit selection process were considered to not contribute to the resonance signals. Also given in Table IV.5 are the normalization factors (exposures) for each channel with the channel correction factor included. The estimated systematic errors given in Table IV.5 include the contributions from the beam contaminations.

Table IV.5

Normalizations and background fractions for the IC 4-prong channels

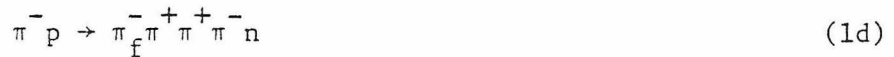
	π^+ experiment		π^- experiment	
	π^0 channel	n channel	π^0 channel	n channel
1. Background fraction	$9.5 \pm 1.0\%$	$10.3 \pm 1.6\%$	$9.8 \pm 1.6\%$	$10.5 \pm 1.8\%$
2. Lost events fraction	$7.3 \pm 0.7\%$	$10.3 \pm 0.3\%$	$11.4 \pm 1.1\%$	$12.8 \pm 1.5\%$
3. Channel correction (ϵ_{ch})	$.927 \pm .007$	$.897 \pm .003$	$.886 \pm .011$	$.872 \pm .015$
4. Exposure (e in events/ μ b)	79.4 ± 3.6	76.9 ± 3.4	68.6 ± 3.6	67.5 ± 3.6
5. Percent error in normalization	4.5%	4.4%	5.2%	5.3%
6. Estimated systematic error	6.4%	6.4%	6.0%	6.0%

Chapter V

Results for the Five-body Channels

1. Overview

The data to be presented in this chapter are from events of the 1C four prong reactions:



where one of the outgoing pions has been subscripted with an "f" to indicate that it is the fast pion that entered the spectrometer. The online measurement of the fast pion's trajectory was used to trigger the bubble chamber. The fast pion could not be confused with another pion of the same charge since the fast pion had to have at least half of the available energy of the event to enter the spectrometer at all. This experiment's trigger thus selected events of the type shown in Fig. V.1a. However, there is some contribution from events with the production of fast meson resonances (Fig. V.1b). The events with fast meson resonances represent a background in our experiment. Our observations of processes like that in Fig. V.1b are heavily biased by the trigger since not all of the decays of the fast meson resonances will have triggered the experiment. As will be seen in this chapter, reactions (1a) through (1d) are dominated by single and multiple resonance production, including fast meson resonance production.

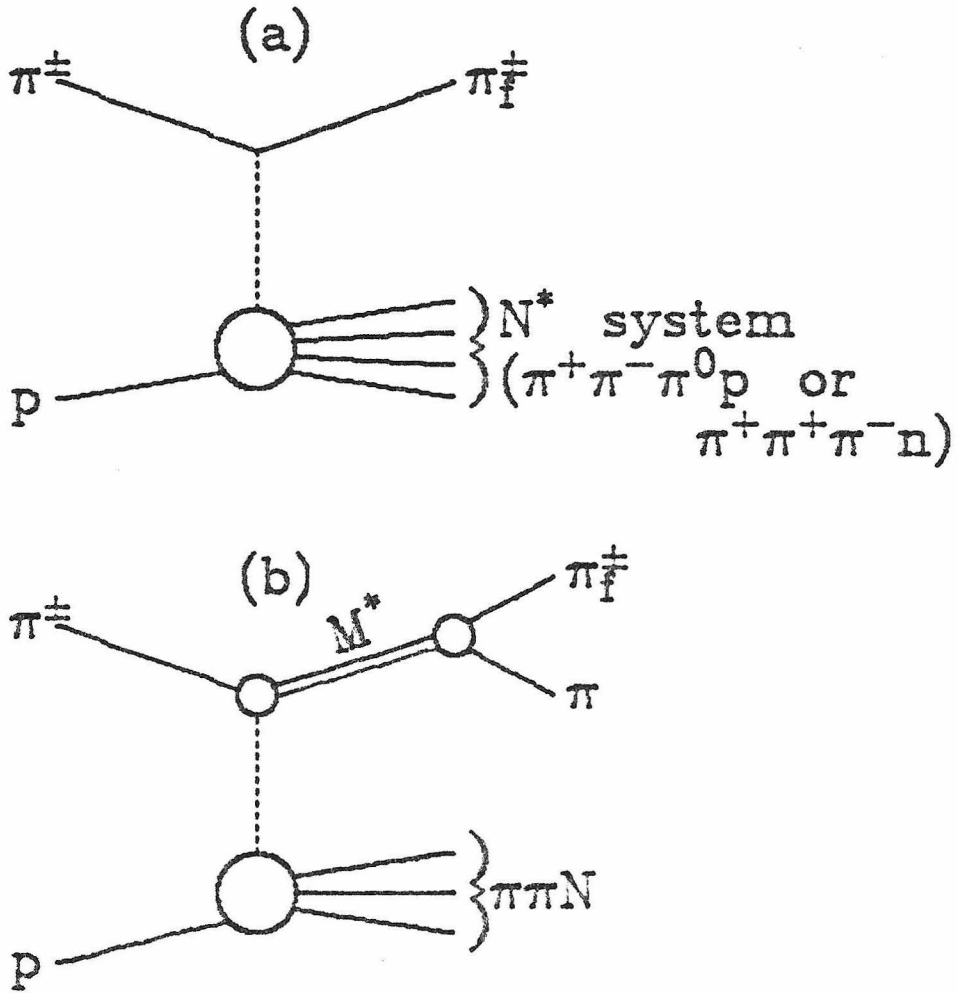


Figure V.1

General Feynman diagrams used to represent processes occurring in the data. The major contribution is shown in (a) where the components of the N^* (or slow) system may involve resonances among all or some of the particles. The N^* system may also involve non-resonant sub-processes not specified here. The diagram in (b) illustrates production of a fast meson resonance (usually a ρ or f^0) which decays into the fast pion and a slower pion. The comments made about the N^* system in (a) also apply to the $\pi\pi N$ system at the lower vertex of diagram (b).

The events used in the final analysis were required to have the invariant mass m_{N^*} of the particles other than the π_f^\pm less than 3.7 GeV and an invariant momentum transfer from the beam to the fast pion ($t_{\pi\pi} = (p_{\mu f} - p_{\mu b})^2$) greater than -0.6 (GeV/c)^2 . These cuts served to eliminate events with low acceptance (i.e., large weights). A few remaining events with weights greater than 20 left after the m_{N^*} and $t_{\pi\pi}$ cuts were also removed. Since these events represented only a few percent (3-5%) of the sample and because we were unsure whether these events belonged in the sample, we did not correct the cross sections for their loss. In any case the resulting error was within our systematic error and well within the combined statistical and systematic errors. The cuts used to define the 1C data samples are summarized in Table V.1.

Table V.1

Cuts used to define the 1C data sample

Kinematic fit confidence level (CL) cut:	$CL \geq 5\%$
Cut on invariant mass of slow system ($\pi^+ \pi^- \pi^0 p$ or $\pi^+ \pi^+ \pi^- n$):	$m_{N^*} < 3.7 \text{ GeV}$
Cut on momentum transfer from beam to fast π :	$ t_{\pi\pi} < 0.6 \text{ (GeV/c)}^2$
Cut on event weights:	$w_i \leq 20$

Table V.2 gives the final weight-sums and corrected cross sections for reactions (1a) to (1d). These cross sections are the portion of the total cross section seen by this experiment and as seen in Table V.2 are only a quarter to a third of the total cross sections predicted

for these reactions at our beam energies (see Table I.3). However, these partial cross sections cannot be directly compared with other experiments as one third to one half of them are from the biased fast resonance production. In this chapter, we will estimate the contribution of the fast resonance production and subtract it from the observed cross sections to give cross sections for the diffractive process in Fig. V.1a (see section 3 of this chapter).

The cross sections in Table V.2 were calculated using the corrected channel exposure factors discussed in Chapter IV (see Table IV.5). In addition, these cross sections were corrected for background events left in the channel data samples (again see Chapter IV) and for the loss of events with low $|t_{\pi\pi}|$ due to the acceptance cutoff (events with $|t_{\pi\pi}|$ below 0.003 (GeV/c)^2 were completely lost). The errors of the cross sections in Table V.2 include the contributions from the channel normalization errors (see Table IV.5). The table also lists the fraction error in the cross section and the fraction of the predicted total cross section actually observed (see Table I.3).

Table V.2

<u>Observed channel cross sections</u>				
<u>Channel</u>	<u>Weight-sum</u>	σ (μb) <u>(% error)</u>	$d\sigma/dt$ <u>correction</u>	<u>fraction of</u> <u>predicted σ_{tot}</u>
$\pi_f^+ \pi^+ \pi^- \pi^0 \text{ p}$	27336 ± 351	320 ± 15 (4.9%)	$2.76 \pm 0.26\%$	$24.8 \pm 1.8\%$
$\pi_f^+ \pi^+ \pi^+ \pi^- \text{ n}$	11467 ± 225	137 ± 7 (5.2%)	$2.29 \pm 0.43\%$	$29.8 \pm 6.7\%$
$\pi_f^- \pi^+ \pi^- \pi^0 \text{ p}$	19319 ± 295	261 ± 15 (5.8%)	$2.84 \pm 0.30\%$	$26.6 \pm 3.9\%$
$\pi_f^- \pi^+ \pi^+ \pi^- \text{ n}$	10597 ± 222	145 ± 9 (6.1%)	$3.26 \pm 0.46\%$	$32.2 \pm 5.4\%$

The low $|t_{\pi\pi}|$ corrections were gotten by fitting the data shown in Fig. V.2 with:

$$\frac{d\sigma}{dt} = A \exp(Bt_{\pi\pi}) \quad (2)$$

in the range from 0.02 to 0.6 (GeV/c)². The results of these fits are given in Table V.3. The low $|t_{\pi\pi}|$ correction was taken to be the difference between the data and the fit for the lowest $t_{\pi\pi}$ bin (from 0.0 to 0.01 (GeV/c)²).

Table V.3

<u>Results of the fits to $d\sigma/dt_{\pi\pi} = A \exp(B t_{\pi\pi})$</u>		
<u>Channel</u>	<u>A (mb/GeV²/c²)</u>	<u>B ((GeV/c)⁻²)</u>
$\pi_f^+ \pi^+ \pi^- \pi^0 p$	1.617±0.037	-4.36±0.10
$\pi_f^+ \pi^+ \pi^+ \pi^- n$	0.677±0.024	-4.14±0.15
$\pi_f^- \pi^+ \pi^- \pi^0 p$	1.322±0.036	-4.25±0.12
$\pi_f^- \pi^+ \pi^+ \pi^- n$	0.832±0.031	-5.03±0.18

For most of the remainder of this chapter, we shall present invariant mass distributions for combinations of the particles in reactions (1a)-(1d). We shall use this data to estimate the production of resonances in these reactions by a method discussed in section 3 of this chapter. The estimates of fast meson resonance production (section 3) will be used, as mentioned earlier, to extract the cross sections of the diffractive parts of reactions (1a)-(1d). By selecting fast ρ 's we will see that there is only a small amount of A meson pro-

duction in these reactions (section 4). We will see that the slow system ($\pi\pi\pi N$ without π_f^\pm) is dominated by resonance production (section 5). By selecting on a Δ or ρ in the slow system or by selecting a fast ρ , section 6 will show that there is considerable quasi-2-body (see also section 3) and quasi-3-body reactions involving fast meson resonances and associated slow system resonances. The lack of a detailed model for the fast meson resonance production prevents us from correcting these estimates for the events lost due to our trigger (see section 3). However, in section 7 we will discuss double resonance production and cascade decays involving only slow system resonances and so unaffected by the loss of a part of a fast resonance decay distribution. As a general observation, we find that reactions (1a)-(1d) are incredibly rich in resonance production as they are the final states of many quasi-2-body and quasi-3-body reactions. As a contrast to this complexity, the $d\sigma/dt_{\pi\pi}$ distributions were seen to be essentially pure exponentials. Similarly, the $d\sigma/dt_{pN}$ distributions also show rather simple behavior as discussed in the next section.

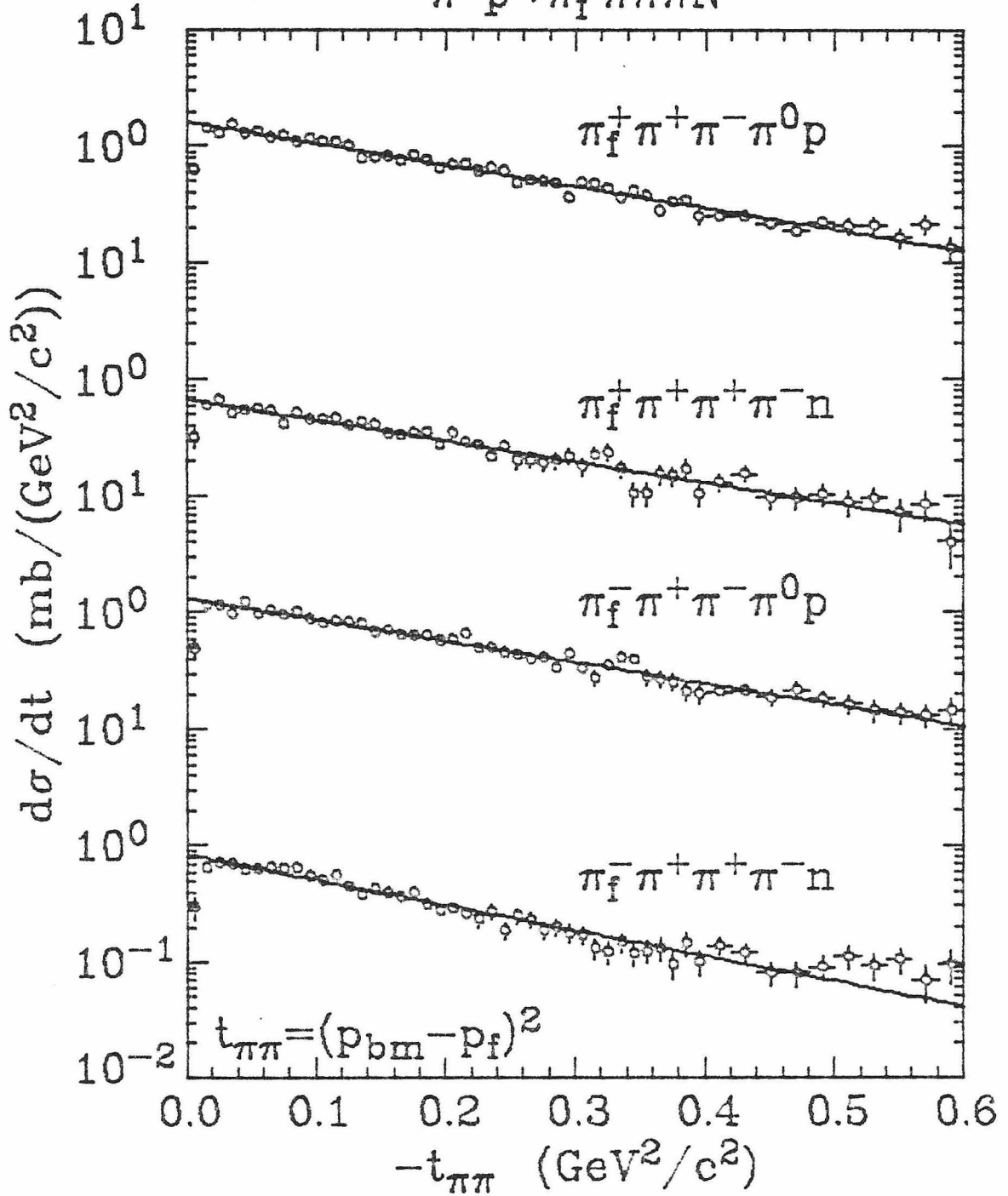


Figure V.2

Plot of $d\sigma/dt_{\pi\pi}$ for the four 1C reactions. The error bars include the errors quoted for the exposure factors (Chapter IV). The curves are the results of the fits to the data discussed in the text.

2. The $d\sigma/dt_{pN}$ Distributions

Fig. V.3 shows $d\sigma/dt_{pN}$ where t_{pN} is the invariant momentum transfer from the target proton to the outgoing nucleon (proton or neutron).

Fits of the form:

$$\frac{d\sigma}{dt_{pN}} = A \exp(Bt_{pN} + Ct_{pN}^2) \quad (3)$$

to this data are shown in the figure. The results of the fits are given in Table V.4 below. These distributions should be contrasted with those given in Fig. V.4 showing $d\sigma/dt_{pp}$ for the 4C reactions $\pi^\pm p \rightarrow \pi_f^\pm \pi^+ \pi^- p$. Whereas the 1C reactions (1a) to (1d) have $d\sigma/dt_{pN}$ distributions which are very nearly pure exponentials, the $d\sigma/dt_{pp}$ distributions for the four-body reactions show a marked change in slope at about -0.6 (GeV/c)^2 . The 4C events with $|t_{pp}|$ below 0.6 (GeV/c)^2 have a preponderance of events from the reactions of the form:



whereas those above the break show a very strong peak at about 1700 MeV in the $\pi^+ \pi^- p$ mass indicative of copious N^* resonance production. The lack of a steep forward slope in the 1C $d\sigma/dt_{pN}$ distributions and a slope (of 1.5 to 2.0 (GeV/c)^{-2}) comparable to that above 0.6 (GeV/c)^2 in the 4C $d\sigma/dt_{pp}$ distributions can be interpreted as a relative lack of heavy fast meson production in the 1C four-prong data as compared

to the 4C four-prong data. This conjecture is supported by the fast invariant mass distributions discussed below.

Table V.4

Results of fits to $d\sigma/dt_{pN} = A \exp(B|t_{pN}| + Ct_{pN}^2)$

<u>Channel</u>	<u>A (mb/GeV²/c²)</u>	<u>B ((GeV/c)⁻²)</u>	<u>C ((GeV/c)⁻⁴)</u>
$\pi_f^+ \pi^+ \pi^- \pi^0 p$	0.481±0.023	-1.59±0.01	0.110±0.043
$\pi_f^+ \pi^+ \pi^+ \pi^- n$	0.171±0.007	-1.236±0.042	—————
$\pi_f^- \pi^+ \pi^- \pi^0 p$	0.351±0.020	-1.54±0.12	0.163±0.050
$\pi_f^- \pi^+ \pi^+ \pi^- n$	0.235±0.018	-1.77±0.17	0.175±0.075

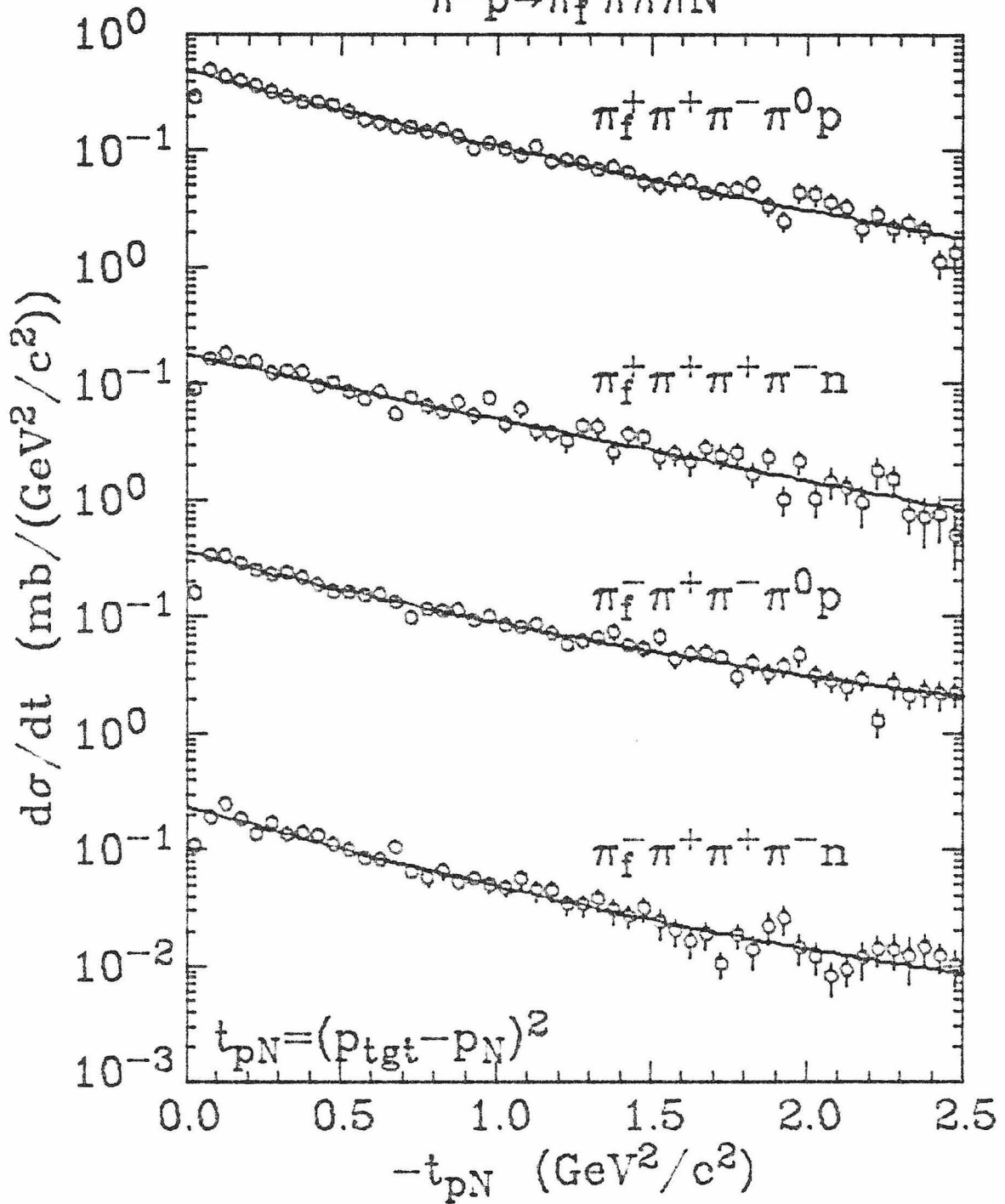


Figure V.3

Plot of $d\sigma/dt_{pN}$ for the four 1C reactions. The error bars include the errors quoted for the exposure factors. The lines are the curves resulting from fits to the data discussed in the text.

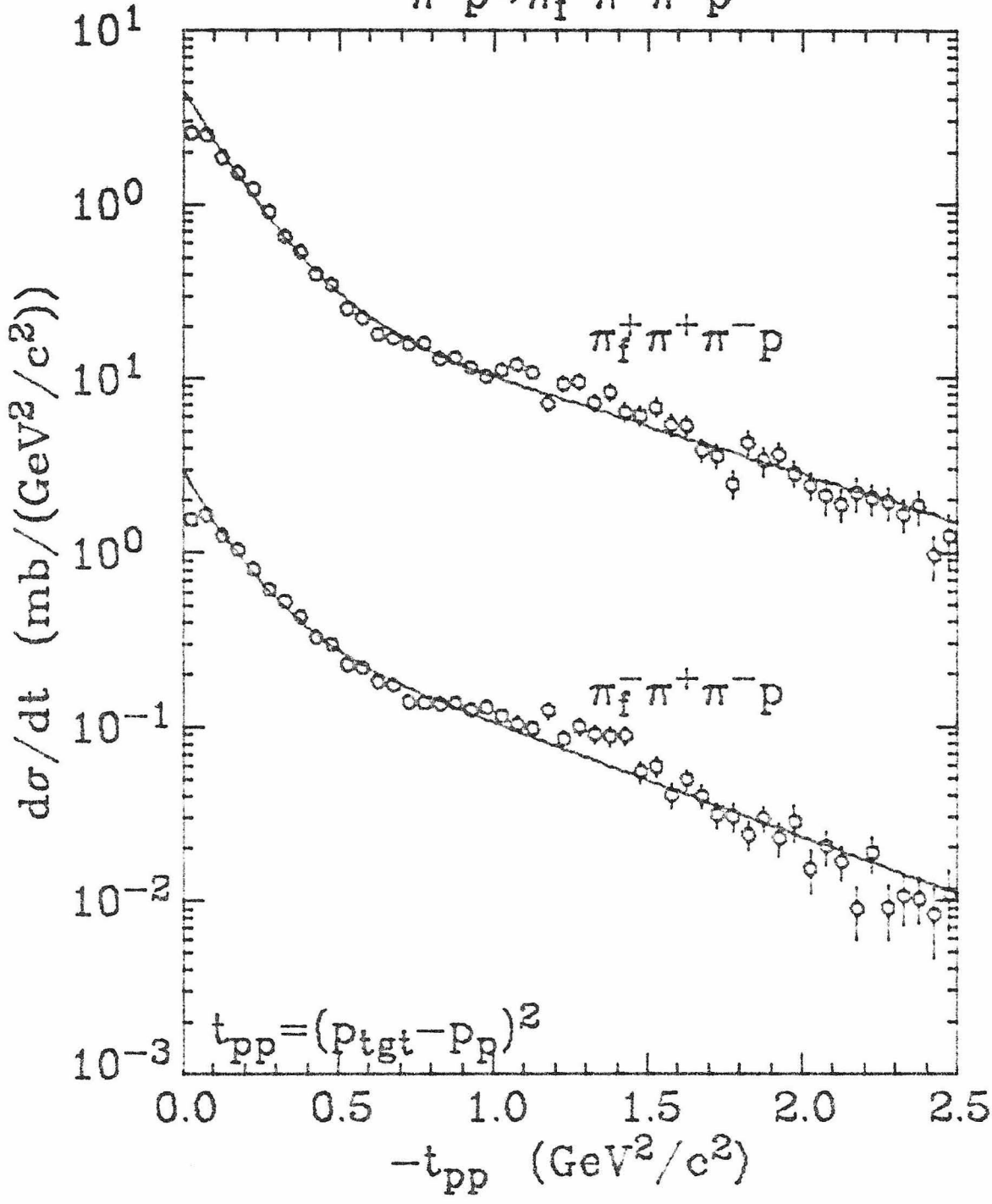


Figure V.4

Plot of $d\sigma/dt_{pp}$ for the reactions $\pi^\pm p \rightarrow \pi_f^\pm \pi^+ \pi^- p$. The invariant momentum transfer t_{pp} is from the target proton to the outgoing proton.

3. Invariant Masses Involving the Fast Pion

Figs. V.5a thru 8 show the invariant mass distributions for masses of the fast pion (π_F^\pm) with one, two, or all three of the remaining pions in reactions (1a)-(1d). The distributions are given in terms of weighted events per bin where the contents of a bin are given by the sum of weights of the events within that bin. We have done this rather than present the distributions in terms of the cross section ($d\sigma/dm$) due to the difficulty of correcting for effects of the trigger on the angular distributions of the fast resonances. For instance, of the events with a fast resonance decaying into two pions, only those cases in which the forward (fast) pion has the same charge as the beam will trigger the apparatus and so be a part of the data sample. Thus an experimentally undetermined fraction of the fast meson resonance events are lost since we do not accept events over the full decay angular distribution. We have not attempted to correct for the unseen events using theoretical models because of their unreliability. The estimation of the amount of fast meson resonance production is thus the determination of a background in this experiment. This background is then subtracted from the observed channel cross sections (Table V.2) to yield estimates for the diffractive portion (Fig. V.1a) of reactions (1a)-(1d).

We have extracted the resonance signals by fitting the data with a Breit-Wigner of mass m_R and width Γ_R and a polynomial background:

$$\frac{dN}{dm} = \frac{N}{2\pi} \frac{\Gamma(m)}{(m-m_R)^2 + \Gamma^2(m)/4} + \sum_i a_i m^i \quad (5)$$

where the mass-dependent width function has the form (from Jackson

[1964]):

$$\Gamma(m) = \Gamma_R \left(\frac{q(m)}{q(m_R)} \right)^{2\ell+1} \quad (6)$$

The parameter ℓ is the decay angular momentum of the resonance and $q(m)$ is the magnitude of the momentum of the decay products (two-body decay) in the rest frame of the resonance. For these fits, the masses and widths of the resonances were fixed at the nominal values given by the Particle Data Tables [Particle Data Group 1978] and listed in Table V.5. The exceptions where we allowed the mass (m_R) and width (Γ_R) to vary in the fit are noted in the text.

Table V.5

Resonance masses and widths used in the fits

<u>Resonance</u>	<u>m_R (MeV)</u>	<u>Γ_R (MeV)</u>	<u>ℓ</u>
$\rho(770)$	770	155	1
$f(1270)$	1270	180	2
$g(1680)$	1680	180	3
$A_2(1310)$	1312	102	2
$A_3(1640)$	1640	300	2
$\Delta(1232)$	1230	115	1
$\Delta(1890)$	1890	250	3
$N(1470)$	1470	200	1
$N(1688)$	1688	140	3
$N(1700)$	1700	150	0

The most prominent peaks visible in Figs. V.5a-l are those of the $\rho(770)$ resonance in the $\pi_f^\pm \pi^\mp$ mass distributions (Figs. V.5a and d) and in the $\pi_f^\pm \pi^0$ mass distributions (Fig. V.5c). The $f^0(1270)$ is also seen in the $\pi_f^\pm \pi^\mp$ mass distributions. The results of the fits to the ρ and f^0 peaks are given in Table V.6 in terms of the sum of event weights and as a fraction of the total observed channel production. Note that the fast meson resonance production represents a background to the events for which this experiment was designed to study (Fig. V.1a).

Table V.6

Major fast resonance production estimates

Resonance	Weight-sums (channel fractions)			
	$\pi_f^+ \pi^+ \pi^- \pi^0 p$	$\pi_f^- \pi^+ \pi^- \pi^0 p$	$\pi_f^+ \pi^+ \pi^+ \pi^- n$	$\pi_f^- \pi^+ \pi^+ \pi^- n$
$\rho^0 \rightarrow \pi_f^\pm \pi^\mp$	6722±412 (24.6±1.5%)	4209±300 (21.8±1.6%)	3331±248 (29.0±2.2%)	4663±312 (44.0±3.1%)
$f^0 \rightarrow \pi_f^\pm \pi^\mp$	1093±296 (4.0±1.1%)	324±221 (1.7±1.1%)	183±165 (1.6±1.4%)	879±246 (8.3±2.3%)
$\rho^\pm \rightarrow \pi_f^\pm \pi^0$	3003±344 (11.0±1.3%)	1455±242 (7.5±1.3%)	—	—

The $\pi_f^\pm \pi^+ \pi^- \pi^0 p$ channels also show several other fast resonances with smaller signals than those given in Table V.6. The estimates of these signal sizes are given in Table V.7. The $g^0 \rightarrow \pi_f^+ \pi^-$ estimate was obtained along with the ρ^0 and f^0 values in the fit to the $\pi_f^+ \pi^-$ mass distribution. The evidence for the $g^+(1680)$ is the narrow peak seen in Fig. V.5k in the $\pi_f^+ \pi^+ \pi^- \pi^0$ mass distribution. The fit, which used $\Gamma(m) = \Gamma_R$ and allowed Γ_R to vary found an anomalously small width of 40 ± 25 MeV

compared to the accepted value of 180 ± 30 MeV [Particle Data Group 1978]. In addition, we only seem to see the g^+ via a 4π or $\pi\pi\rho$ decay mode and not in the $\rho\rho$, $A_2\pi$, or $\omega\pi$ decay modes. The enhancement in the $\pi_f^+ \pi^+ \pi^- \pi^0$ mass at 1680 MeV is evident but of rather low statistics, but its interpretation as the $g(1680)$ may not be correct given these anomalies. Finally, no corresponding signal of the g^- is seen in the $\pi_f^- \pi^+ \pi^- \pi^0$ mass distribution (Fig. V.5k).

Table V.7

Additional fast resonances in the $\pi_f^\pm \pi^+ \pi^- \pi^0$ channels

<u>Resonance</u>	<u>Weight-sums (channel fractions)</u>	
	$\frac{\pi_f^+ \pi^+ \pi^- \pi^0}{p}$	$\frac{\pi_f^- \pi^+ \pi^- \pi^0}{p}$
$g^0 \rightarrow \pi_f^\pm \pi^\mp$	915 ± 223 ($3.3 \pm 0.8\%$)	~ 0
$\omega^0 \rightarrow \pi_f^\pm \pi^\mp \pi^0$	568 ± 106 ($2.1 \pm 0.4\%$)	51 ± 61 ($0.26 \pm 0.32\%$)
$A_2^\pm \rightarrow \pi_f^\pm \eta^0$	131 ± 24 ($0.48 \pm 0.09\%$)	56 ± 18 ($0.29 \pm 0.09\%$)
$g^\pm \rightarrow \pi_f^\pm \pi^+ \pi^- \pi^0$	398 ± 156 ($1.5 \pm 0.6\%$)	~ 0
$\eta^0 \rightarrow \pi_f^\pm \pi^\mp \pi^0$	28 ± 13 ($0.10 \pm 0.05\%$)	~ 0

The $\omega^0 \rightarrow \pi_f^\pm \pi^\mp \pi^0$ signals were obtained by fitting the mass spectra with a Breit-Wigner form with $\Gamma(m) = \Gamma_R$ and allowing m_R and Γ_R to vary. The shape of the ω^0 peak is entirely due to our resolution in the $\pi_f^\pm \pi^\mp \pi^0$ mass; the fits gave widths (FWHM) of 43 ± 11 MeV for the $\omega^0 \rightarrow \pi_f^+ \pi^- \pi^0$ peak and 62 ± 66 MeV for the $\omega^0 \rightarrow \pi_f^- \pi^+ \pi^0$ peak. The fast ω^0 events

for the π^+ data were found to be mostly a result of the reaction (309±59 events out of 568±106 total):



in which the trigger selected only those events with a forward π_f^+ from the ω^0 decay. The corresponding π^- reaction of:



is barely visible in our experiment. The number of events of reaction (8) found by the fit is in fair agreement with the expected number of 34±7 (by isospin the $\omega^0 \Delta^0$ cross section is 1/9 that of the $\omega^0 \Delta^{++}$ final state cross section). The $\eta^0 \rightarrow \pi_f^+ \pi^- \pi^0$ estimate is due to a small cluster of events at the η^0 mass (Fig. V.5h) which seem to come from the analogue of reaction (7) with an η^0 replacing the ω^0 . The corresponding η^0 signal in the π^- data is just too small to be observable. The existence of the $A_2^\pm \rightarrow \pi_f^\pm \eta^0$ is discussed in the section on the η^0 production in Chapter VI.

The $\pi_f^+ \pi^+ \pi^- \pi^0 p$ and $\pi_f^- \pi^+ \pi^+ \pi^- n$ channels show the largest percentage of fast resonance production. This is due in part to the associated production of Δ^{++} and Δ^- resonances with enhanced cross sections (due

to isospin) relative to the Δ^0 and Δ^+ that can be made in the other two channels in association with a fast meson resonance. The associated production of fast meson and slow baryon or meson resonances will be discussed in a later section of this chapter. For now, we have subtracted the contributions of the fast resonance production to obtain cross section estimates for the diffractive process illustrated in Fig. V.1a. These reduced cross sections with the fast meson resonance backgrounds removed are given in Table V.8. These cross sections include the same corrections as used for the observed channel cross sections given in Table V.2. The error on the cross sections includes the contribution from the normalization error. The predicted total cross section is once again that from Table I.3.

Table V.8

Channel cross sections with fast resonance production removed

<u>Channel</u>	<u>Removed Weight-sum</u>	<u>Removed Percentage</u>	<u>Remaining σ (μb) (% error)</u>	<u>Fraction of predicted σ_{tot}</u>
$\pi_f^+ \pi^+ \pi^- \pi^0 p$	12858±680	47.0±2.5%	173±12 (7.1%)	13.4±1.2%
$\pi_f^+ \pi^+ \pi^+ \pi^- n$	3514±298	30.6±2.6%	95.8±6.4(6.7%)	20.8±4.7%
$\pi_f^- \pi^+ \pi^- \pi^0 p$	6076±445	31.5±2.3%	181±12 (6.9%)	18.5±2.7%
$\pi_f^- \pi^+ \pi^+ \pi^- n$	5542±397	52.3±3.8%	71.6±7.7(10.7%)	15.9±3.0%

The distributions of invariant masses with the fast pion and the outgoing nucleon (p or n) are not shown. In these distributions most of the events are above 3 GeV with a fairly sharp cutoff between 4 and 5 GeV (depending on the particular invariant mass). They show no structure as they smoothly rise to a peak at (or just below) the cutoff.

Table V.9

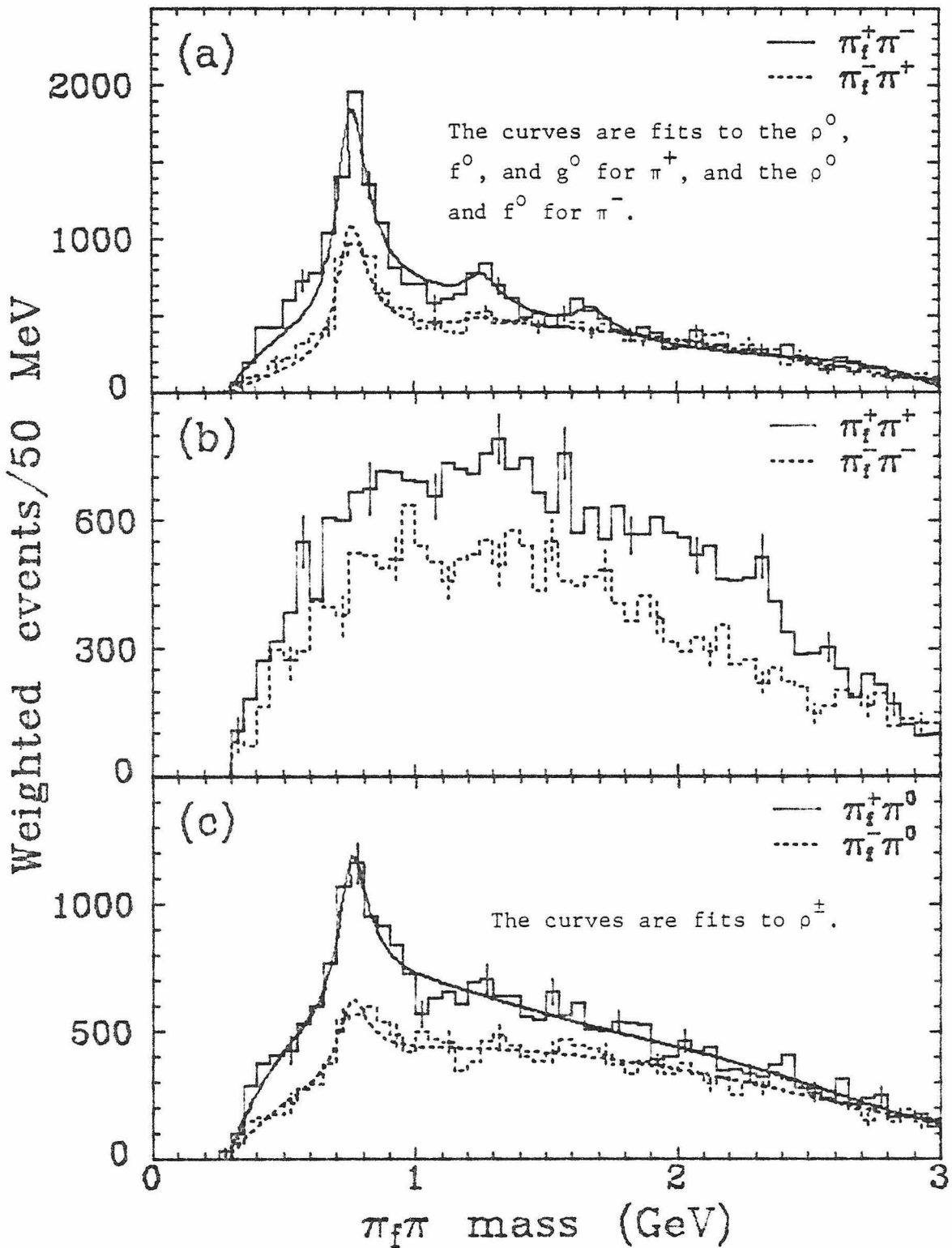
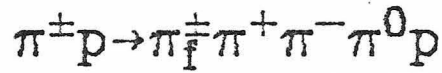
Background fractions and total events within fast ρ cuts

Cut on <u>resonance</u>	<u>Total weight-sum within cut</u>		<u>Fraction of events in cut from background</u>	
	$\frac{+ + - 0}{\pi_f \pi \pi \pi p}$	$\frac{- + - 0}{\pi_f \pi \pi \pi p}$	$\frac{+ + - 0}{\pi_f \pi \pi \pi p}$	$\frac{- + - 0}{\pi_f \pi \pi \pi p}$
$\rho_f^0 \rightarrow \pi_f^\pm \pi^\mp$	9167±215	5290±166	48.5±1.6%	43.5±2.0%
$\rho_f^\pm \rightarrow \pi_f^\pm \pi^0$	7019±191	3826±134	70.2±1.8%	73.7±2.5%
	$\frac{+ + + -}{\pi_f \pi \pi \pi n}$	$\frac{- + + -}{\pi_f \pi \pi \pi n}$	$\frac{+ + + -}{\pi_f \pi \pi \pi n}$	$\frac{- + + -}{\pi_f \pi \pi \pi n}$
$\rho_f^0 \rightarrow \pi_f^\pm \pi^\mp$	3708±138	5061±162	52.4±2.4%	37.7±2.2%

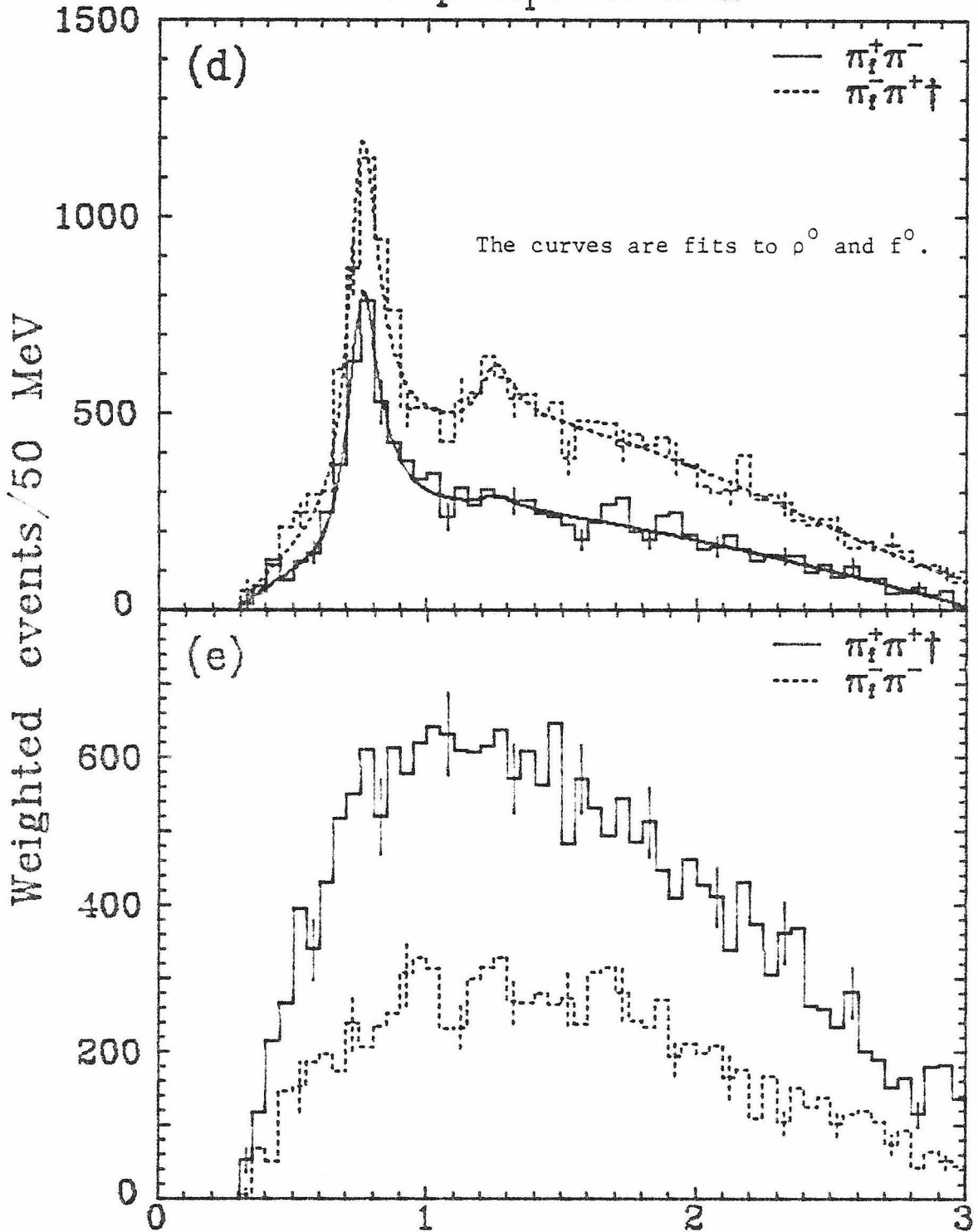
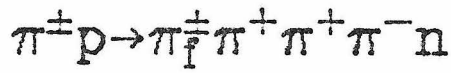
— π^+ (data & fits)
 - - - π^- (data & fits)
 $\pi^\pm p \rightarrow \pi_f^\pm \pi^+ \pi^- \pi^0 p$
 $\pi^\pm p \rightarrow \pi_f^\pm \pi^+ \pi^+ \pi^- n$
 $\text{Prob}(\chi_{\text{fit}}^2) \geq 5\%$
 $-t_{\pi\pi(f)} < 0.6 \text{ GeV}^2/c^2$
 $(\pi\pi\pi N) \text{ mass} < 3.7 \text{ GeV}$

Figures V.5a-l

Invariant mass distributions of masses with the fast pion and one or more other pions ($\pi_f^\pm \pi$, $\pi_f^\pm \pi\pi$, and $\pi_f^\pm \pi\pi\pi\pi$ masses). The distributions are shown in terms of weighted events as discussed in the text. The curves shown with some of the distributions are the results of fits to the distributions with one or more resonances and a polynomial background (see the text). For those distributions for the n channel reactions (Figs. V.5d, e, and j) in which only a single π^+ appears in the invariant mass (other than the π_f^+), each event appears twice in the distribution.

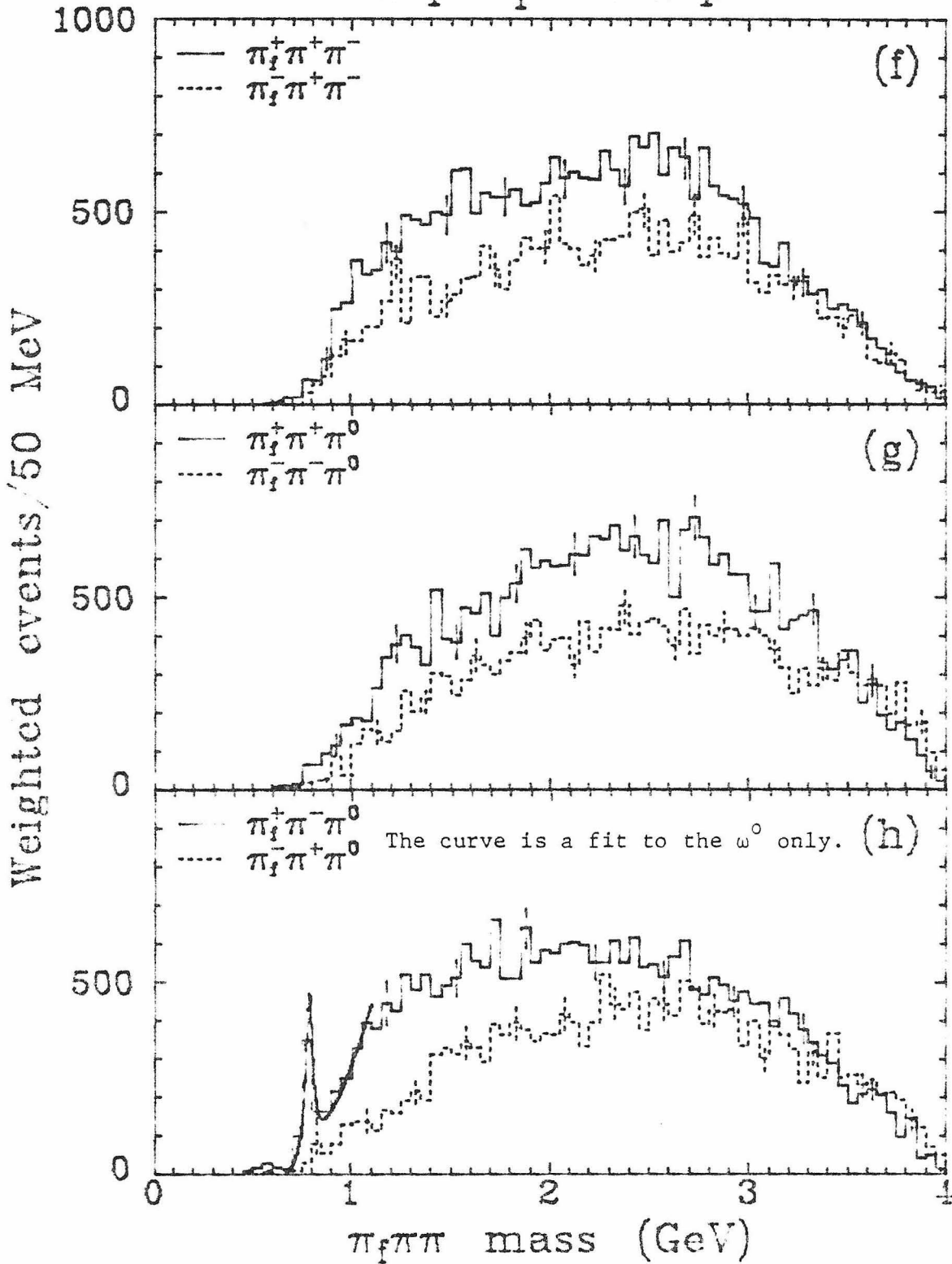
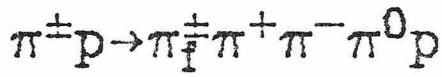


Figures V.5a-c

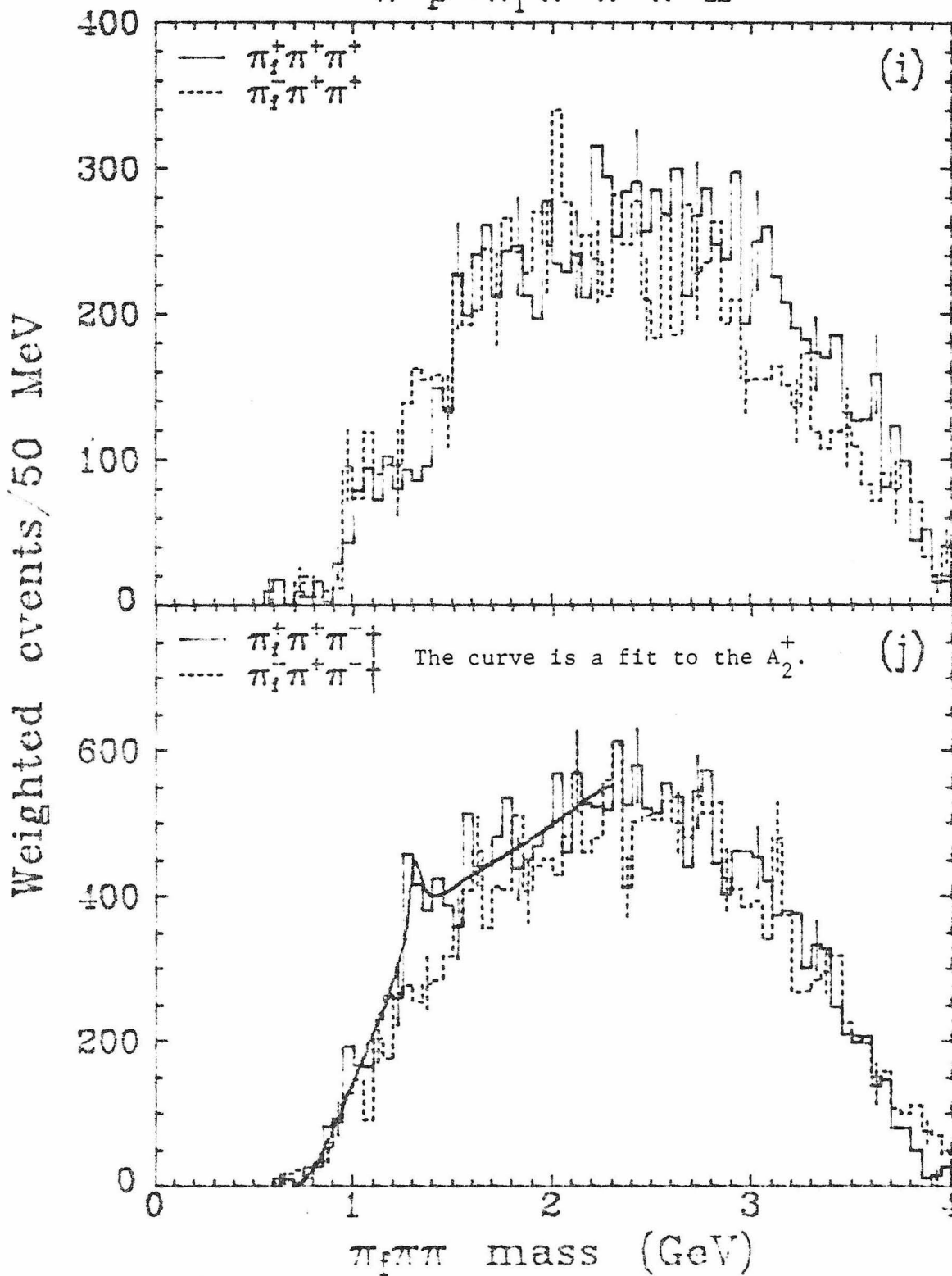
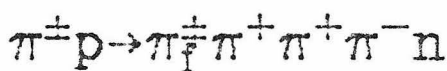


(† each event appears twice)

Figures V.5d-e

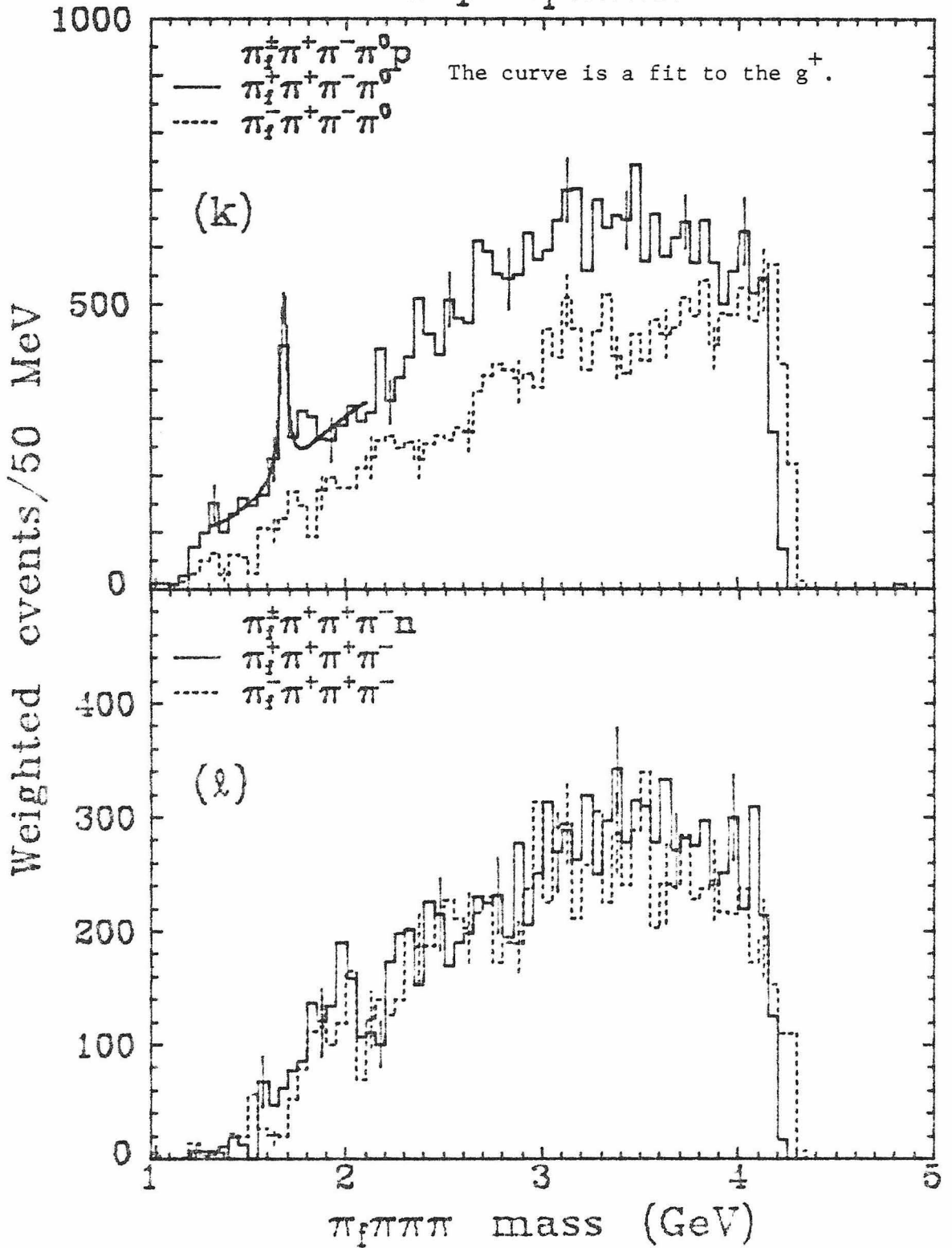


Figures V.5f-h



(† each event appears twice)

Figures V.5i-j



Figures V.5k-l

4. Fast Invariant Masses Selected on a Fast ρ Meson

Figs. V.6a-k show the 3π and 4π fast invariant mass distributions for events that were required to have a fast ρ meson. This cut was defined by requiring the $\pi_f^\pm \pi^\mp$ mass (ρ_f^0) or the $\pi_f^\pm \pi^0$ mass (ρ_f^\pm) to be between 0.6 and 1.0 GeV. Since the fits were made with fixed mass and width for the ρ , the ratio of all the ρ signal to that portion within the cut is 1.46 for all the fast ρ cuts. Table V.9 lists the fraction of events within the ρ cuts that are expected to be from the backgrounds under the ρ peaks. The table also gives the total weight-sum of the events within the cut.

A small amount of $A_2(1310)$ production is observed in the $\pi_f^+ \pi^- \pi^0$ mass (Fig. V.6c) and in the n channel $\pi_f^+ \pi^+ \pi^-$ mass (Fig. V.6e) for events within the ρ_f^0 . Fits to these peaks gave signals of 179 ± 174 events and 413 ± 159 events respectively. The A_2 in the n channel $\pi_f^+ \pi^+ \pi^-$ mass is also evident in the uncut distribution (Fig. V.5j) for which the fit gave a signal of 400 ± 177 events. This result seems to indicate that the n channel A_2 is being observed solely through the decay of the A_2 to a fast ρ and a pion; the $A_2 \rightarrow \rho \pi$ branching ratio is about 70% [Particle Data Group 1978]. The A_2 in the $\pi_f^+ \pi^- \pi^0$ mass is not seen in the uncut distribution (Fig. V.5h) due to its being a small signal on top of a large background. However, the $\pi_f^+ \pi^- \pi^0$ mass shows a large enhancement in the $A_1(1100)$ and $A_2(1310)$ regions for the ρ_f^+ cut (Fig. V.6h) in which the A_2 contribution is unresolvable and so not estimated. The lack of A production in the 1C four-prong channels can

be contrasted to the large A production cross sections in the 4C four prongs. As discussed earlier, the 4C A production shows up as a forward peak in the $d\sigma/dt_{pp}$ distributions in addition to peaks in the $\pi_{\rho_f}^{\pm} \pi^+ \pi^-$ mass distributions. The A mesons in the 4C channels are produced by diffractive dissociation of the beam pions off the target protons. In the case of the 1C channels, the proton must also be diffracted to produce an extra pion and apparently the double diffraction amplitude is considerably smaller than the single diffraction amplitude.

The $g^+(1680)$ for which evidence was found in the uncut $\pi_{\rho_f}^+ \pi^+ \pi^- \pi^0$ mass (Fig. V.5k) also appears in that mass distribution for the ρ_f^0 and ρ_f^+ cuts (Figs. V.6i and V.6k). In both of these cases, the g^+ again appears abnormally narrow. Also the size of the signal appears to be the same in all three cases making the exact interpretation of this peak very unclear.

— π^+ (data & fits)

----- π^- (data & fits)

$$\pi^\pm p \rightarrow \rho_f^0 \pi^\pm \pi^0 p \quad \rho_f^0 \rightarrow \pi_f^\pm \pi^\mp$$

$$\pi^\pm p \rightarrow \rho_f^0 \pi^\pm \pi^+ n \quad \rho_f^0 \rightarrow \pi_f^\pm \pi^\mp$$

$$\pi^\pm p \rightarrow \rho_f^\pm \pi^\mp \pi^0 p \quad \rho_f^\pm \rightarrow \pi_f^\pm \pi^0$$

$$\text{Prob}(\chi_{\text{fit}}^2) \geq 5\%$$

$$-t_{\pi\pi(f)} < 0.6 \text{ GeV}^2/c^2$$

$$(\pi\pi\pi N) \text{ mass} < 3.7 \text{ GeV}$$

$\rho_f^0 \rightarrow \pi_f^\pm \pi^\mp$ definition:

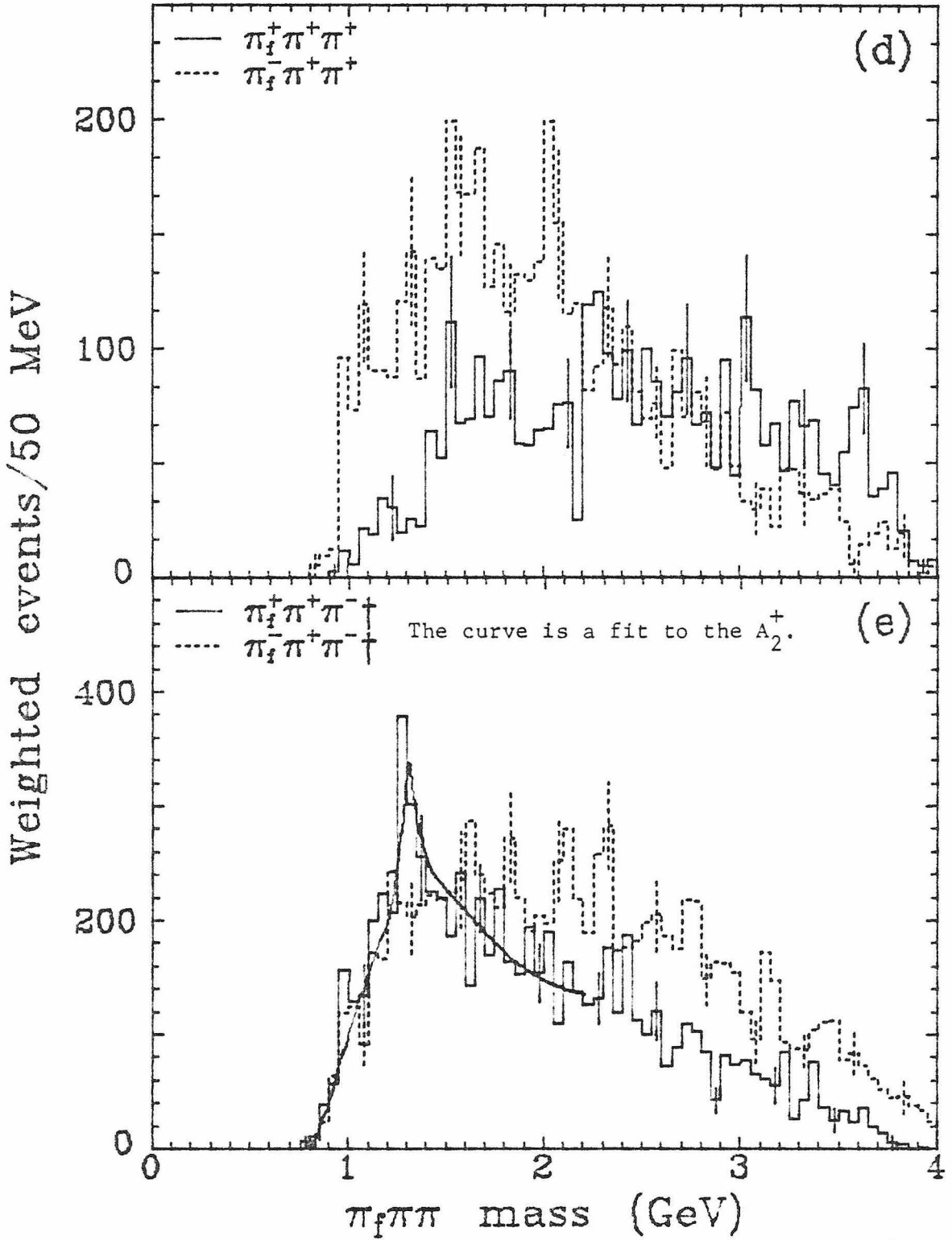
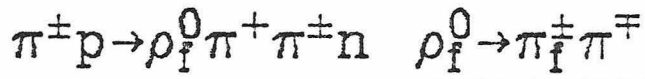
$$0.6 \leq \pi_f^\pm \pi^\mp \text{ mass} < 1.0 \text{ GeV}$$

$\rho_f^\pm \rightarrow \pi_f^\pm \pi^0$ definition:

$$0.6 \leq \pi_f^\pm \pi^0 \text{ mass} < 1.0 \text{ GeV}$$

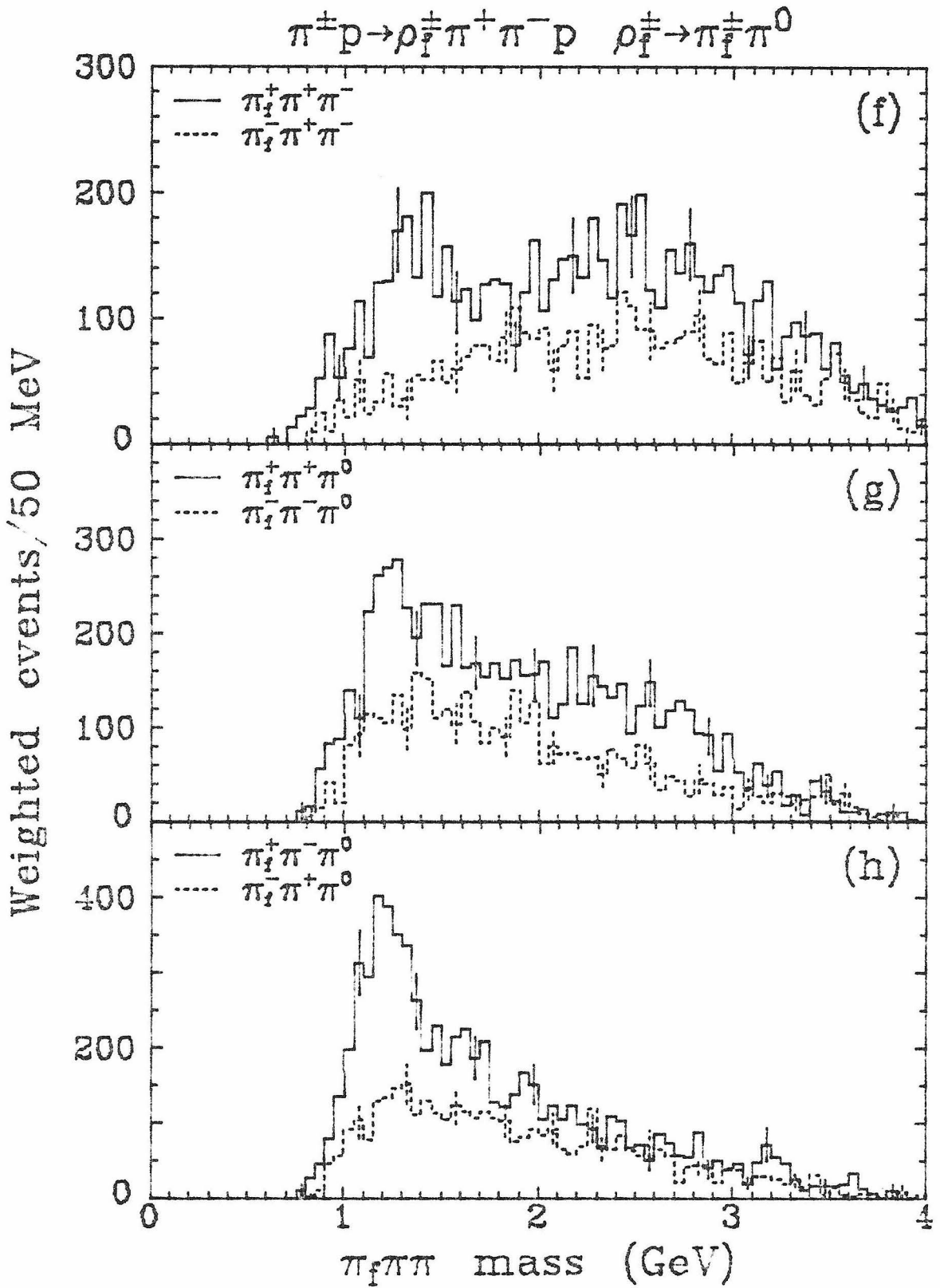
Figures V.6a-k

Invariant mass distributions of masses with the fast pion and two or all three of the remaining pions for events in which the fast pion forms a ρ with one of these pions (see above).



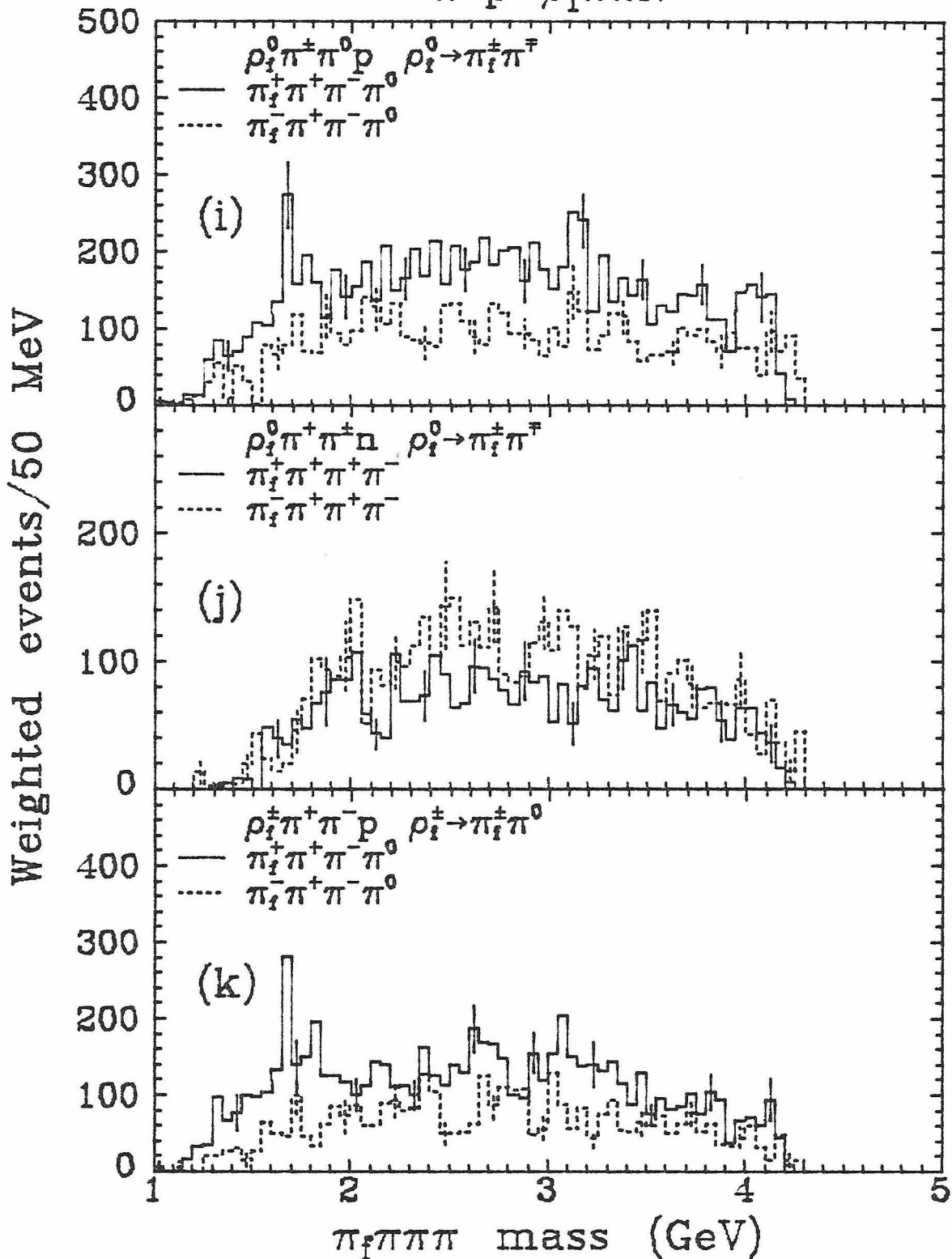
(† each event appears twice)

Figures V.6d-e



Figures V.6f-h

$\pi^\pm p \rightarrow \rho_f \pi \pi N$



Figures V.6i-k

5. Invariant Masses Involving the Slow System Particles

In the laboratory frame, the particles other than the π_f^\pm in reactions (1) are relatively slow, having momenta usually substantially below 1 GeV/c while the fast pion has a momentum above 8 GeV/c or so. The slow invariant mass distributions for the π^0 channel are given in Figs. V.7a-k and those for the n channel are given in Figs. V.8a-h. The estimates for resonance production in the slow system are given in Table V.10. The errors in the cross sections given in the table include the errors in the normalization but not the general 6% systematic error (Chapter IV). The estimates listed in Table V.10 were made by fitting the mass distributions with the Breit-Wigner form and polynomial background used to fit the fast system masses (equation (5) in section 3). This procedure introduces a systematic error in the estimation of the resonance production due to the lack of a model for the background other than a polynomial shape. This systematic error was estimated from the variations in the results from doing several fits to the data with different numbers of terms in the background polynomial. The size of the systematic error seems to be dependent upon the signal-to-noise ratio for the resonance and to the nearness of the resonance to the invariant mass threshold. Thus the fast meson resonances, the η^0 and ω^0 peaks, and the slow ρ 's have moderate systematic errors (in the range of 15 to 30%) as the background under these resonances is fairly well determined by the non-resonant parts of the invariant mass distribution both below and above the resonances. The systematic errors in the baryonic resonance estimates are very

large (ranging from 25% to over 100%) due to the uncertainty in the shape of the background. The estimates for the Δ^{++} , the Δ^- , and the four-body invariant mass ($\pi\pi\pi N$) resonances are more moderate due mostly to the larger signal-to-noise ratios as compared to the other baryon resonances.

The figures and the table of resonance cross sections show that the slow system invariant masses are rich with many resonances being produced. The largest signals are for the Δ^{++} and Δ^- resonances. In the π^+ data, about one half of the channel cross section is invested in the Δ^{++} production while in the π^- data the Δ^{++} only accounts for about 35% of the channel cross section. The Δ^{++} in the π^+ data can be produced in conjunction with a fast ρ_f^0 or ρ_f^+ while in the π^- data only a ρ_f^- can be made. The question of associated fast and slow resonance production will be considered in more detail in the next section. For now we will make the observation that the occurrence of a fast resonance in the 1C channels enhances the likelihood of a resonance in the slow system.

The η^0 and ω^0 production is also a very striking aspect of our data. This is due to the narrowness of the peaks (widths due to our

Table V.10

Estimated slow system resonance production

Resonance	$\pi_f^+ \pi^+ \pi^- \pi^0 p$			$\pi_f^- \pi^+ \pi^- \pi^0 p$		
	Weight-sum	Channel fraction	σ (μb)	Weight-sum	Channel fraction	σ (μb)
$\Delta^{++} \rightarrow \pi^+ p$	12775 \pm 468	46.7 \pm 1.8%	160.9 \pm 9.3	6709 \pm 343	34.7 \pm 1.9%	97.8 \pm 7.1
$\Delta^+ \rightarrow \pi^0 p$	1127 \pm 381	4.1 \pm 1.4%	14.2 \pm 4.8	4143 \pm 343	21.5 \pm 1.8%	60.4 \pm 5.9
$\Delta^0 \rightarrow \pi^- p$	3454 \pm 373	12.6 \pm 1.4%	43.5 \pm 5.1	2291 \pm 302	11.9 \pm 1.6%	33.4 \pm 4.7
$N(1470) \rightarrow \pi^- p$	151 \pm 738	\leq 0.6 \pm 2.7%	\leq 1.9 \pm 9.3	\sim 0	—	—
$N(1470) \rightarrow \pi^0 p$	\sim 0	—	—	165 \pm 576	\leq 0.9 \pm 3.0%	\leq 2.4 \pm 8.4
$\rho^0 \rightarrow \pi^+ \pi^-$	2191 \pm 548	8.0 \pm 2.0%	27.6 \pm 7.0	2428 \pm 604	12.6 \pm 3.1%	35.4 \pm 9.0
$\rho^+ \rightarrow \pi^+ \pi^0$	5177 \pm 572	18.9 \pm 2.1	65.2 \pm 7.8	1976 \pm 597	10.2 \pm 3.1%	28.8 \pm 8.8
$\rho^- \rightarrow \pi^- \pi^0$	3938 \pm 540	14.4 \pm 2.0%	49.6 \pm 7.2	3217 \pm 535	16.7 \pm 2.8%	46.9 \pm 8.2
$\eta^0 \rightarrow \pi^+ \pi^- \pi^0$	200 \pm 31	0.7 \pm 0.1%	2.52 \pm 0.41	91 \pm 23	0.5 \pm 0.1%	1.33 \pm 0.35
$\omega^0 \rightarrow \pi^+ \pi^- \pi^0$	3089 \pm 199	11.3 \pm 0.7%	38.9 \pm 3.1	2518 \pm 192	13.0 \pm 1.0%	36.7 \pm 3.4
$\Delta(1890) \rightarrow \pi^+ \pi^0 p$	2731 \pm 699	10.0 \pm 2.6%	34.4 \pm 8.9	\sim 0	—	—
$N(1790) \rightarrow \pi^+ \pi^- \pi^0 p$	627 \pm 230	2.3 \pm 0.8%	7.9 \pm 2.9	494 \pm 199	2.6 \pm 1.0%	7.2 \pm 2.9

Table V.10 (cont.)

Resonance	$\pi_f^{++\pi\pi n}$		$\pi_f^{+\pi\pi n}$		$\pi_f^{-\pi\pi n}$	
	Weight-sum	Channel fraction σ (μb)	Weight-sum	Channel fraction σ (μb)	Weight-sum	Channel fraction σ (μb)
$\Delta^+ \rightarrow \pi^+ n$	938 \pm 400	8.2 \pm 3.5%	3281 \pm 344	12.2 \pm 5.2	31.0 \pm 3.3%	48.6 \pm 5.7
$\Delta^- \rightarrow \pi^- n$	4030 \pm 392	35.1 \pm 3.5%	2707 \pm 311	52.4 \pm 3.9	25.6 \pm 3.0%	40.1 \pm 5.1
$N(1470) \rightarrow \pi^+ n$	1438 \pm 777	12.5 \pm 6.8%	~ 0	18.7 \pm 10.1	—	—
$N(1688) \rightarrow \pi^+ n$	638 \pm 408	5.6 \pm 3.6%	~ 0	8.3 \pm 5.3	—	—
$\rho^0 \rightarrow \pi^+ \pi^-$	3653 \pm 700	31.9 \pm 6.1%	2795 \pm 695	47.5 \pm 9.3	26.4 \pm 6.6%	41.4 \pm 10.5
$N(1470) \rightarrow \pi^+ \pi^- n$	784 \pm 161	6.8 \pm 1.4%	398 \pm 149	10.2 \pm 2.2	3.8 \pm 1.4%	5.9 \pm 4.2
$N(1688) \rightarrow \pi^+ \pi^- n$	~ 0	—	494 \pm 169	—	4.7 \pm 1.6%	7.3 \pm 2.5
$N(1700) \rightarrow \pi^+ \pi^- n$	385 \pm 77	3.4 \pm 0.7%	392 \pm 88	5.0 \pm 1.0	3.7 \pm 0.8%	5.8 \pm 1.3



— π^+ fits

..... π^- fits

$$\text{Prob}(\chi_{\text{fit}}^2) \geq 5\%$$

$$-t_{\pi\pi(i)} < 0.6 \text{ GeV}^2/c^2$$

$$(\pi^+ \pi^- \pi^0 p) \text{ mass} < 3.7 \text{ GeV}$$

Figures V.7a-k

Invariant mass distributions for the slow particles (other than the π_f^\pm) of the π^0 channel. The distributions are given as $d\sigma/dm$ and include curves from the resonance fits described in the text.

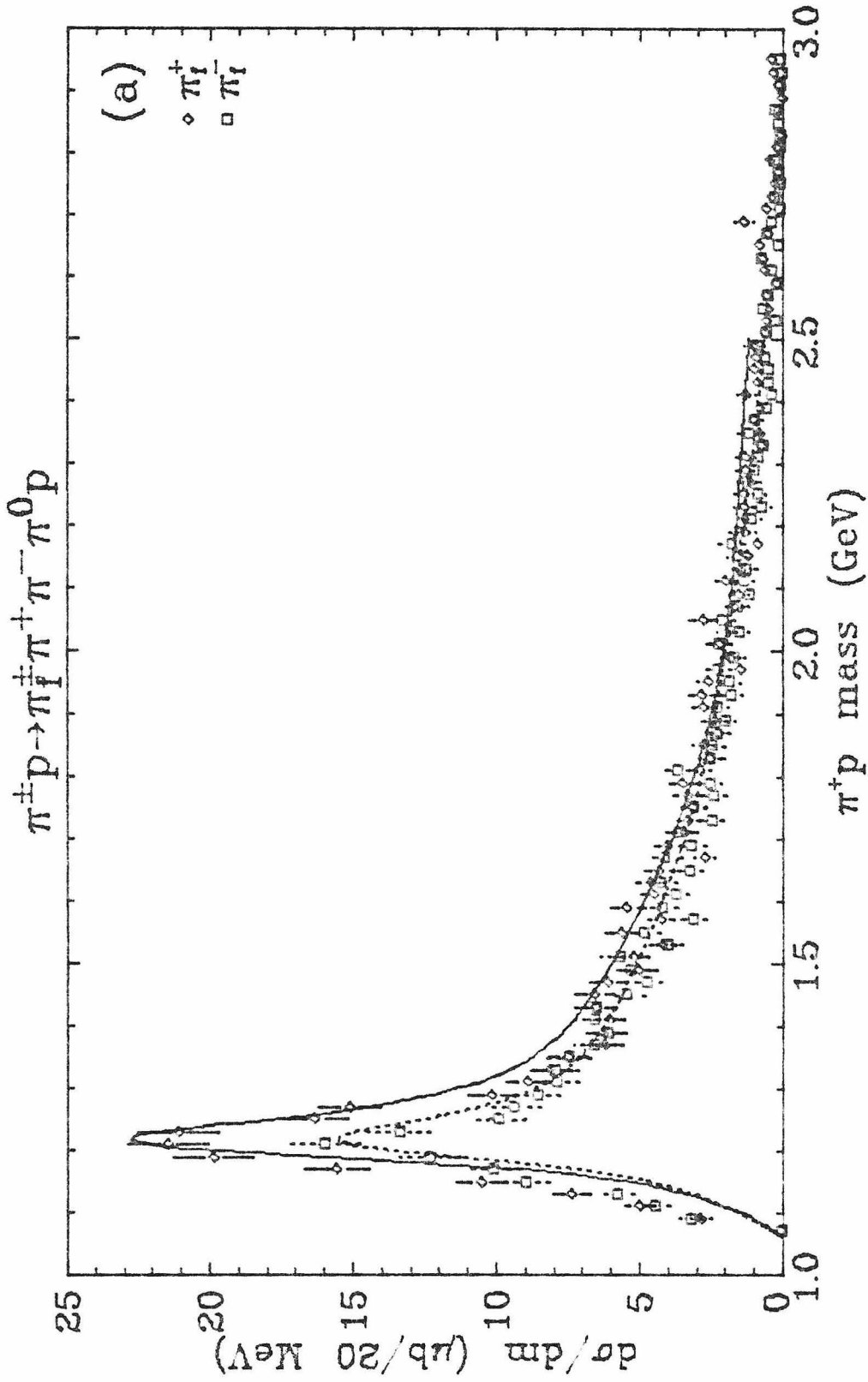


Figure V.7a

The curves are fits to the Δ^{++} .

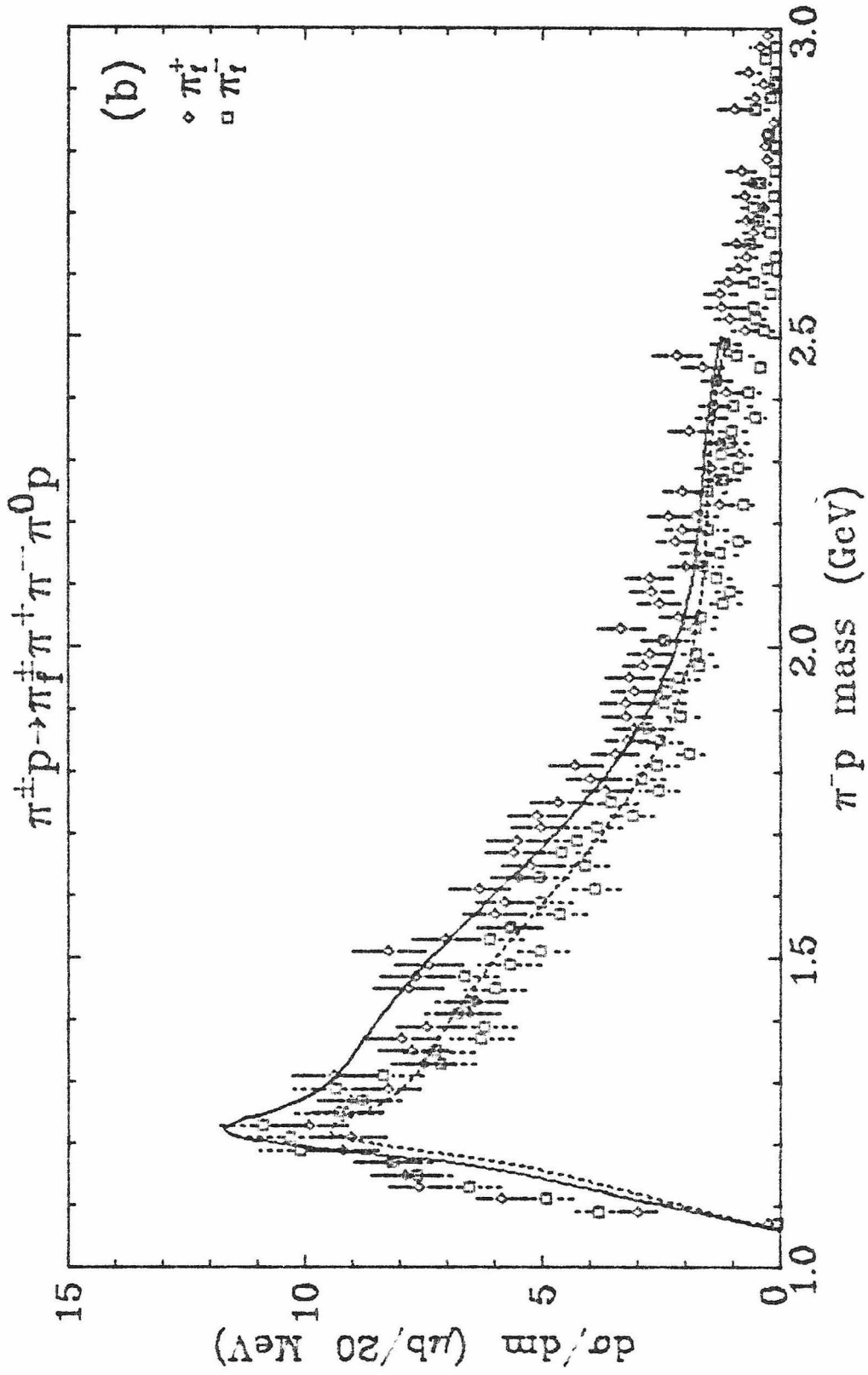


Figure V.7b

The curves are fits to the Δ^0 .

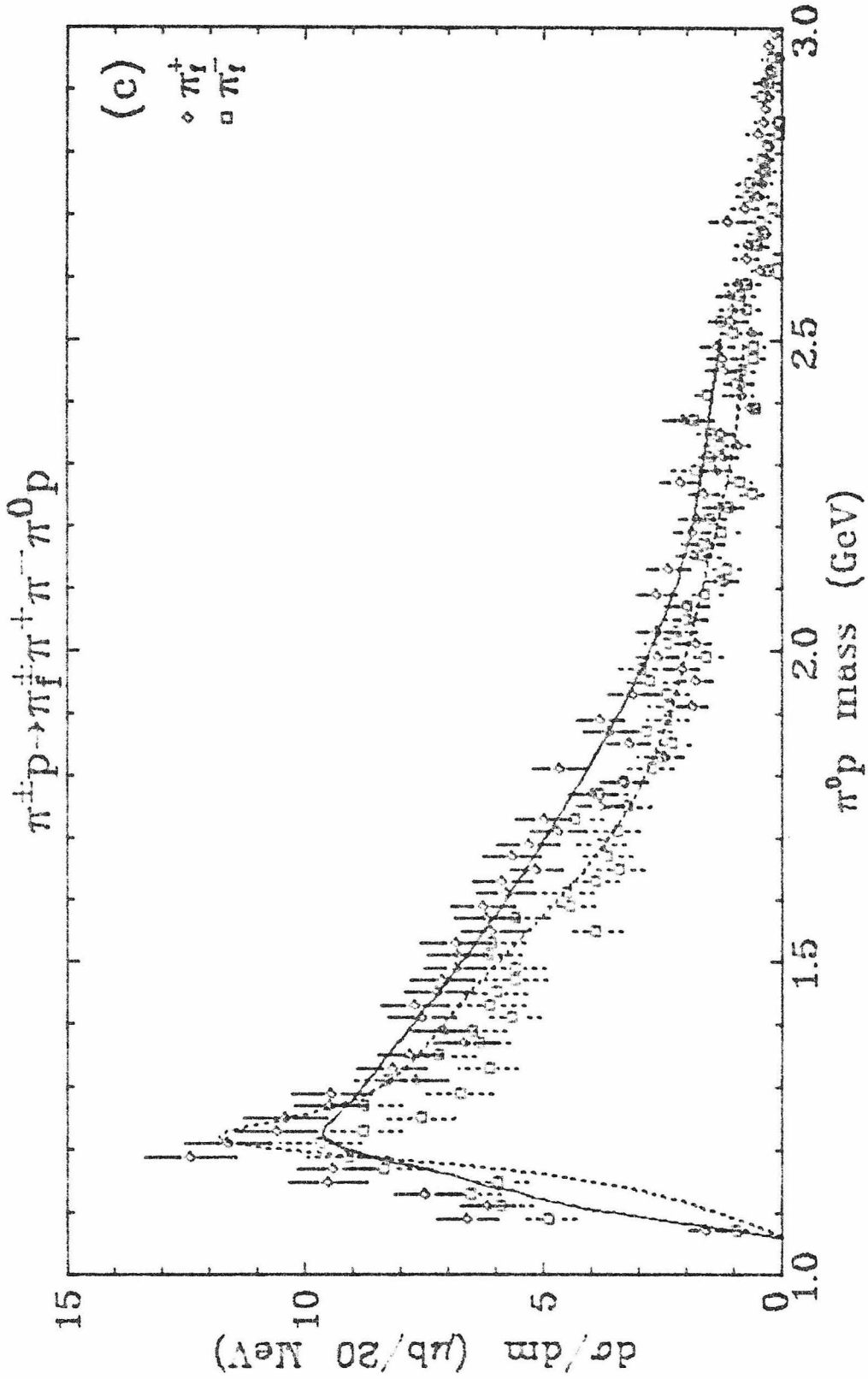


Figure V.7c

The curves are fits to the Δ^+ .

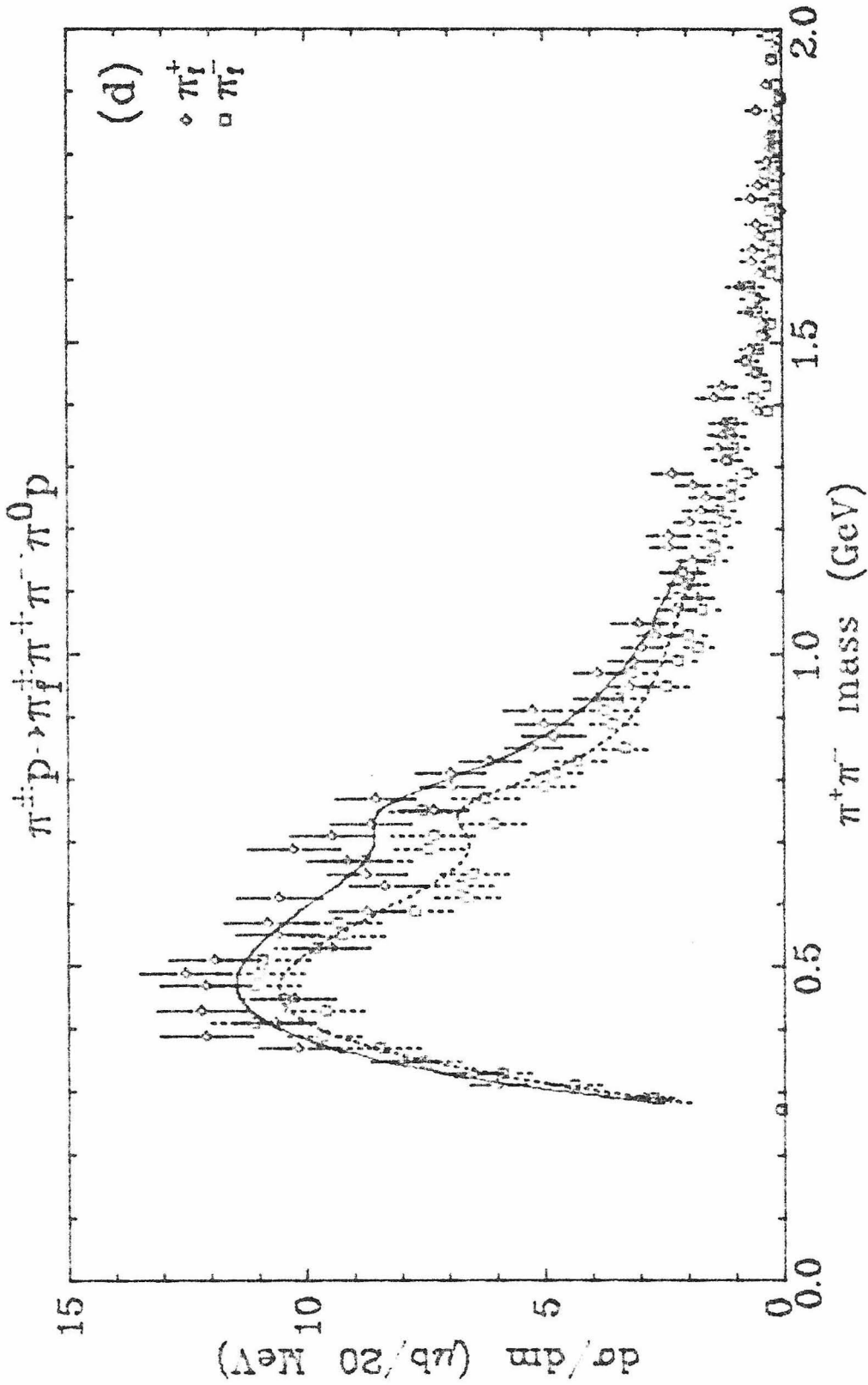


Figure V.7d

The curves are fits to the ρ^0 .

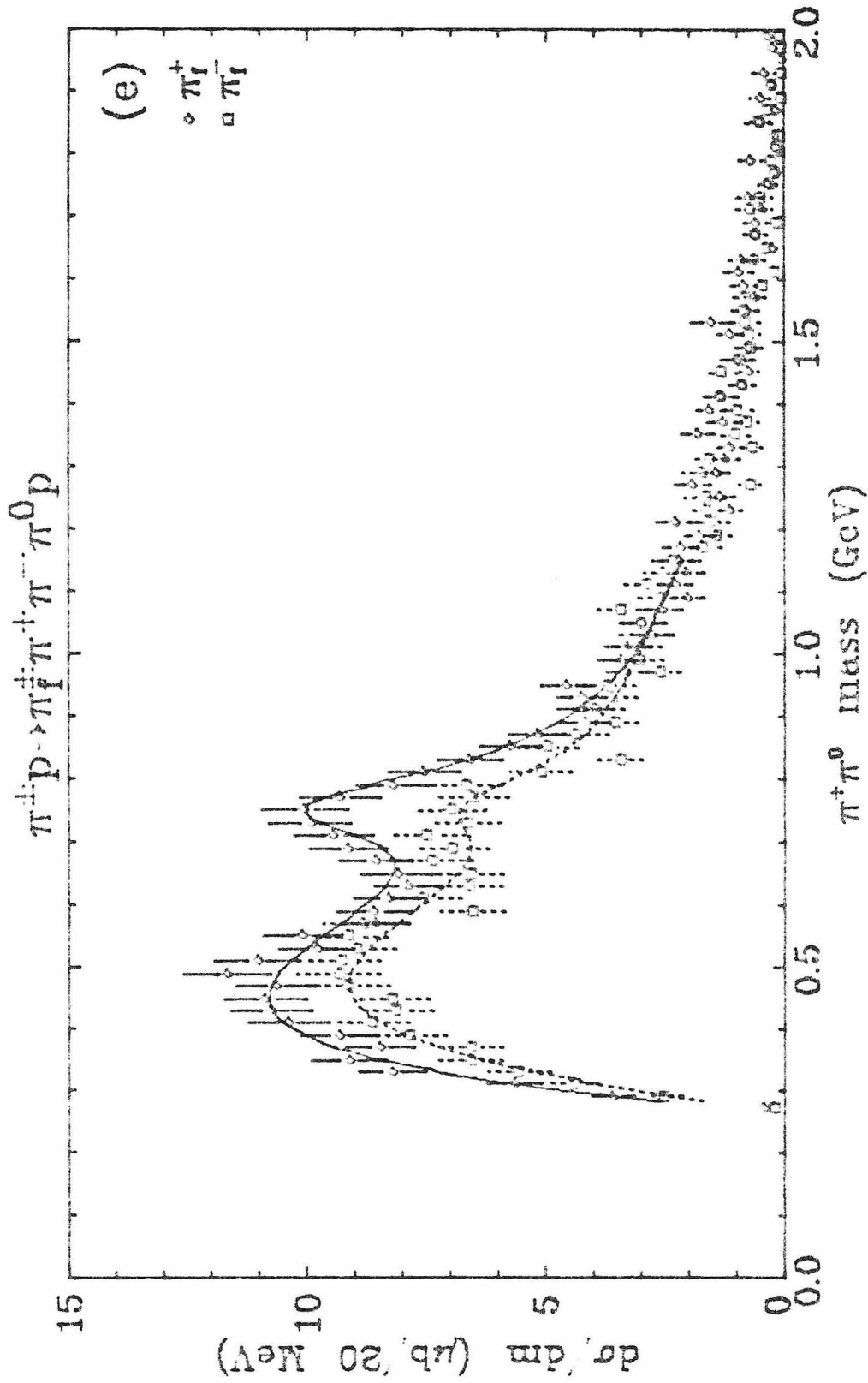


Figure V.7e

The curves are fits to the ρ^+ .

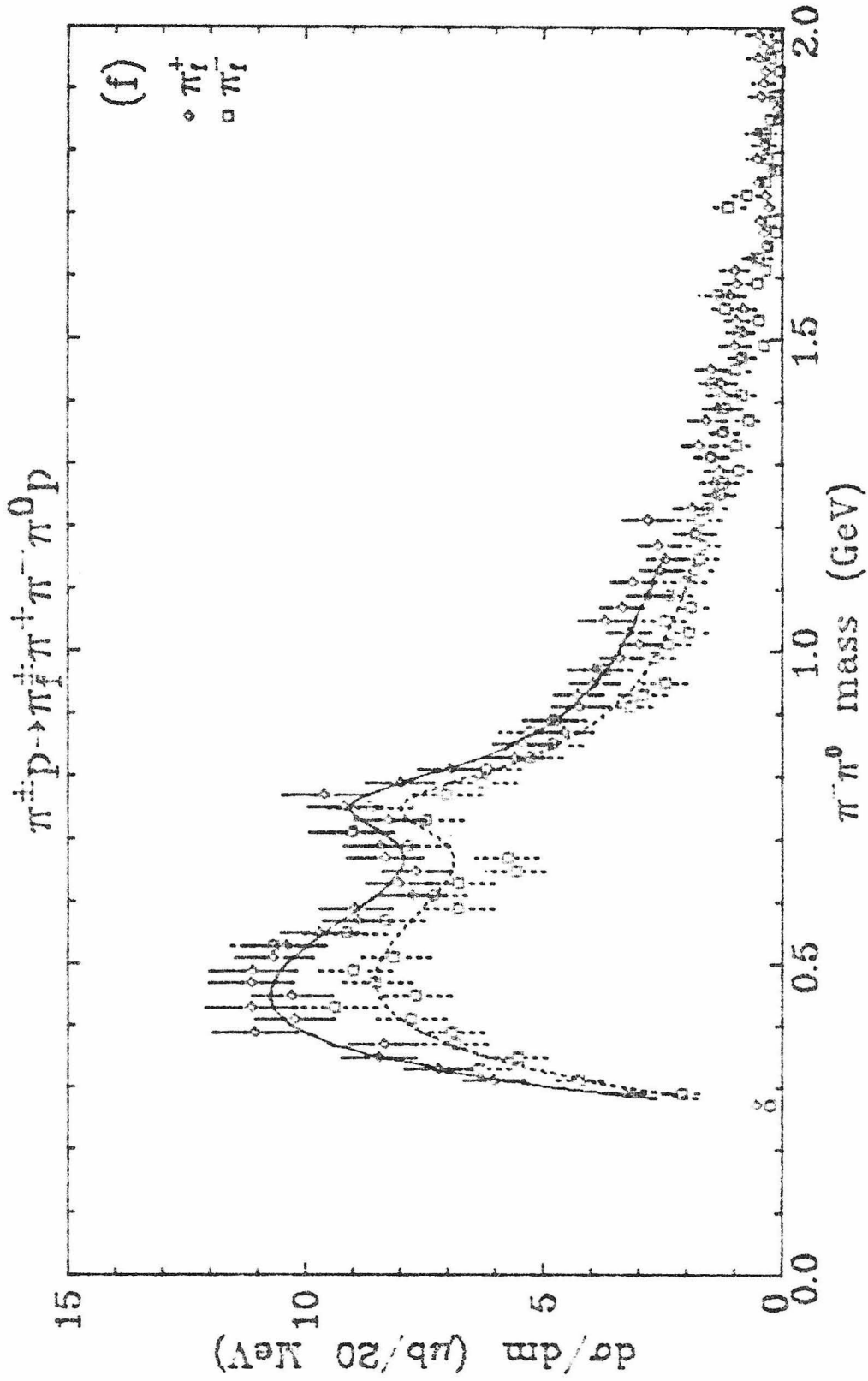


Figure V.7f

The curves are fits to the ρ^- .

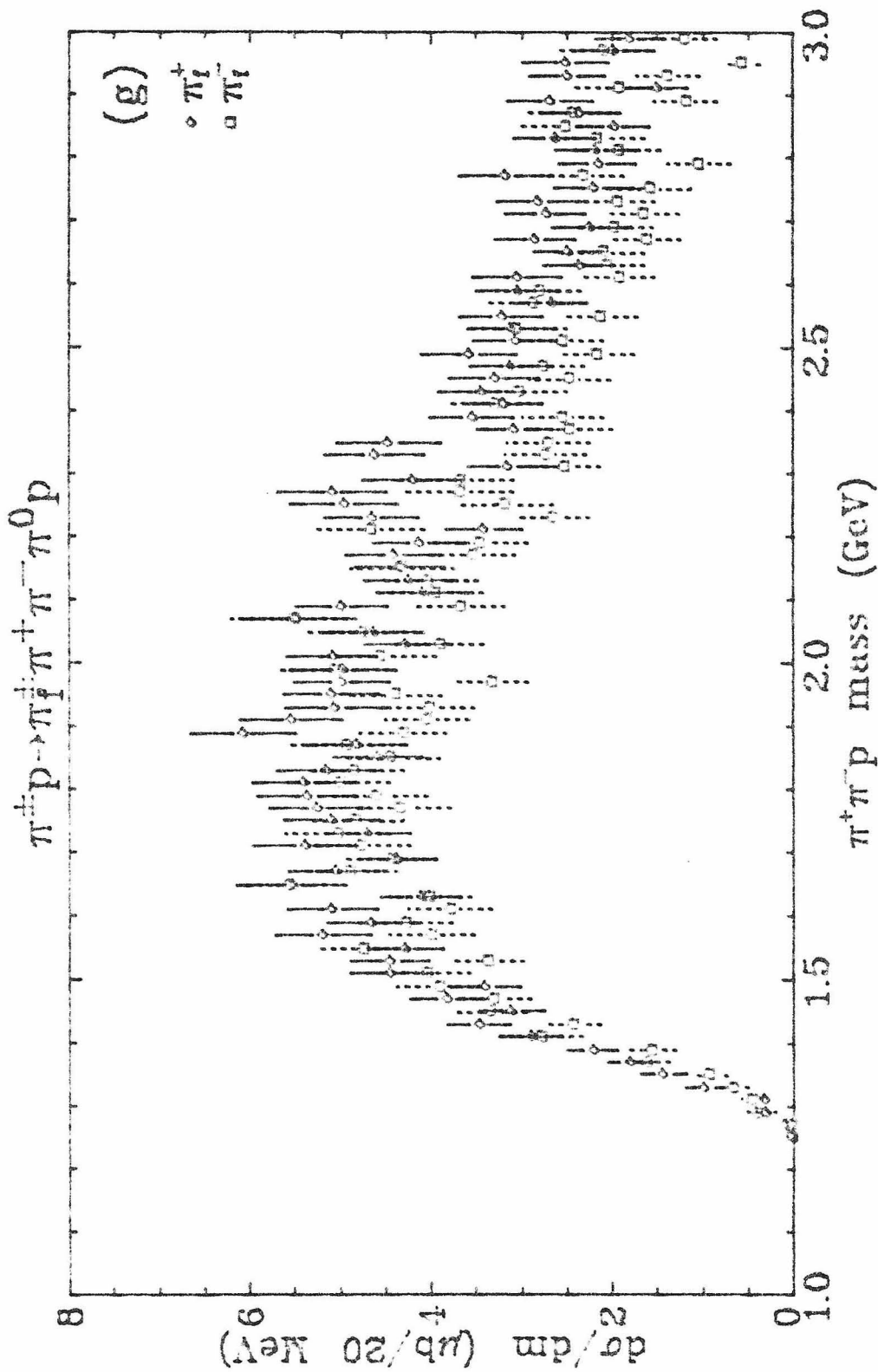


Figure V.7g

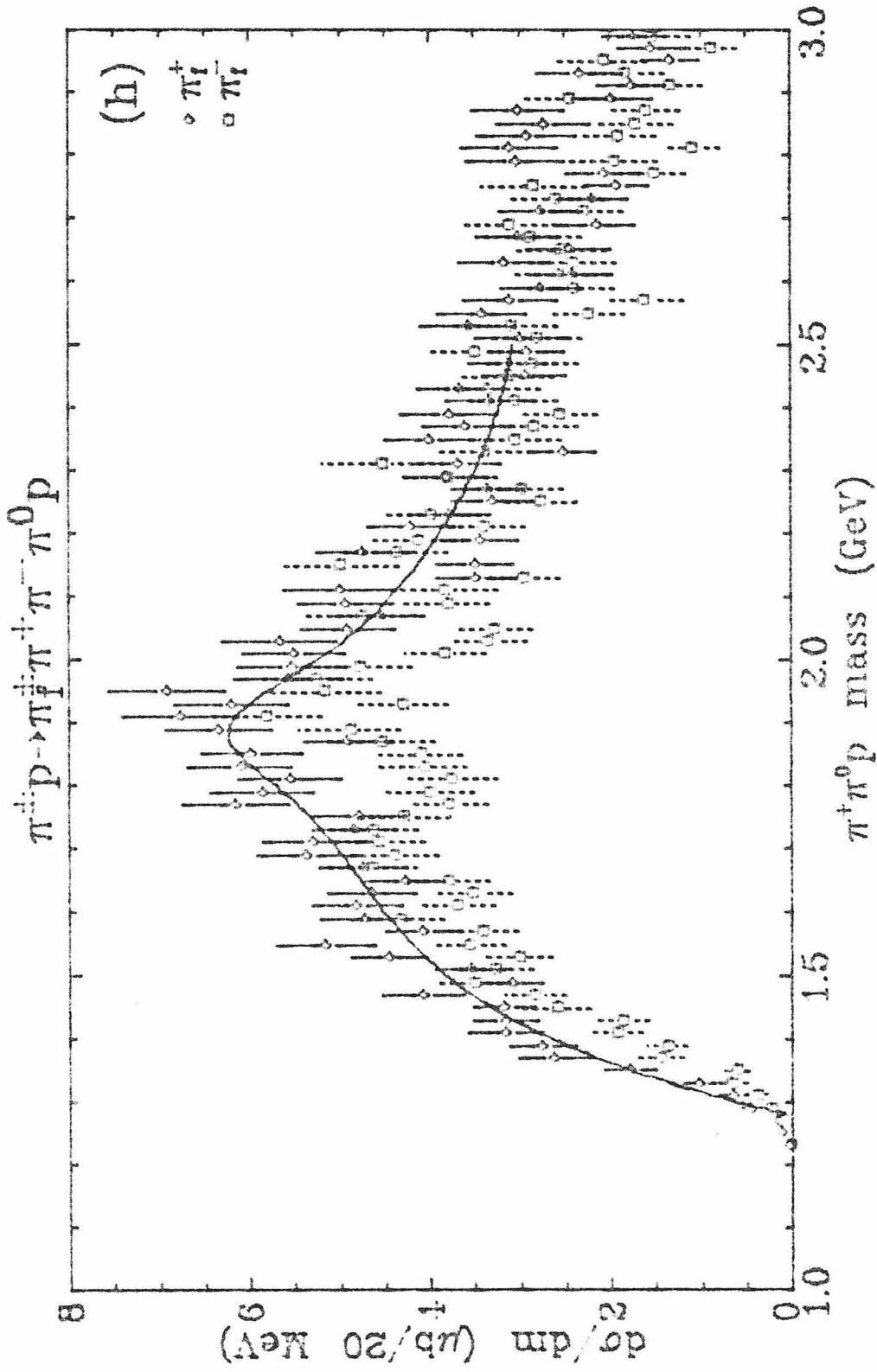


Figure V.7h

The curve is a fit to the Δ^{++} (1890).

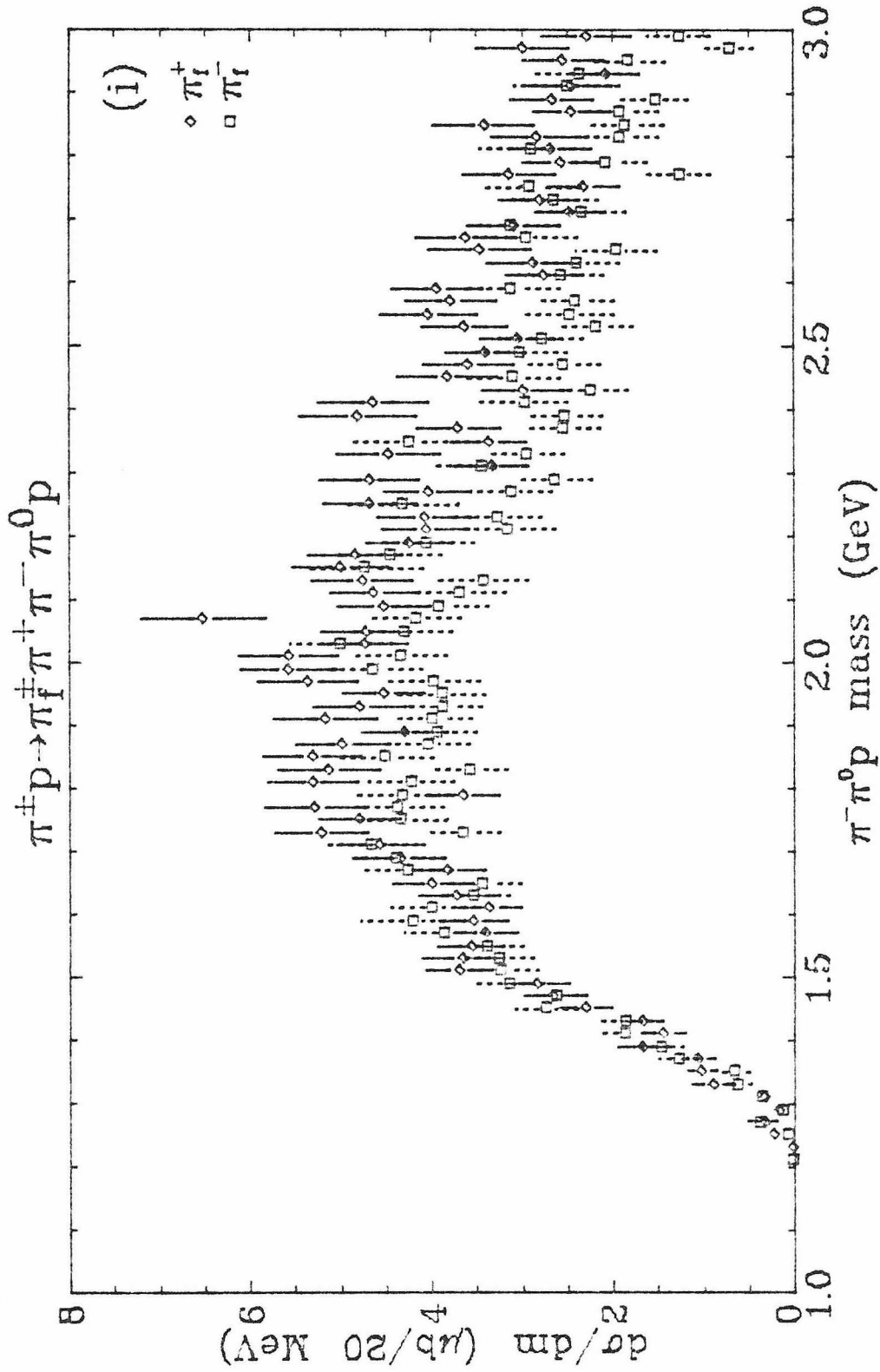


Figure V.71

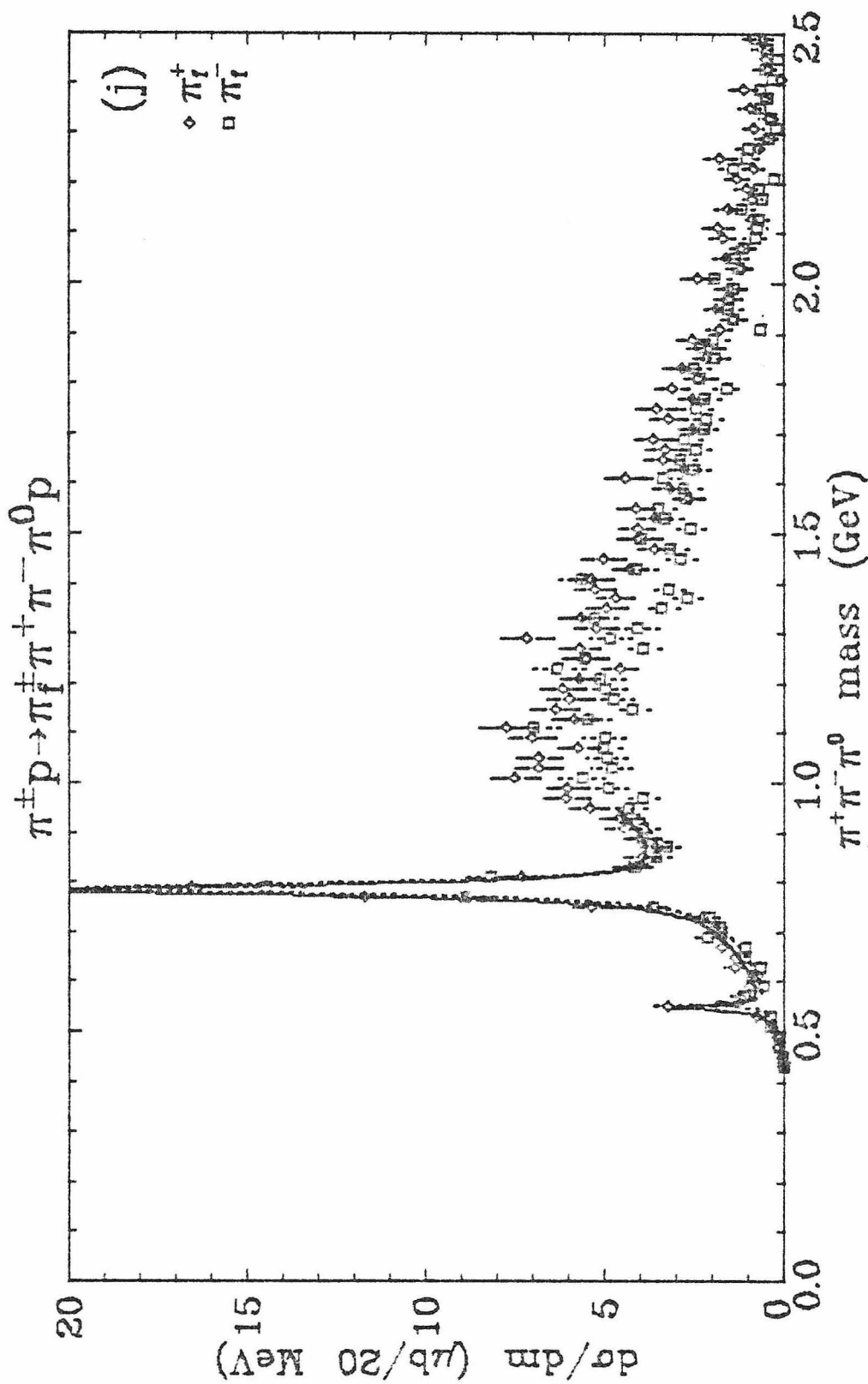


Figure V.7j

The curves are fits to the η^0 and ω^0 .

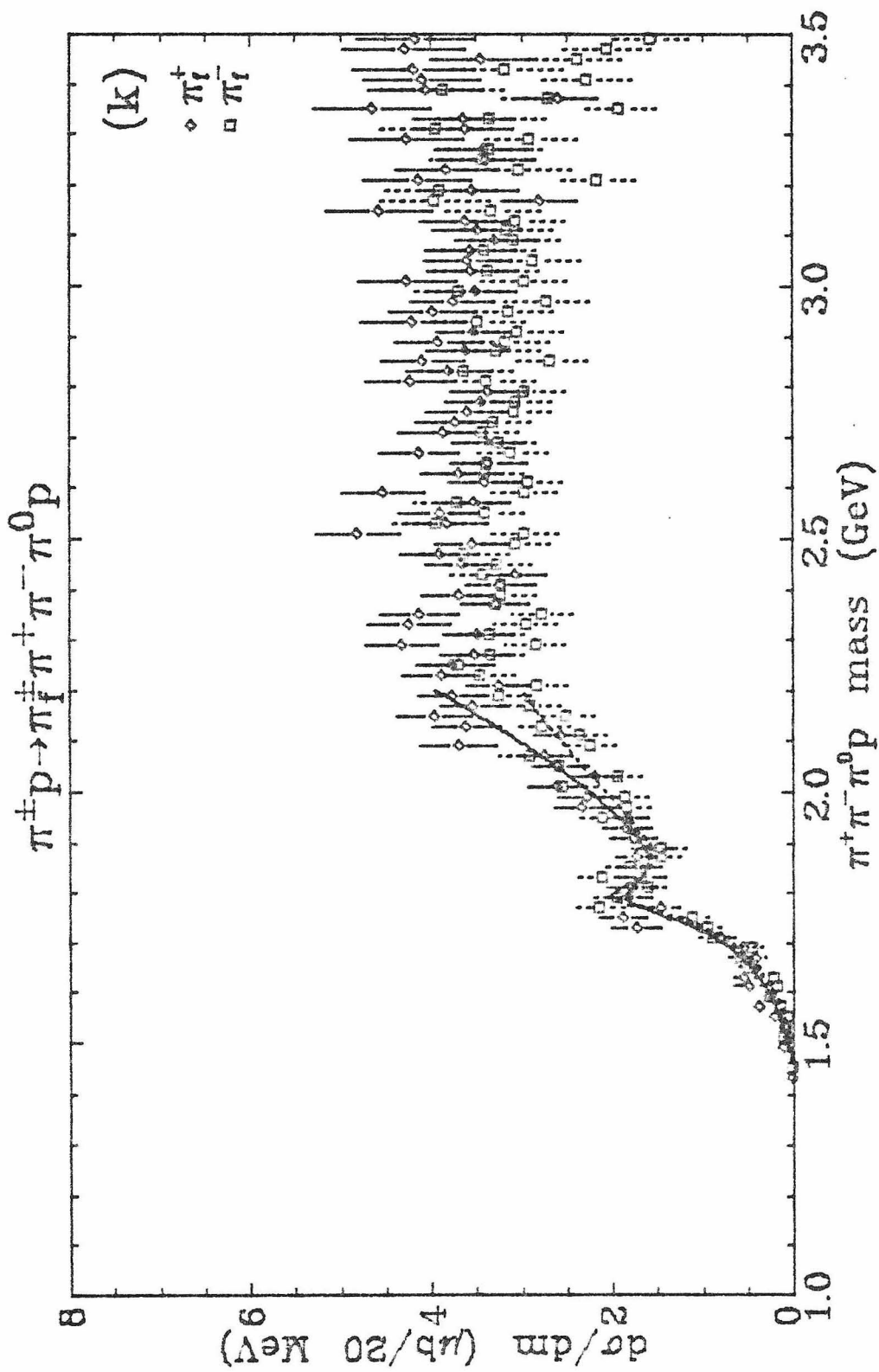


Figure V.7k

The curves are fits to the $N^+(1790)$.



— π^+ fits

----- π^- fits

$$\text{Prob}(\chi_{\text{fit}}^2) \geq 5\%$$

$$-t_{\pi\pi(f)} < 0.6 \text{ GeV}^2/c^2$$

$$(\pi^+ \pi^+ \pi^- n) \text{ mass} < 3.7 \text{ GeV}$$

Figures V.8a-h

Invariant mass distributions for the slow particles (other than the π_f^+) of the n channel. For those $d\sigma/dm$ distributions in which only a single π^+ appears in the invariant mass, each event appears twice in the distribution.

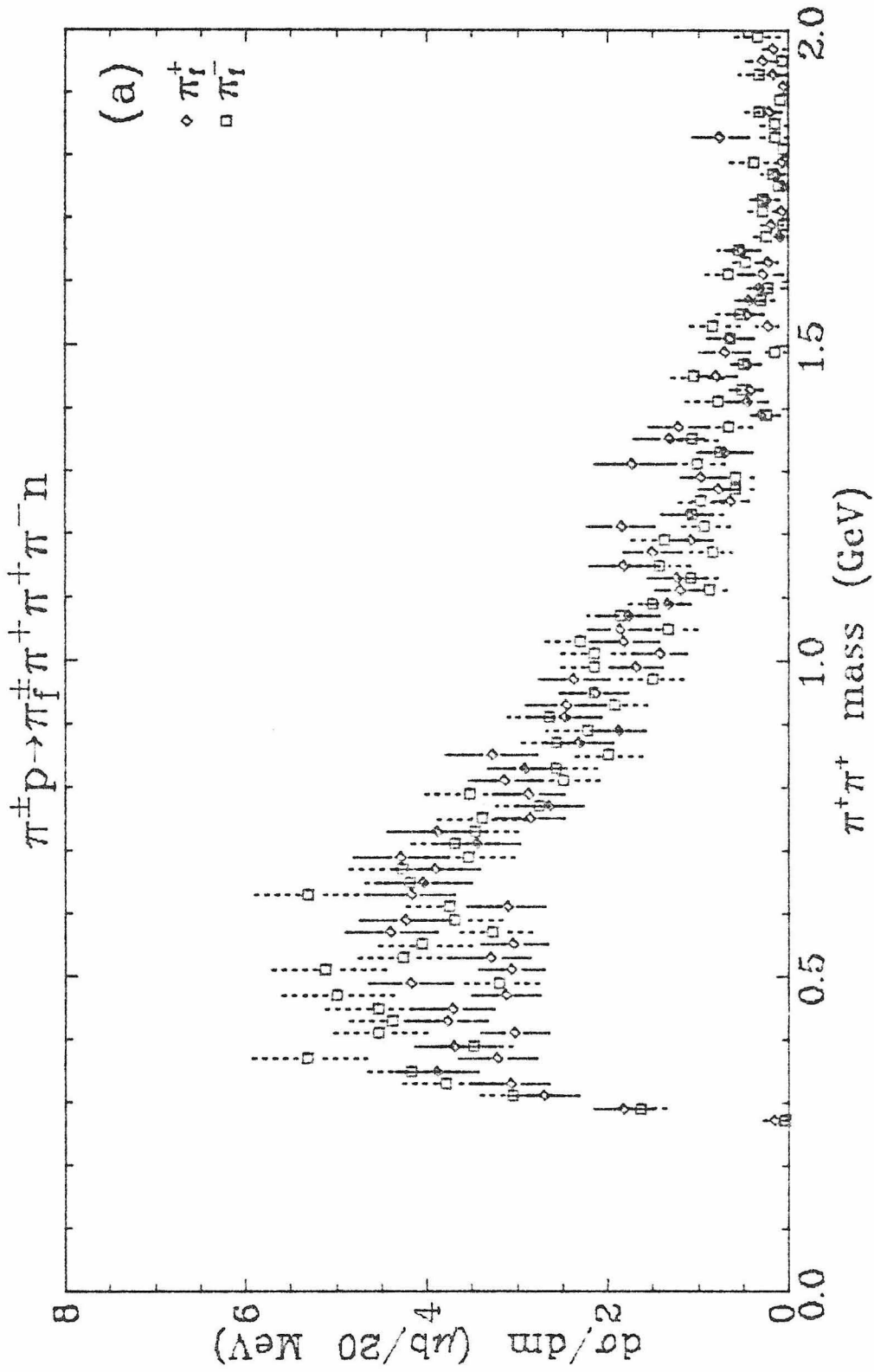


Figure V.8a

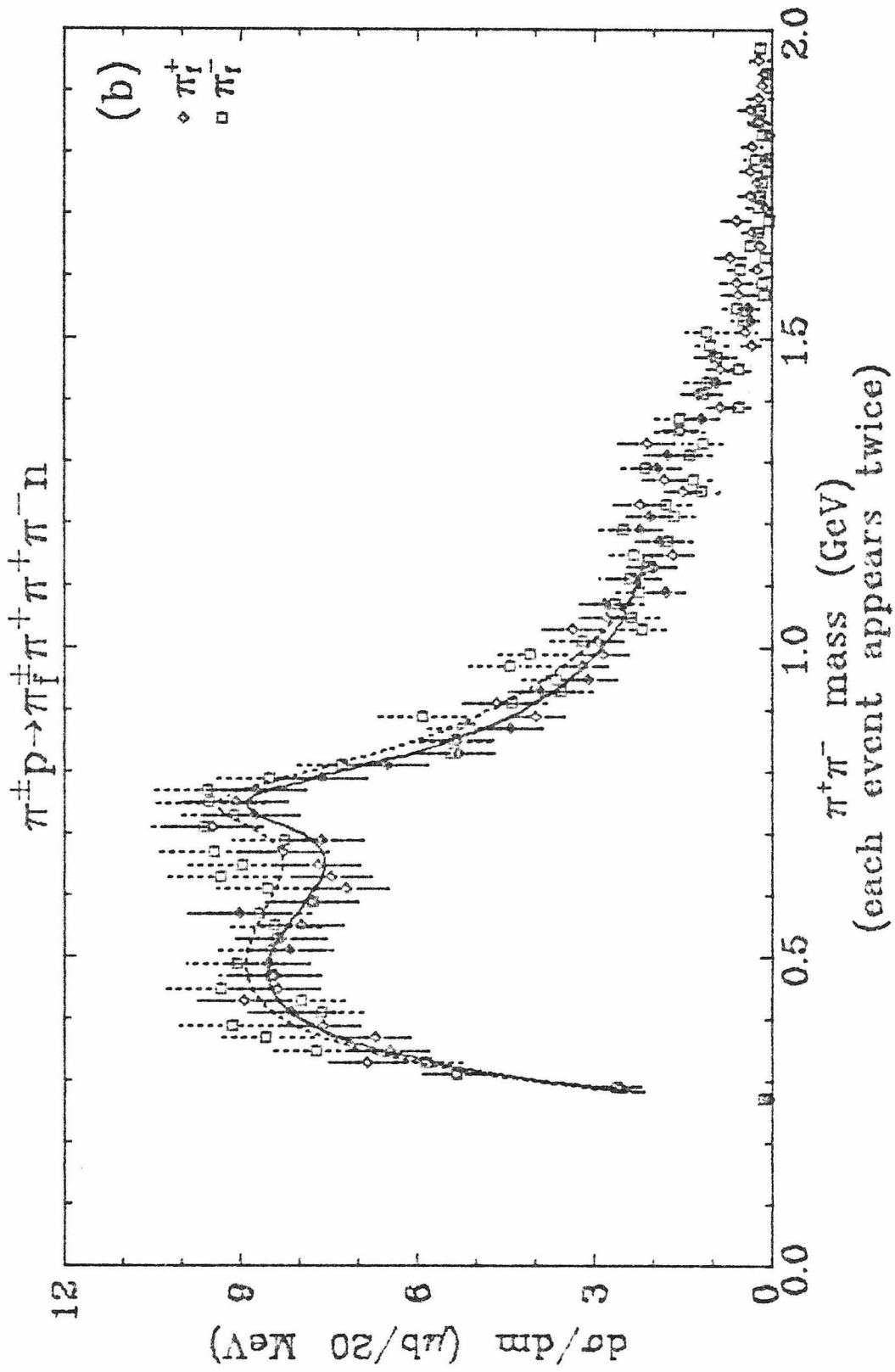


Figure V.8b

The curves are fits to the ρ^0 .

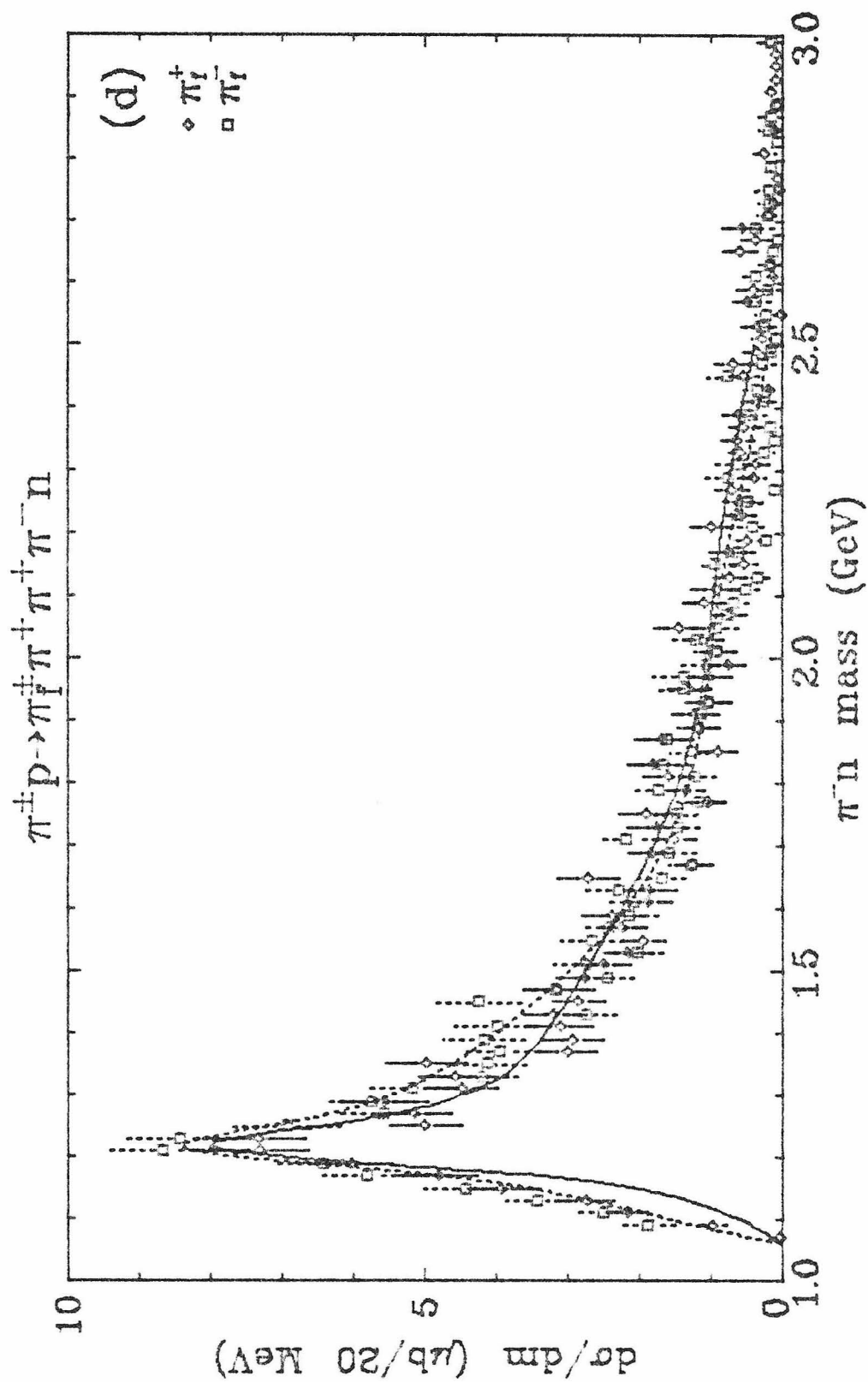


Figure V.8d

The curves are fits to the Δ^- .

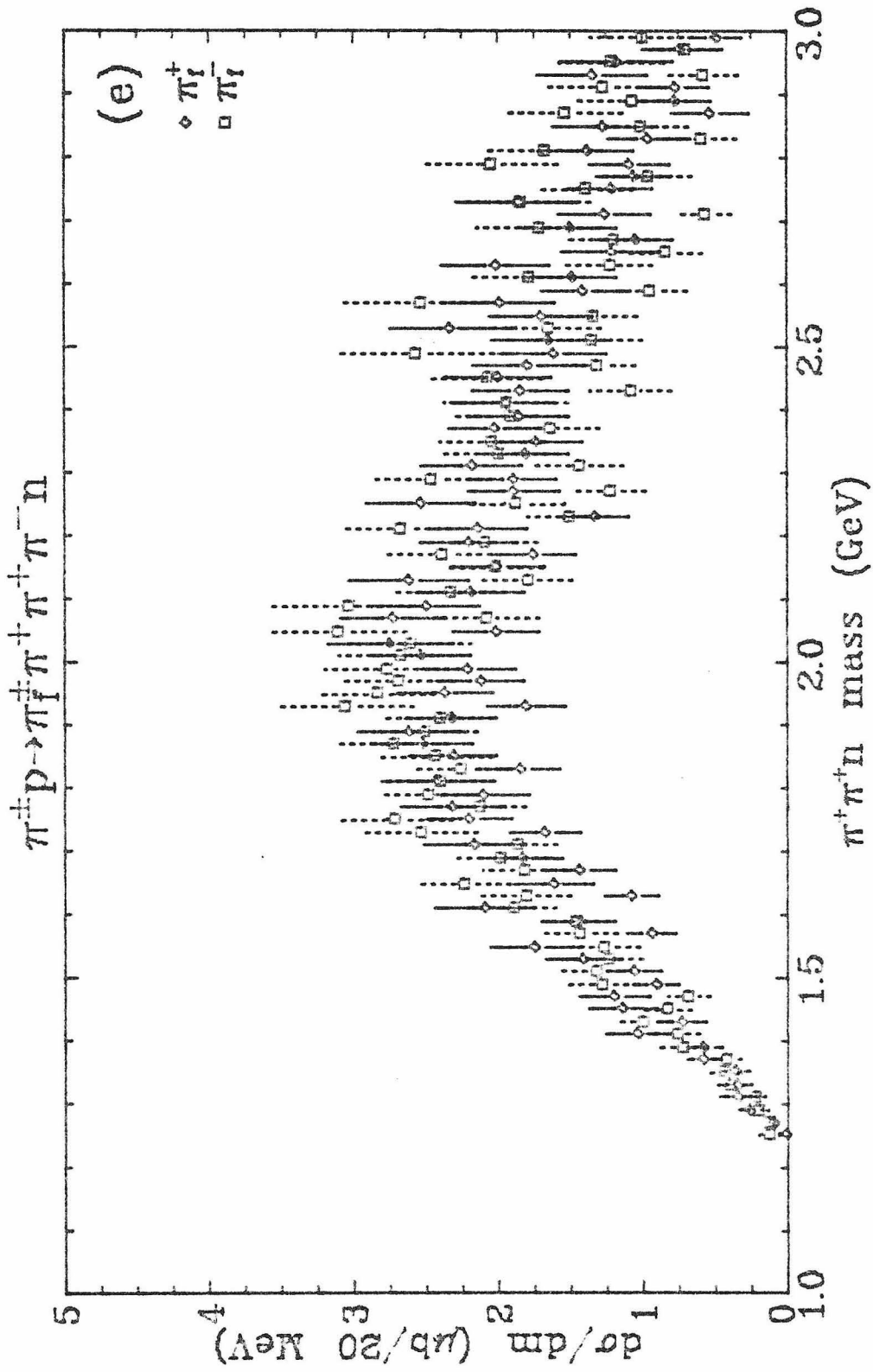


Figure V.8e

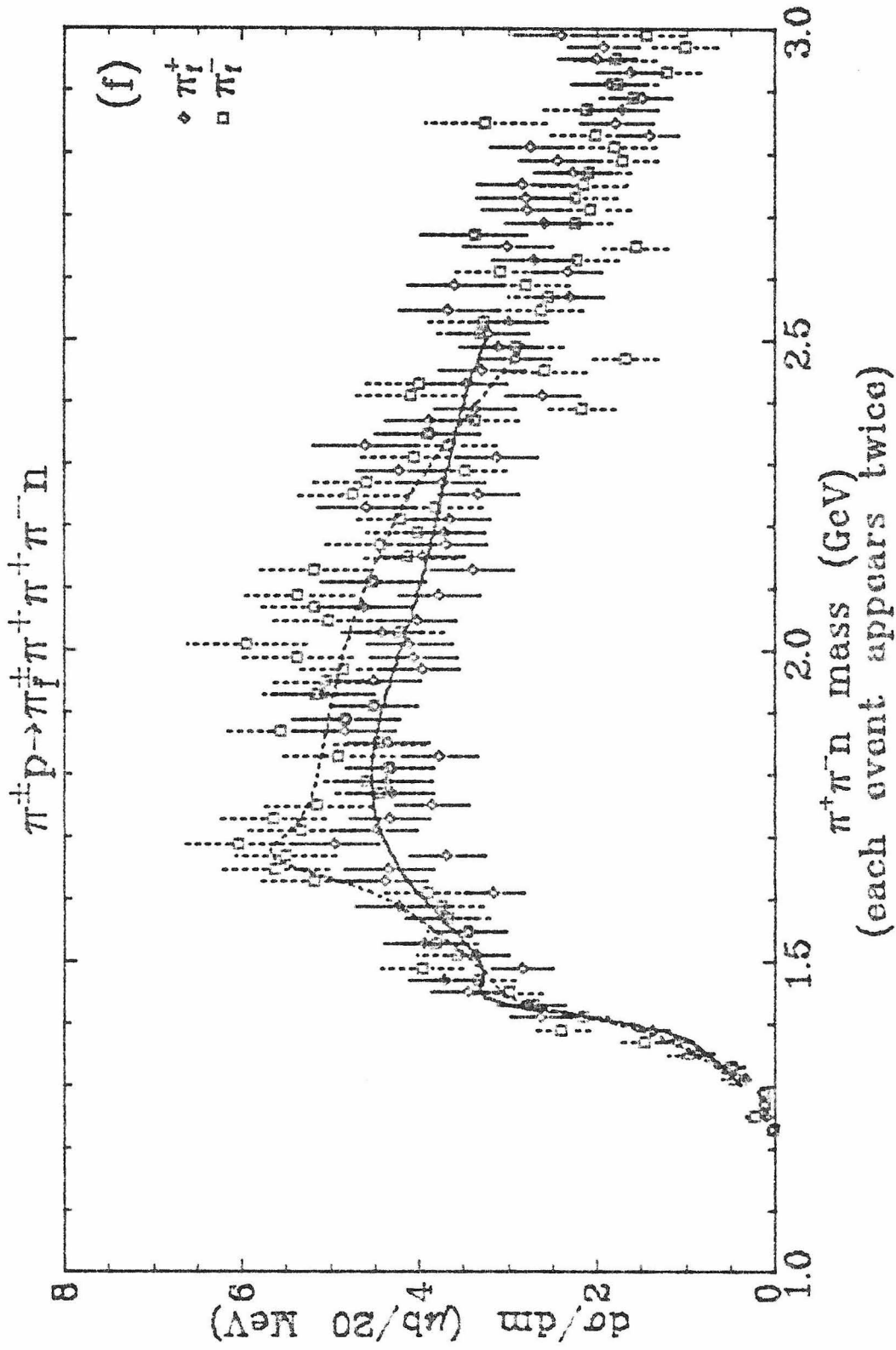


Figure V.8f

The π^+ curve is a fit to the $N^0(1470)$; the π^- curve is a fit to the $N^0(1470)$ and $N^0(1688)$.

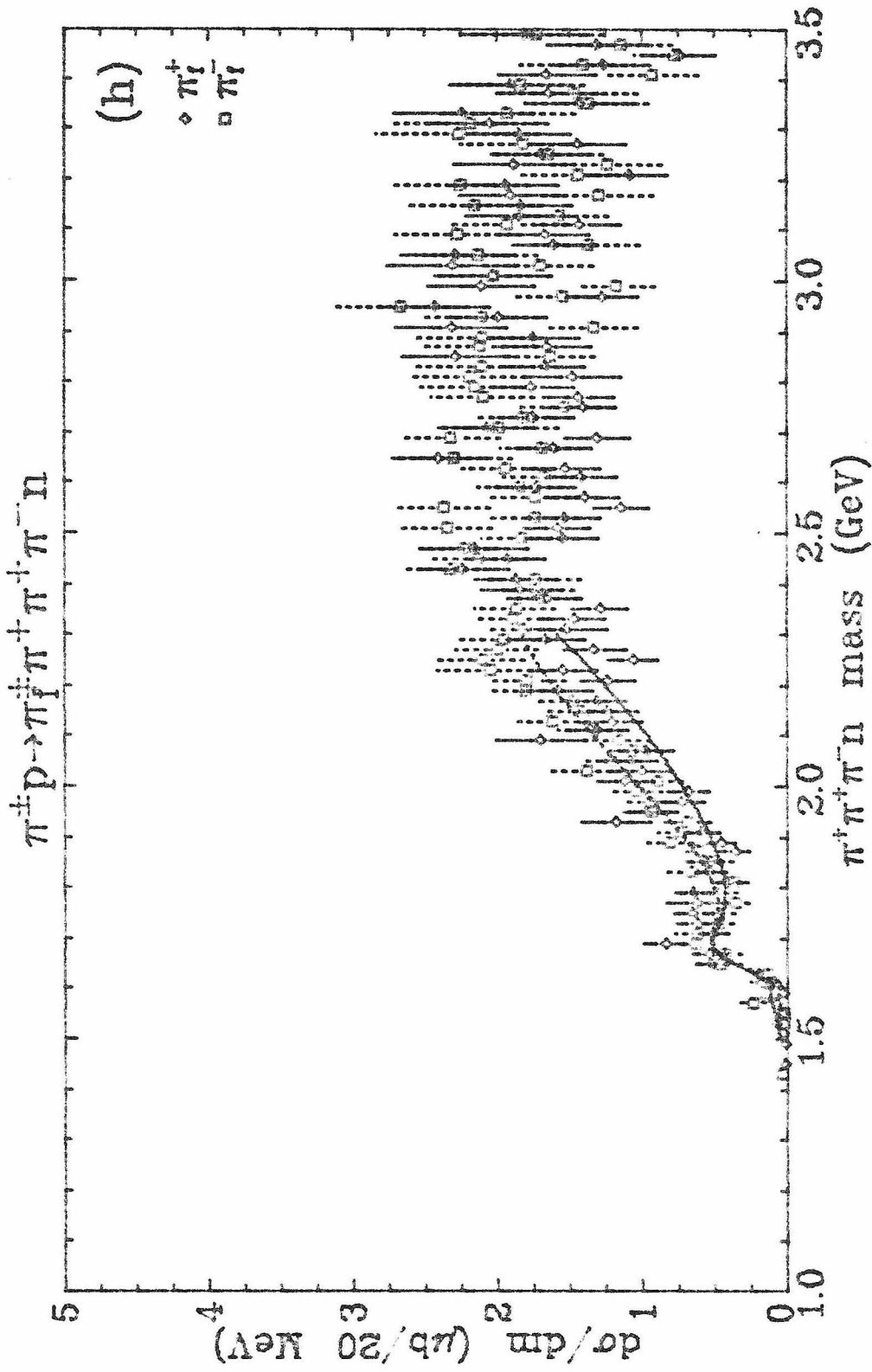


Figure V.8h

The curves are fits to the $N^+(1700)$.

6. Associated Fast Meson and Slow System Resonance Production

We have investigated the associated production of a fast meson resonance ($\rho(770)$, $f^0(1270)$, or $\omega(1680)$) and a slow system resonance (usually $\Delta(1232)$ or a slow $\rho(770)$). This associated production was found by examining scatterplots of two invariant masses where each event was a single dot. The associated production showed up as the overlap of the two bands (enhanced concentrations of events) of two resonances. We did not use the scatterplots to estimate the associated resonance production. Instead we used the projected plots of the distribution in a single invariant mass primarily due to their ease of interpretation. These plots were made by selecting events in either a slow resonance (Δ or ρ) or a fast ρ with a mass cut about the resonance peak. The same scheme was used to generate the plots in Figs. V.6 discussed in section 4 of this chapter. This procedure has the difficulty of dealing with events coming from the background under the resonance peak within the defining cut. As can be seen from Tables V.9 and V.11, 30% to 80% of the events within the defining cuts come from the contributions of these backgrounds. As will be seen in the plots, non-physical peaks are observed in some of those cases in which one of the particles forming the invariant mass upon which the defining cut is made also appears in the invariant mass being plotted (Fig. V.13a for example).

The slow system invariant masses for cuts requiring fast ρ mesons are given in Figs. V.9a-g for the π^0 channel with the ρ_f^0 cut, in Figs.

V.10a-f for the n channel with the ρ_f^0 cut, and in Figs. V.11a-d for the π^0 channel again but now for the ρ_f^\pm cuts. We have fitted the resonance peaks in these distributions and listed the resulting estimates for their production in Table V.12 in terms of the weight-sums. Table V.12 also gives the fraction of the uncut resonance production (see Table V.10) contained within the cut (see "Resonance fraction" column). The column labeled "Fraction of cut events" in Table V.12 is the fraction of the events within the cut (see Table V.9) which were found to be in the fitted resonance. It is unknown how many of the events in the fitted resonance are actually part of the resonance the cut selects rather than being events from the background under the resonance peak within the cut.

The data may also be presented in the obverse manner by cutting on the slow system masses and plotting the fast invariant masses. The Δ^{++} or Δ^- cuts were defined by requiring the π^+p mass or the π^-n mass to be less than 1.36 GeV. The ratio of the total Δ signal to that portion below 1.36 GeV is 1.55. Similarly, the slow ρ cuts were defined by requiring the $\pi\pi$ mass to be between 0.64 and 0.84 GeV which gave a total resonance signal to in-cut signal ratio of 2.01. Table V.11 lists the fraction of events within the defining cuts that are due to the backgrounds under the slow resonances. Table V.11 also gives the total weight-sum of the events within each cut.

Table V.11

Background fractions and total events within slow Δ and ρ cuts

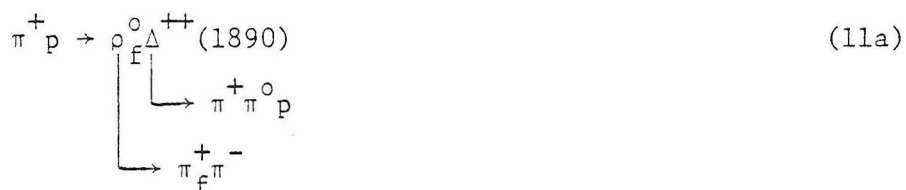
Cut on resonance	Total weight-sum within cut		Fraction of events in cut from background	
	$\frac{\pi^+ \pi^+ \pi^- \pi^0 p}{\pi_f^+ \pi^+ \pi^- \pi^0 p}$	$\frac{\pi^- \pi^+ \pi^- \pi^0 p}{\pi_f^- \pi^+ \pi^- \pi^0 p}$	$\frac{\pi^+ \pi^+ \pi^- \pi^0 p}{\pi_f^+ \pi^+ \pi^- \pi^0 p}$	$\frac{\pi^- \pi^+ \pi^- \pi^0 p}{\pi_f^- \pi^+ \pi^- \pi^0 p}$
$\Delta^{++} \rightarrow \pi^+ p$	13251±234	8622±181	31.4±1.3%	44.2±1.7%
$\rho^0 \rightarrow \pi^+ \pi^-$	6526±179	4395±145	82.8±2.1%	71.6±2.4%
$\rho^+ \rightarrow \pi^+ \pi^0$	6907±178	4382±140	62.3±2.7%	77.3±2.7%
$\rho^- \rightarrow \pi^- \pi^0$	6438±167	4745±147	69.2±2.0%	66.7±2.4%
	$\frac{\pi^+ \pi^+ \pi^+ \pi^- n}{\pi_f^+ \pi^+ \pi^+ \pi^- n}$	$\frac{\pi^- \pi^+ \pi^+ \pi^- n}{\pi_f^- \pi^+ \pi^+ \pi^- n}$	$\frac{\pi^+ \pi^+ \pi^+ \pi^- n}{\pi_f^+ \pi^+ \pi^+ \pi^- n}$	$\frac{\pi^- \pi^+ \pi^+ \pi^- n}{\pi_f^- \pi^+ \pi^+ \pi^- n}$
$\Delta^- \rightarrow \pi^- n$	5003±136	4948±140	40.3±2.1%	63.3±2.7%
$\rho^0 \rightarrow \pi^+ \pi^-$	5207±153	5025±156	69.7±2.8%	75.5±2.9%

The fast invariant mass distributions cut on the Δ^{++} or Δ^- are given in Figs. V.12a-j, those for the slow ρ^0 cuts (π^0 and n channels) in Figs. V.13a-l, and those for the slow ρ^\pm cuts (π^0 channel only) in Figs. V.14a-n. The fit results providing estimates for the observed resonances are listed in Table V.13. This table is organized in a fashion similar to Table V.12 (see discussion above) except that the uncut resonance estimates are in Tables V.6 and V.7 and the total cut weight-sums are in Table V.11

Comparing the numbers in Tables V.12 and V.13, the effects of the uncertainty in the estimation of the resonance signal due to the background events within the defining cuts can be seen as a disagreement in the results found by the two obverse methods. As an example consider the results for the $\rho_f^0 \Delta^{++} \pi^0$ final state in the π^+ data (corrected

for the resonance cuts): by cutting on the ρ_f^0 we have 5634 ± 430 events while the Δ^{++} cut gives 4242 ± 421 events for the same process. This discrepancy may be due to the background events as they contribute about 50% of the events in the ρ_f^0 cut and about 30% of the events in the Δ^{++} cut. An unknown fraction of these background events under the peaks in the cuts then contribute to the resonance peaks observed in the cut invariant mass distributions. Because of this difficulty, we present no estimates for resonance production in a diffractively produced slow system in analogy to our earlier estimation of the total channel cross section for diffractive production of the slow system (see Table V.8 in section 3 of this chapter).

The difficulties discussed above do not change the conclusion that there is substantial associated fast meson and slow system (either baryon or meson) resonance production. For instance, a large fraction of the Δ^{++} signal appears to be produced along with a fast ρ (either neutral or charged). Similarly there are large $\rho\rho N$ signals present in the data. However, the quasi-2-body processes seem not to be as prevalent in the data as the quasi-3-body processes such as $\rho\pi\Delta$ or $\rho\rho N$. In section 3 we discussed the observation of the $\omega^0\Delta^{++}$ and $\eta^0\Delta^{++}$ final states in the π^+ data. Tables V.12 and V.13 show evidence for the reactions:



and:



There also appears to be some weak evidence for the $A_2^0 \Delta^{++}$ and $A_3^0 \Delta^{++}$ final states in the π^+ data.

Table V.12

Estimated slow system resonance production for the fast ρ cuts

Cut on	Resonance	$\pi_f^+ \pi_f^- \pi \pi p$		$\pi_f^- \pi_f^+ \pi \pi p$	
		Weight-sum	Resonance fraction	Weight-sum	Resonance fraction
$\rho_f^0 \rightarrow \pi_f^\pm \pi^\mp$	$\Delta^{++} \rightarrow \pi^+ p$	3859±375	30.2±3.1%	42.1±4.2%	—
$\rho_f^0 \rightarrow \pi_f^\pm \pi^\mp$	$\Delta^+ \rightarrow \pi^0 p$	378±274	33.5±26.8%	4.1±3.0%	11.7±3.9%
$\rho_f^0 \rightarrow \pi_f^\pm \pi^\mp$	$\Delta^0 \rightarrow \pi^- \bar{p}$	—	—	—	9.7±3.7%
$\rho_f^\pm \rightarrow \pi_f^\pm \pi^0$	$\Delta^{++} \rightarrow \pi^+ p$	3456±250	27.1±2.2%	49.2±3.8%	46.2±4.6%
$\rho_f^\pm \rightarrow \pi_f^\pm \pi^0$	$\Delta^0 \rightarrow \pi^- \bar{p}$	688±163	19.9±5.2%	9.8±2.3%	6.3±4.2%
$\rho_f^0 \rightarrow \pi_f^\pm \pi^\mp$	$\rho^+ \rightarrow \pi^+ \pi^0$	2164±350	41.8±8.2%	23.6±3.9%	—
$\rho_f^0 \rightarrow \pi_f^\pm \pi^\mp$	$\rho^- \rightarrow \pi^- \pi^0$	—	—	—	—
$\rho_f^\pm \rightarrow \pi_f^\pm \pi^\mp$	$\rho^0 \rightarrow \pi^+ \pi^-$	799±288	36.5±16.0%	11.4±4.1%	15.8±5.8%
$\rho_f^0 \rightarrow \pi_f^\pm \pi^\mp$	$\Delta(1890) \rightarrow \pi^+ \pi^0 p$	1205±309	44.1±16.0%	13.1±3.4%	—

Table V.12 (cont.)

Cut on	Resonance	$\pi_f^+ \pi^+ \pi^- n$	$\pi_f^- \pi^+ \pi^- n$	
		Weight-sum	Resonance fraction	
			Fraction of cut events	
$\rho_f^0 \rightarrow \pi_f^\pm \pi^\mp$	$\Delta^+ \rightarrow \pi^+ n$	639±221	68.1±37.4%	17.2±6.0%
$\rho_f^0 \rightarrow \pi_f^\pm \pi^\mp$	$\Delta^- \rightarrow \pi^- n$	---	---	---
$\rho_f^0 \rightarrow \pi_f^\pm \pi^\mp$	$\rho^0 \rightarrow \pi^+ \pi^-$	---	---	---
$\rho_f^0 \rightarrow \pi_f^\pm \pi^\mp$	$N(1688) \rightarrow \pi^+ \pi^- n$	---	---	---
		1130±211	41.7±9.2%	22.3±4.2%
		1615±444	57.8±21.4%	31.9±8.8%
		320±180	64.8±42.7%	6.3±3.6%

$$\diamond \pi^+ p \rightarrow \rho_f^0 \pi^+ \pi^0 p \quad \rho_f^0 \rightarrow \pi_f^+ \pi^-$$

$$\square \pi^- p \rightarrow \rho_f^0 \pi^- \pi^0 p \quad \rho_f^0 \rightarrow \pi_f^- \pi^+$$

— π^+ fits

----- π^- fits

$$\text{Prob}(\chi_{\text{fit}}^2) \geq 5\%$$

$$-t_{\pi\pi(f)} < 0.6 \text{ GeV}^2/c^2$$

$$(\pi^+ \pi^- \pi^0 p) \text{ mass} < 3.7 \text{ GeV}$$

$\rho_f^0 \rightarrow \pi_f^\pm \pi^\mp$ definition:

$$0.6 \leq \pi_f^\pm \pi^\mp \text{ mass} < 1.0 \text{ GeV}$$

Figures V.9a-g

Invariant mass distributions for the slow particles of the π^0 channel for events in the fast ρ^0 peak (see above).

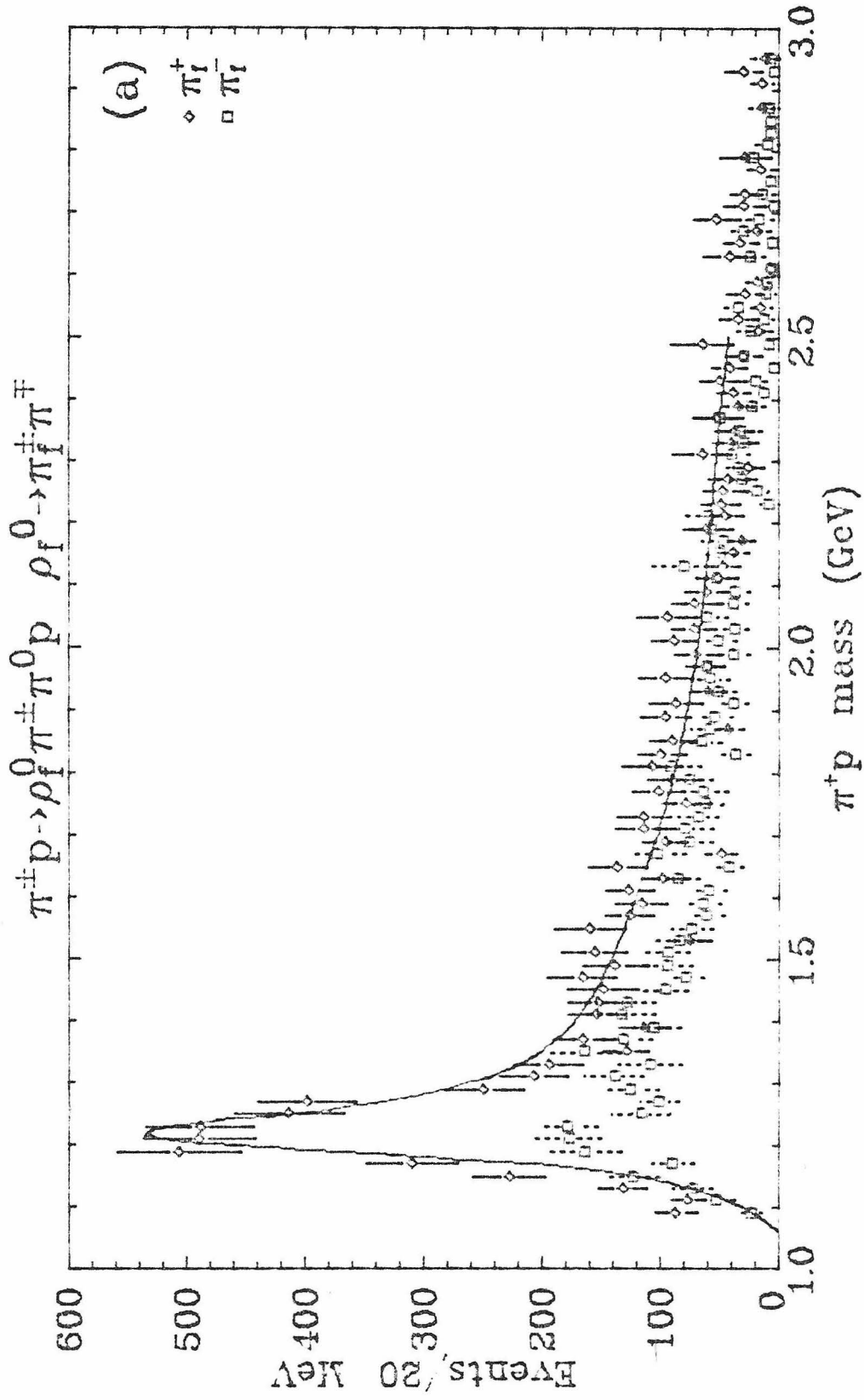


Figure V.9a

The curve is a fit to the Δ^{++} .

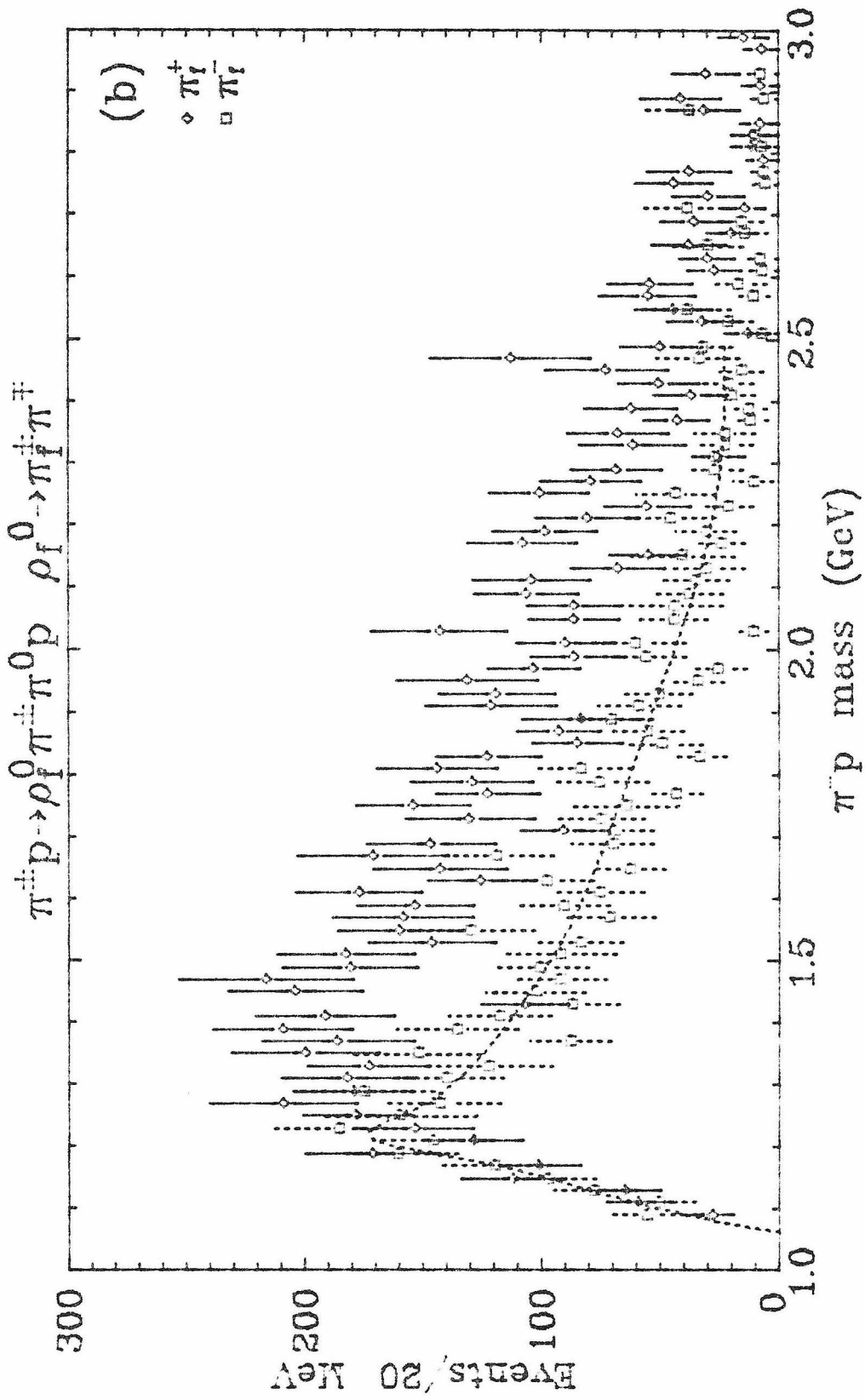


Figure V.9b

The curve is a fit to the Δ^0 .

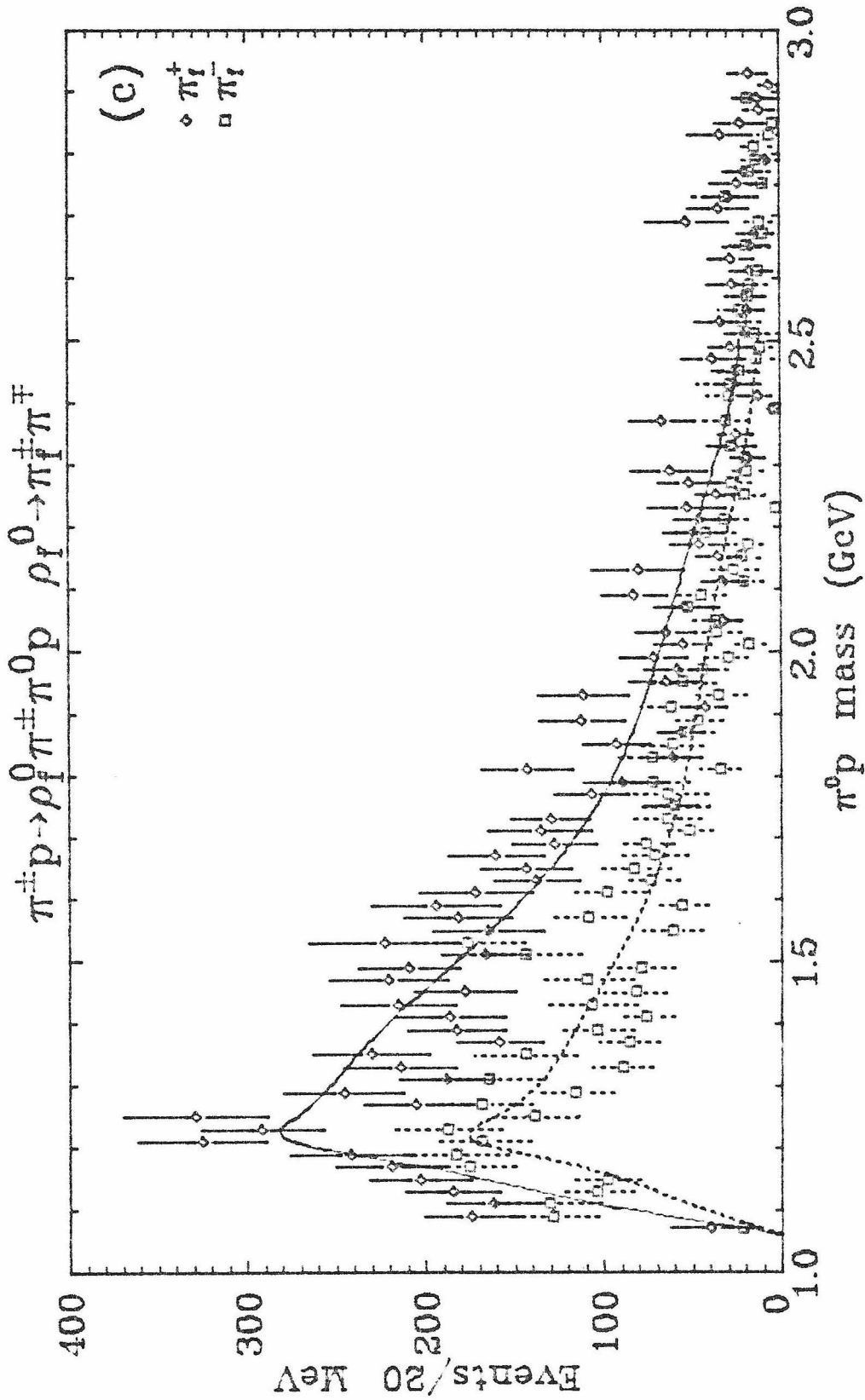


Figure V.9c

The curves are fits to the Δ^+ .

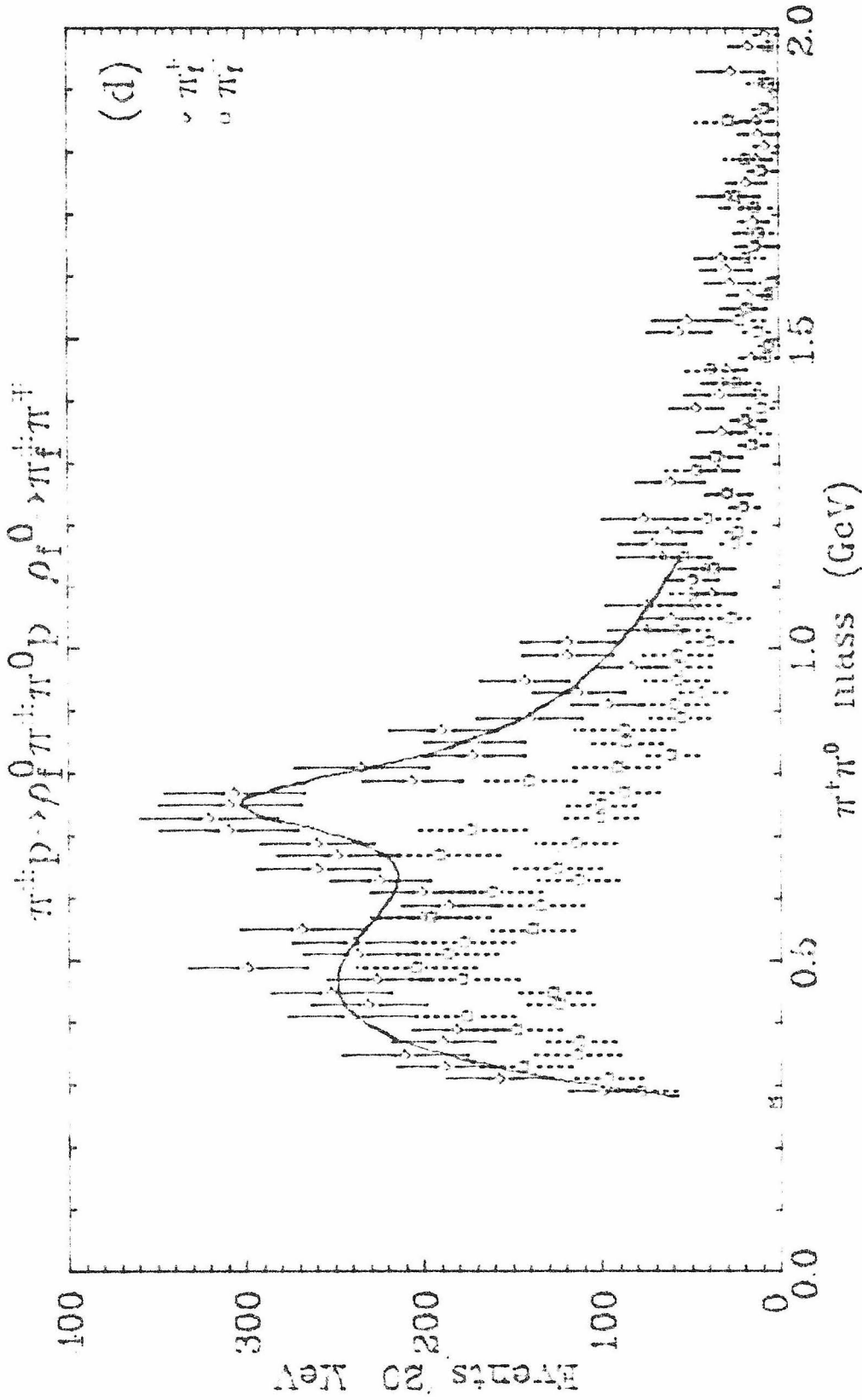


Figure V.9d

The curve is a fit to the ρ^+ .

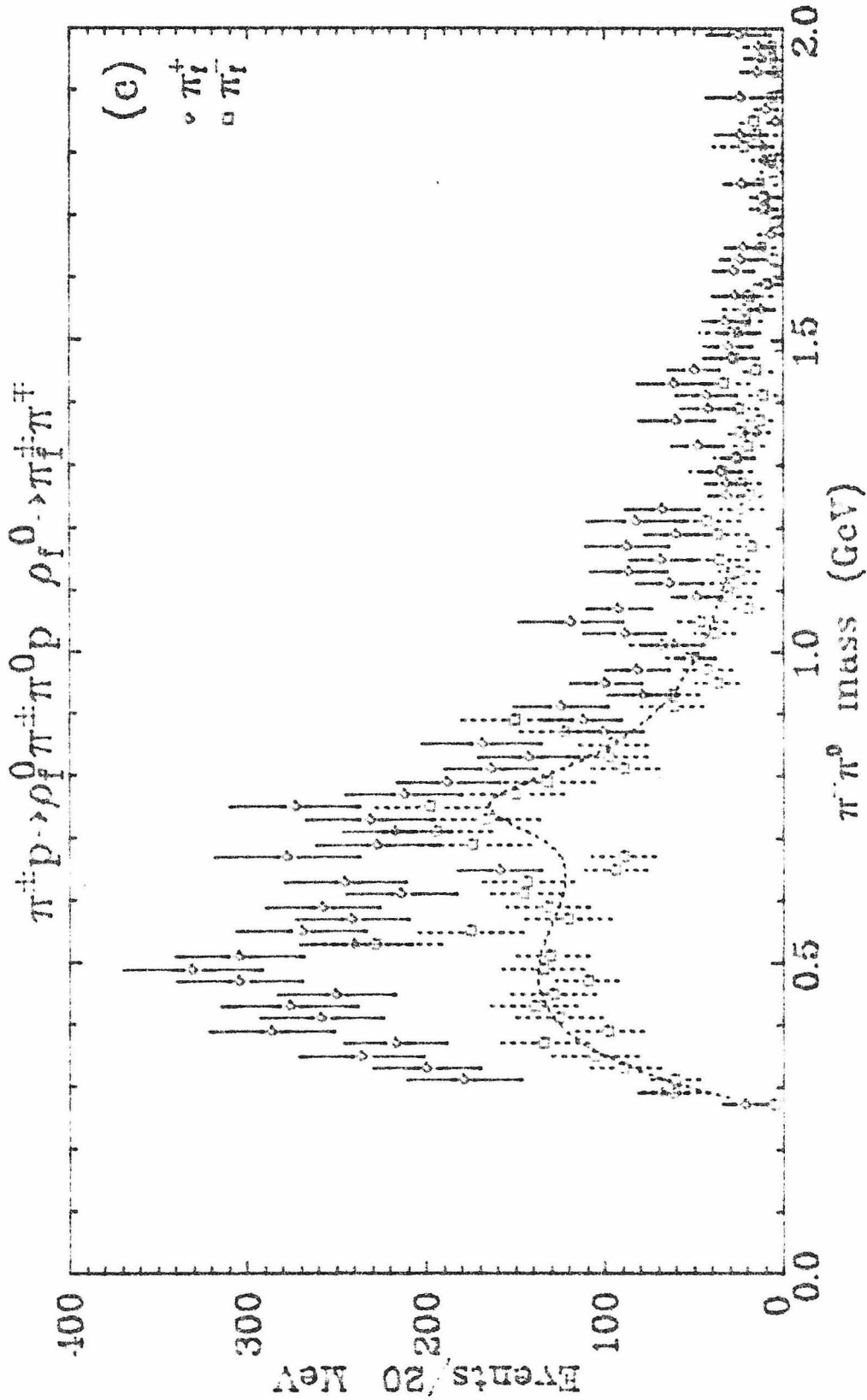


Figure V.9e

The curve is a fit to the ρ^- .

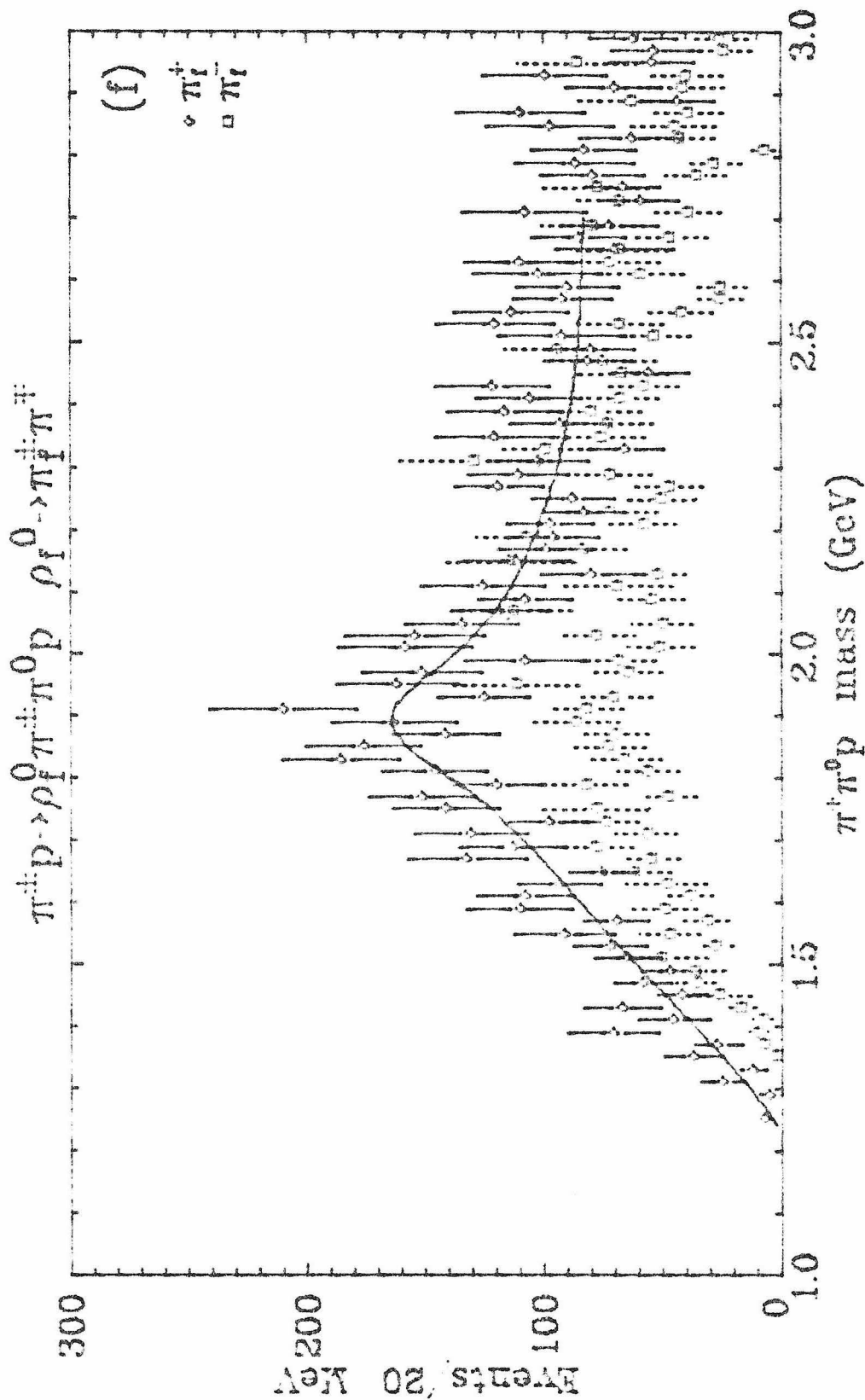


Figure V.9f

The curve is a fit to the Δ^{++} (1890).

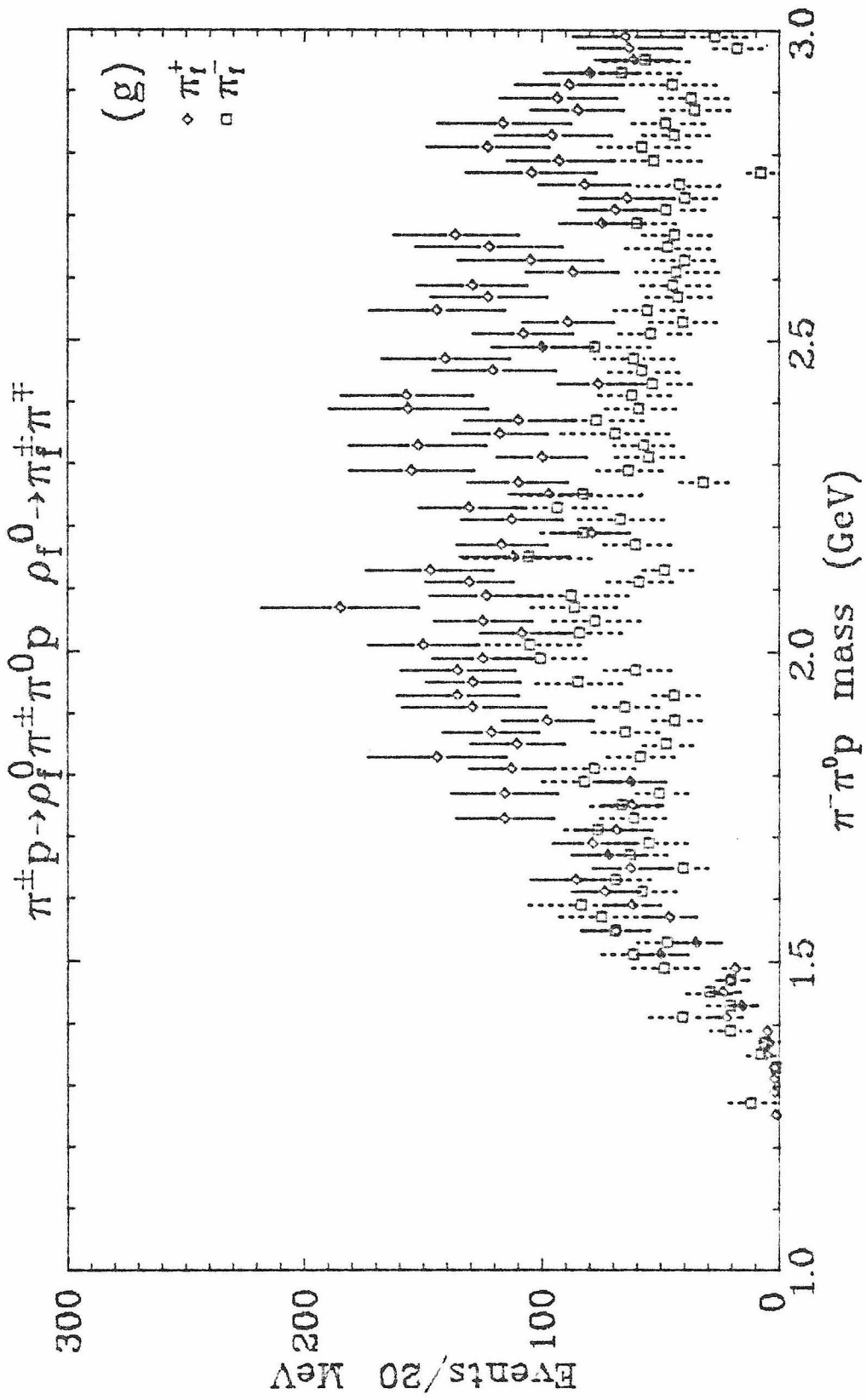


Figure V.9g

$$\diamond \pi^+ p \rightarrow \rho_f^0 \pi^+ \pi^+ n \quad \rho_f^0 \rightarrow \pi_f^+ \pi^-$$

$$\square \pi^- p \rightarrow \rho_f^0 \pi^+ \pi^- n \quad \rho_f^0 \rightarrow \pi_f^- \pi^+$$

— π^+ fits

----- π^- fits

$$\text{Prob}(\chi_{\text{fit}}^2) \geq 5\%$$

$$-t_{\pi\pi(f)} < 0.6 \text{ GeV}^2/c^2$$

$$(\pi^+ \pi^+ \pi^- n) \text{ mass} < 3.7 \text{ GeV}$$

$\rho_f^0 \rightarrow \pi_f^\pm \pi^\mp$ definition:

$$0.6 \leq \pi_f^\pm \pi^\mp \text{ mass} < 1.0 \text{ GeV}$$

Figures V.10a-f

Invariant mass distributions for the slow particles of the n channel for events within the fast ρ^0 peak (see above).

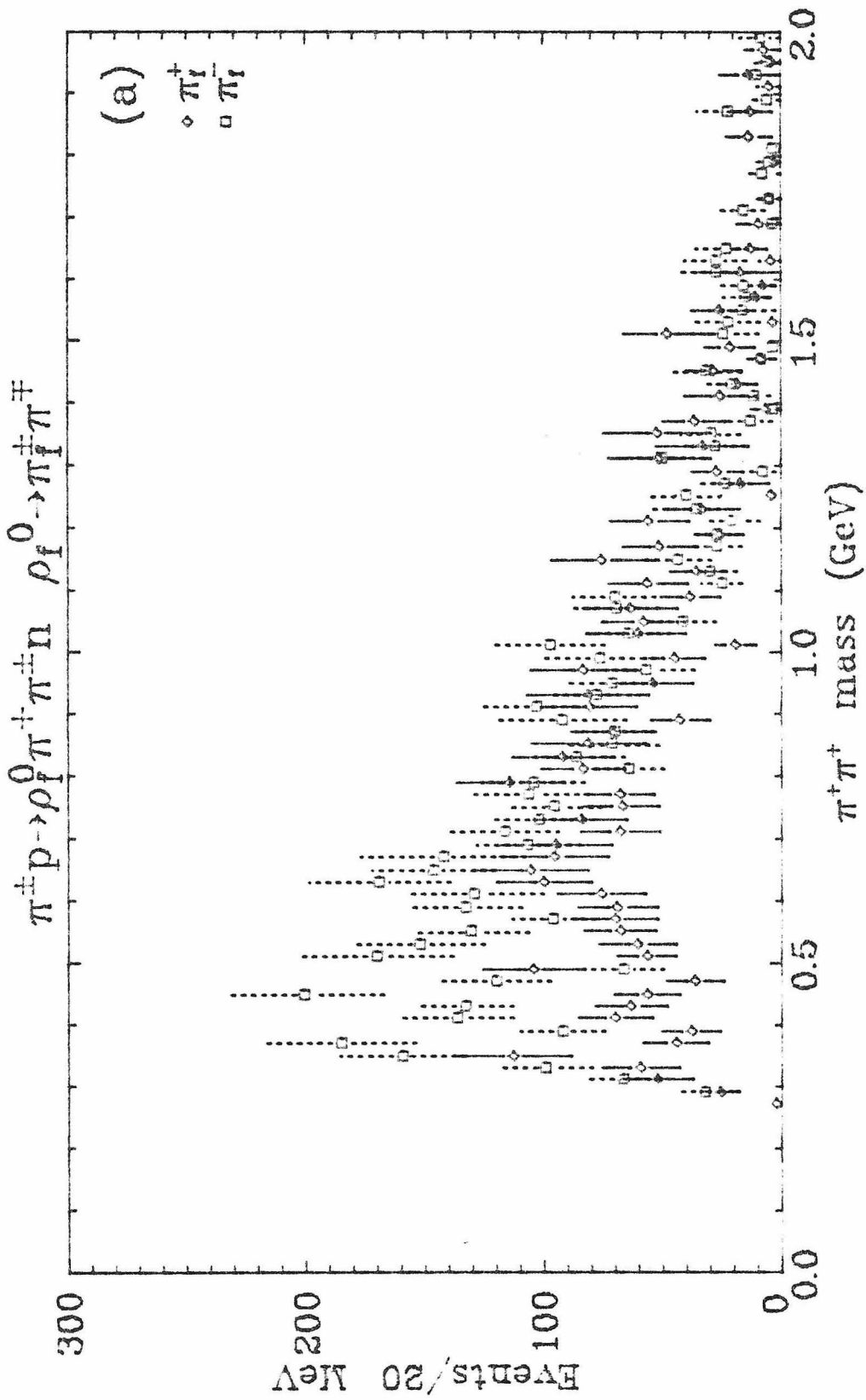


Figure V.10a

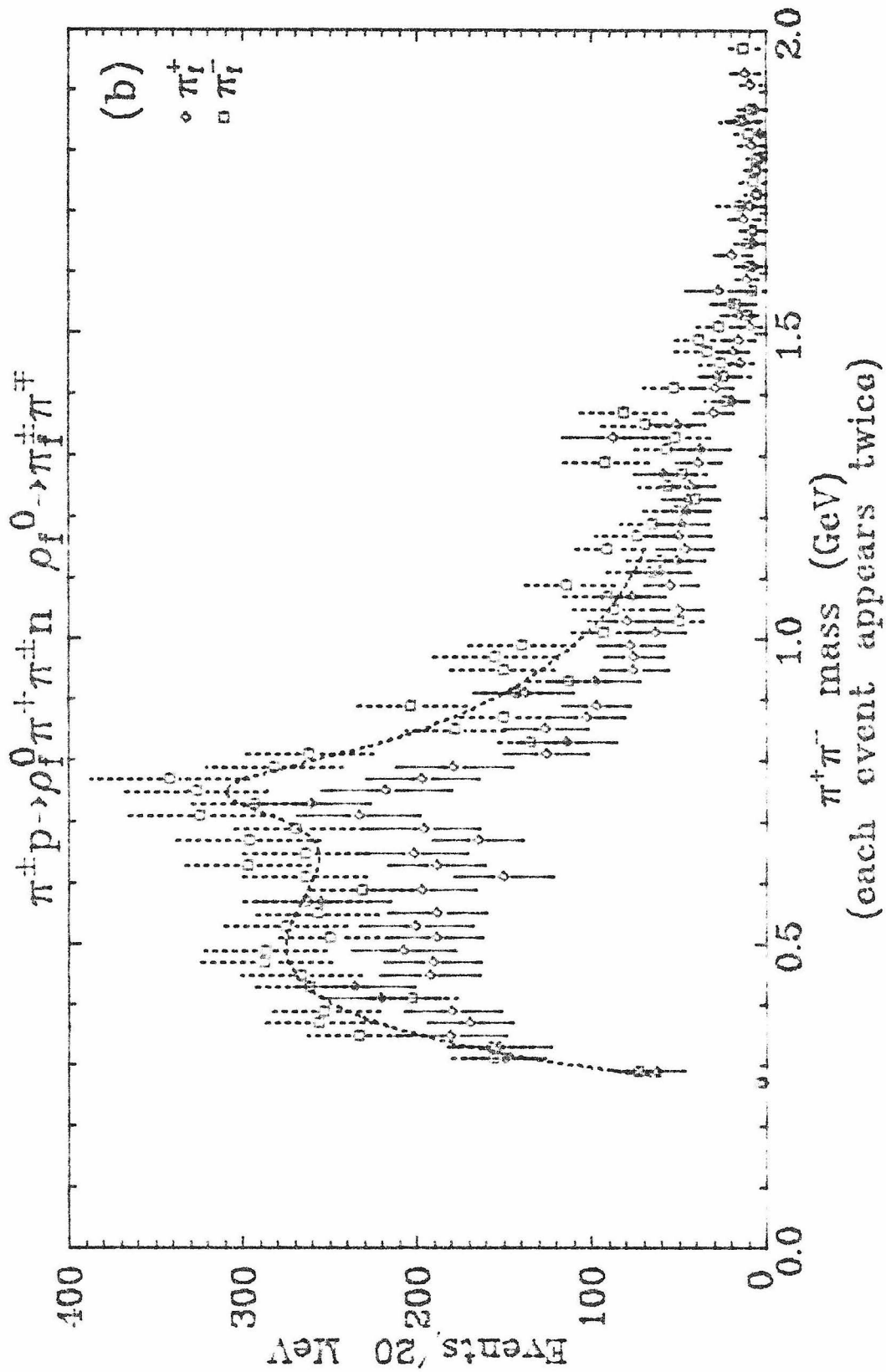


Figure V.10b

The curve is a fit to the ρ^0 .

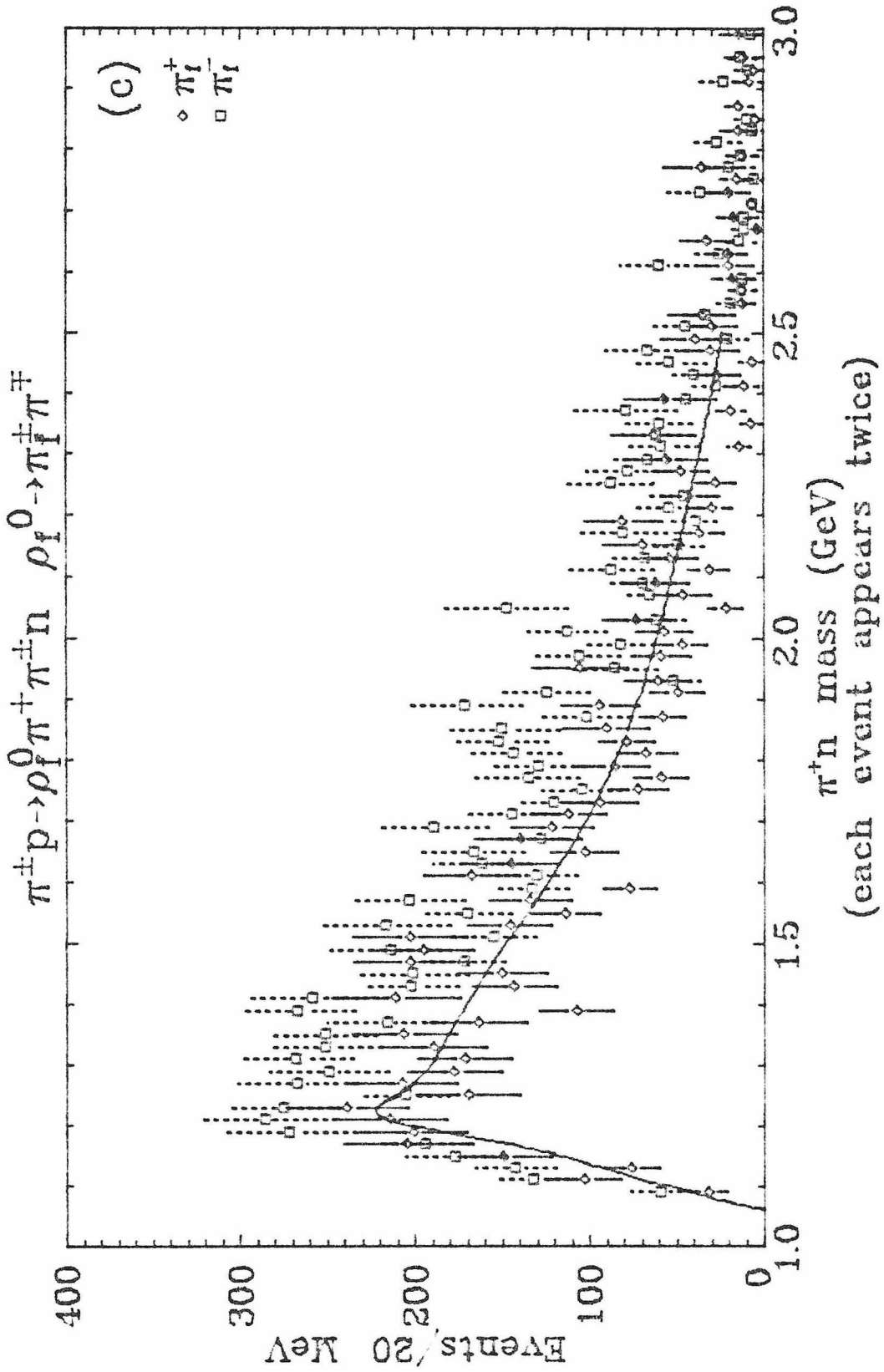


Figure V.10c

The curve is a fit to the Δ^+ .

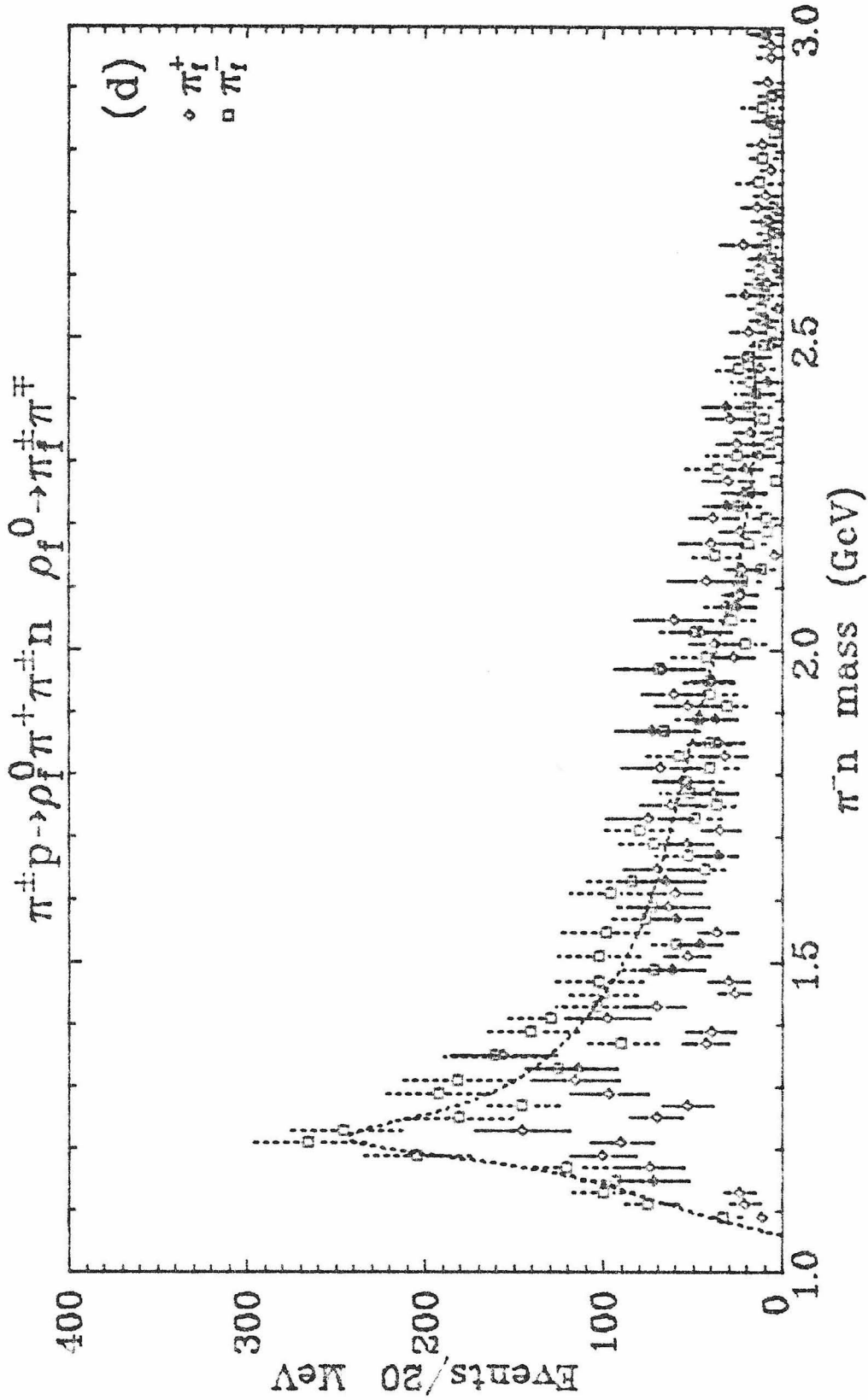


Figure V.10d

The curve is a fit to the Δ^- .

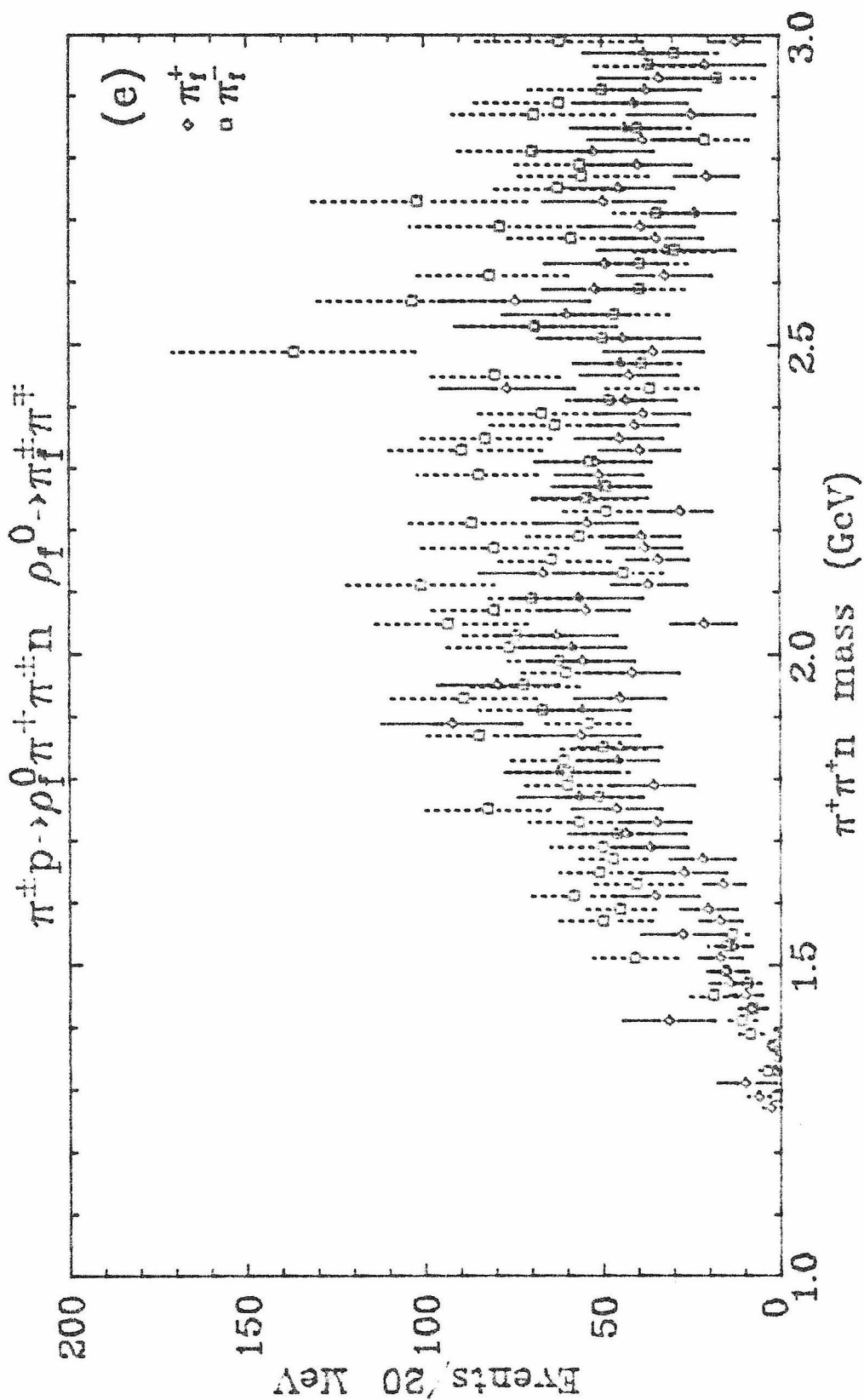


Figure V.10e

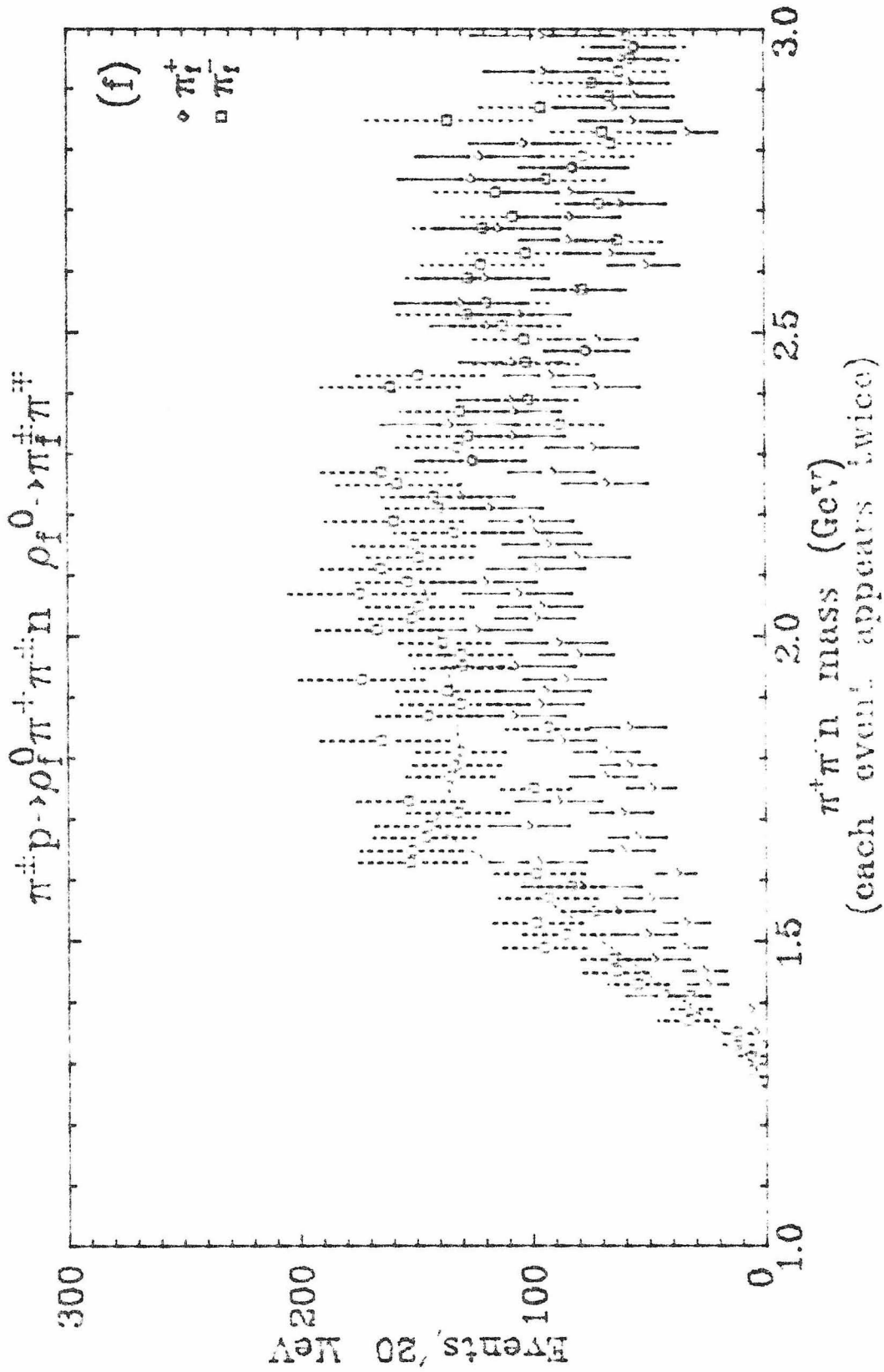
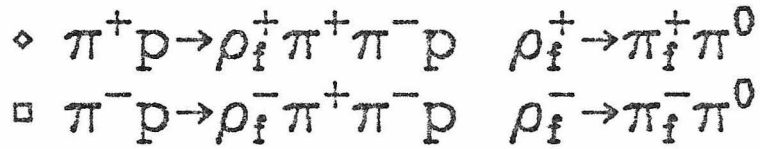


Figure V.10f

The curve is a fit to the $N^0(1688)$.



— π^+ fits

----- π^- fits

Prob(χ_{fit}^2) $\geq 5\%$

$-t_{\pi\pi(f)} < 0.6 \text{ GeV}^2/c^2$
($\pi^+ \pi^- \pi^0 p$) mass $< 3.7 \text{ GeV}$

$\rho_f^\pm \rightarrow \pi_f^\pm \pi^0$ definition:
 $0.6 \leq \pi_f^\pm \pi^0$ mass $< 1.0 \text{ GeV}$

Figures V.11a-d

Invariant mass distributions for the slow particles of the π^0 channel for events within the fast ρ^\pm peaks (see above).

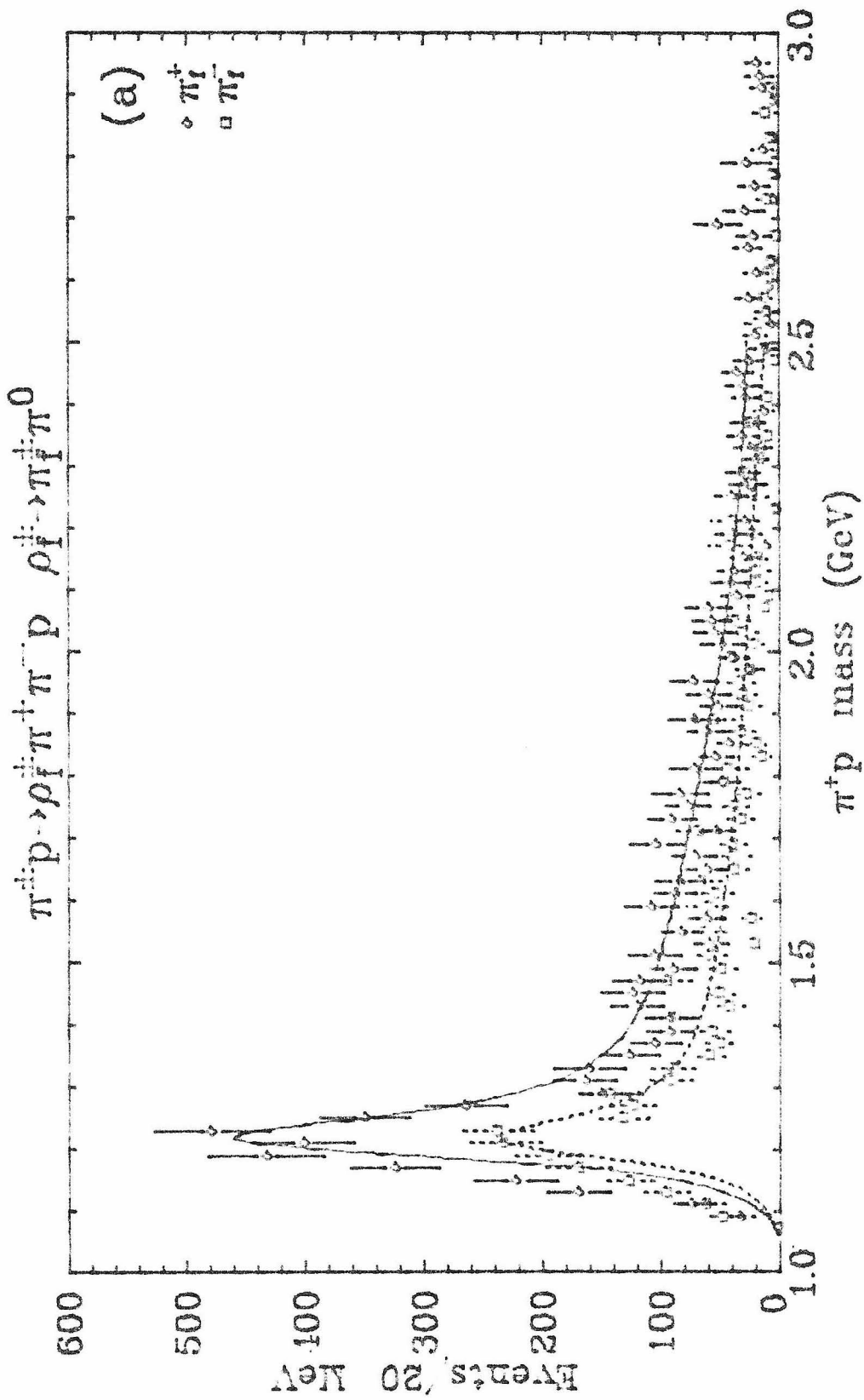


Figure V.11a

The curves are fits to the Δ^{++} .

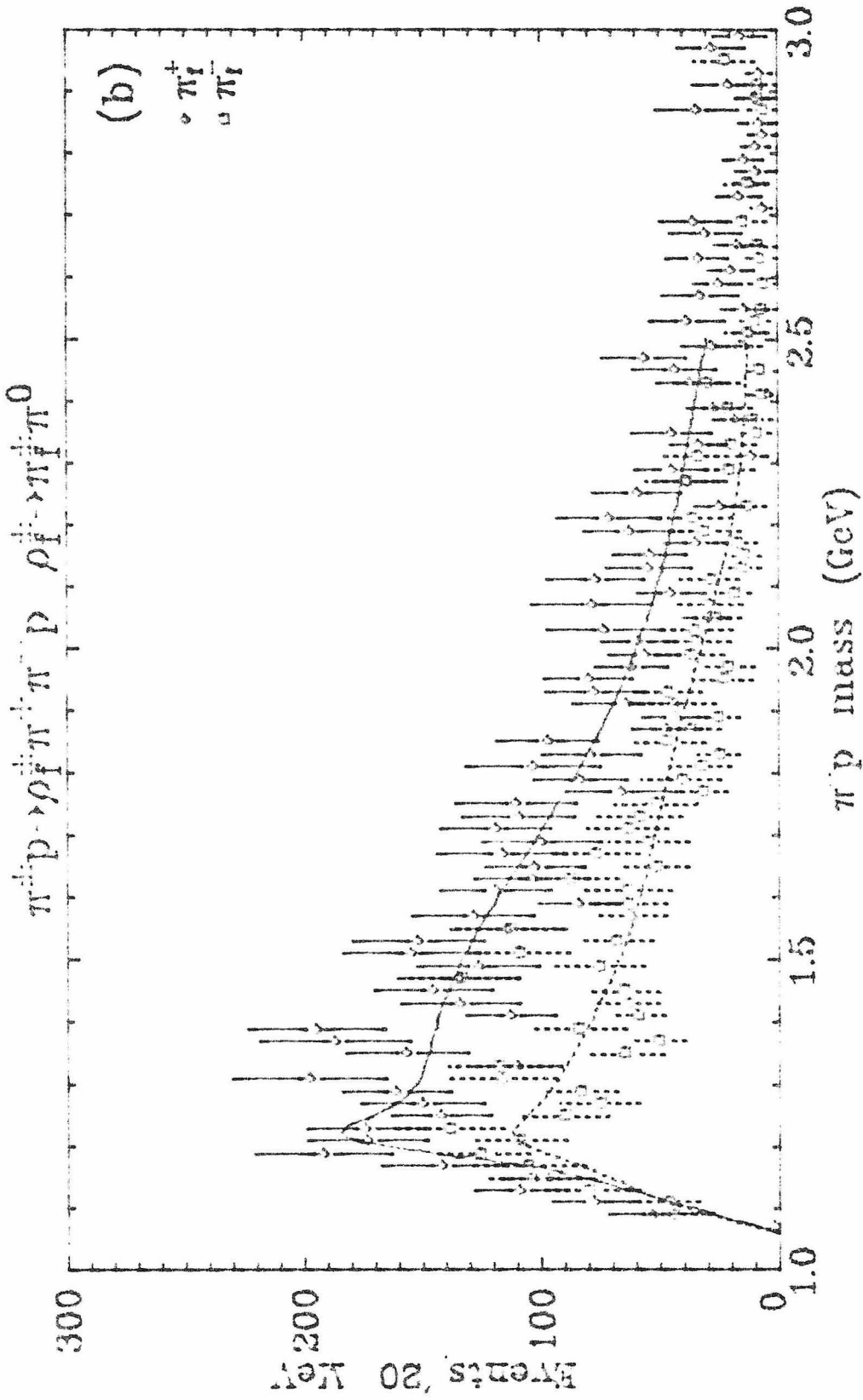


Figure V.11b

The curves are fits to the Δ^0 .

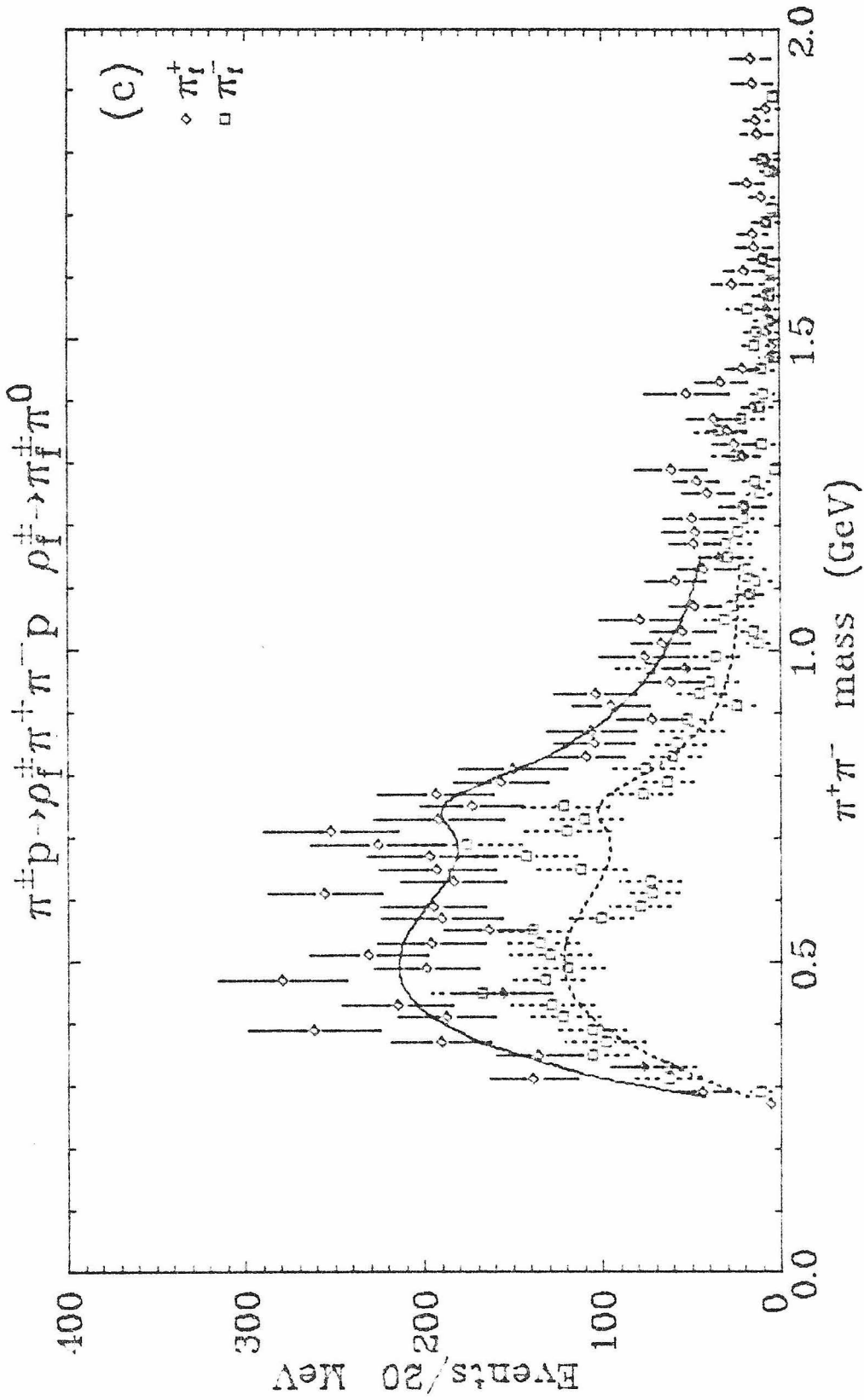


Figure V.11c

The curves are fits to the ρ^0 .

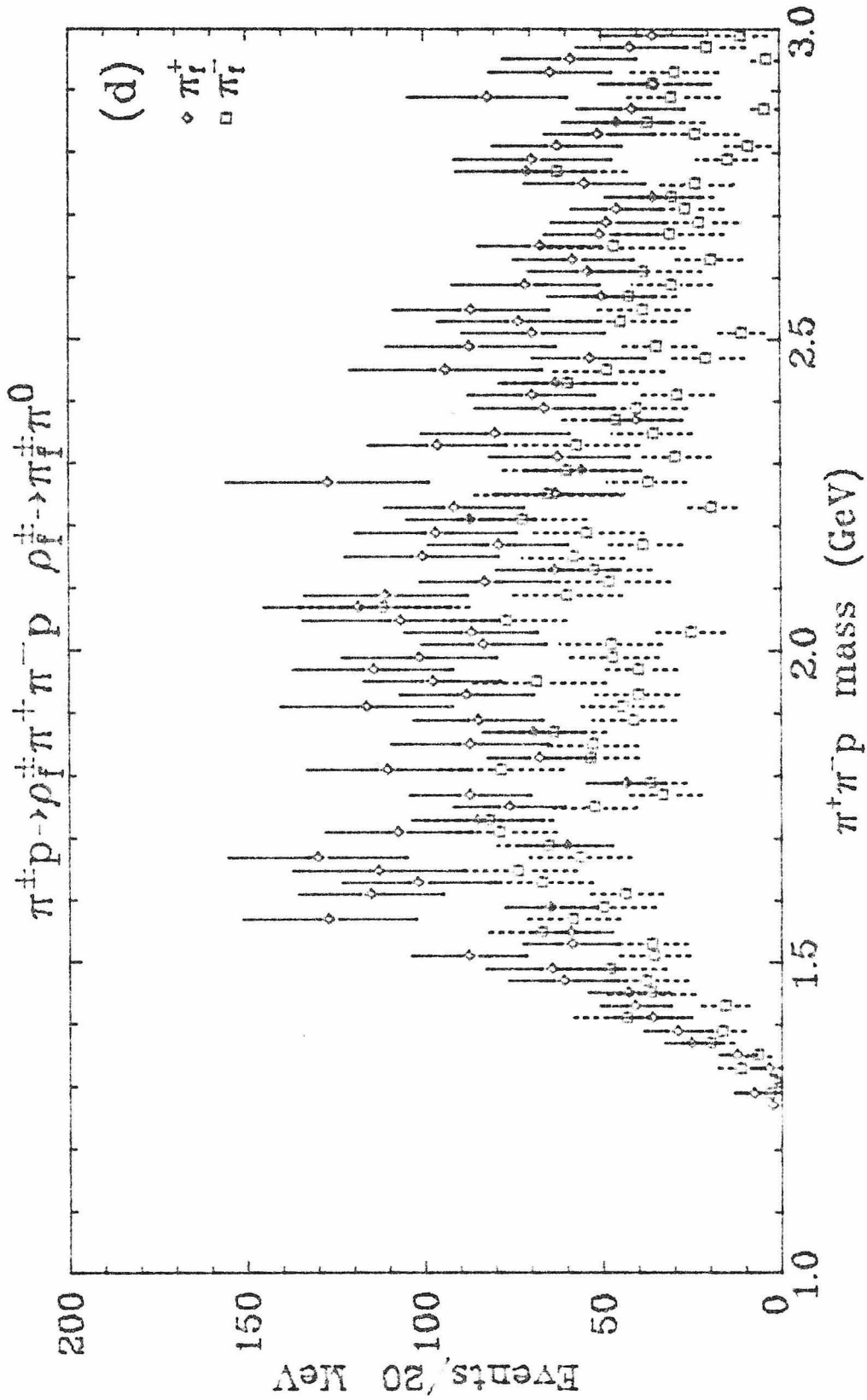


Figure V.11d

Table V.13

Estimated fast meson resonance production for slow system resonance cuts

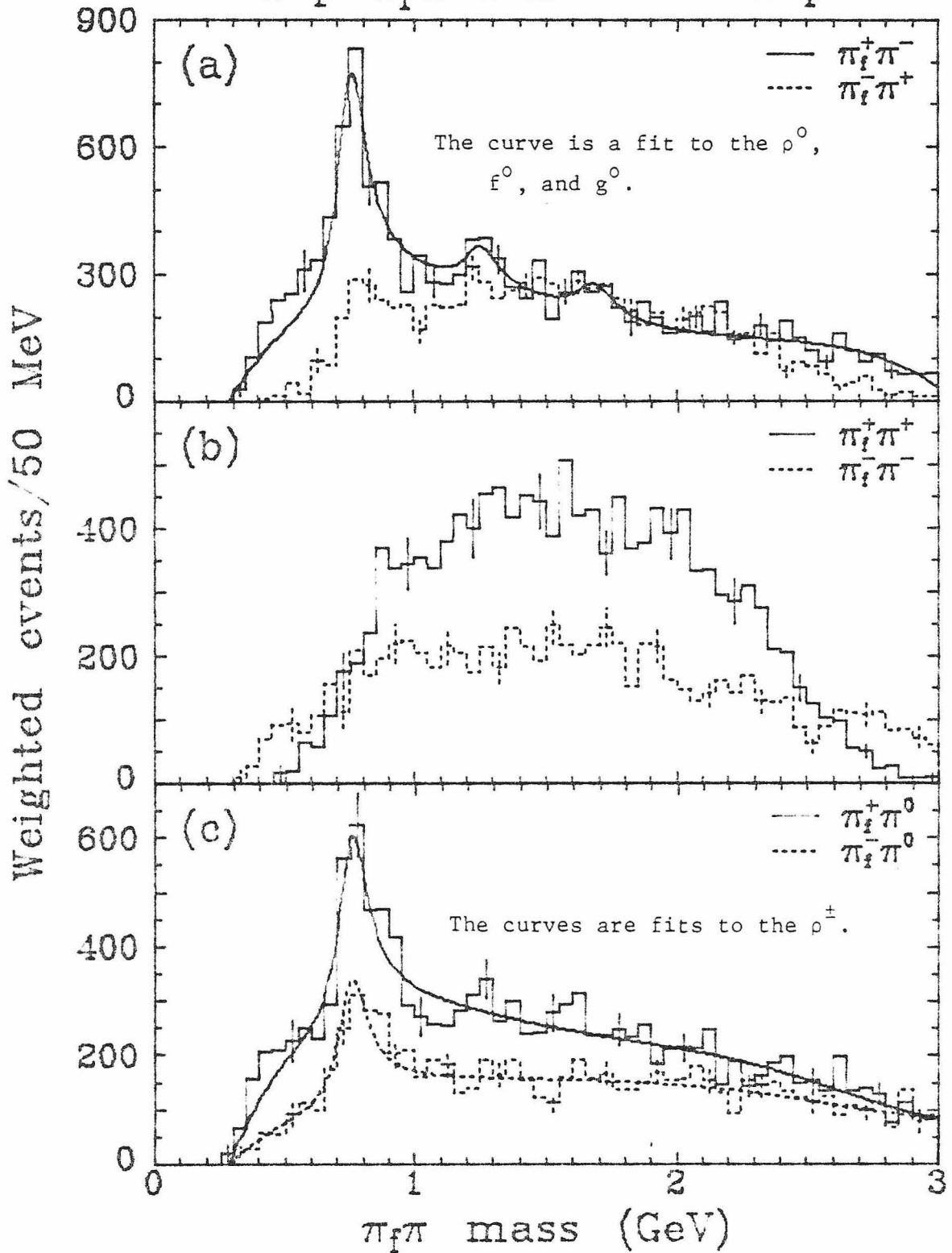
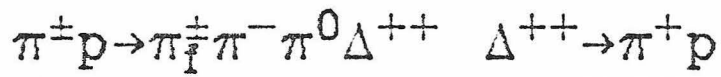
Cut on	Resonance	$\pi_f^+ \pi^+ \pi^- \pi^0 p$		$\pi_f^- \pi^+ \pi^- \pi^0 p$	
		Weight-sum	Fraction of cut events	Weight-sum	Fraction of cut events
$\Delta^{++} \rightarrow \pi^+ p$	$\rho^+ \rightarrow \pi^+ \pi^- f^+$	2737±257	40.7±4.6%	20.2±1.9%	—
$\Delta^{++} \rightarrow \pi^+ p$	$f^0 \rightarrow \pi^+ \pi^- f^+$	557±192	51.0±22.3%	4.1±1.4%	—
$\Delta^{++} \rightarrow \pi^+ p$	$\rho^0 \rightarrow \pi^+ \pi^- f^+$	430±140	47.0±19.1%	3.2±1.0%	—
$\Delta^{++} \rightarrow \pi^+ p$	$\rho^+ \rightarrow \pi^+ \pi^- f^0$	1762±244	58.7±10.5%	13.0±1.8%	1158±154
$\rho^0 \rightarrow \pi^+ \pi^-$	$\rho^+ \rightarrow \pi^+ \pi^- f^0$	1243±173	41.4±7.5%	19.0±2.7%	619±129
$\rho^+ \rightarrow \pi^+ \pi^-$	$\rho^0 \rightarrow \pi^+ \pi^- f^+$	2406±214	35.8±3.9%	34.8±3.2%	—
$\rho^+ \rightarrow \pi^+ \pi^-$	$f^0 \rightarrow \pi^+ \pi^- f^+$	333±139	30.5±15.2%	4.8±2.0%	—
$\rho^+ \rightarrow \pi^+ \pi^-$	$\rho^0 \rightarrow \pi^+ \pi^- f^+$	133±95	14.5±11.0%	1.9±1.4%	—
$\rho^- \rightarrow \pi^- \pi^0$	$\rho^0 \rightarrow \pi^- \pi^+ f^-$	—	—	—	1054±140
$\Delta^{++} \rightarrow \pi^+ p$	$A_2^0 \rightarrow \pi^+ \pi^- \pi^0 f^+$	≤69±110	—	≤0.5±0.8%	—
$\Delta^{++} \rightarrow \pi^+ p$	$A_3^0 \rightarrow \pi^+ \pi^- \pi^0 f^+$	298±204	—	2.2±1.5%	—
$f^0 \rightarrow \pi^- \pi^0$	$A_2^0 \rightarrow \pi^- \pi^+ \pi^0 f^-$	303±113	—	4.4±1.6%	—
$\rho^- \rightarrow \pi^- \pi^0$	$A_3^0 \rightarrow \pi^- \pi^+ \pi^0 f^-$	508±200	—	7.4±2.9%	—
					22.2±3.0%

— π^+ (data & fits)
----- π^- (data & fits)
 $\pi^\pm p \rightarrow \pi_f^\pm \pi^- \pi^0 \Delta^{++} \quad \Delta^{++} \rightarrow \pi^+ p$
 $\pi^\pm p \rightarrow \pi_f^\pm \pi^+ \pi^+ \Delta^- \quad \Delta^- \rightarrow \pi^- n$
Prob(χ_{fit}^2) $\geq 5\%$
 $-t_{\pi\pi(f)} < 0.6 \text{ GeV}^2/c^2$
($\pi\pi\pi N$) mass $< 3.7 \text{ GeV}$

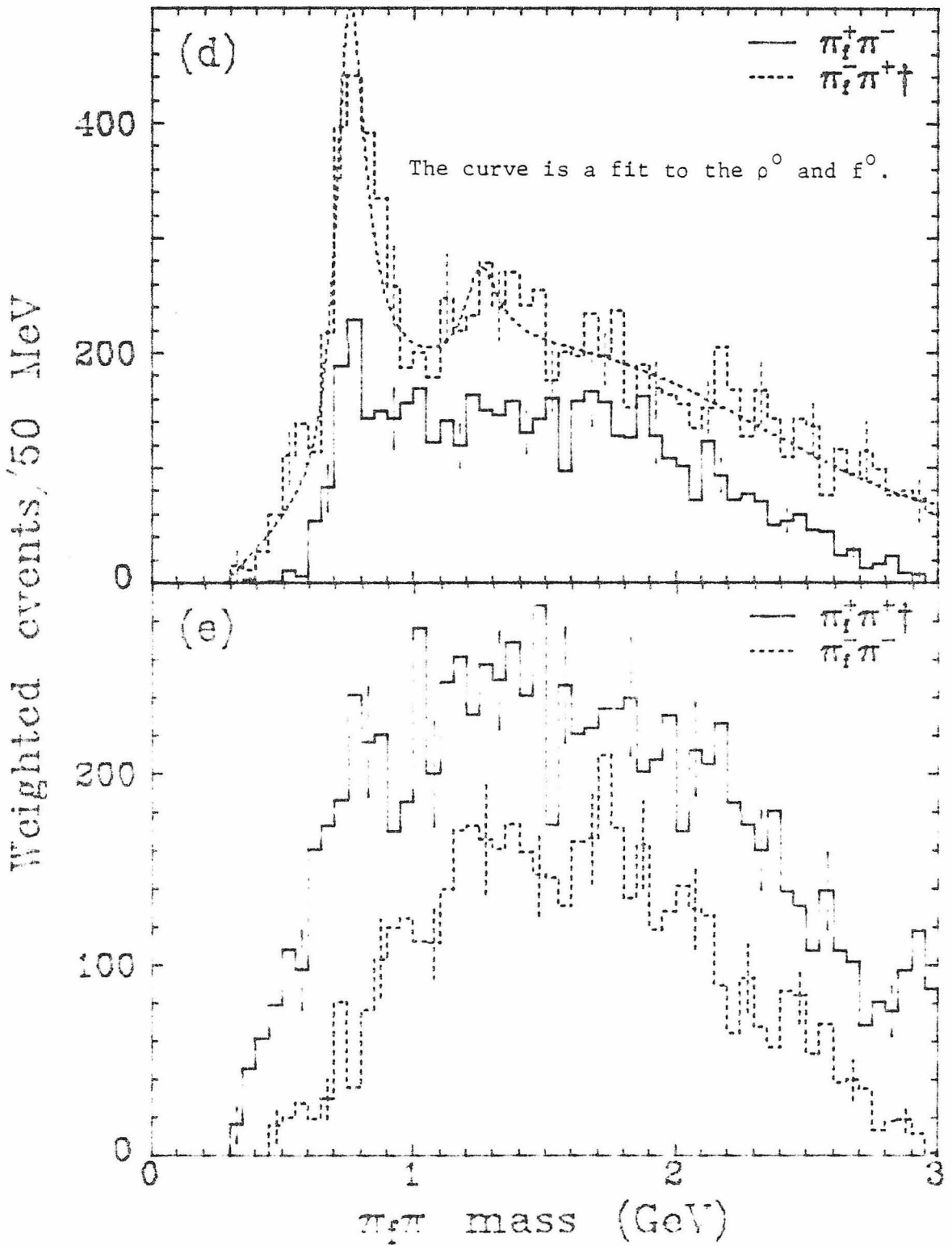
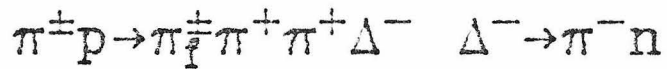
$\Delta^{++} \rightarrow \pi^+ p$ definition:
 $\pi^+ p$ mass $< 1.36 \text{ GeV}$
 $\Delta^- \rightarrow \pi^- n$ definition:
 $\pi^- n$ mass $< 1.36 \text{ GeV}$

Figures V.12a-j

Invariant mass distributions of masses with the fast pion and one or two of the remaining pions. The events have been selected by the above cuts to be in the Δ^{++} peak (π^0 channel) or the Δ^- peak (n channel).

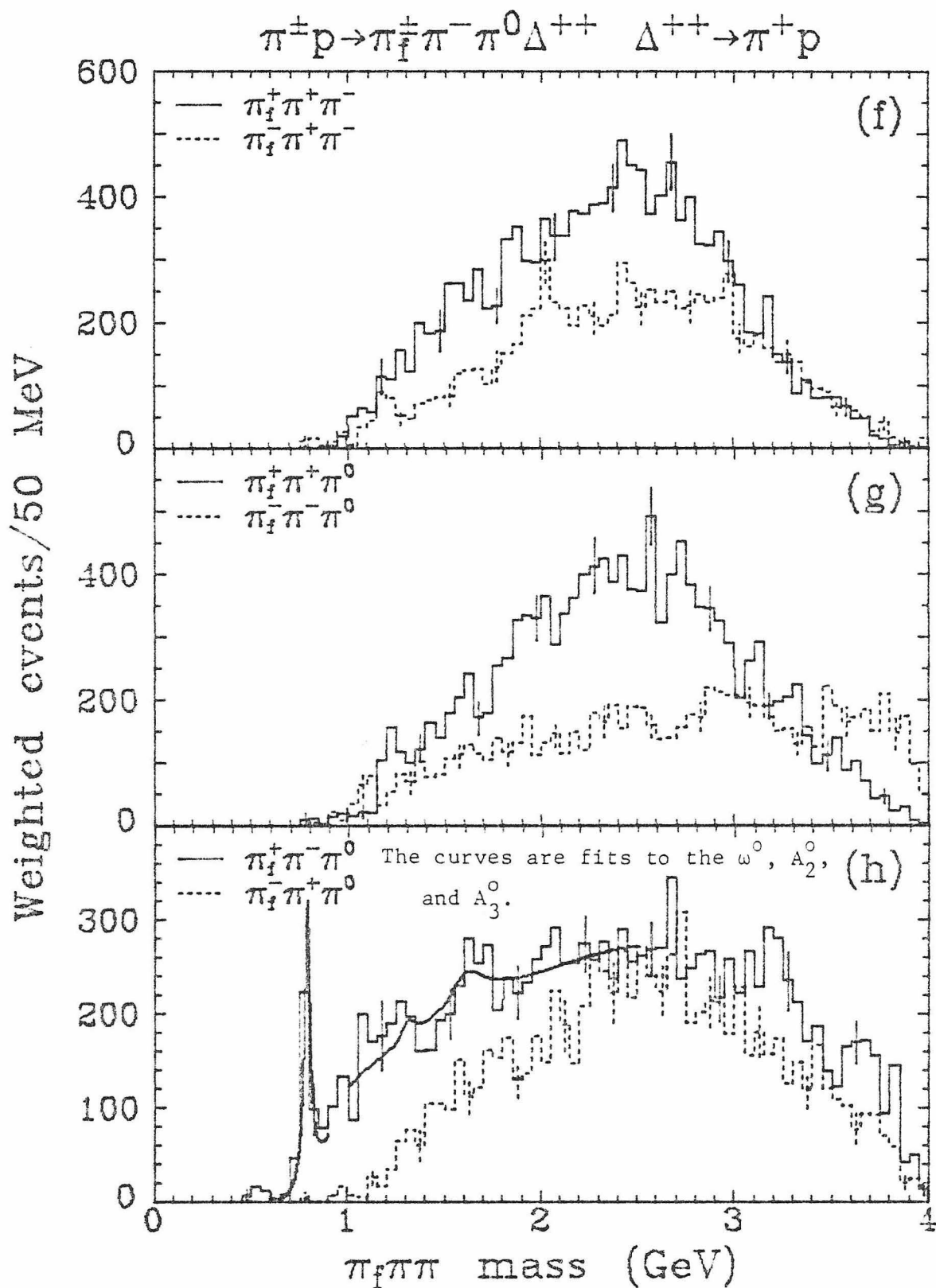


Figures V.12a-c



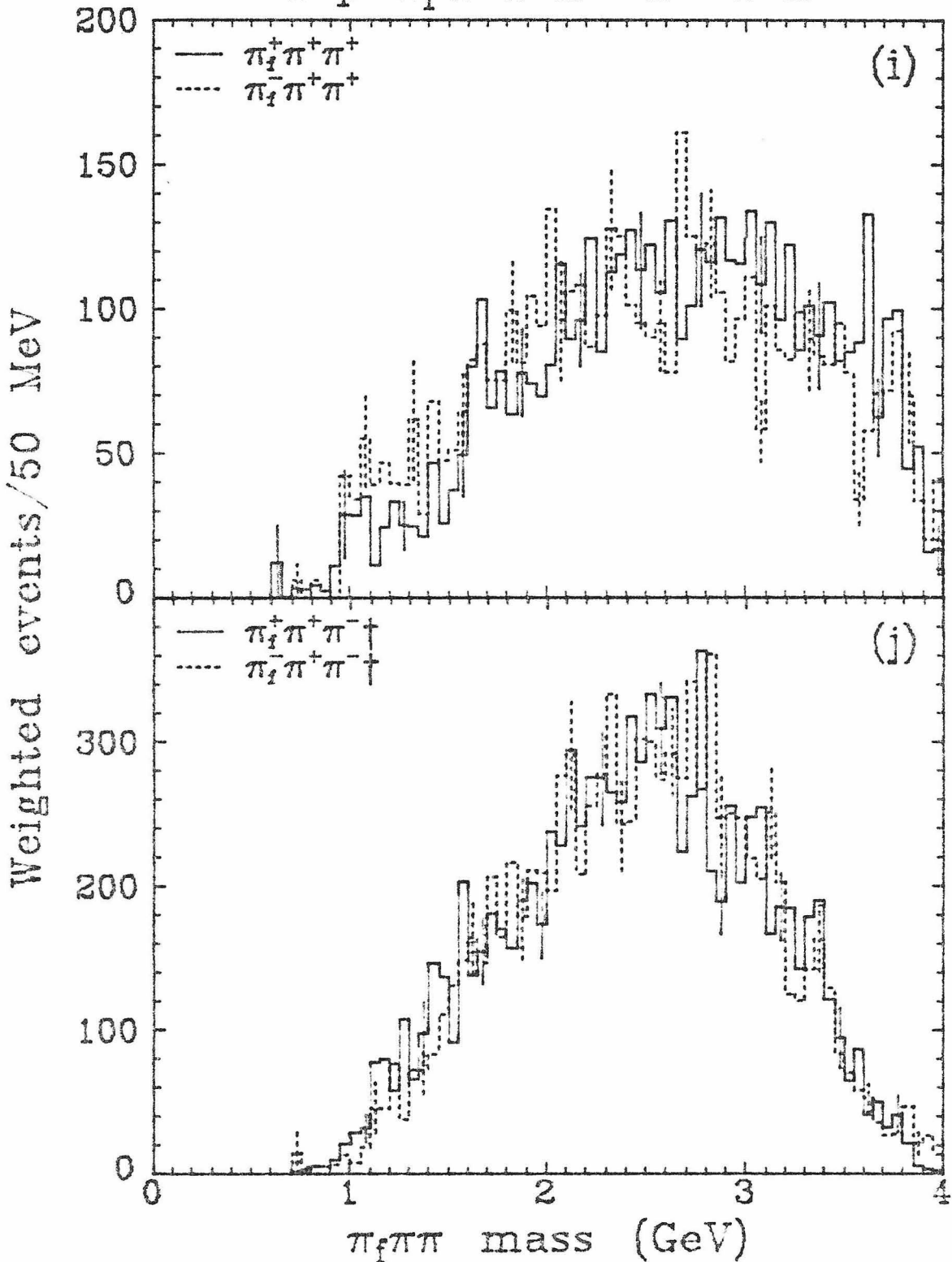
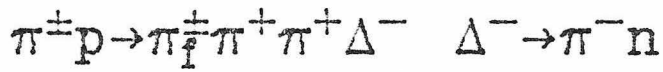
(† each event appears twice)

Figures V.12d-e



The curves are fits to the ω^0 , A_2^0 , and A_3^0 .

Figures V.12f-h



(† each event appears twice)

Figures V.12i-j

— π^+ (data & fits)

----- π^- (data & fits)

$\pi^\pm p \rightarrow \pi_f^\pm \rho^0 \pi^0 p$ $\rho^0 \rightarrow \pi^+ \pi^-$

$\pi^\pm p \rightarrow \pi_f^\pm \rho^0 \pi^+ n$ $\rho^0 \rightarrow \pi^+ \pi^-$

$\text{Prob}(\chi_{\text{fit}}^2) \geq 5\%$

$-t_{\pi\pi(f)} < 0.6 \text{ GeV}^2/c^2$

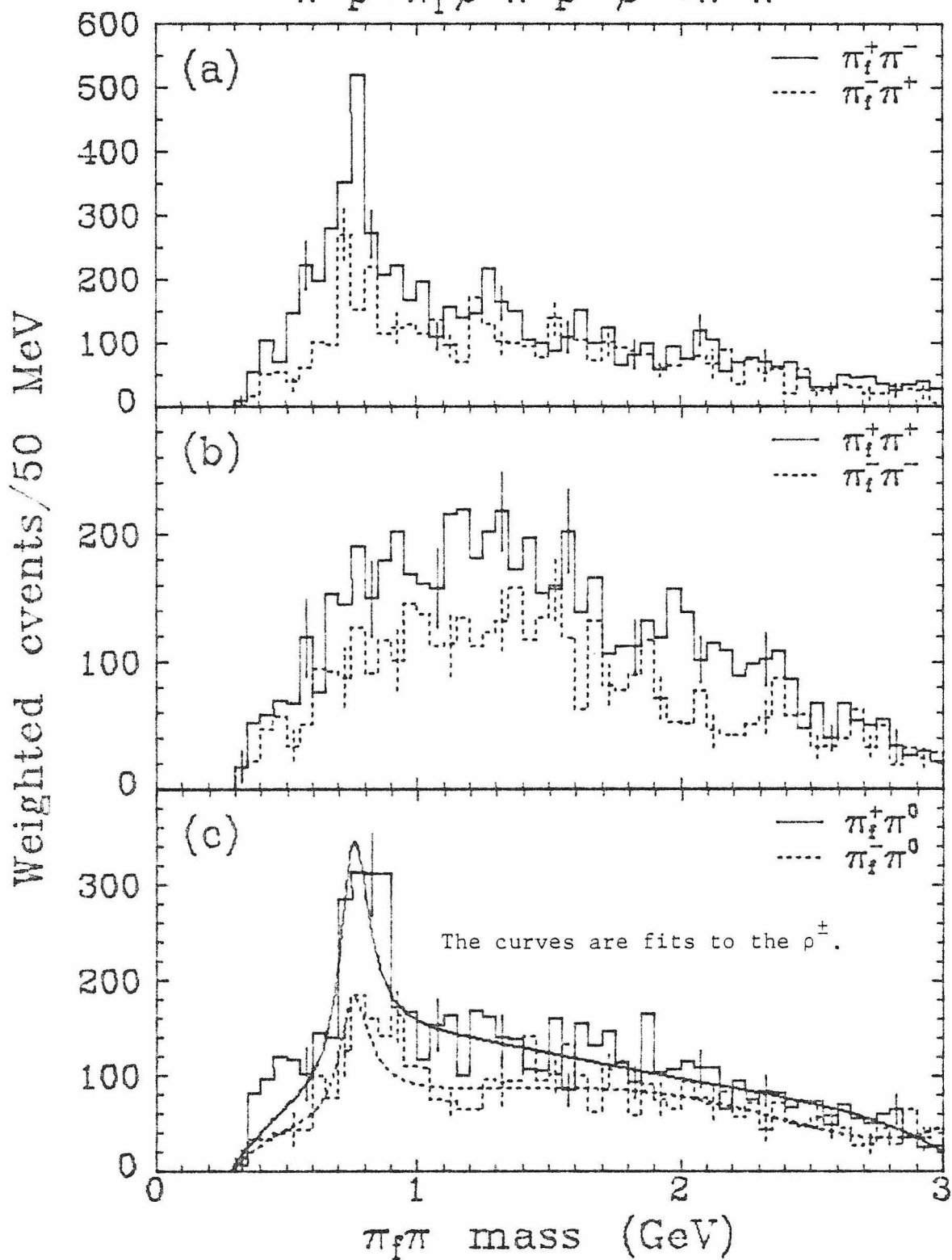
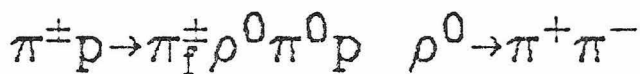
$(\pi\pi\pi N)$ mass $< 3.7 \text{ GeV}$

$\rho^0 \rightarrow \pi^+ \pi^-$ definition:

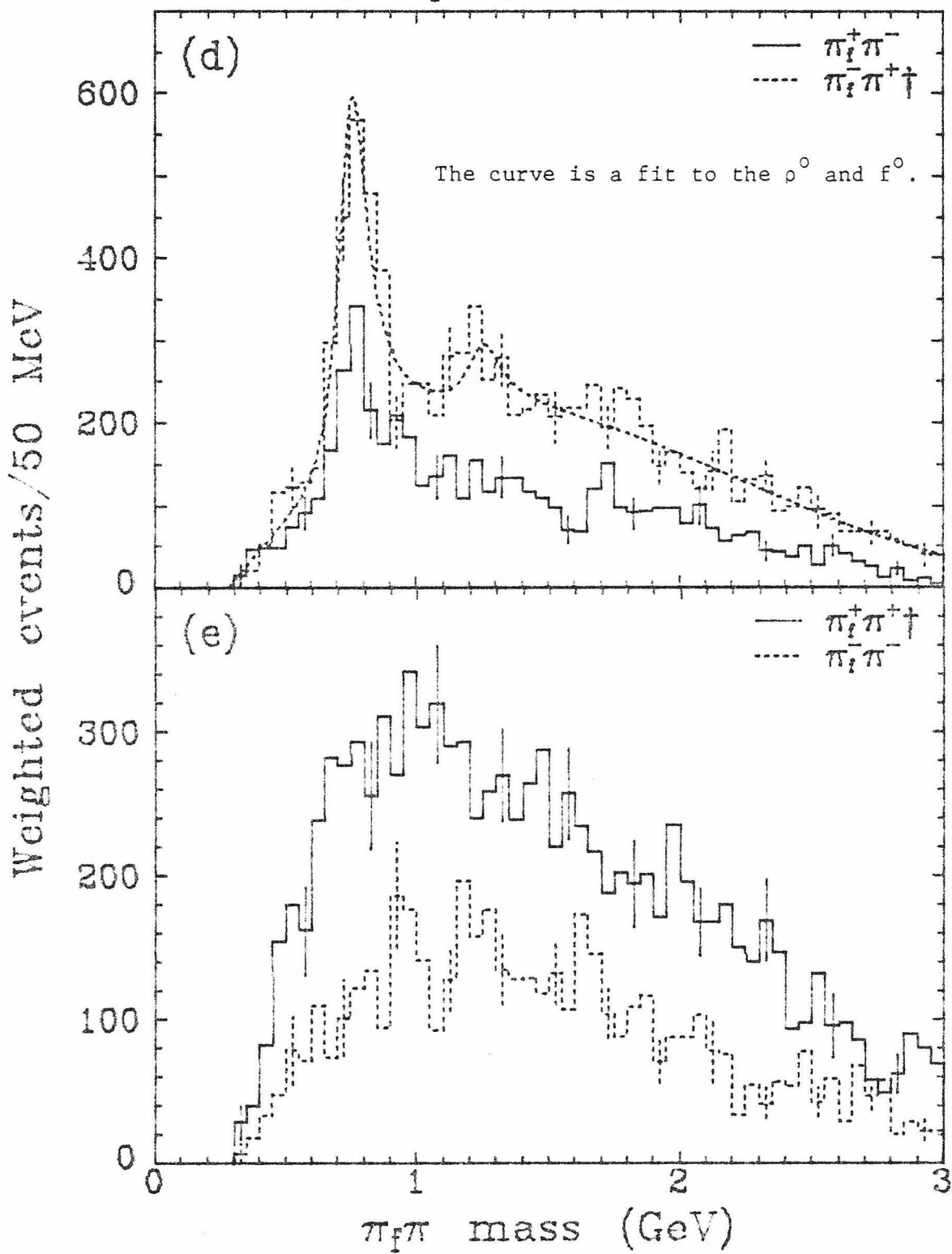
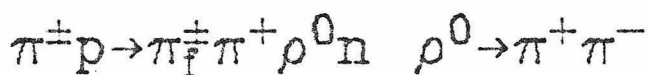
$0.64 \leq \pi^+ \pi^- \text{ mass} < 0.84 \text{ GeV}$

Figures V.13a-2

Invariant mass distributions of masses with the fast pion and one, two, or all three of the remaining pions for events in the slow system ρ^0 peak (see above).

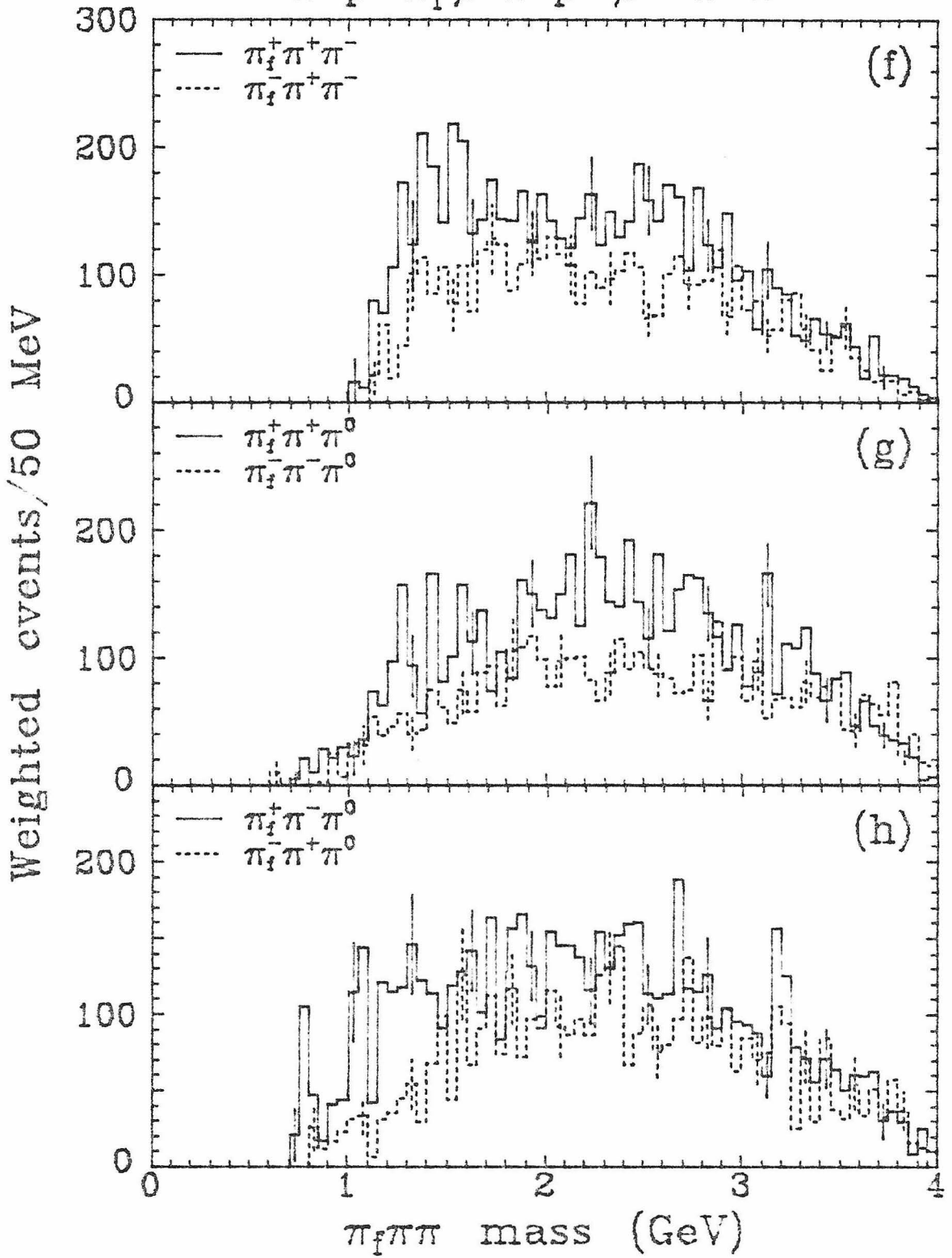


Figures V.13a-c

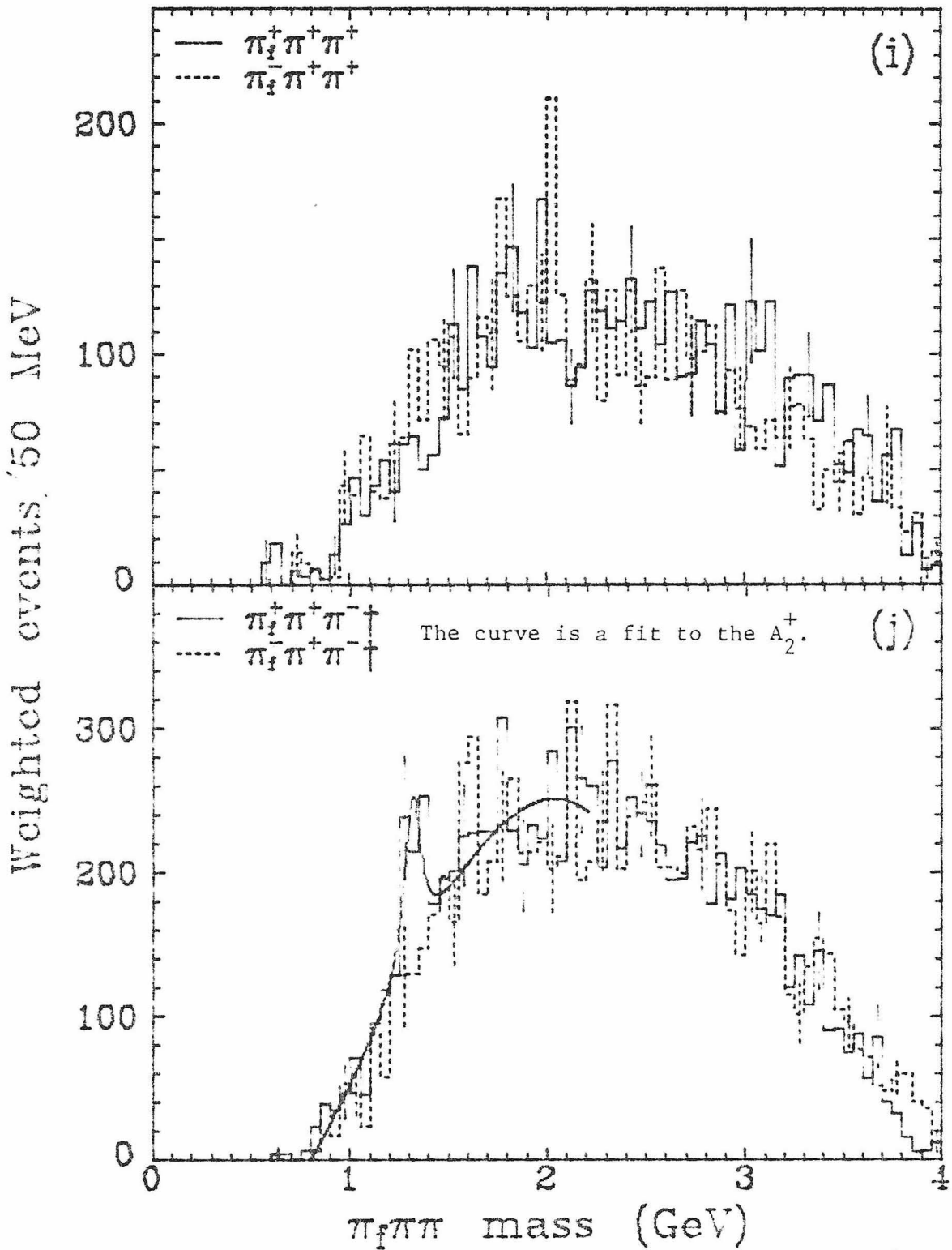
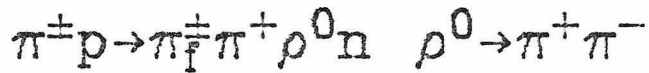


(† each event appears twice)

Figures V.13d-e

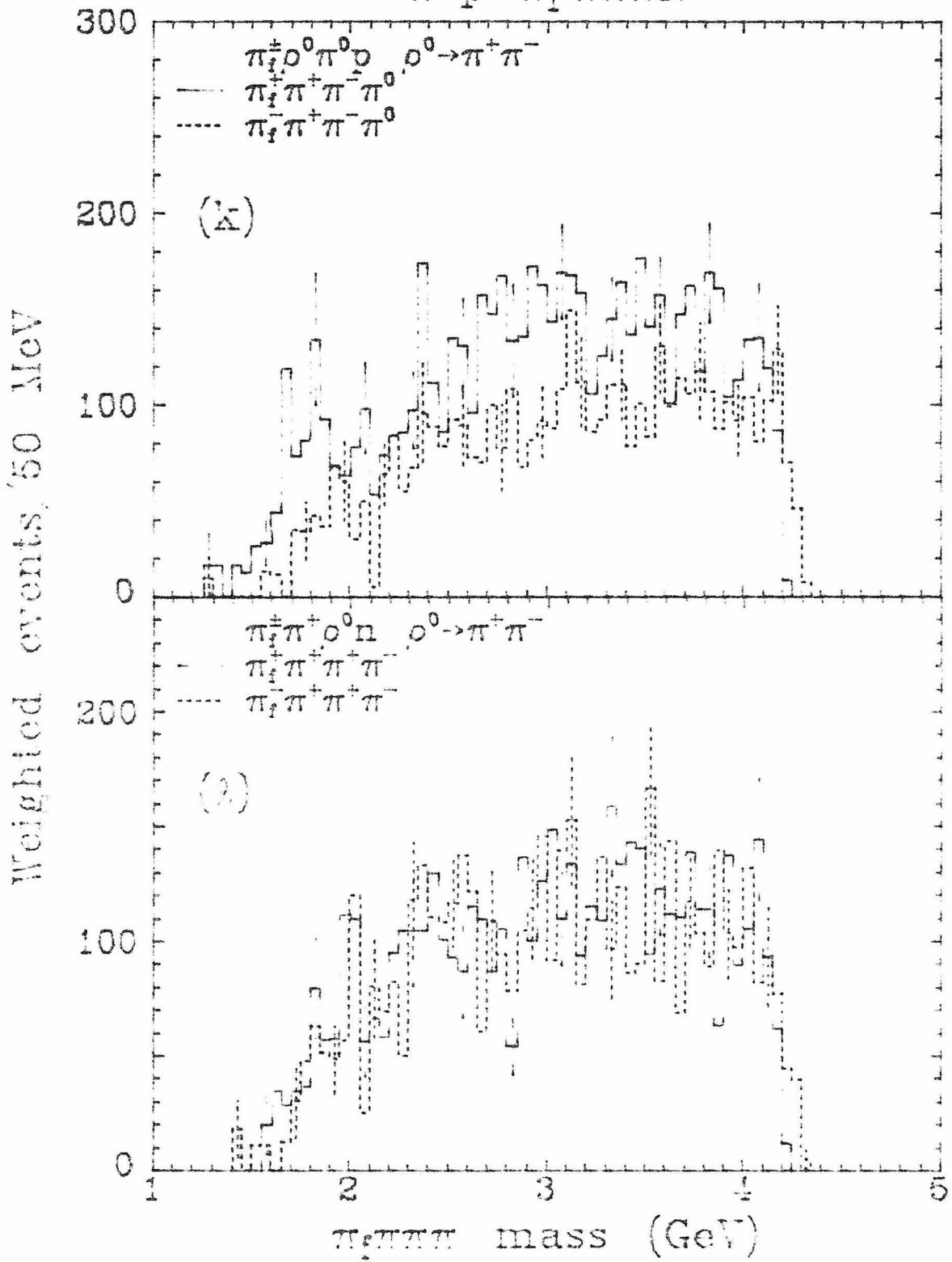


Figures V.13f-h



(† each event appears twice)

Figures V.13i-j



Figures V.13k-2

— π^+ (data & fits)

----- π^- (data & fits)

$$\pi^\pm p \rightarrow \pi_i^\pm \rho^\pm \pi^\mp p \quad \rho^+ \rightarrow \pi^+ \pi^0$$

$$\pi^\pm p \rightarrow \pi_i^\pm \rho^\mp \pi^\mp p \quad \rho^- \rightarrow \pi^- \pi^0$$

$$\text{Prob}(\chi_{\text{fit}}^2) \geq 5\%$$

$$-t_{\pi\pi(i)} < 0.6 \text{ GeV}^2/c^2$$

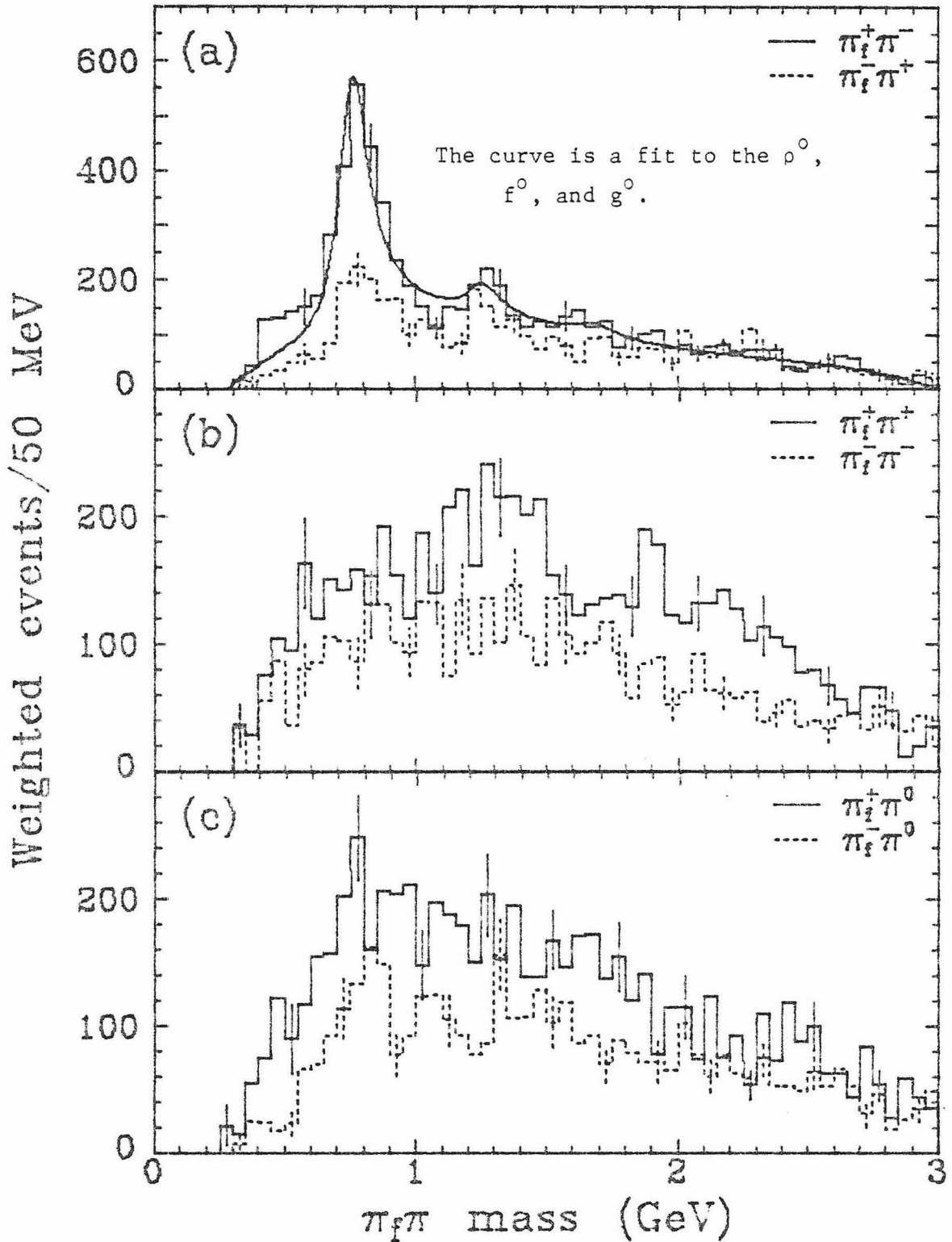
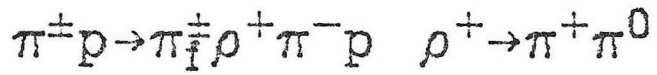
$$(\pi^+ \pi^- \pi^0 p) \text{ mass} < 3.7 \text{ GeV}$$

$\rho^\pm \rightarrow \pi^\pm \pi^0$ definition:

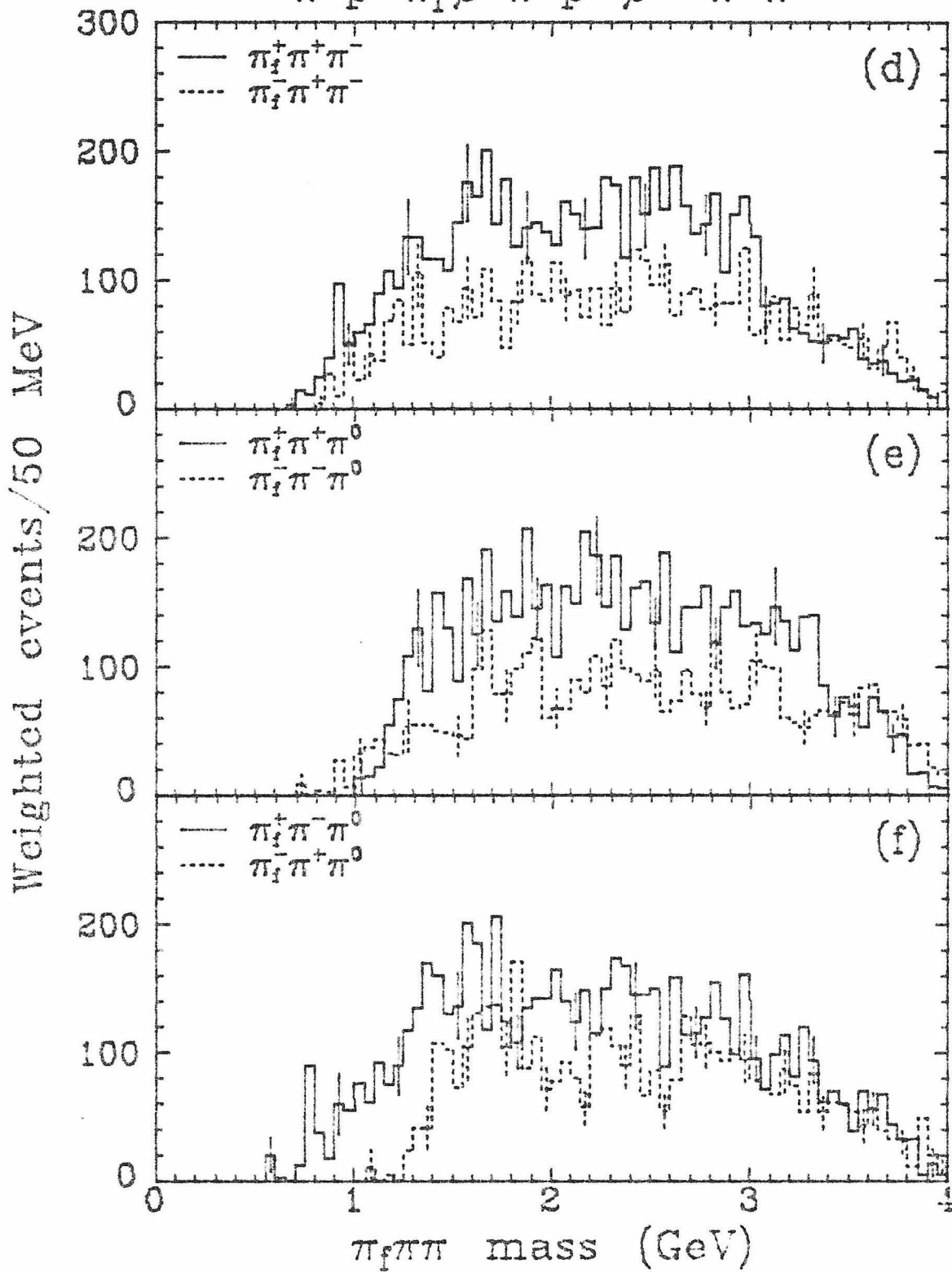
$$0.64 \leq \pi^\pm \pi^0 \text{ mass} < 0.84 \text{ GeV}$$

Figures V.14a-n

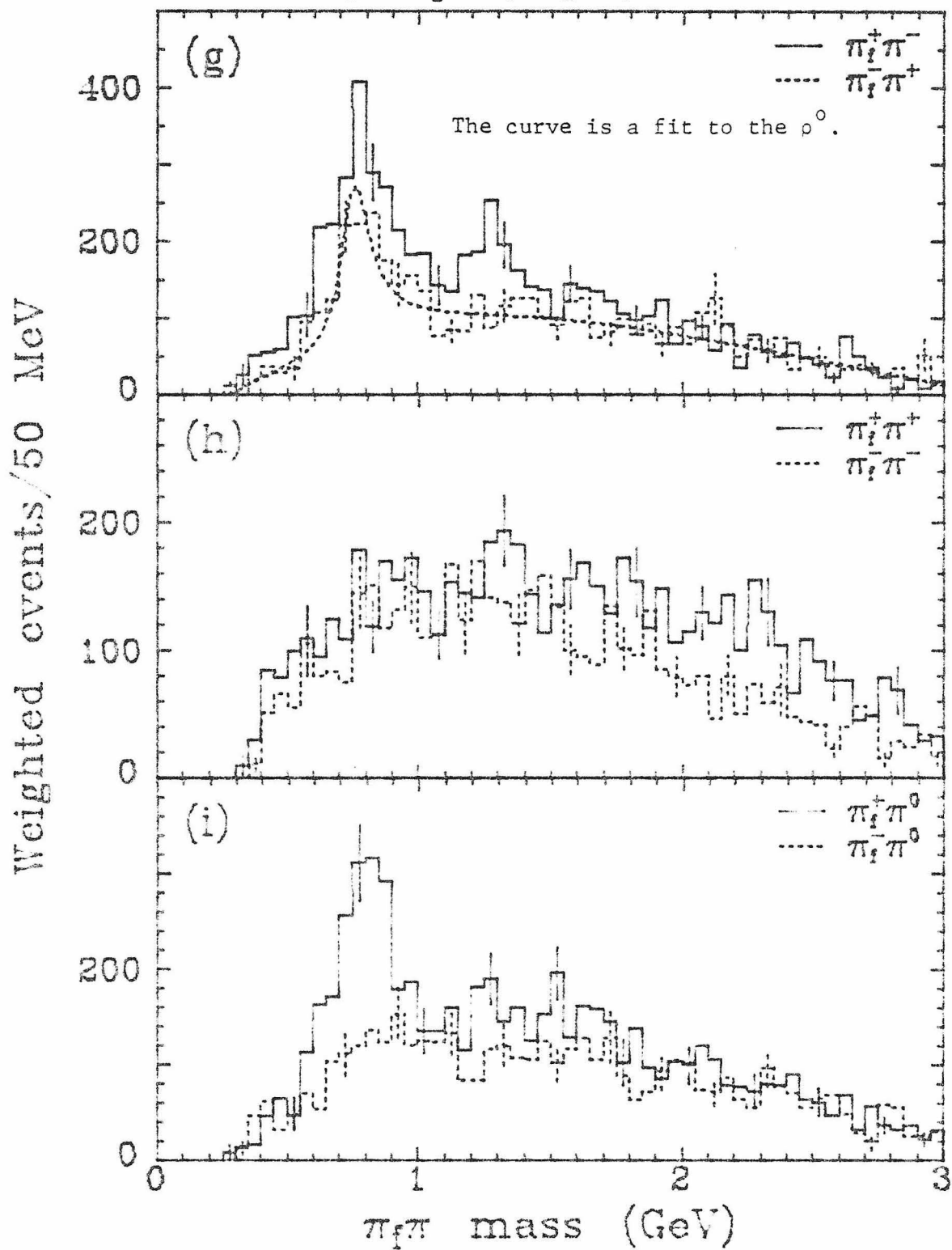
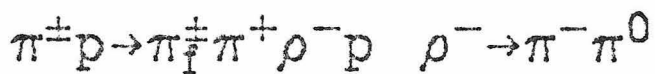
Invariant mass distributions of masses with the fast pion and one, two, or all three of the remaining pions for events within the slow system ρ^\pm peaks (see above).



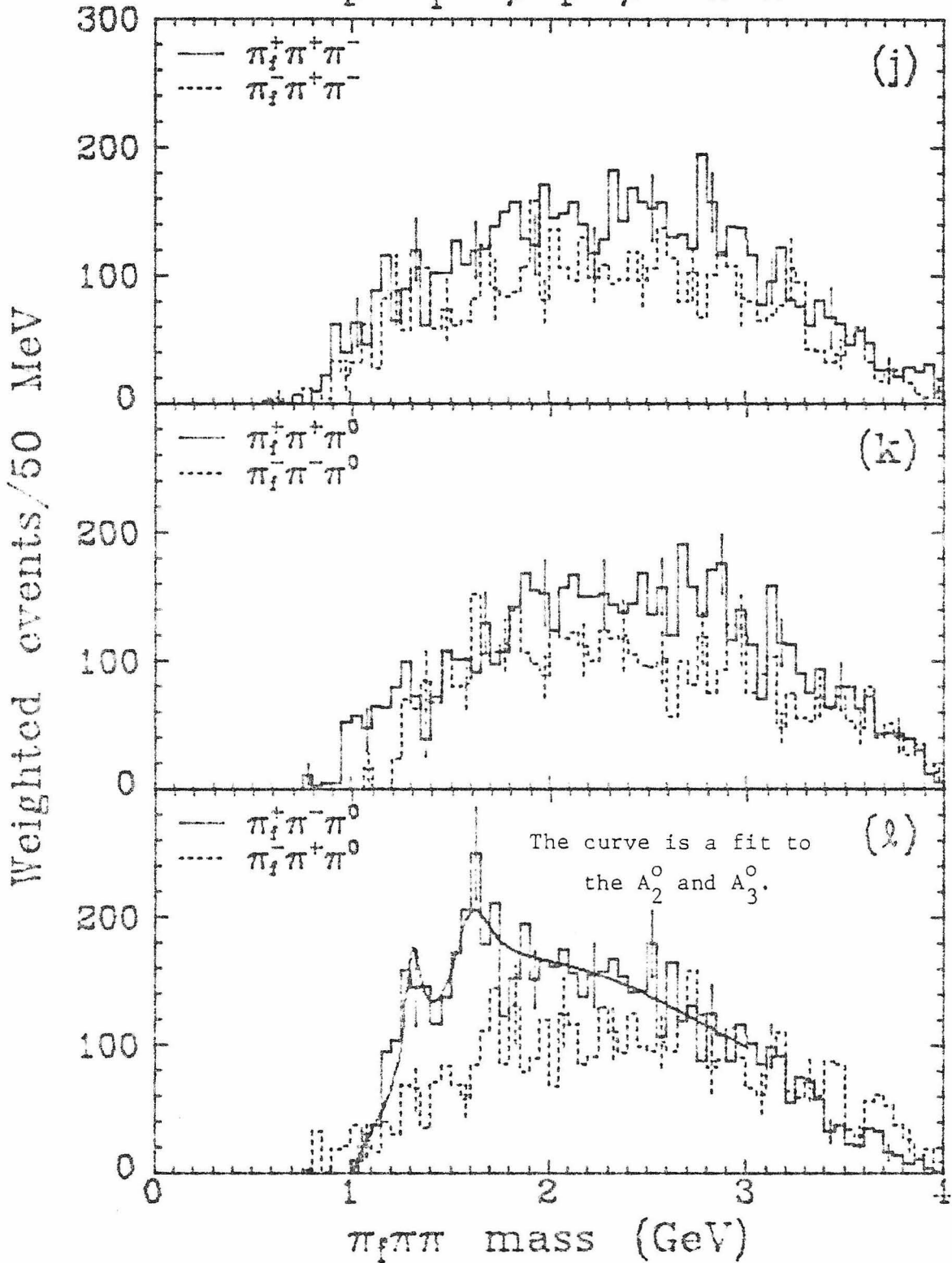
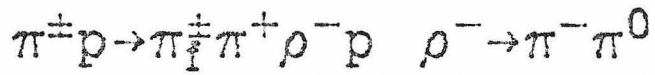
Figures V.14a-c



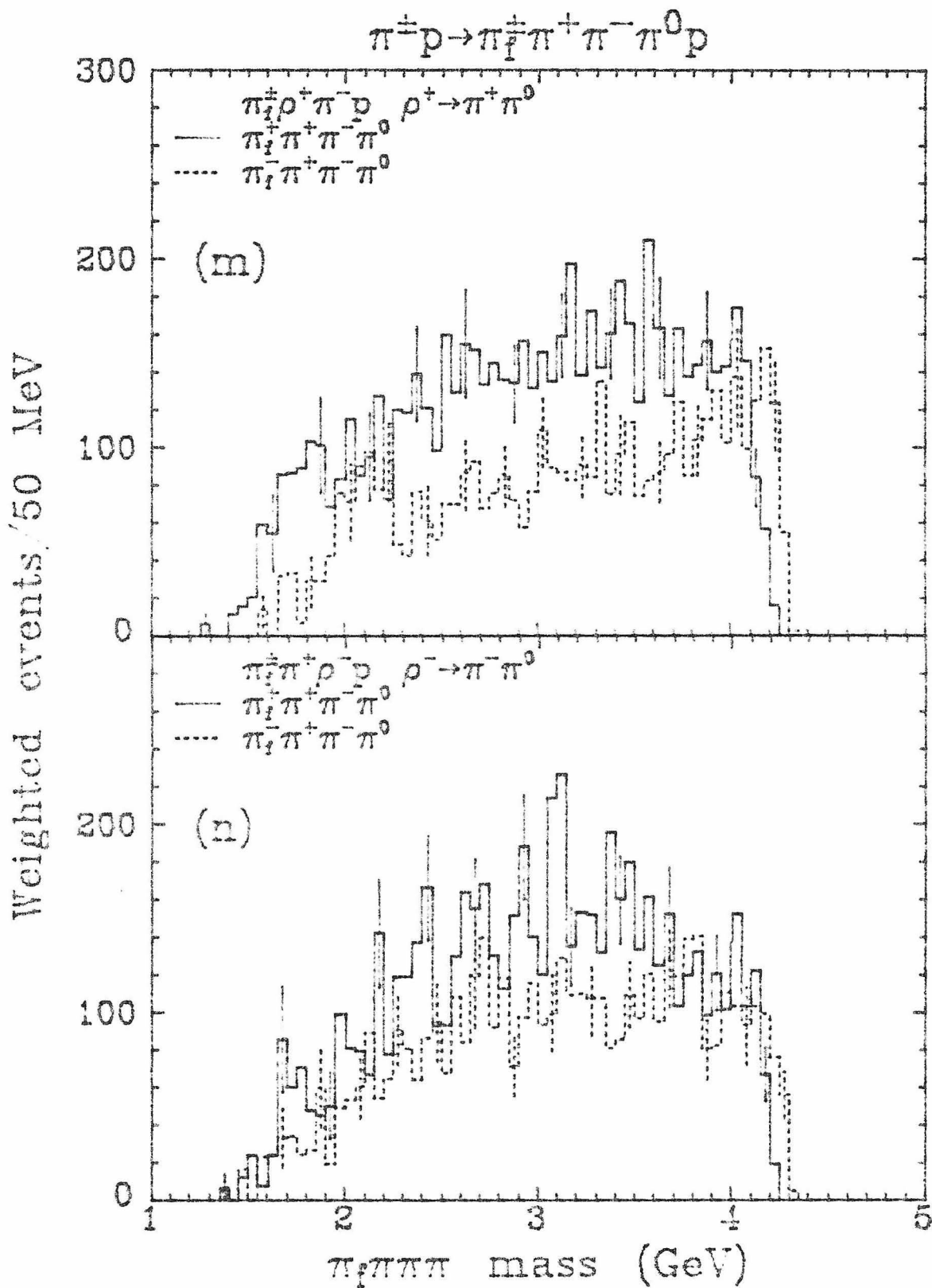
Figures V.14d-f



Figures V.14g-i



Figures V.14h-2



Figures V.14m-n

7. Double Slow Resonance Production and Sequential Decays

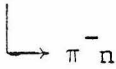
Finally we present the slow invariant mass distributions cut on the requirement of a resonance in a subgroup of the particles in the invariant mass (resonance decays into another resonance) or in the particles not in the invariant mass (double slow resonance production). Note that these estimates are not plagued by backgrounds from fast meson resonance production as they involve only resonances within the slow system. The mass distributions cut on the Δ^{++} and the Δ^- are given in Figs. V.15a-d and V.16a-b respectively. Figs. V.17a-d and V.18a-d show the mass distributions for the ρ^0 cut for the π^0 channel and the n channel respectively. The mass distributions for the ρ^\pm cuts are in Figs. V.19a-d and V.20a-d. The estimates for double resonance production are given in Table V.14. The most prominent process observed is:



only a small fraction of which can be explained by the production of a fast A meson and a slow Δ^{++} (see previous section).

Table V.15 lists the estimates for the production of slow resonances followed by their decay into another resonance (cascade decay). As discussed in section 5, the N(1700) observed in the $\pi^+ \pi^+ \pi^- n$ mass is consistent with the cascade decay for the entire observed cross

section:

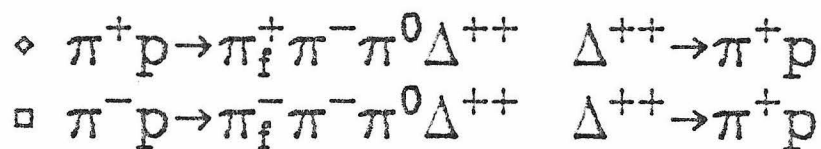
$$N^+(1700) \rightarrow \pi^+ \pi^+ \Delta^- \quad (12)$$


The $N(1790)$ also appears in the $\pi^+ \pi^- \pi^0 p$ mass distribution for the Δ^{++} cut. However, from studies of this resonance for the $\pi^{\pm} \omega^0 p$ events, it was found that the $\pi^+ p$ mass peaks at about 1150 MeV and satisfies the Δ^{++} cut for almost all the events in the ω^0 peak even though the $\pi^+ p$ system does not form a Δ^{++} .

Table V.14

Estimated slow system double resonance production

Cut Resonances	$\pi_f^+ \pi^+ \pi^- \pi^0 p$		$\pi_f^- \pi^+ \pi^- \pi^0 p$	
	Weight-sum	σ (μb)	Resonance fraction	Fraction of cut events
Δ^{++}	2184±357	27.5±4.7	55.5±11.8%	16.2±2.7%
ρ^0	699±206	8.8±2.6	62.0±27.8%	10.7±3.2%
ρ^+	556±167	7.0±2.1	16.1±5.1%	8.0±2.4%
ρ^+ N(1470)	~ 0	—	—	—
ρ^-	3041±238	38.3±3.5	23.8±2.1%	47.3±3.9%
<hr/>				
ρ^0	723±269	9.4±3.5	74.5±38.6%	13.9±5.2%
ρ^0 N(1470)	1000±469	13.0±6.1	69.5±49.8%	19.2±9.0%
<hr/>				
			Resonance fraction	Fraction of cut events
			Weight-sum	σ (μb)
			1482±268	21.6±4.1
			501±164	7.3±2.4
			691±159	8.7±2.1
			246±254	≤3.1±3.2
			1427±192	20.8±3.0
				46.1±11.3%
				12.1±4.1%
				30.2±8.0%
				≤5.6±5.8%
				30.1±4.2%
				17.2±3.1%
				11.4±3.8%
				15.8±3.7%
				~ 0
				—
				—



— π^+ fits

----- π^- fits

$$\text{Prob}(\chi_{\text{fit}}^2) \geq 5\%$$

$$-t_{\pi\pi(f)} < 0.6 \text{ GeV}^2/c^2$$
$$(\pi^+ \pi^- \pi^0 p) \text{ mass} < 3.7 \text{ GeV}$$

$\Delta^{++} \rightarrow \pi^+ p$ definition:
 $\pi^+ p$ mass < 1.36 GeV

Figures V.15a-d

Invariant mass distributions for the slow particles of the π^0 channel for events within the Δ^{++} peak (see above).

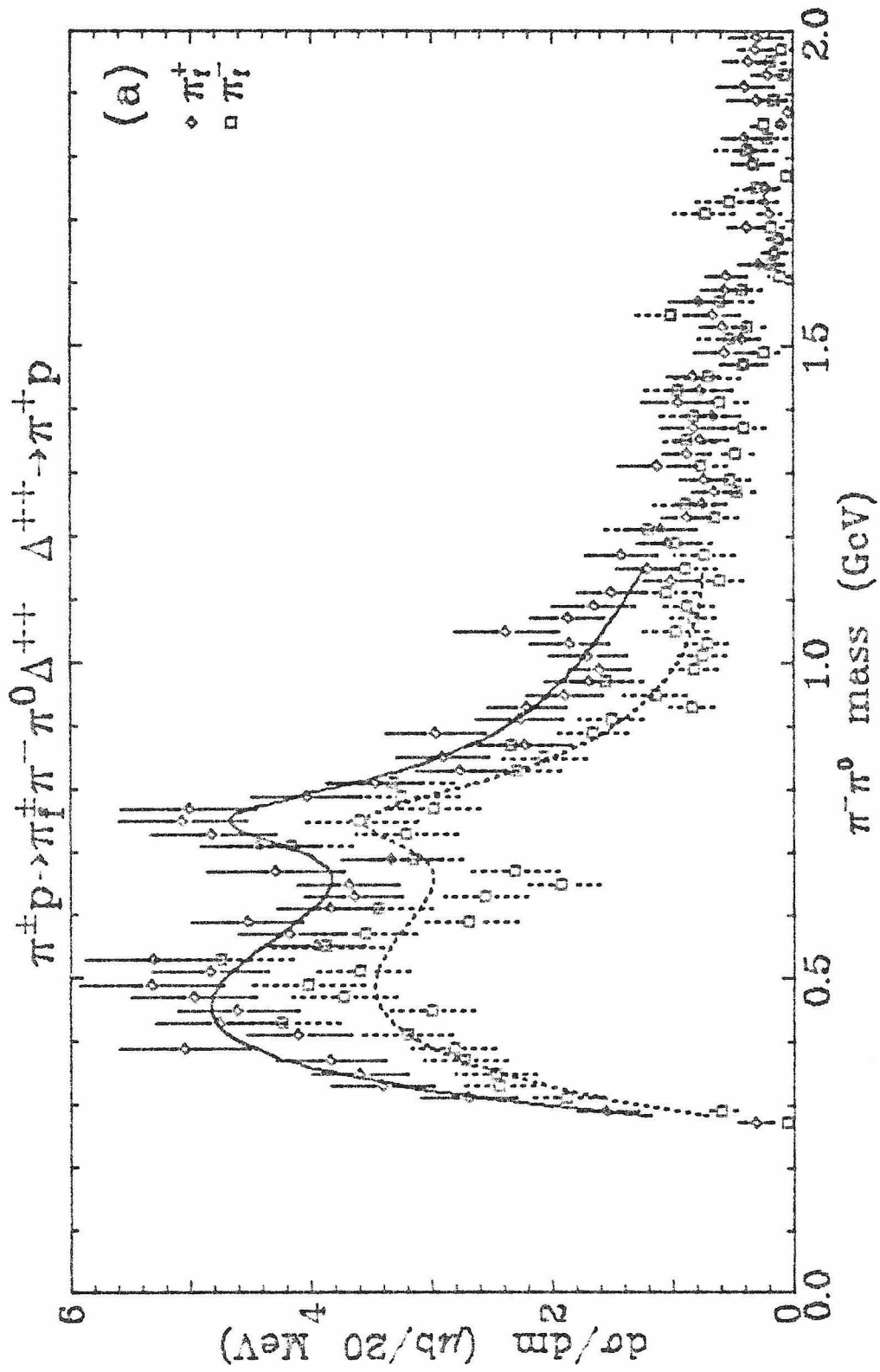


Figure V.15a

The curves are fits to the ρ^- .

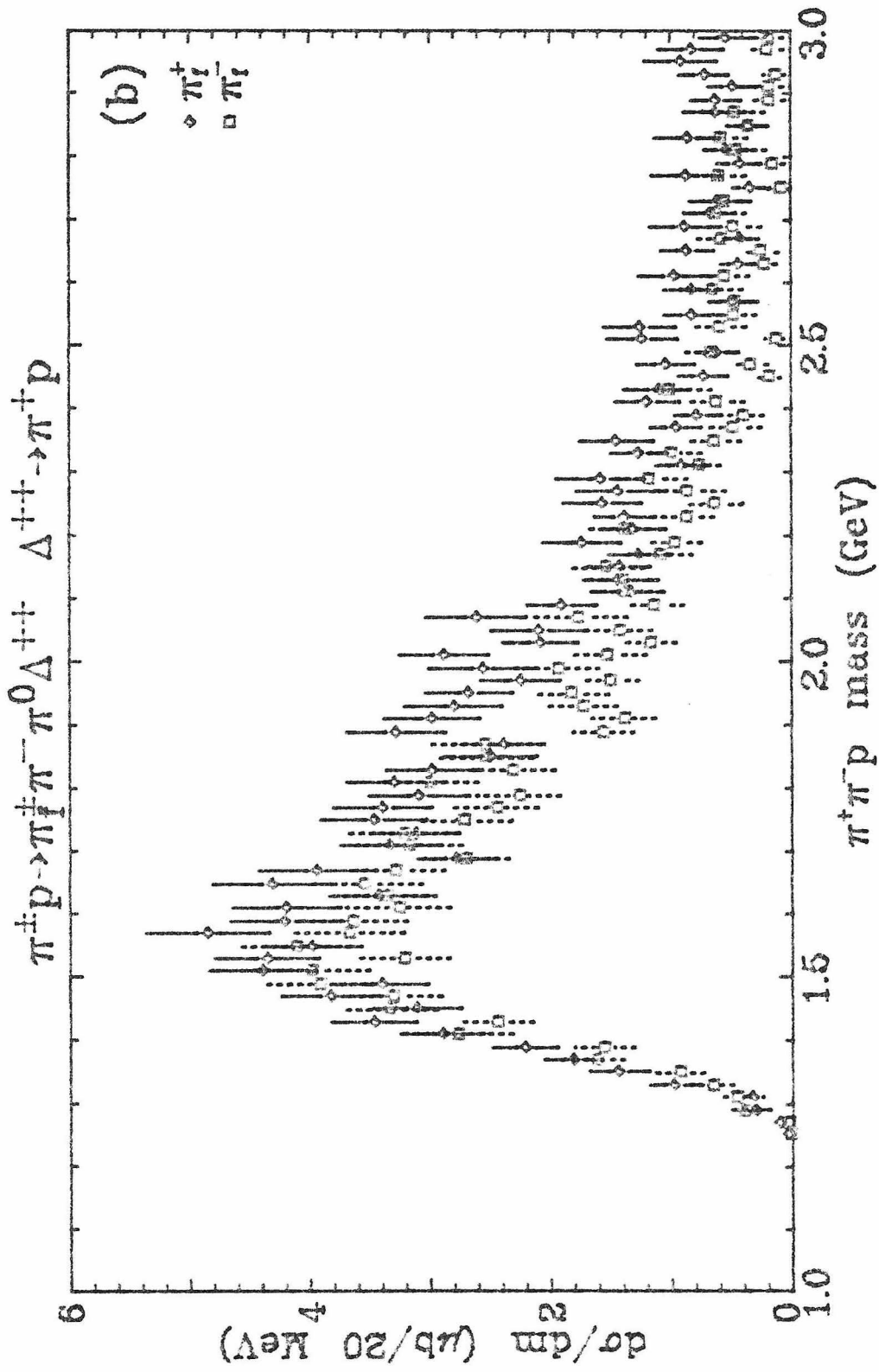


Figure V.15b

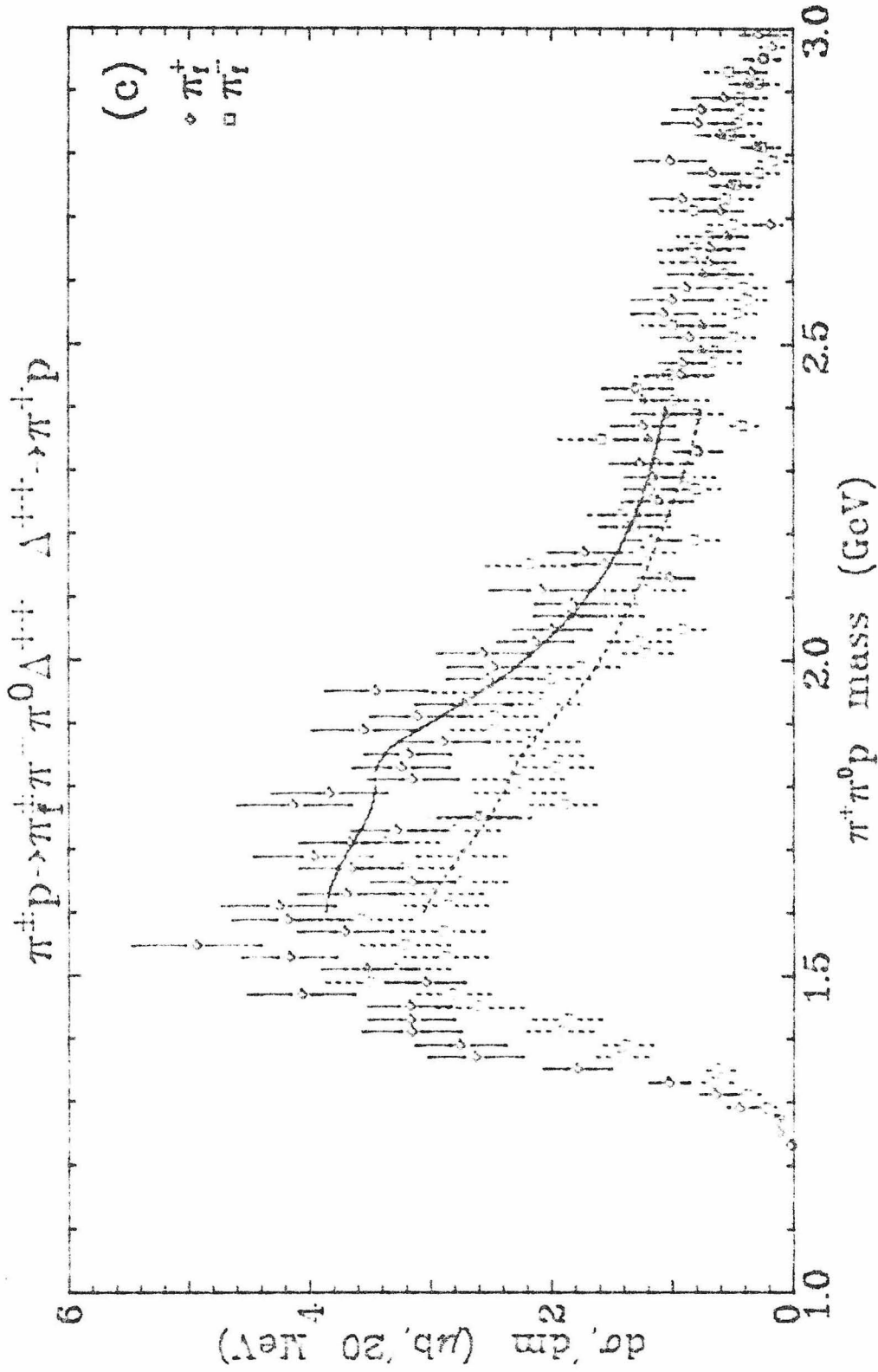


Figure V.15c

The curves are fits to the Δ^{++} (1890).

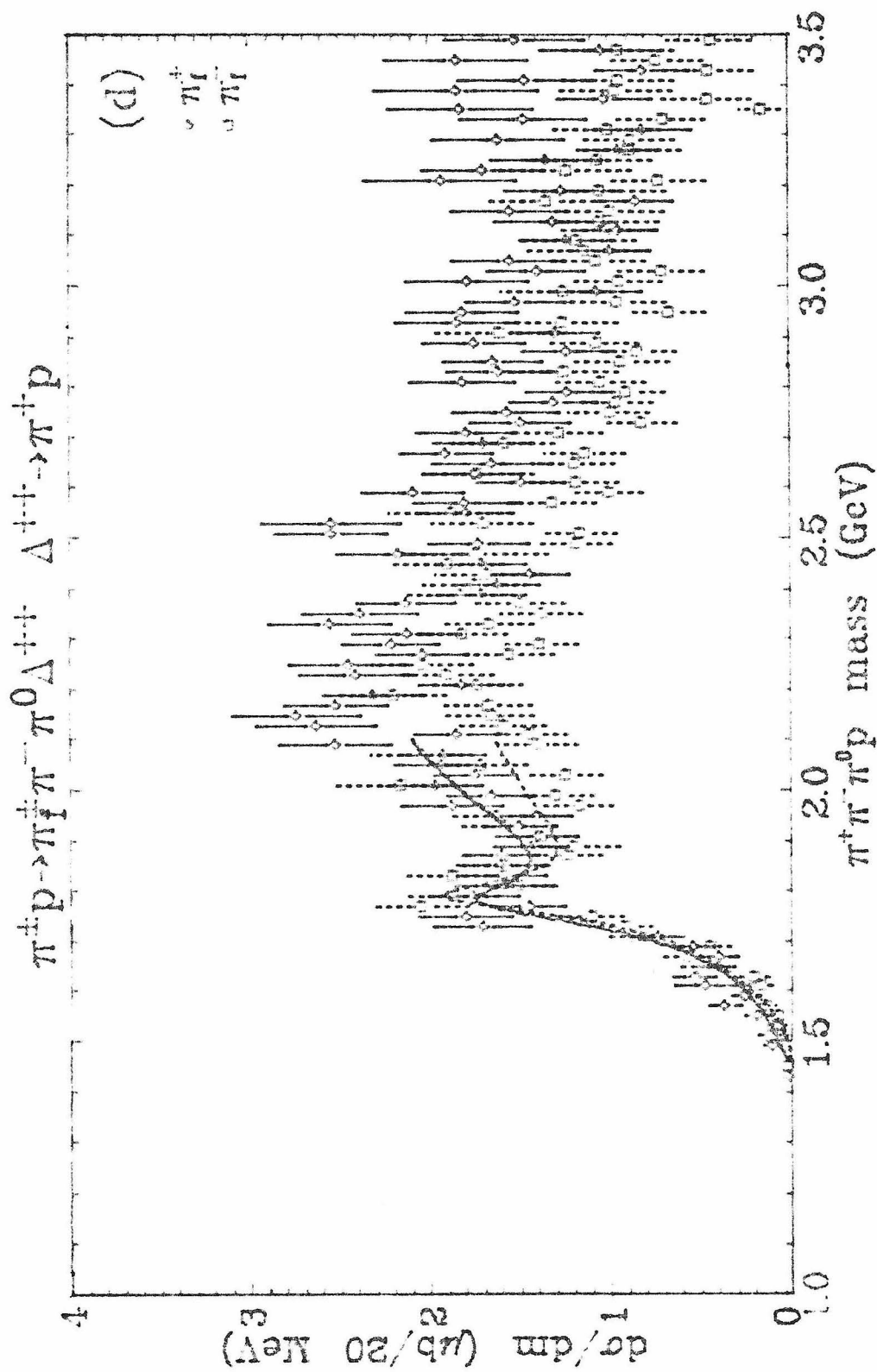


Figure V.15d

The curves are fits to the $N^+(1790)$.

$$\diamond \pi^+ p \rightarrow \pi_f^+ \pi^+ \pi^+ \Delta^- \quad \Delta^- \rightarrow \pi^- n$$

$$\square \pi^- p \rightarrow \pi_f^- \pi^+ \pi^+ \Delta^- \quad \Delta^- \rightarrow \pi^- n$$

— π^+ fits

----- π^- fits

$$\text{Prob}(\chi_{\text{fit}}^2) \geq 5\%$$

$$-t_{\pi\pi(f)} < 0.6 \text{ GeV}^2/c^2$$

$$(\pi^+ \pi^+ \pi^- n) \text{ mass} < 3.7 \text{ GeV}$$

$\Delta^- \rightarrow \pi^- n$ definition:

$$\pi^- n \text{ mass} < 1.36 \text{ GeV}$$

Figures V.16a-b

Invariant mass distributions for the slow particles of the n channel for events within the Δ^- peak (see above).

$$\diamond \pi^+ p \rightarrow \pi_f^+ \rho^0 \pi^0 p \quad \rho^0 \rightarrow \pi^+ \pi^-$$

$$\square \pi^- p \rightarrow \pi_f^- \rho^0 \pi^0 p \quad \rho^0 \rightarrow \pi^+ \pi^-$$

— π^+ fits

----- π^- fits

$$\text{Prob}(\chi_{\text{fit}}^2) \geq 5\%$$

$$-t_{\pi\pi(f)} < 0.6 \text{ GeV}^2/c^2$$

$$(\pi^+ \pi^- \pi^0 p) \text{ mass} < 3.7 \text{ GeV}$$

$\rho^0 \rightarrow \pi^+ \pi^-$ definition:

$$0.64 \leq \pi^+ \pi^- \text{ mass} < 0.84 \text{ GeV}$$

Figures V.17a-d

Invariant mass distributions for the slow particles of the π^0 channel for events within the ρ^0 peak (see above).

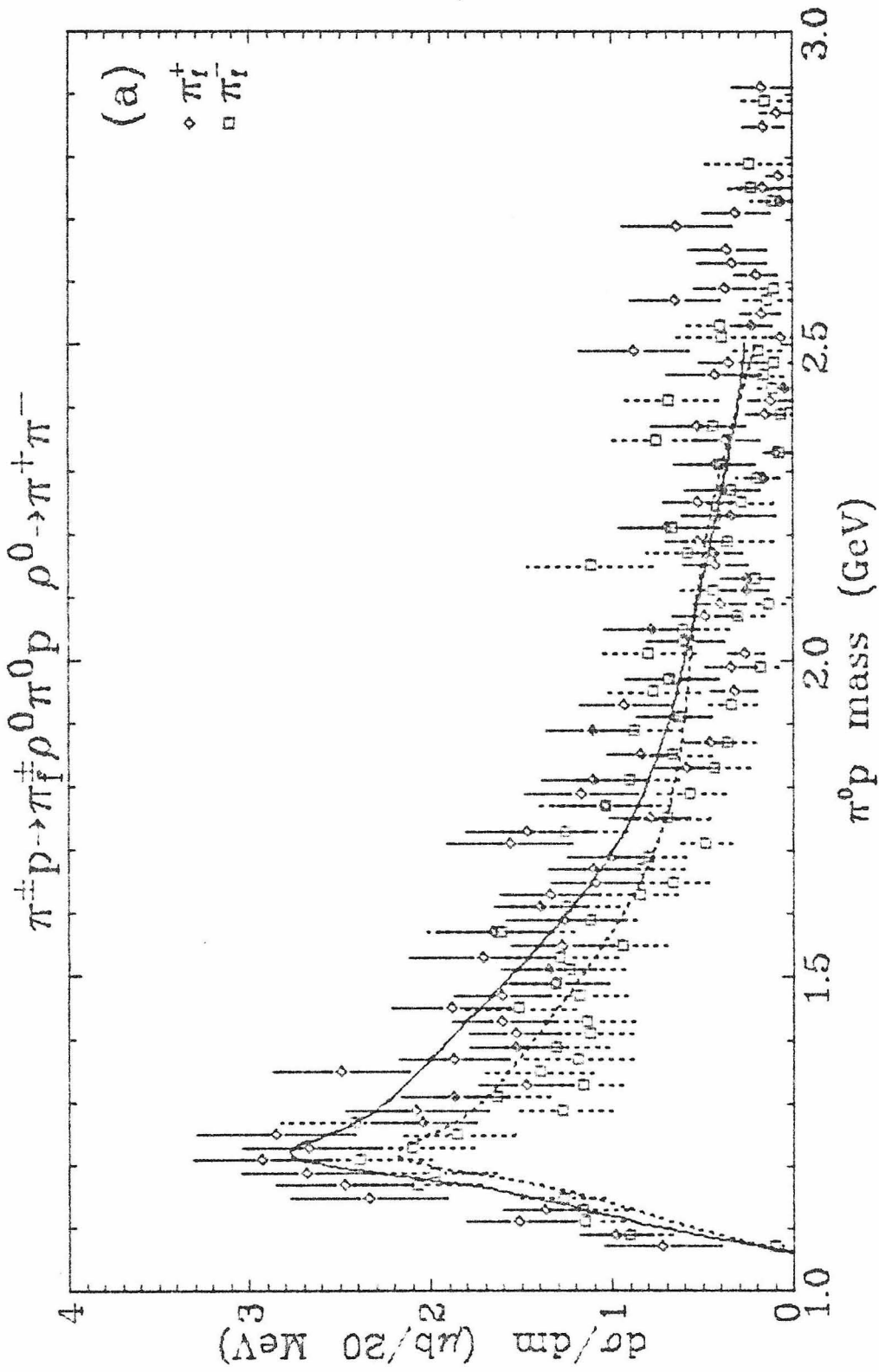


Figure V.17a

The curves are fits to the Δ^+ .

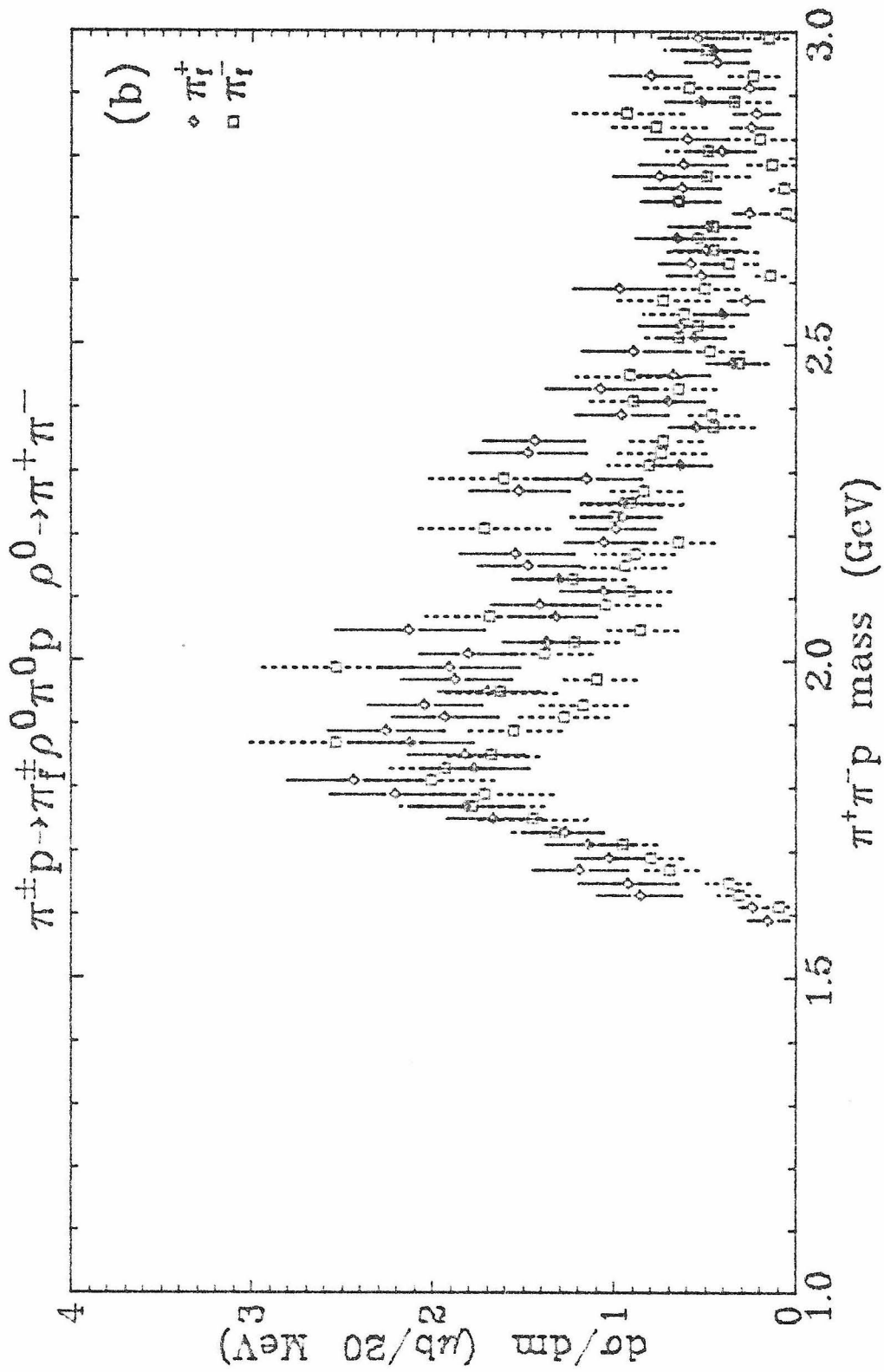


Figure V.17b

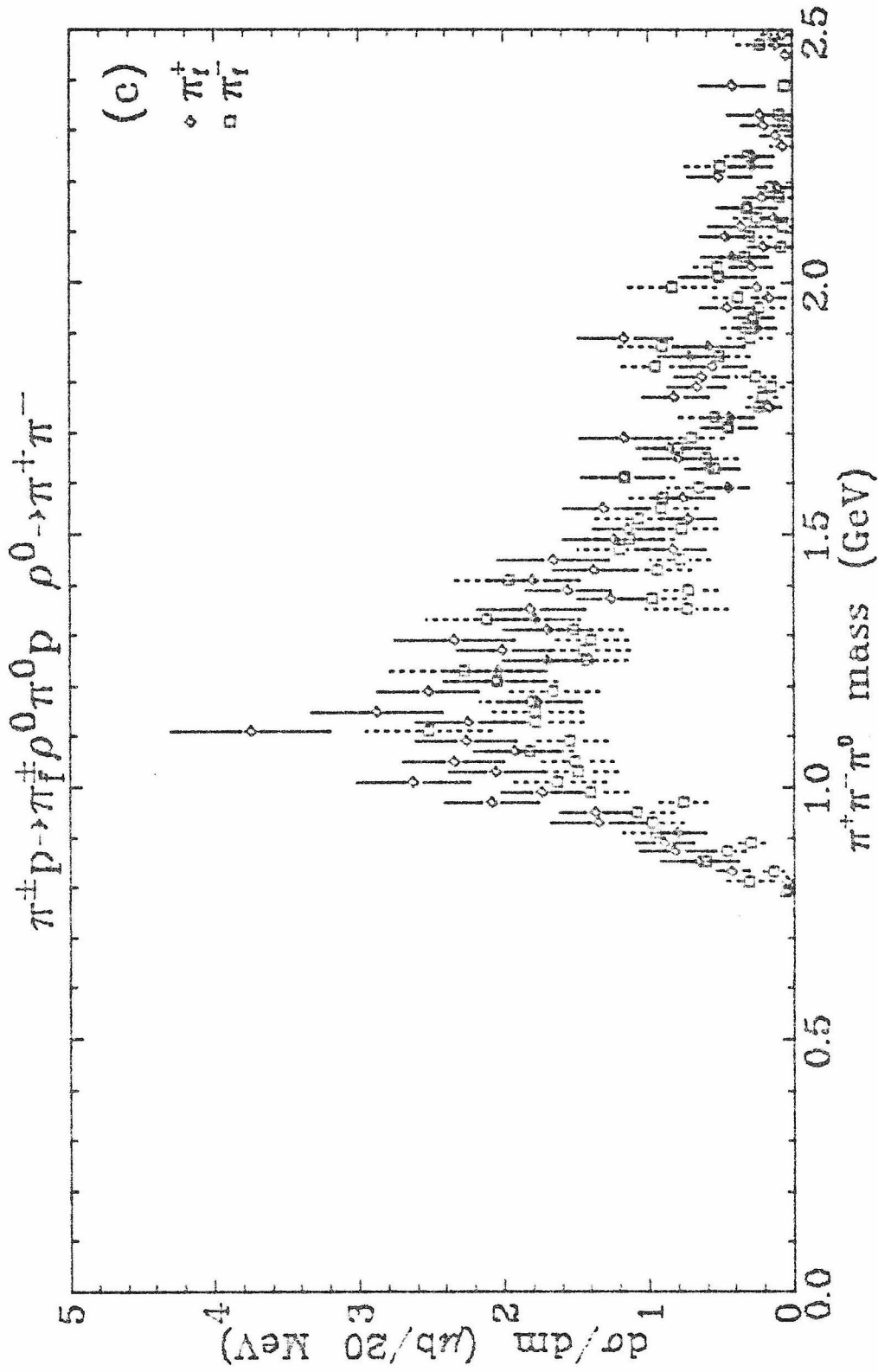


Figure V.17c

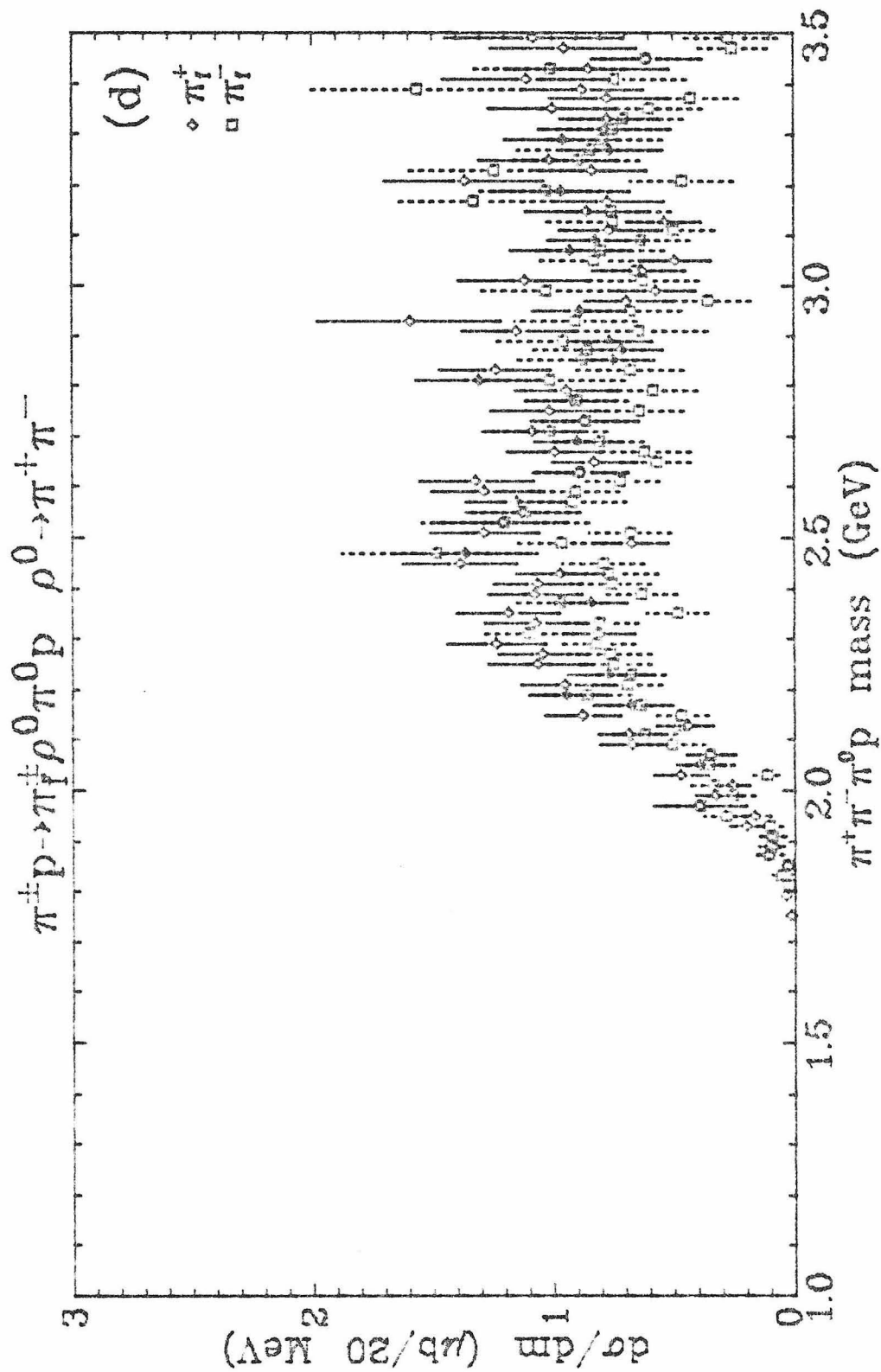


Figure V.17d

$$\diamond \pi^+ p \rightarrow \pi_f^+ \rho^0 \pi^+ n \quad \rho^0 \rightarrow \pi^+ \pi^-$$

$$\square \pi^- p \rightarrow \pi_f^- \rho^0 \pi^+ n \quad \rho^0 \rightarrow \pi^+ \pi^-$$

— π^+ fits

----- π^- fits

$$\text{Prob}(\chi_{\text{fit}}^2) \geq 5\%$$

$$-t_{\pi\pi(f)} < 0.6 \text{ GeV}^2/c^2$$

$$(\pi^+ \pi^+ \pi^- n) \text{ mass} < 3.7 \text{ GeV}$$

$\rho^0 \rightarrow \pi^+ \pi^-$ definition:

$$0.64 \leq \pi^+ \pi^- \text{ mass} < 0.84 \text{ GeV}$$

Figures V.18a-d

Invariant mass distributions for the slow particles of the n channel for events within the ρ^0 peak (see above).

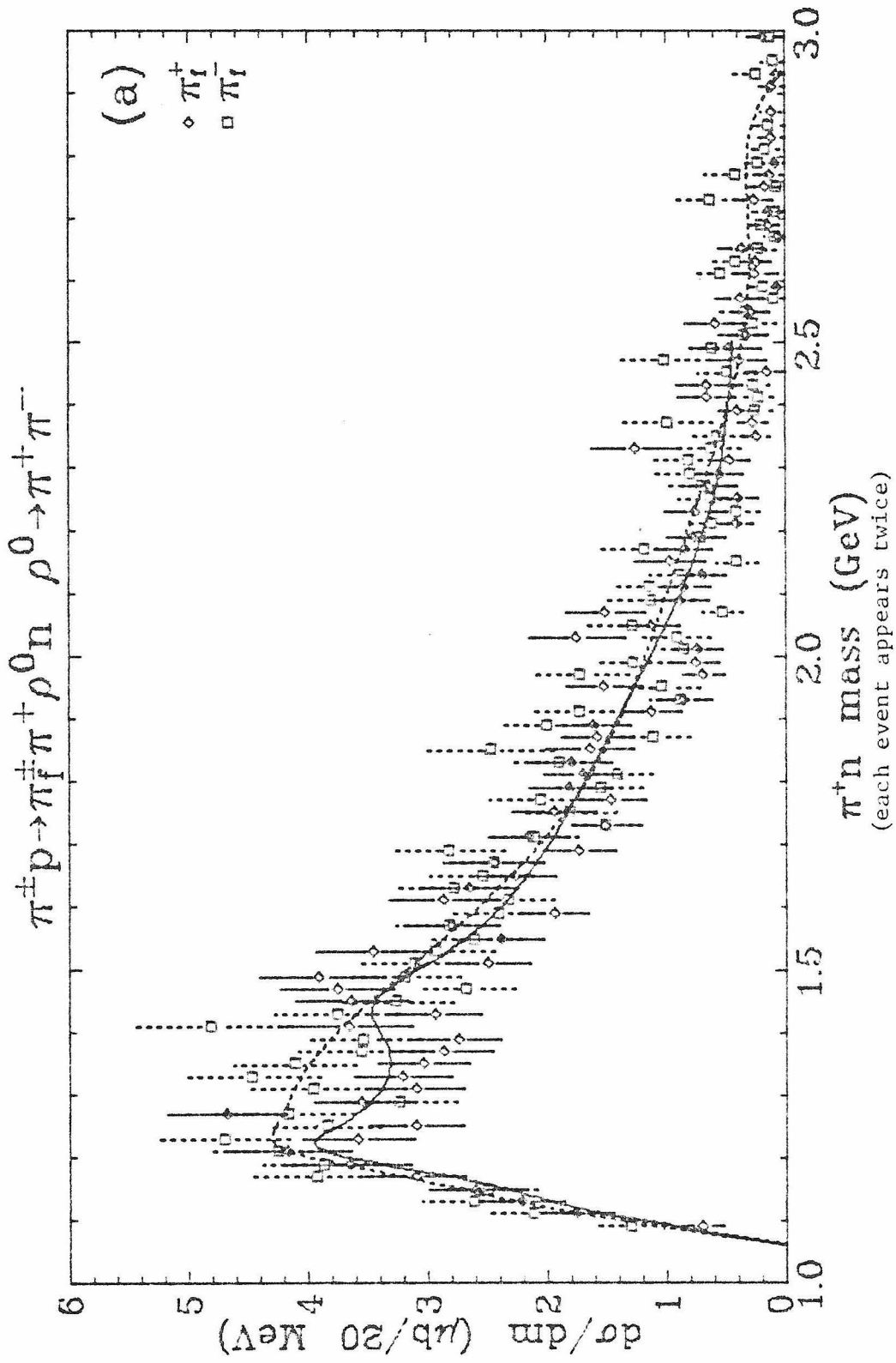


Figure V.18a

The π^+ curve is a fit to the Δ^+ and $N^+(1470)$; the π^- curve is a fit to the Δ^+ .

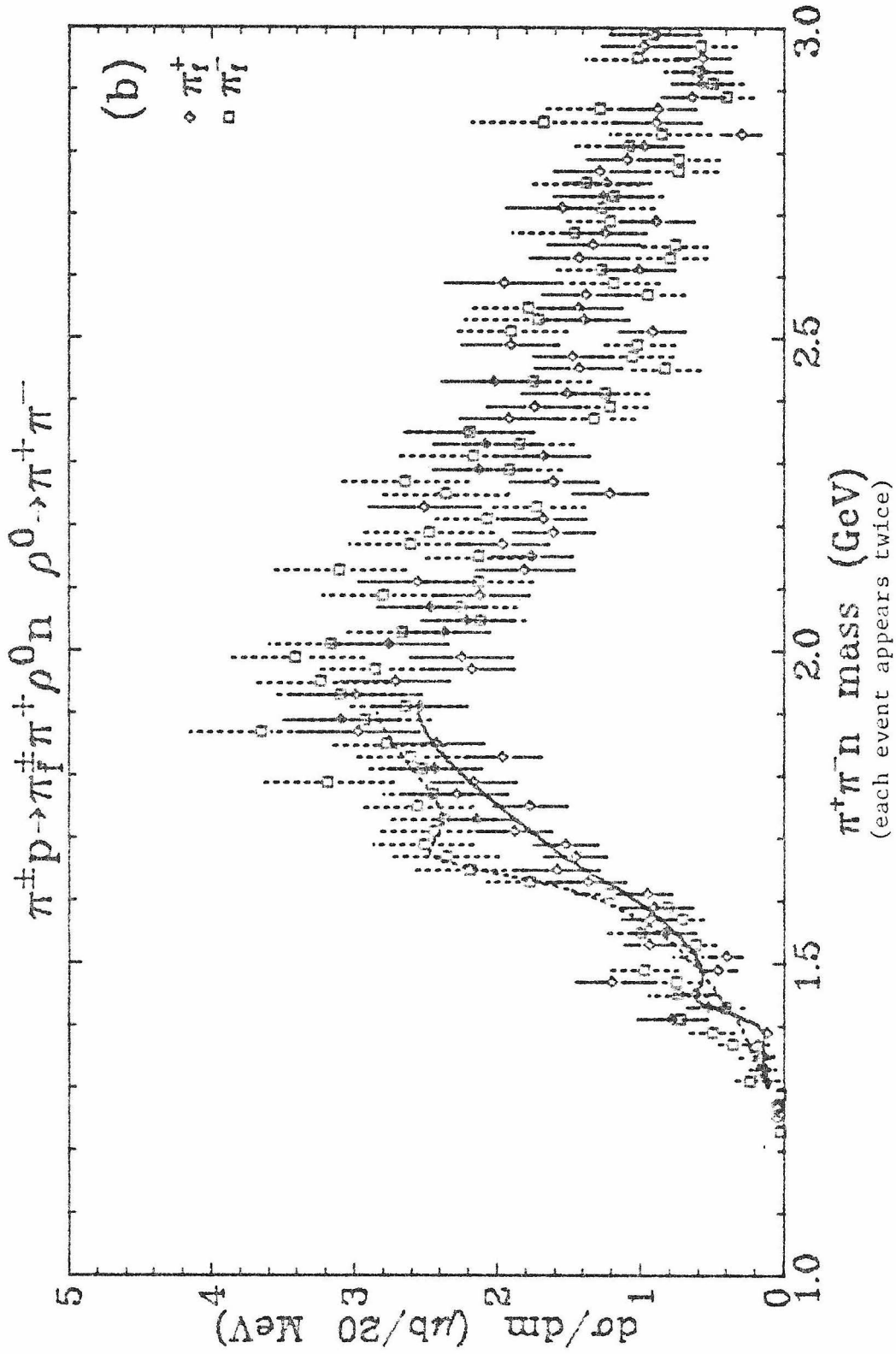


Figure V.18b

The π^+ curve is a fit to the $N^0(1470)$; the π^- curve is a fit to the $N^0(1470)$ and $N^0(1688)$.

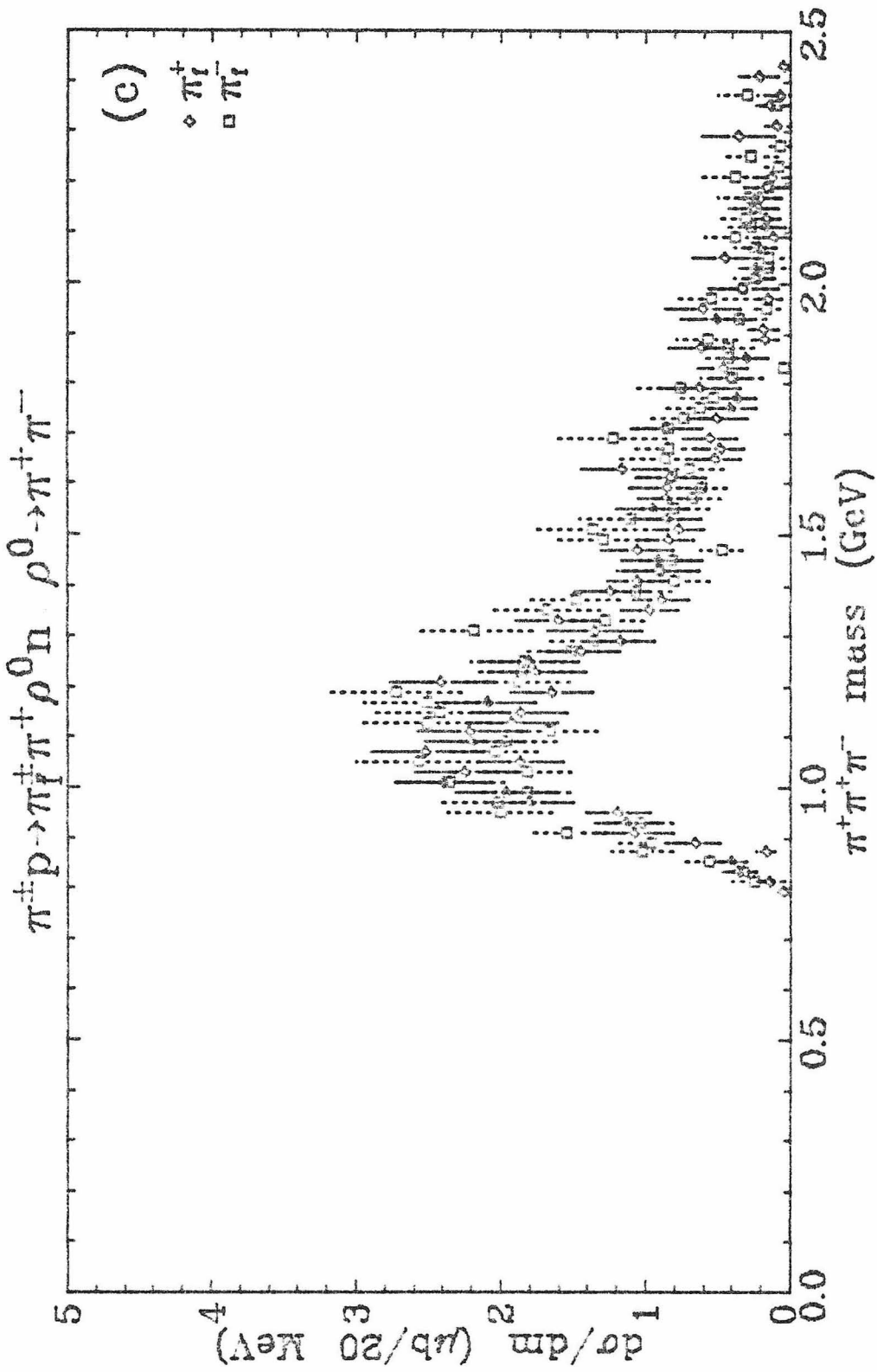


Figure V.18c

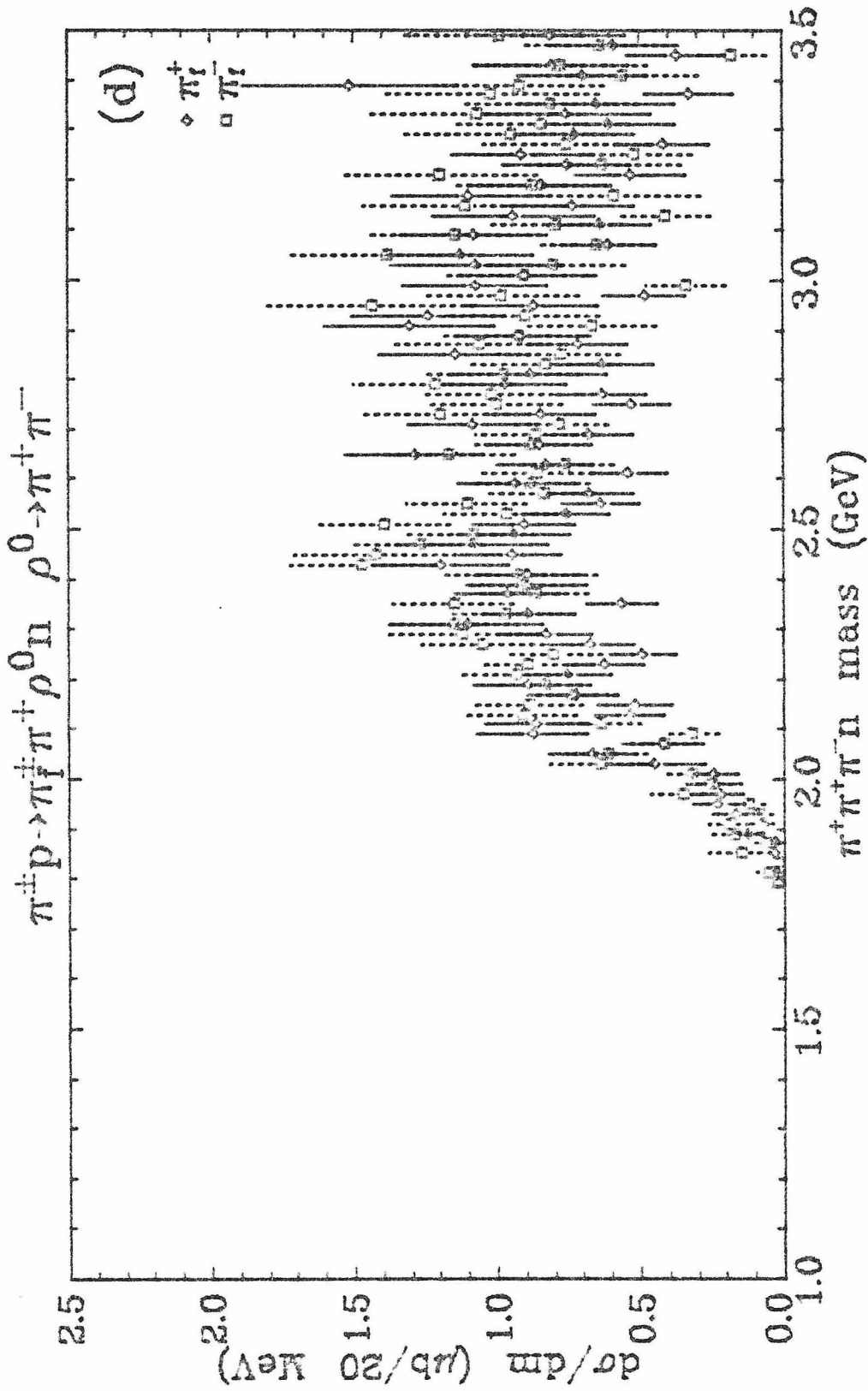


Figure V.18d

$$\diamond \pi^+ p \rightarrow \pi_f^+ \rho^+ \pi^- p \quad \rho^+ \rightarrow \pi^+ \pi^0$$

$$\square \pi^- p \rightarrow \pi_f^- \rho^+ \pi^- p \quad \rho^+ \rightarrow \pi^+ \pi^0$$

— π^+ fits

..... π^- fits

$$\text{Prob}(\chi_{\text{fit}}^2) \geq 5\%$$

$$-t_{\pi\pi(f)} < 0.6 \text{ GeV}^2/c^2$$

$$(\pi^+ \pi^- \pi^0 p) \text{ mass} < 3.7 \text{ GeV}$$

$\rho^+ \rightarrow \pi^+ \pi^0$ definition:

$$0.64 \leq \pi^+ \pi^0 \text{ mass} < 0.84 \text{ GeV}$$

Figures V.19a-d

Invariant mass distributions for the slow particles of the π^0 channel for events within the ρ^+ peak (see above).

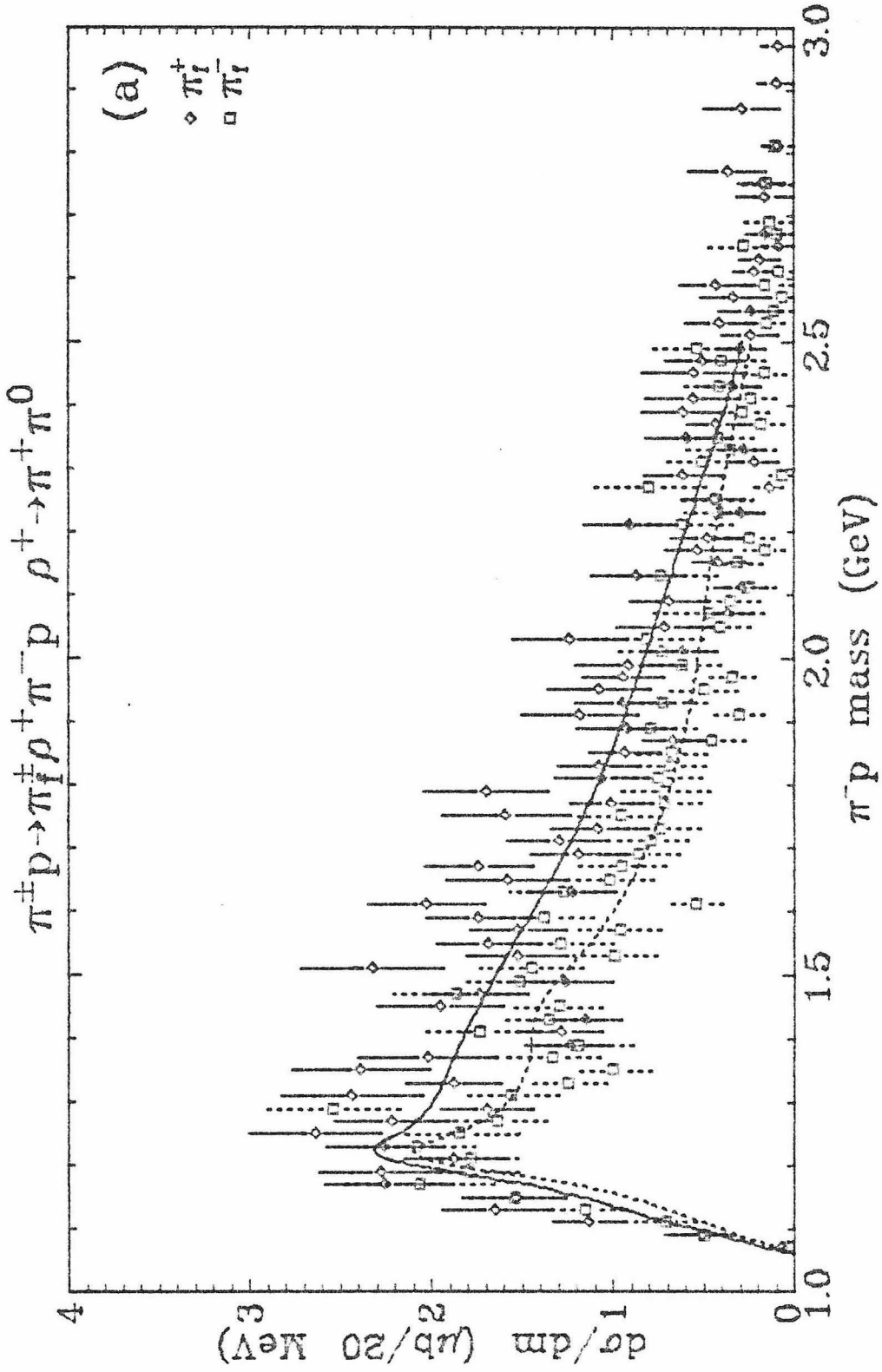


Figure V.19a

The π^+ curve is a fit to the Δ^0 ; the π^- curve is a fit to the Δ^0 and $N^0(1470)$.

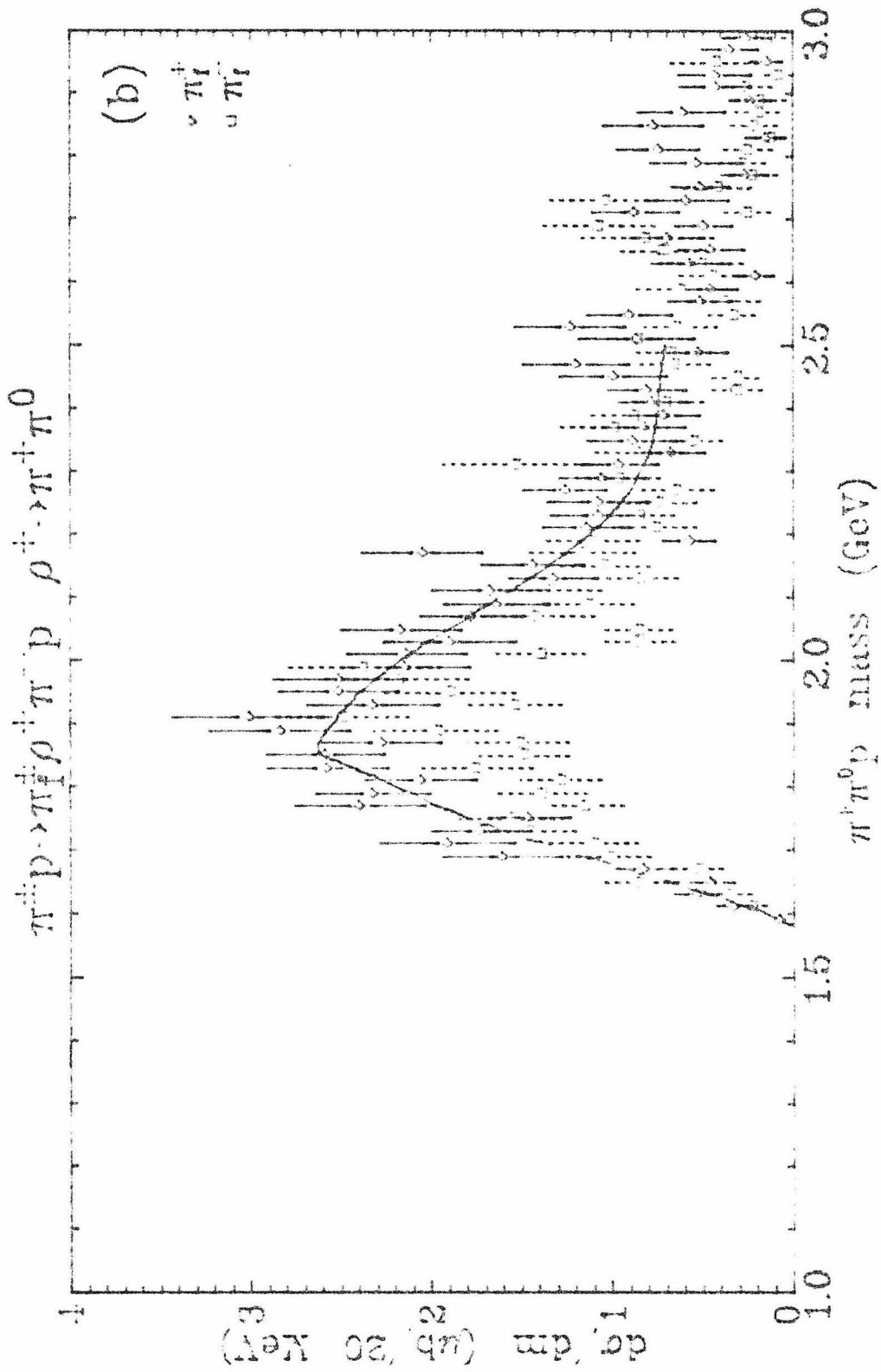


Figure V.19b

The curve is a fit to the Δ^{++} (1890).

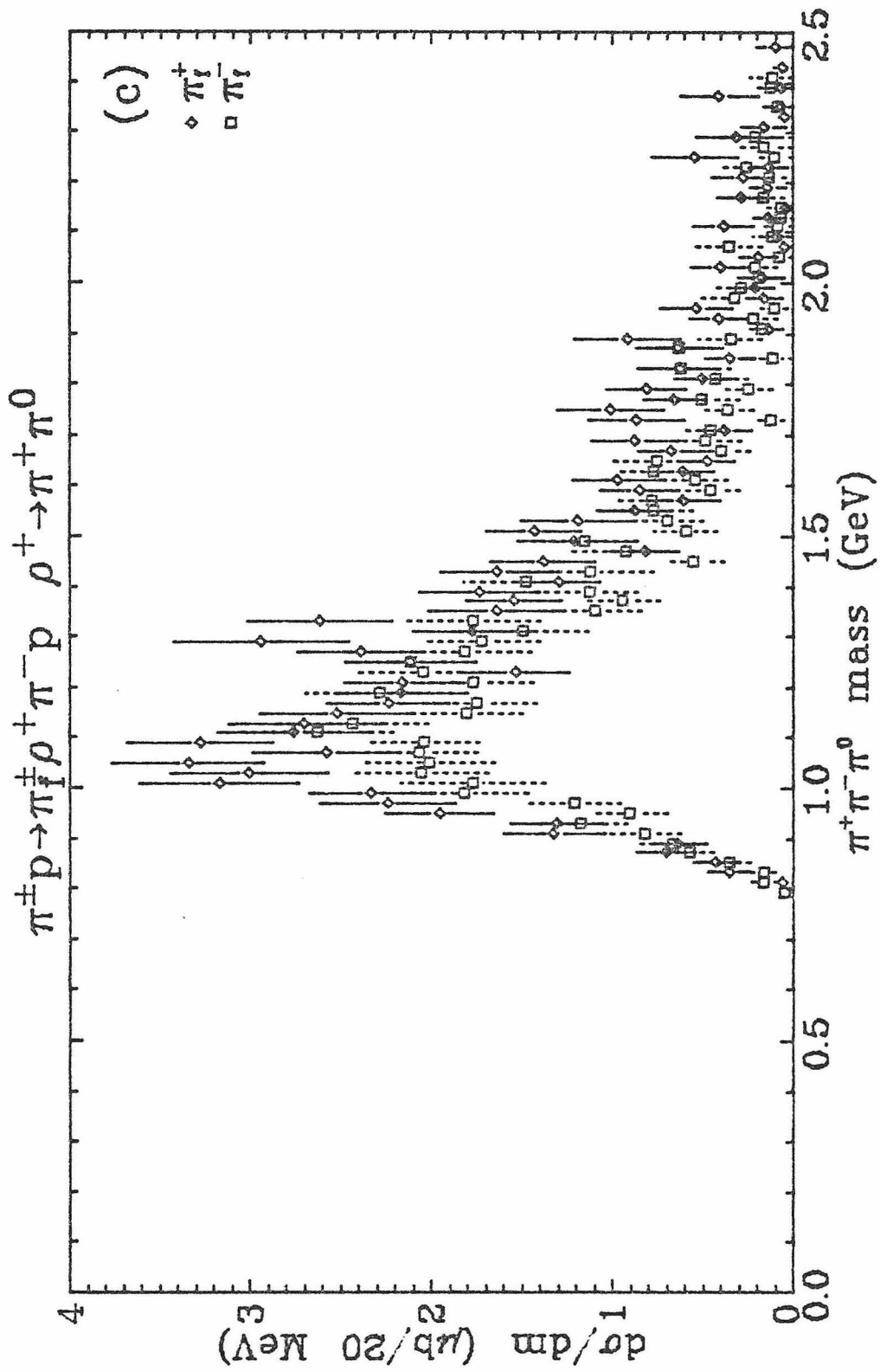


Figure V.19c

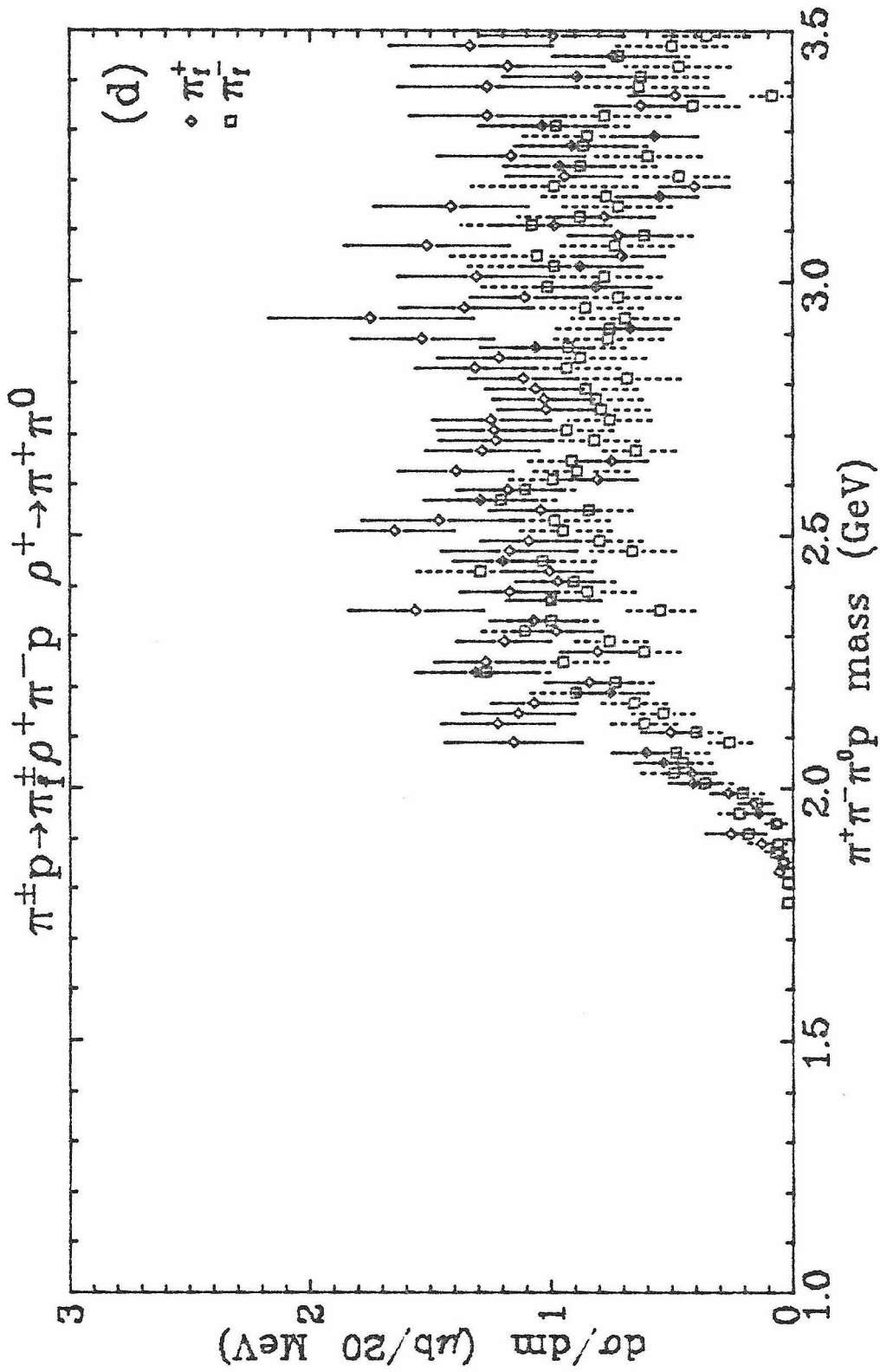


Figure V.19d

$$\diamond \pi^+ p \rightarrow \pi_f^+ \rho^- \pi^+ p \quad \rho^- \rightarrow \pi^- \pi^0$$

$$\square \pi^- p \rightarrow \pi_f^- \rho^- \pi^+ p \quad \rho^- \rightarrow \pi^- \pi^0$$

— π^+ fits

----- π^- fits

$$\text{Prob}(\chi_{\text{fit}}^2) \geq 5\%$$

$$-t_{\pi\pi(f)} < 0.6 \text{ GeV}^2/c^2$$

$$(\pi^+ \pi^- \pi^0 p) \text{ mass} < 3.7 \text{ GeV}$$

$\rho^- \rightarrow \pi^- \pi^0$ definition:

$$0.64 \leq \pi^+ \pi^0 \text{ mass} < 0.84 \text{ GeV}$$

Figures V.20a-d

Invariant mass distributions for the slow particles of the π^0 channel for events within the ρ^- peak (see above).

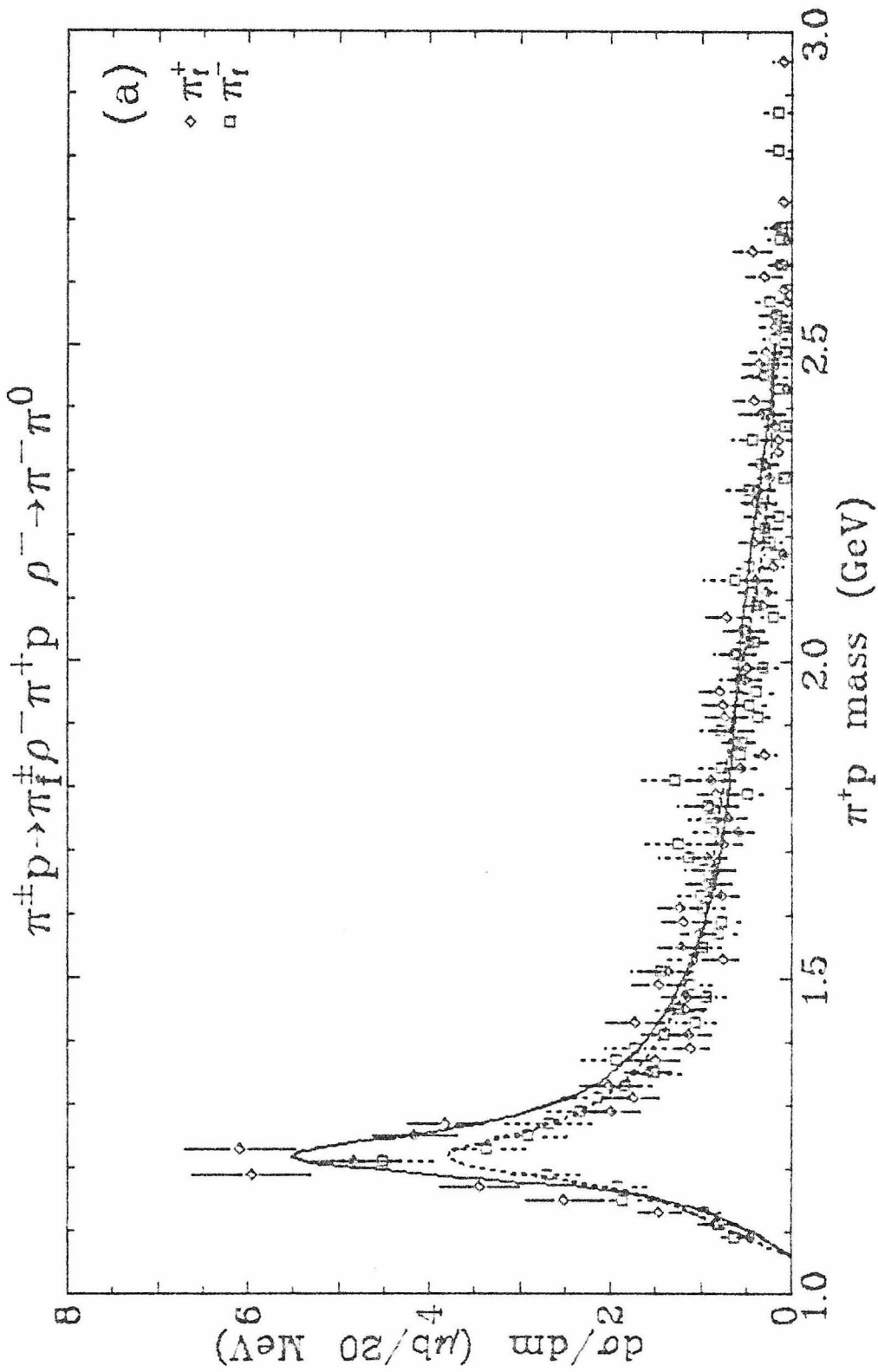


Figure V.20a

The curves are fits to the Δ^{++} .

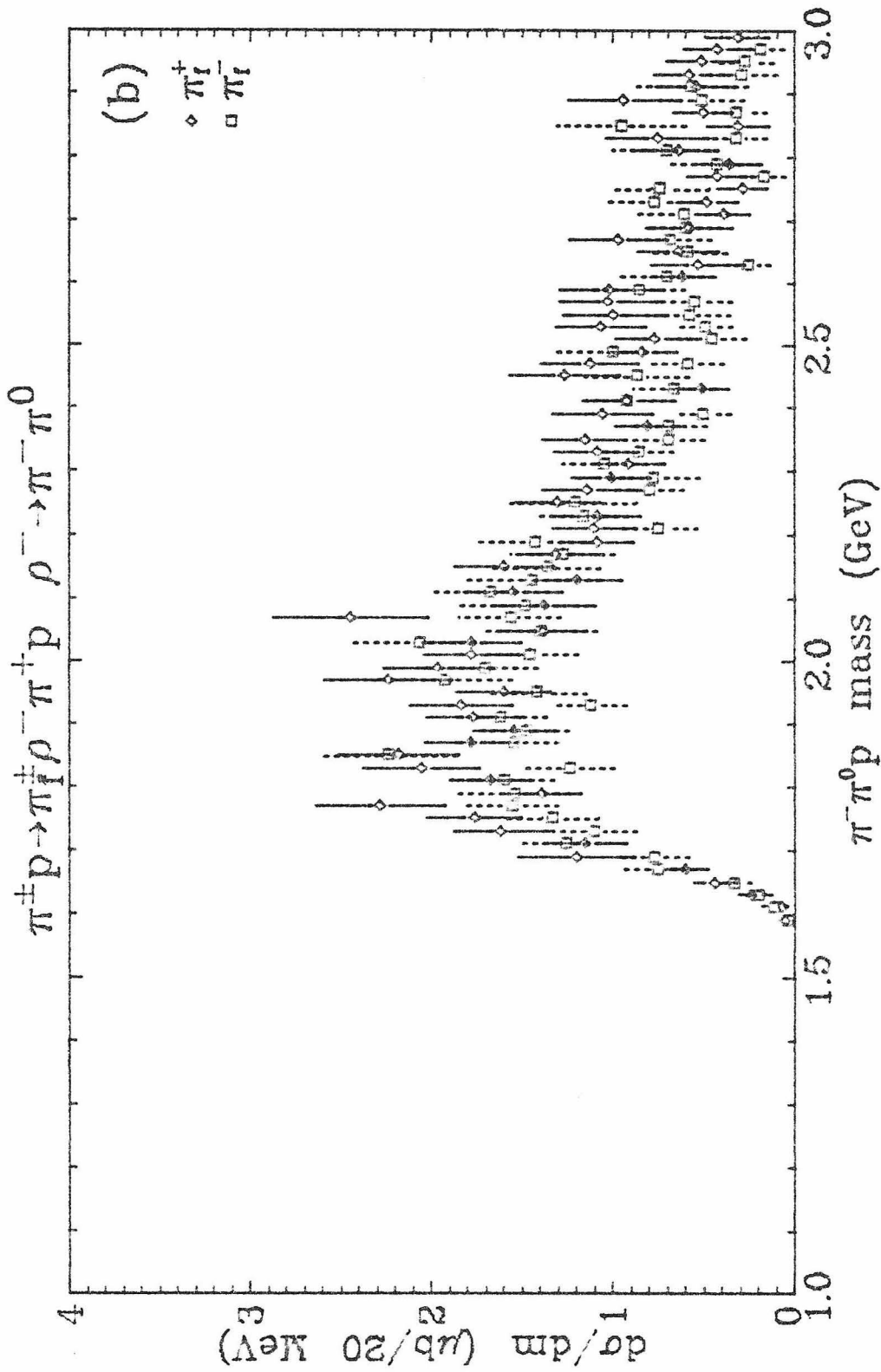


Figure V.20b

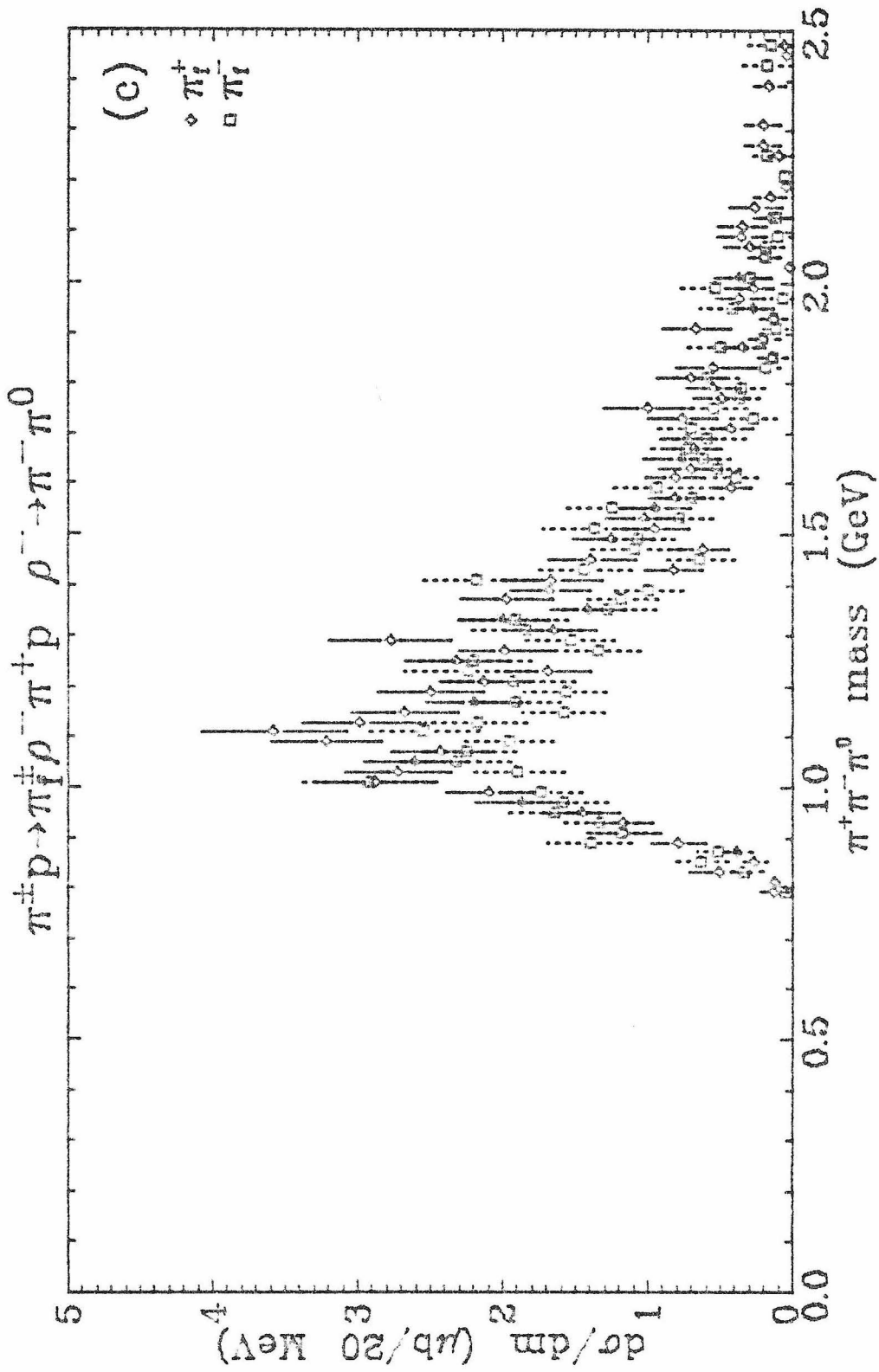


Figure V.20c

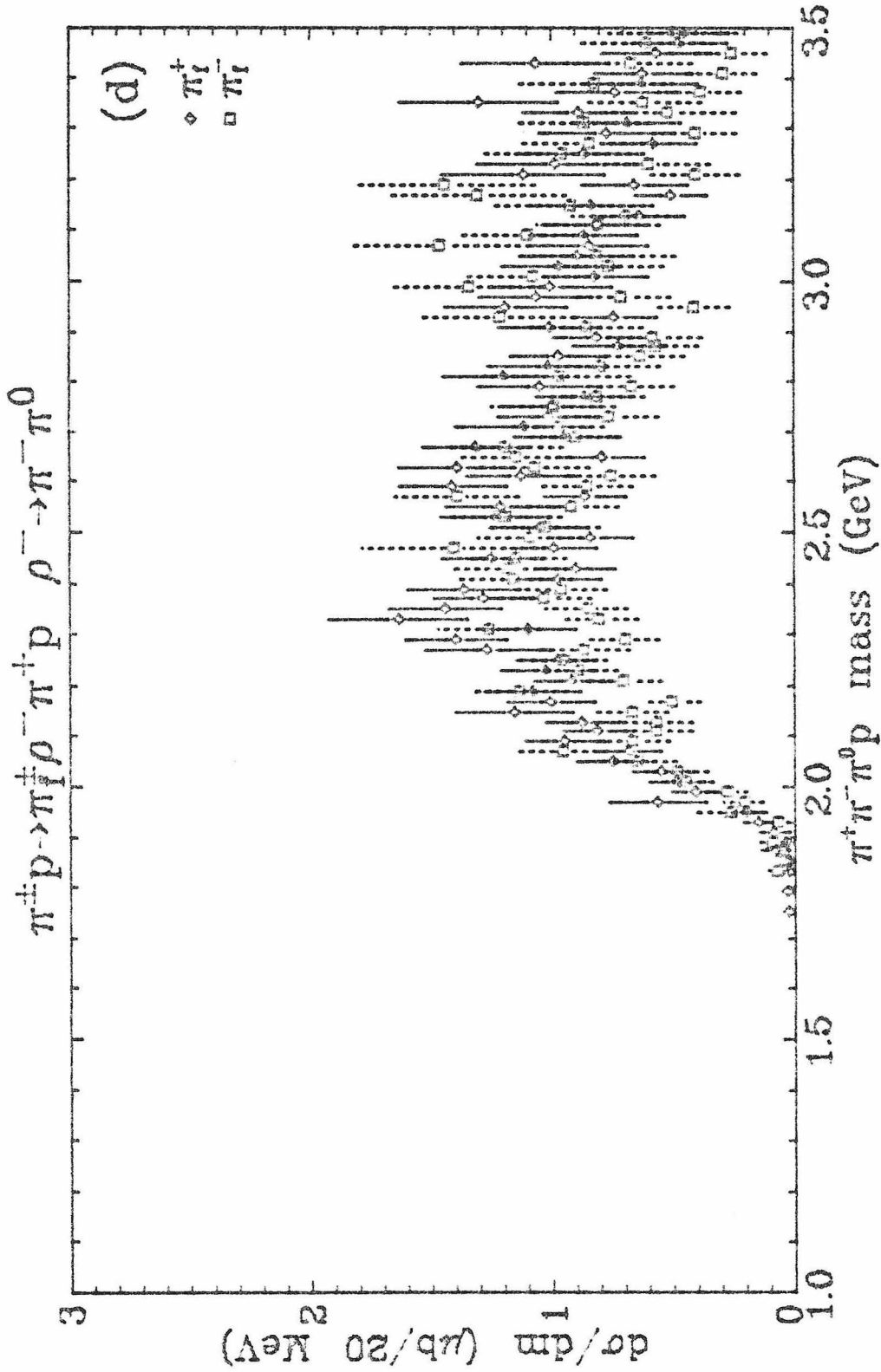


Figure V.20d

Chapter VI

Production of the η^0 and ω^0 Mesons

1. Introduction

We can study the quasi-3-body reactions involving the η^0 and ω^0 mesons:

$$\pi^{\pm} p \rightarrow \pi_{\text{F}}^{\pm} \eta^0 p \quad (1a)$$

$$\pi^{\pm} p \rightarrow \pi_{\text{F}}^{\pm} \omega^0 p \quad (1b)$$

by virtue of the $\pi^+ \pi^- \pi^0$ decays of these mesons. These reactions have been studied in other experiments (see Chapter I) which for the most part concentrated on studies of the B(1235), A_2 (1310), and g(1680) mesons which decay into $\pi \eta^0$ (A_2) or $\pi \omega^0$ (B and g) or studies of the quasi-2-body reactions with a Δ (1232) produced along with the η^0 or ω^0 meson. By probing the diffractive dissociation region, our experiment has accumulated events in a relatively unexplored kinematic region for reactions (1a) and (1b). Our experiment observes relatively small cross sections for reactions (1a) as compared to those cross sections observed by other experiments. However, few of the η 's we observe come from A_2 decays while other experiments found the A_2 to account for a substantial portion of the η^0 production [Baltay 1978, Kennedy 1978, and Sisterson 1972]. Our trigger rejects most events from the conversion of a beam pion into an A_2 meson. The $\pi_{\text{F}}^{\pm} \eta^0$ mass distributions show an A_2^{\pm} peak (see Fig. VI.1) which was removed by a cut to avoid the trigger-imposed biases. The remaining η^0 events come from nucleon diffractive dissociation processes, but we observe that the

cross section for $\pi_{\text{f}}^{+}\eta^{\circ}\text{p}$ is about twice the cross section for $\pi_{\text{f}}^{-}\eta^{\circ}\text{p}$. This is a surprising result as the cross section for diffraction of the proton into an $\eta^{\circ}\text{p}$ system would be expected to be independent of the type of the beam particle. The data and a further discussion of this result are given in the next section of this chapter.

Our experiment also observed ω° production in the quasi-3-body reactions (1b). Here again, as for the η° , our data is limited to a kinematic region relatively unstudied by other experiments. The B and g mesons and the $\omega^{\circ}\Delta$ final state have been extensively studied in many experiments (including those listed in Tables I.3 and I.4). We do have some events from these sources (except that the B is not seen at all) as was discussed in Chapter V. However, in contrast to our η° data where we have no overlap with other published results, ω° production in our kinematic region has been studied by other experiments with rather small statistics. These studies have been of the low mass $\omega^{\circ}\text{p}$ enhancement (see Chapter I, especially Table I.7). Several experiments (including ours) have attributed this enhancement to the $\omega^{\circ}\text{p}$ decay of an N^{*} [see for example Atherton 1975 and Milgram 1970]. We have examined the angular distributions of the $\omega^{\circ}\text{p}$ system but have not determined the spin-parity of the N^{*} due to inconsistencies discussed in the final section of this chapter.

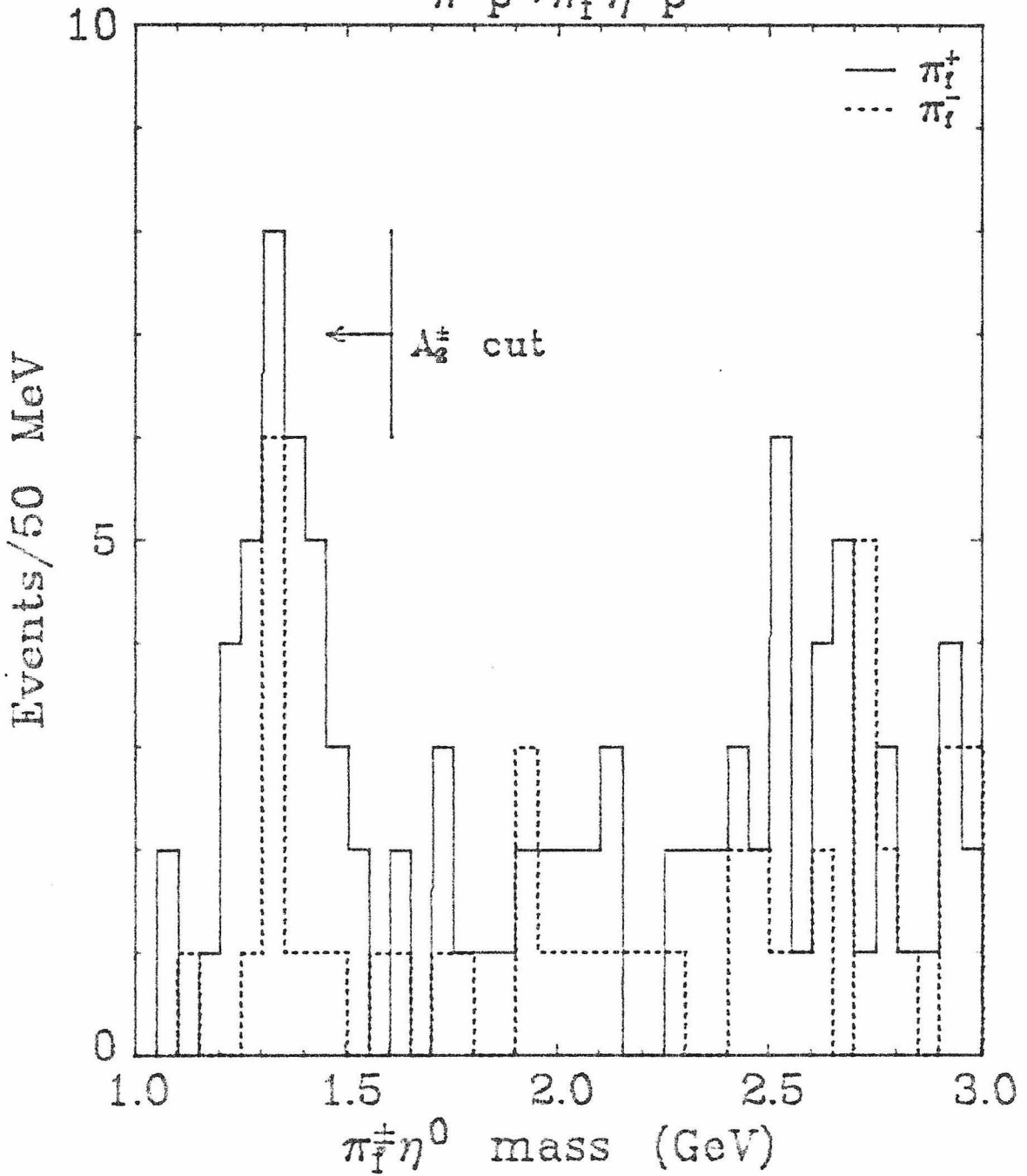
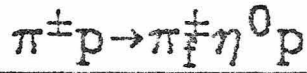


Figure VI.1

Plot of the $\pi_F^\pm \eta^0$ mass spectra for $\pi^+ \pi^- \eta^0$ masses within the η^0 cut (see text). Events below 1.6 GeV were excluded from the η^0 analysis as due to A_2^\pm decays. Most of the η^0 events have a $\pi_F^\pm \eta^0$ mass above 3.0 GeV.

2. $\pi_f^\pm \eta^0 p$ Final State

We have observed reactions (1a) as part of the final states:

$$\pi_f^\pm p \rightarrow \pi_f^\pm \pi^+ \pi^- \pi^0 p \quad (2)$$

by virtue of the $\pi^+ \pi^- \pi^0$ decay mode of the η^0 meson. Fig. VI.2 shows the $d\sigma/dm$ distributions for the $\pi^+ \pi^- \pi^0$ mass in the region of the η^0 . The curves in the figure are the result of fitting a Breit-Wigner resonance shape (with $\Gamma(m)=\Gamma_R$) and a quadratic background to the data. Although the width of the η^0 peak is due to our resolution (see below), the existence of a spectrum of errors in the $\pi^+ \pi^- \pi^0$ mass (rather than a single fixed value) modulates a gaussian into a Breit-Wigner shape. The results of the fits are given in Table VI.1 below.

Table VI.1

Fitted parameters for $\eta^0 \rightarrow \pi^+ \pi^- \pi^0$ peak

	π^+	π^-
Mass (MeV)	548.3±1.2	554.6±1.9
Fixed width (FWHM, MeV)	12.5	12.5
Events in peak	200±31	91±23
Observed cross section (μb)	2.52±0.41	1.33±0.35
Corrected σ (μb) (for unseen decays)	10.7±1.8	5.6±1.5
Fraction of estimated $\sigma(\pi p \rightarrow \pi \eta^0 p)$ (Table I.6)	28±8%	25±14%

Figure VI.2

Plot of $d\sigma/dm$ for the $\pi^+\pi^-\pi^0$ invariant mass in the region of the η^0 . The curves show the results of the fit to the η^0 peak as described in the text. The dotted curve shows the background distribution resulting from the fit.

$\pi^\pm p \rightarrow \pi^\pm p \pi^+ \pi^- \pi^0$
Fits to η^0 peak

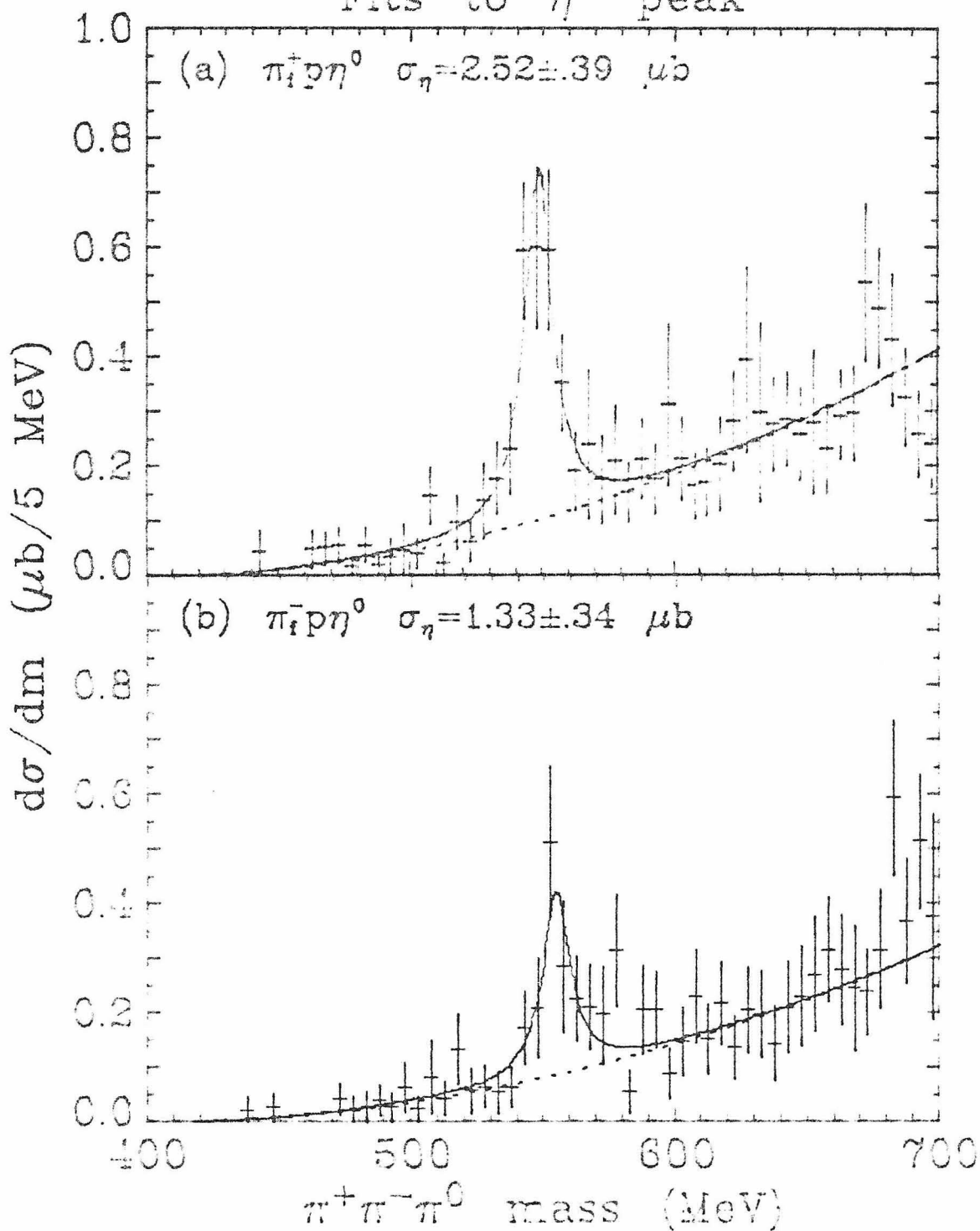


Figure VI.2

The mass of the η^0 from the π^+ experiment is in good agreement with the accepted value of $548.8(\pm 0.6)$ MeV [Particle Data Group 1978], and that from the π^- experiment is high due to a slightly incorrect value used for the bubble chamber magnetic field while processing the π^- data (see also Chapter IV). This same shift is also evident in the ω^0 results (see below) but does not otherwise affect our results. The fixed widths of the η^0 are from our resolution of 12 to 15 MeV (FWHM) in the $\pi^+\pi^-\pi^0$ mass. A fixed width was used as the low statistics and narrow peak make the width poorly determined by the fit. The results from varying the width in the fit are 12.5 ± 3.4 MeV for the π^+ and 9.1 ± 4.2 MeV for the π^- peak.

The cross section is given in the table as fitted and also corrected for the $\eta^0 \rightarrow \pi^+\pi^-\pi^0$ branching ratio ($23.6\pm 0.6\%$ [Particle Data Group 1978]). The error on the corrected η^0 cross section is dominated by the error in the fitted cross section and includes the errors on the normalization factor and in the branching ratio. Immediately apparent is the factor of two in the $\pi_{\text{f}}^{\pm}\eta^0$ p cross section for the change in the charge of the beam.

We have examined the π^- data for an excessive loss of η^0 events in the fit selection process. No evidence was found for losses large enough to account for the cross section difference. We also examined the missing-mass-squared spectra of the two prong reactions:

$$\pi_{\text{f}}^{\pm} \text{p} \rightarrow \pi_{\text{f}}^{\pm} \text{p} + (\text{anything neutral}) \quad (3)$$

(all OC and π^0 two prong events) for η^0 peaks from reaction (1a) with

the η^0 decaying into neutral particles. We found small peaks at m_{η}^2 whose sizes were consistent with the signals from reaction (2) and the factor of about 3 from the ratio of the all neutral and $\pi^+\pi^-\pi^0$ branching fractions. Though reaction (3) has more η^0 events than reaction (2), the large background under the η^0 missing mass peak and the broadening of this peak due to the low missing mass resolution (compared to the $\pi^+\pi^-\pi^0$ peak) make this data serve as a check only and unusable in our analysis. Altogether, we found no evidence for a difference in the π^+ and $\pi^-\eta^0$ cross sections due to a technical problem rather than the physics underlying the η^0 production.

Fig. VI.3 shows the $\eta^0 p$ mass spectra from the two experiments. The η^0 is defined by cuts in the $\pi^+\pi^-\pi^0$ mass: 530 through 570 MeV for the π^+ experiment and 535 through 575 for the π^- experiment. The π^- cut was shifted by 5 MeV since the central value of the η^0 peak was about 5 MeV high. The spectra shown in Fig. VI.3a are for all the events within the η^0 cut except for the events from an $A_2 \rightarrow \pi\eta^0$ decay. The A_2 cut at 1.6 GeV in the $\pi_{\text{F}}^{\pm}\eta^0$ mass only eliminated events with an $\eta^0 p$ mass above about 2 GeV. The histograms in Fig. IV.3a are for events to either side of the η^0 peak. The η^0 wings are defined by the $\pi^+\pi^-\pi^0$ mass region of 420 to 600 MeV except for that portion within the η^0 peak cuts given above. These histograms have been normalized to the number of events in the background under the η^0 peaks as gotten from the fits to the $\pi^+\pi^-\pi^0$ mass spectra discussed earlier. The $\eta^0 p$ mass spectra in Fig. VI.3b have these background distributions subtracted and show no significant changes from those in Fig. VI.3a.

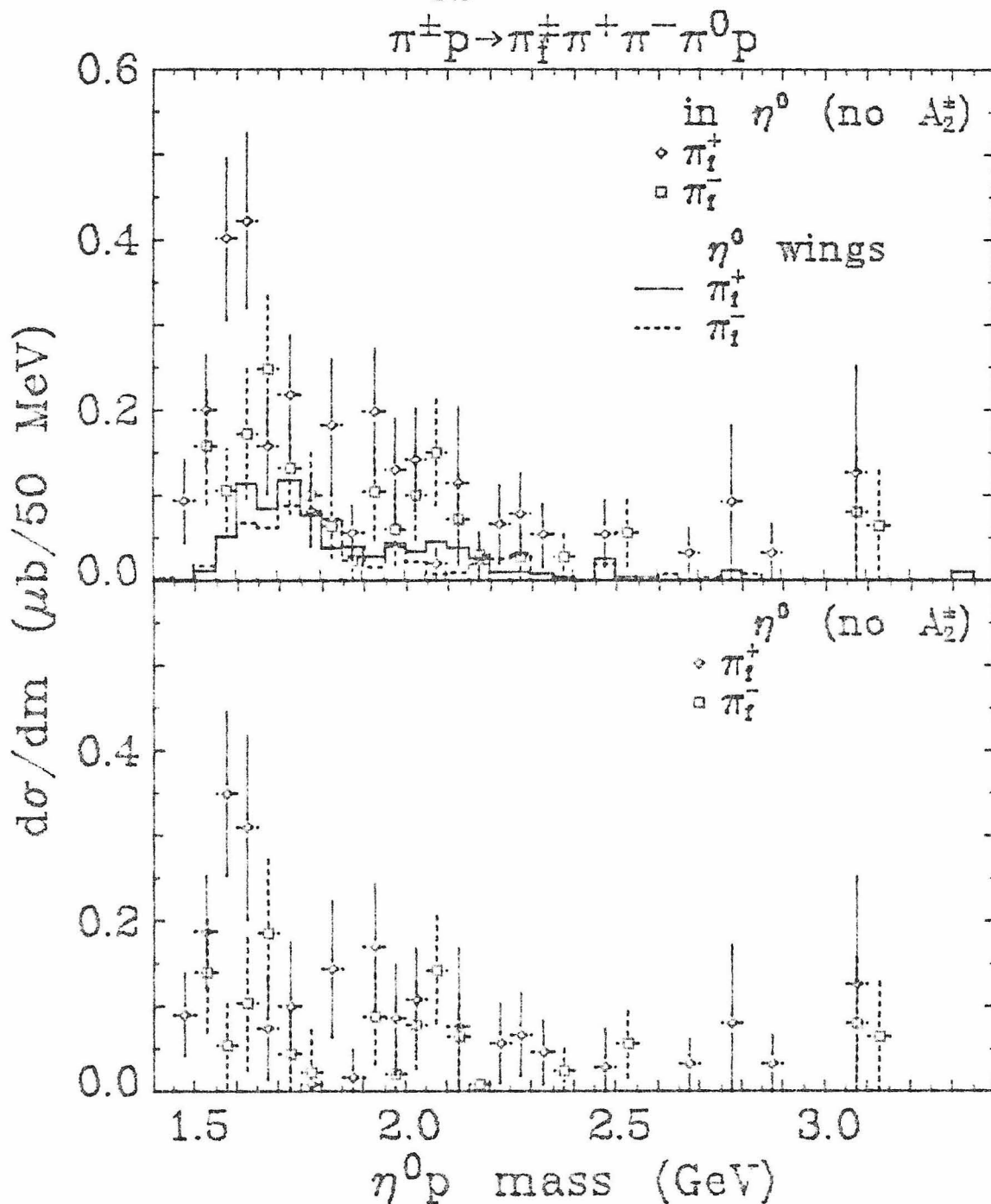


Figure VI.3

Plots of the $\eta^0 p$ mass spectra for the π^+ and π^- experiments. The upper plot (a) is for all events within the η^0 peak cuts (see text). For the lower plot (b), the background distributions from events under the η^0 have been subtracted (see text).

Figs. VI.5 are scatterplots of the $\pi^+\pi^-\pi^0$ mass versus the $\pi^+\pi^-\pi^0 p$ mass (each event corresponds to a single dot). While the η^0 band is clearly seen for the π^+ data (Fig. VI.5a), the η^0 band is barely noticeable in the π^- data. The π^+ data also shows a clustering of events in the η^0 band near an $\eta^0 p$ mass of 1600 MeV where the $\eta^0 p$ mass spectrum shows a peak (Figs. VI.3).

The $d\sigma/dt_{\pi\pi}$ distributions for the η^0 events were fit with the functional form Ae^{bt} giving values for the slope (b) of 6.06 ± 0.97 $(\text{GeV}/c)^{-2}$ for the π^+ data and 6.78 ± 1.58 $(\text{GeV}/c)^{-2}$ for the π^- data. These slopes are significantly larger than those found for the overall $\pi_{\pm}^{\pm}\pi^+\pi^-\pi^0 p$ data (Chapter V) and are consistent with general observations of the t-dependence of N^* production.

The Feynman diagrams in Fig. VI.4 illustrate two processes that could contribute to the observed difference in the π^+ and π^- cross sections for η^0 production. The use of Regge exchange terminology provides a framework for discussion, but not an explicit explanation of the difference. The interference between different Regge exchanges from the top vertex could account for the cross section difference. As a simple example, let us examine an amplitude made up of both Pomeron and ρ exchange parts. When the charge of the beam is changed from π^+ to π^- (i.e. from particle to antiparticle), the sign of the ρ term is changed. This leads to a form for the cross section of:

$$\frac{d\sigma}{dt}(\pi^{\pm}) \propto |P|^2 + |\rho|^2 \pm 2\text{Re}(P\rho^*) \quad (4)$$

where the Pomeron (P) and ρ interference term accounts for the differ-

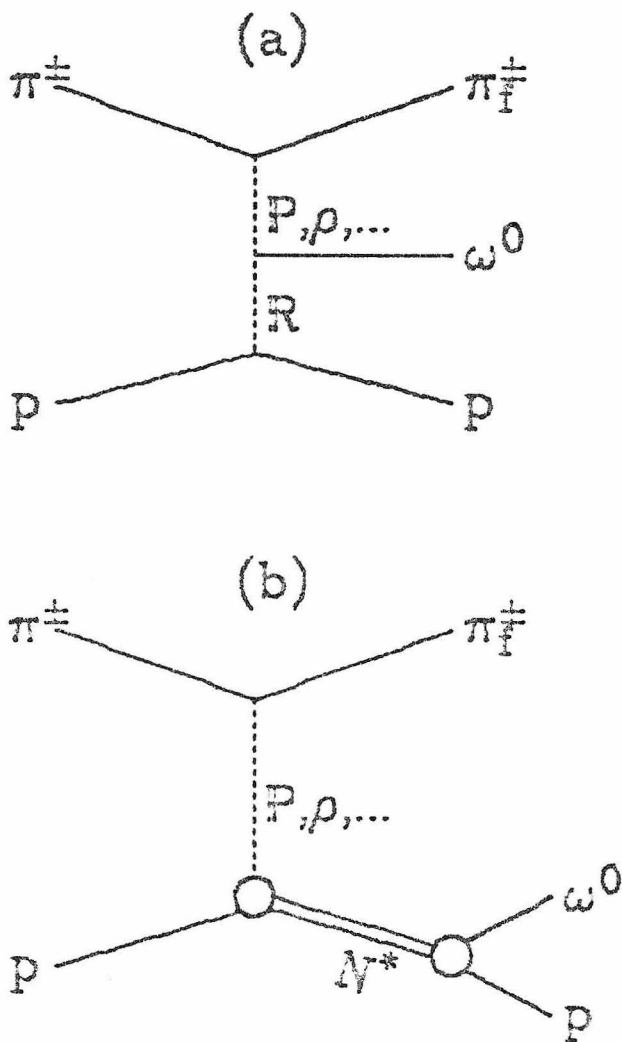


Figure VI.4

Feynman diagrams illustrating possible processes involved in our observed η^0 production, including double Regge exchange (a) and the production of an N^* that couples to $\eta^0 p$ (b).

ence in the π^+ and π^- cross sections. The sign of the interference term in equation (4) as being the same as the sign of the beam was arbitrary and suggested by the data with the assumption that $\text{Re}(P\rho^*)$ is greater than zero.

The $\eta^0 p$ mass spectrum (Figs. VI.3) for the π^+ experiment shows a peak centered at about 1600 MeV with a width of about 100 MeV (FWHM). The π^- mass spectrum is suggestive of a slight dip of marginal statistical significance at the same position as the peak in the π^+ spectrum. About 2/3 of the difference in the $\pi_f^+ \eta^0 p$ and $\pi_f^- \eta^0 p$ cross sections comes from the $\eta^0 p$ mass region below 1.8 GeV. The peak in one mass distribution and the marginal dip in the other are consistent with the simple model discussed above. Here the N^* excitation illustrated by the Feynman diagram in Fig. VI.4b may have both Pomeron and ρ exchange (or some other negative signature trajectory in place of the ρ) contributions which interfere. As discussed before, this could enhance the π^+ cross section and decrease the π^- cross section giving rise to a peak in the one mass spectra and a dip in the other. There is a well known N^* with a large $\eta^0 p$ branching ratio [Particle Data Group 1978]. The $N(1535)$ decays about 65% of the time to $\eta^0 p$, but it has too low a mass to be completely consistent with its interpretation as the cause of the $\eta^0 p$ peak in the π^+ data.

In conclusion, our results on the $\pi_f^\pm \eta^0 p$ final states have shown that the π^+ cross section is larger than the π^- cross section. A significant part of this difference is due to a peak at 1600 MeV in the $\eta^0 p$ mass distribution of the π^+ data and a lack of such a peak in the

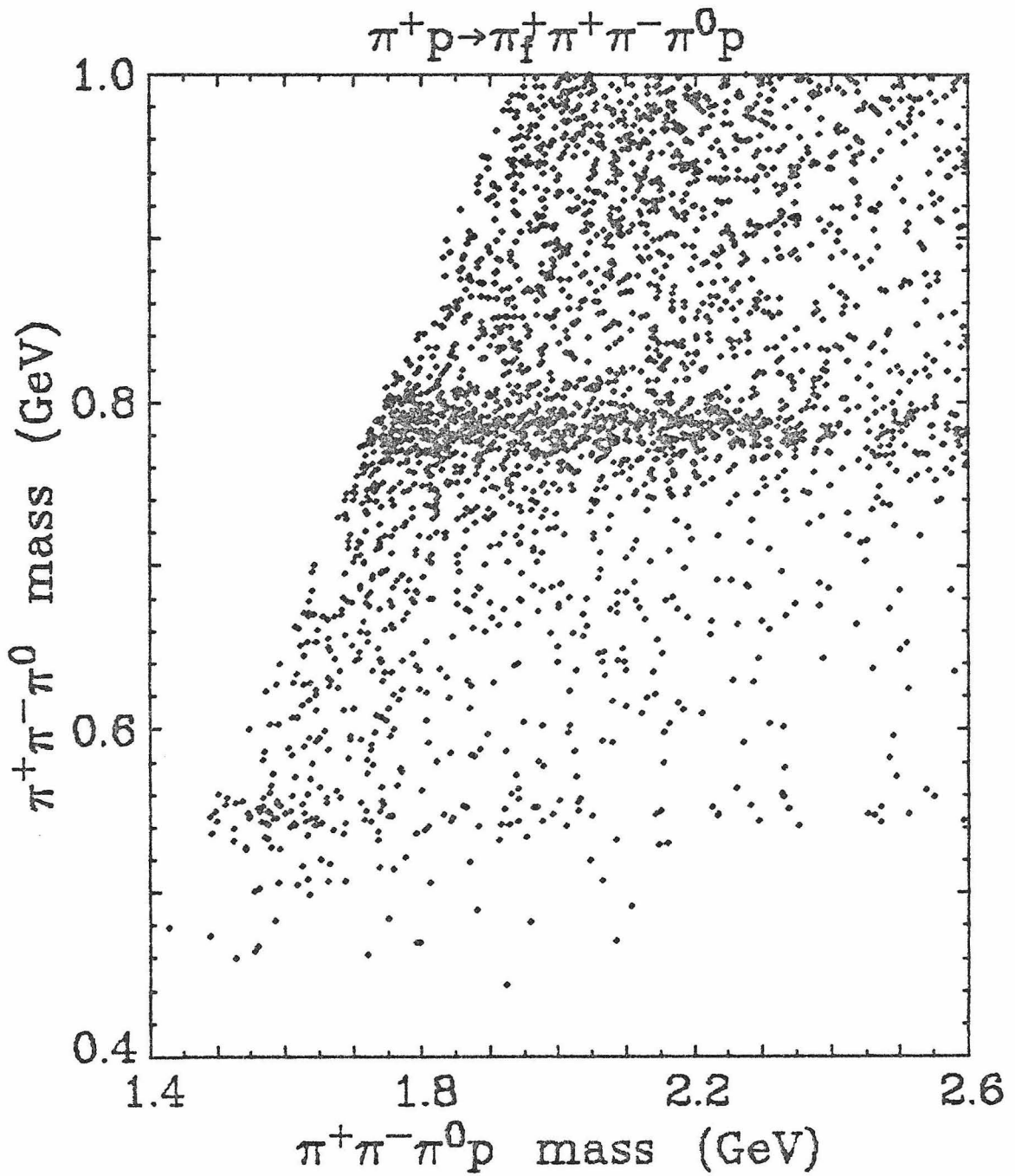


Figure VI.5a

Scatterplot showing the correlations between the $\pi^+ \pi^- \pi^0$ invariant mass and the $\pi^+ \pi^- \pi^0 p$ invariant mass for the $\pi^+ p \rightarrow \pi^+ \pi^+ \pi^- \pi^0 p$ channel.

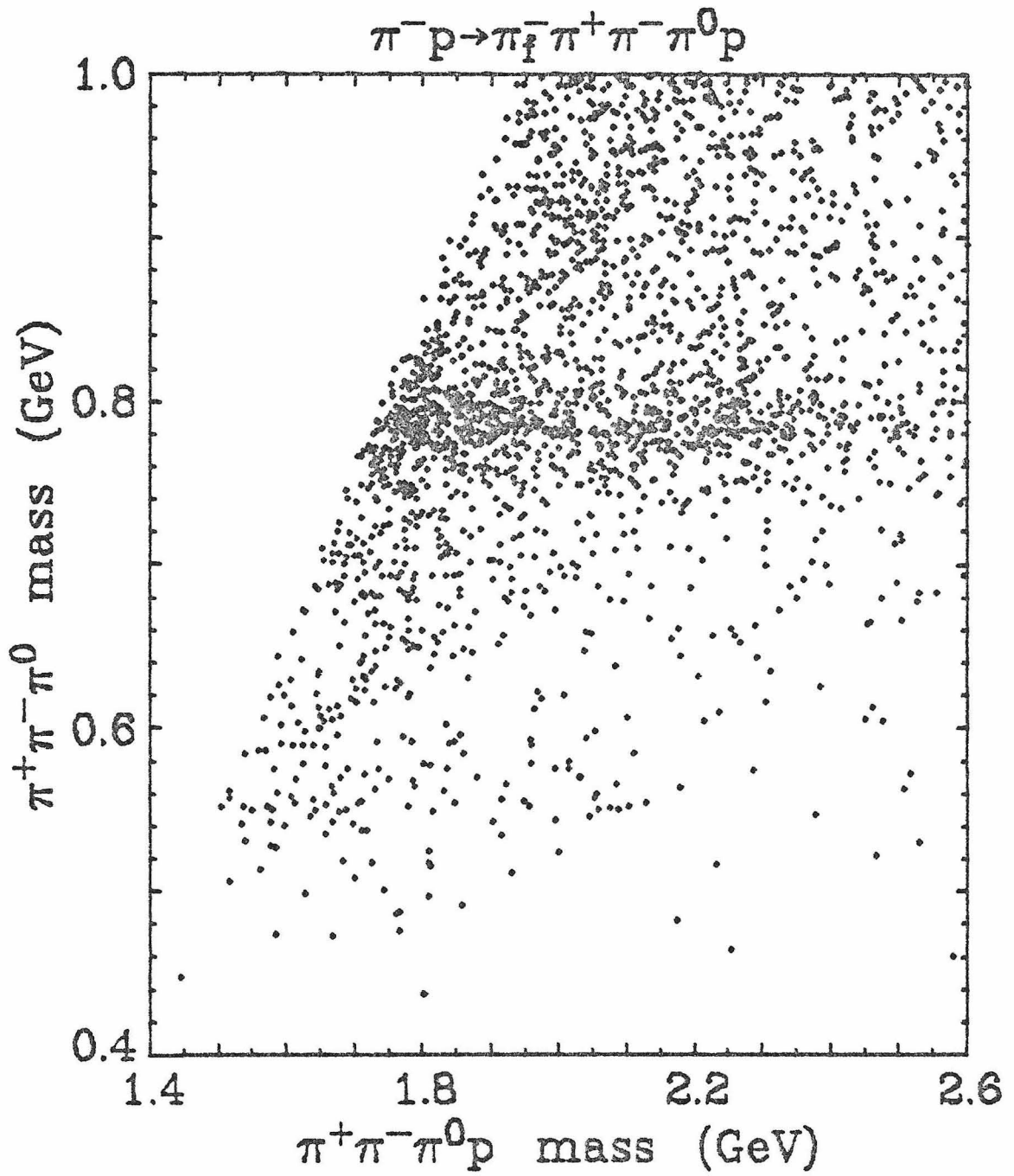


Figure VI.5b

Scatterplot showing the correlations between the $\pi^+ \pi^- \pi^0$ invariant mass and the $\pi^+ \pi^- \pi^0 p$ invariant mass for the $\pi^- p \rightarrow \pi_f^- \pi^+ \pi^- \pi^0 p$ channel.

η^0 p mass distribution of the π^- data. This difference can be understood by a simple Regge exchange model where a vacuum-like trajectory interferes with a negative signature trajectory. The sign of the interference term is dependent upon the charge of the pions at the beam and fast pion vertex, enhancing one cross section and reducing the other.

3. $\pi^\pm \omega^0$ p Final State

By looking at the $\pi^+ \pi^- \pi^0$ decay of the ω^0 as we did for the η^0 , we observe copious production of reactions (1b). The scatterplots in Figs. VI.5 show densely populated bands at the ω^0 mass with a dense clustering of events near the ω^0 p threshold. We find that there is a relatively narrow (compared to many other baryon resonances) enhancement just above the ω^0 p threshold. Previous results on this enhancement by this and other experiments were summarized in Table I.7.

Fig. VI.6 shows the $\pi^+ \pi^- \pi^0$ mass spectra in the region of the ω^0 . The prominent ω^0 peak has been fitted by a Breit-Wigner shape with a quadratic background (see discussion of the η^0 peak). The results of these fits are summarized in Table VI.2 below. The widths of the peaks are due to the finite resolution in the $\pi^+ \pi^- \pi^0$ mass of about 28 MeV in the region of the ω^0 (FWHM). The errors on the cross sections in Table VI.2 include the contributions from the normalization errors. Notice that unlike the η^0 case, the π^+ and π^- production cross sections for the ω^0 are nearly equal (in fact they agree within their errors). The approximately equal cross sections would indicate that

$\pi^\pm p \rightarrow \pi_f^\pm p \pi^+ \pi^- \pi^0$
Fits to ω^0 peak

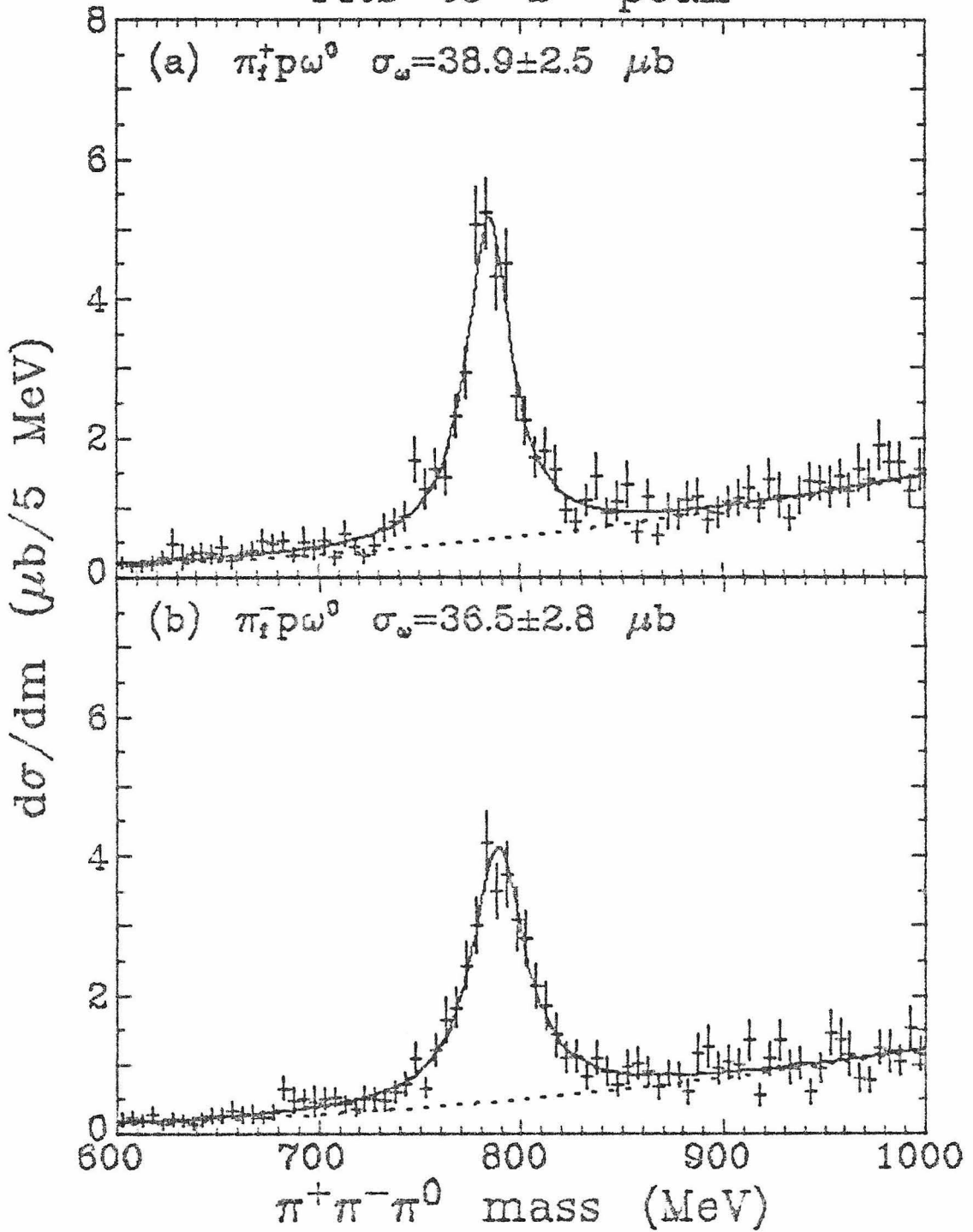


Figure VI.6

Plots of $d\sigma/dm$ for $\pi^+ \pi^- \pi^0$ masses in the region of the ω^0 . The curves are the results of the fits discussed in the text.

only one trajectory was dominately responsible for the ω^0 production (see the discussion of the η^0 production).

Table VI.2

<u>Fitted parameters for $\omega^0 \rightarrow \pi^+ \pi^- \pi^0$ peak</u>		
	<u>π^+</u>	<u>π^-</u>
Mass (MeV)	784.19±0.76	788.45±0.95
Width (FWHM, MeV)	26.7±2.3	31.8±3.1
Events in peak	3086±197	2518±191
Observed cross section (μb)	38.9±3.1	36.7±3.4
Corrected cross sections (μb):		
for low $t_{\pi\pi}$ losses	39.7±3.2	38.2±3.6
$t_{\pi\pi}$ losses and unseen decays	44.3±3.6	42.6±4.0
Fraction of estimated total $\sigma(\pi p \rightarrow \pi \omega^0 p)$ (Table I.6)	48±8%	68±13%

The ω^0 events were selected for further study by cuts on the $\pi^+ \pi^- \pi^0$ mass at the ω^0 peak: 740 to 820 MeV for the π^+ data and 745 to 825 MeV for the π^- data. The ratio of the full ω^0 Breit-Wigner to the portion within these cuts is used to correct cross sections (such as that of the $\omega^0 p$ resonance) for those ω^0 events lost by this mass cut. This ratio is 1.261 ± 0.097 for the π^+ and 1.319 ± 0.090 for the π^- . The events on either side of the ω^0 (the ω^0 wings) were used to study the effect of the background events under the ω^0 peak. The wings were defined by cuts of 600 to 960 MeV excluding the region selected by the ω^0 peak cuts.

Figures VI.7a-b

Plots of the weighted Λ distributions for events in the ω^0 peak (the solid histogram) and in the ω^0 wings (the dotted histogram). The dotted line is a constant fitted to the wings data and the solid line is a fit of $(a+b\Lambda)$ to the ω^0 peak data.

-255-
 $\pi^+ p \rightarrow \pi_1^+ \pi^+ \pi^- \pi^0 p$

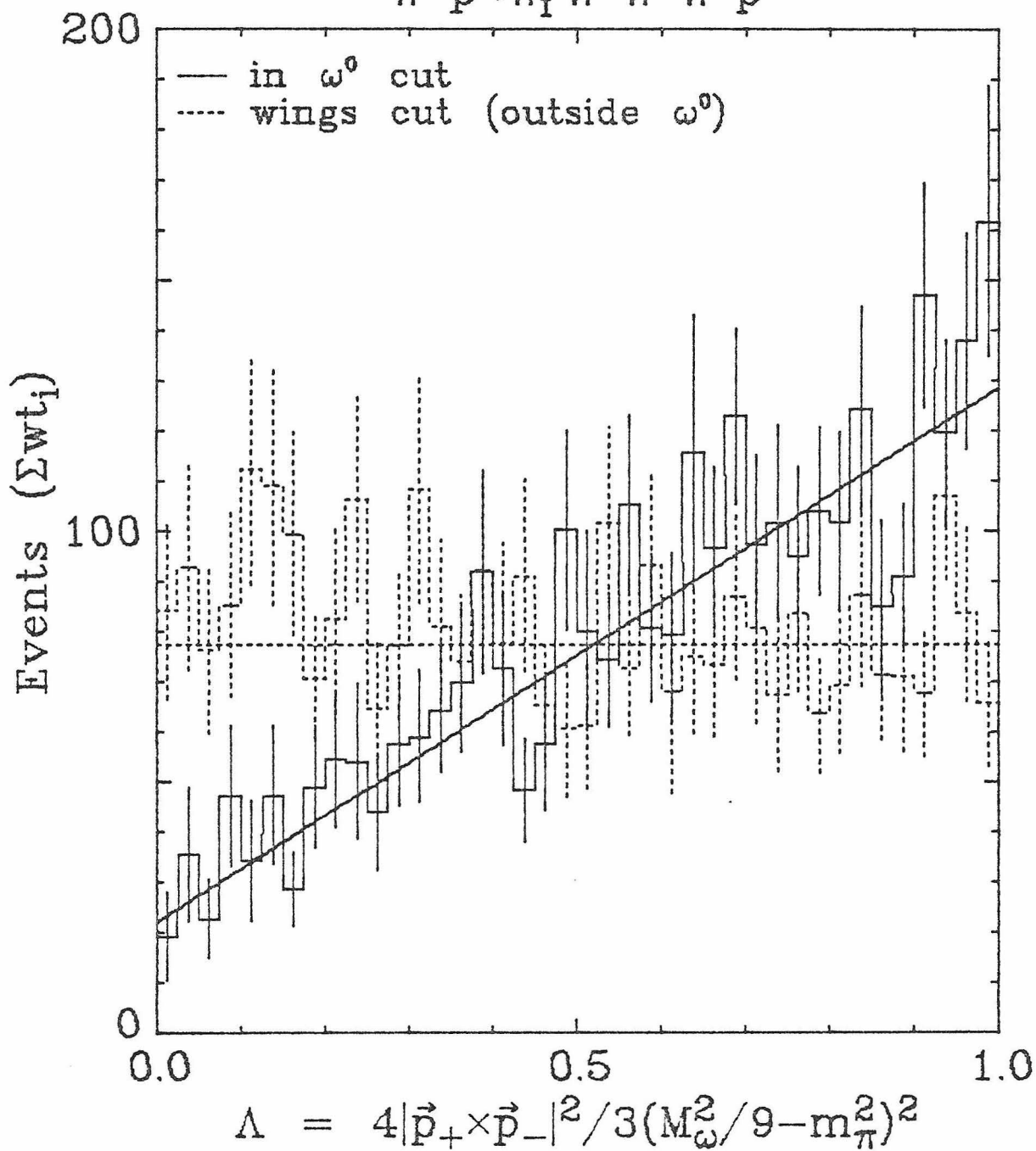


Figure VI.7a

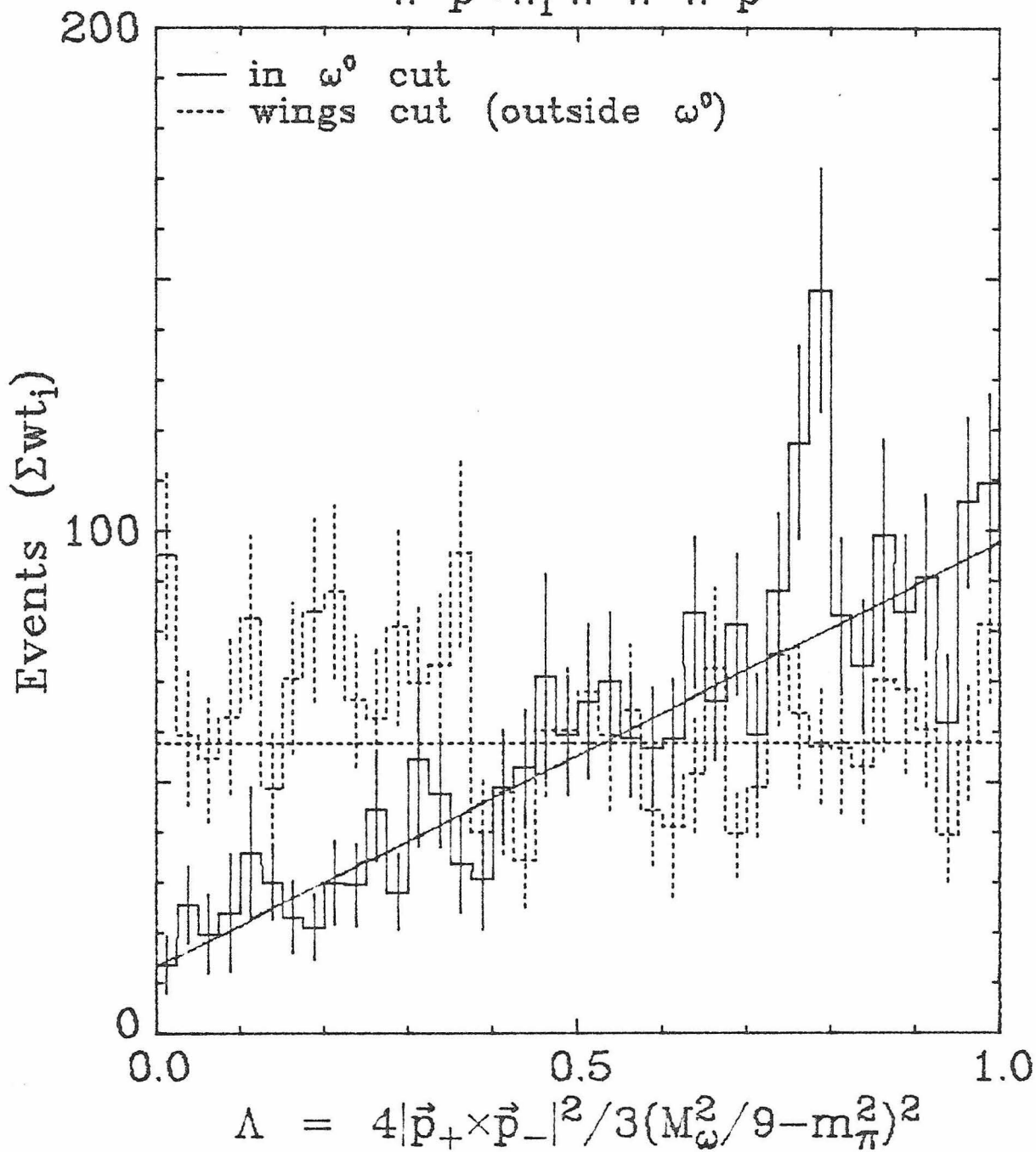
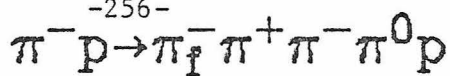


Figure VI.7b

We determined the number of background events in the ω^0 peak cut from the integral of the background distribution gotten from the fit to the $\pi^+\pi^-\pi^0$ mass distribution. This result was checked by studying the distributions of the radial Dalitz variable, Λ , for events in the ω^0 peak and wings (see Figs. VI.7). Λ runs from 1 at the center of the ω^0 Dalitz plot to 0 at the edges and is given by:

$$\Lambda = \frac{4}{3} \frac{|\vec{p}_+ \times \vec{p}_-|^2}{(M_\omega^2/9 - m_\pi^2)^2} \quad (5)$$

where \vec{p}_+ and \vec{p}_- are the 3-vector momenta of the π^+ and π^- in the ω^0 (or $\pi^+\pi^-\pi^0$) rest frame, M_ω is the $\pi^+\pi^-\pi^0$ invariant mass, and m_π is the mass of a pion. For ω^0 decays the Λ distribution is proportional to Λ ; the non- ω^0 events show up as a distribution uniform in Λ [Atherton 1975]. Thus in Figs. VI.7 the Λ distributions for wings events are flat while those for ω^0 peak events are linear in Λ on top of a constant piece from the background under the ω^0 peak. The ω^0 peak data was fit by $a+b\Lambda$ so that the value of a corresponds to the number of background events under the ω^0 peak. The results of these fits agreed with the background integrals from the $\pi^+\pi^-\pi^0$ mass fits. A weighted average of the results for the ω^0 background from fits to the $\pi^+\pi^-\pi^0$ mass distributions and the Λ distributions (Figs. VI.7) gave $23.7 \pm 2.0\%$ for the π^+ and $21.1 \pm 2.4\%$ for the $\pi^- \omega^0$ background.

Fig. VI.8 shows the $d\sigma/dt_{\pi\pi}$ distributions for the π^+ and π^- events in the ω^0 peak. These distributions were fitted by an exponential and gave slopes of 4.68 ± 0.24 (GeV/c) $^{-2}$ for the π^+ data and 4.99 ± 0.27

Figure VI.8

Plots of $d\sigma/dt_{\pi\pi}$ (beam to fast π) for events in the ω^0 peak. The curves are the results of fitting Ae^{bt} to the data.

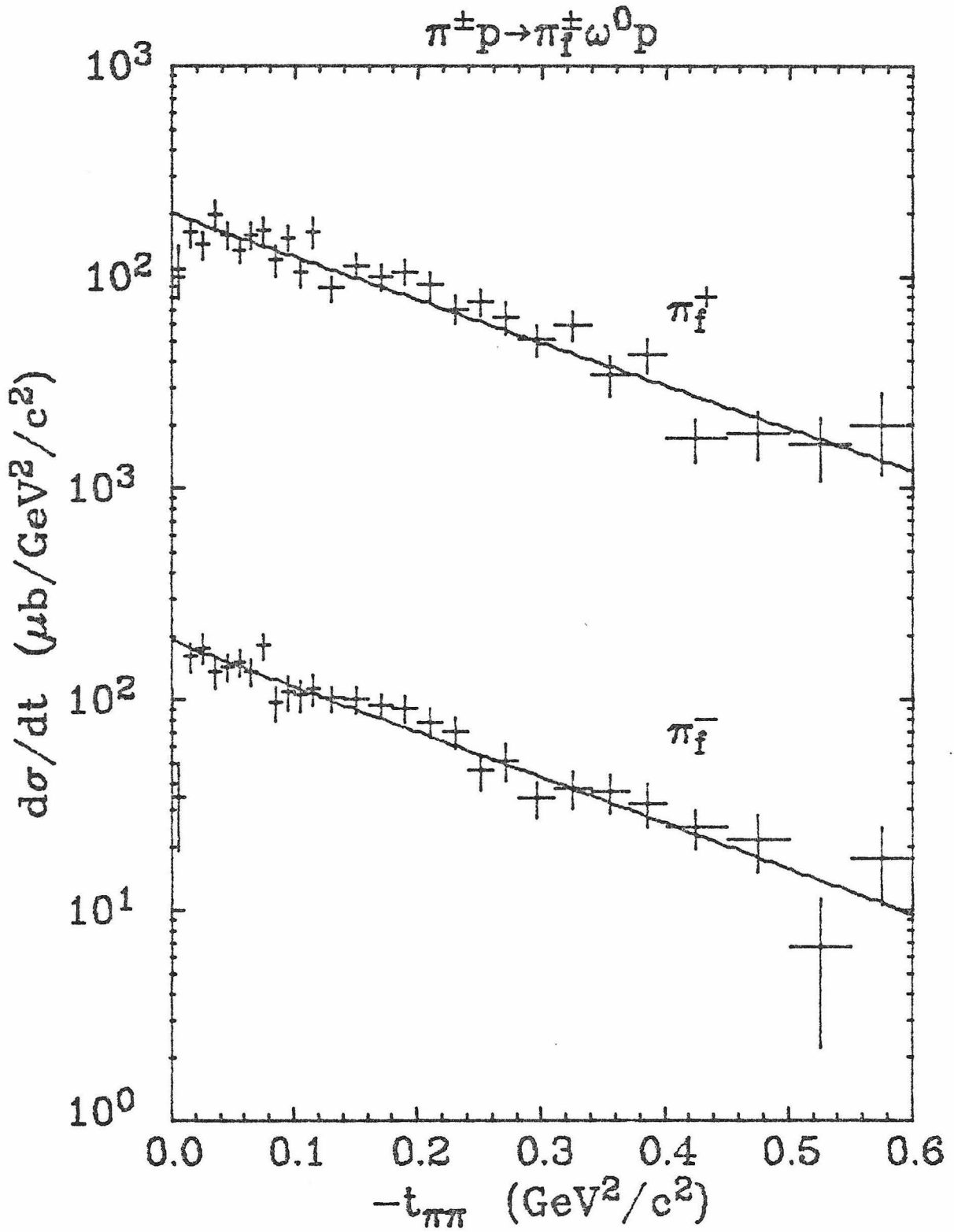


Figure VI.8

$(\text{GeV}/c)^{-2}$ for the π^- data. The results of these fits were then used to correct the ω^0 production cross sections (Table VI.2) for the loss of events at low $|t_{\pi\pi}|$. These corrections amounted to $2.2 \pm 1.8\%$ for the π^+ cross section and $4.1 \pm 1.3\%$ for the π^- cross section. In addition, Table VI.2 gives the ω^0 production cross section corrected for the unseen ω^0 decays by using a branching ratio of $89.6 \pm 0.6\%$ for the $\omega^0 \rightarrow \pi^+ \pi^- \pi^0$ mode [Particle Data Group 1978].

Fig. VI.9 shows the $\omega^0 p$ mass distributions for π^+ and π^- events in the ω^0 peak. The histograms show the $\pi^+ \pi^- \pi^0 p$ mass distributions for events in the ω^0 wings rescaled to the ω^0 peak background integrals so as to represent the non- ω^0 background signal beneath the ω^0 peak. The scatterplots in Fig. VI.10 show that the $\omega^0 p$ peak is not a reflection of a $\pi_f^\pm \omega^0$ resonance. In addition, Fig. VI.11a indicates that the peak is not associated with the Δ^{++} resonance as the $\pi^+ p$ mass distribution has its maximum at about 1150 MeV (well below the Δ mass) in the region of the $\omega^0 p$ peak. The events in the ω^0 wings show some association with the Δ^{++} as can be seen from the band of events just above a $\pi^+ p$ mass of 1200 MeV in Fig. VI.11b.

The curves in Fig. VI.9 are the result of fitting the $\omega^0 p$ mass distribution with a Breit-Wigner shape ($\Gamma(m) = \Gamma_R$) and a polynomial background giving the parameters in Table VI.3. The cross section errors in the table include the contributions from the normalization errors. Table VI.3 also lists the peak cross section corrected for ω^0 events in the Breit-Wigner tails outside the ω^0 peak cut and so lost from the mass distribution. The low $|t_{\pi\pi}|$ loss corrections of $3.9 \pm 5.3\%$

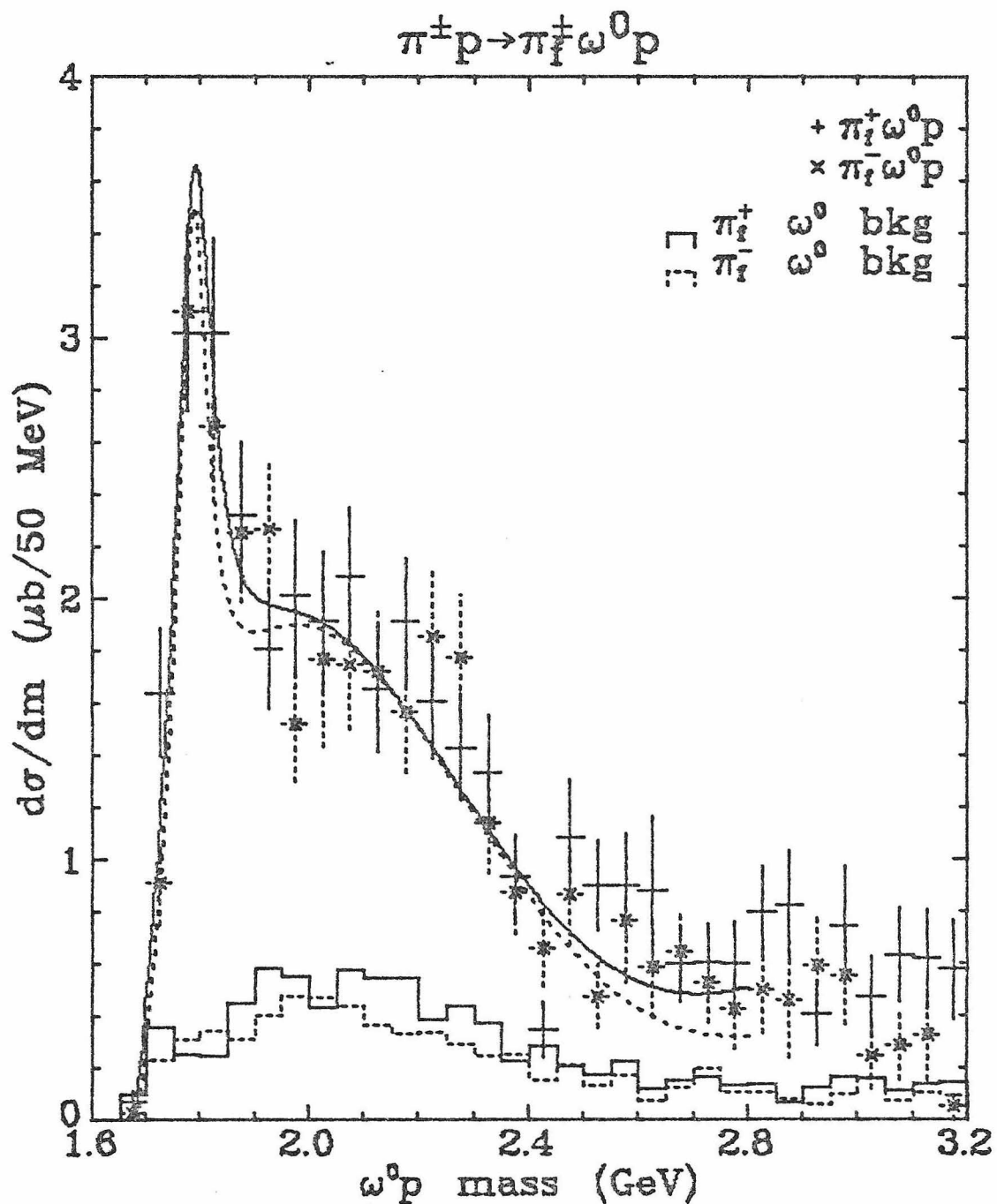


Figure VI.9

$\omega^0 p$ mass distributions for the π^+ and π^- data. The curves are the results of the fits described in the text. The histograms are the $\omega^0 p$ mass distributions from the backgrounds under the ω^0 peaks (see text).

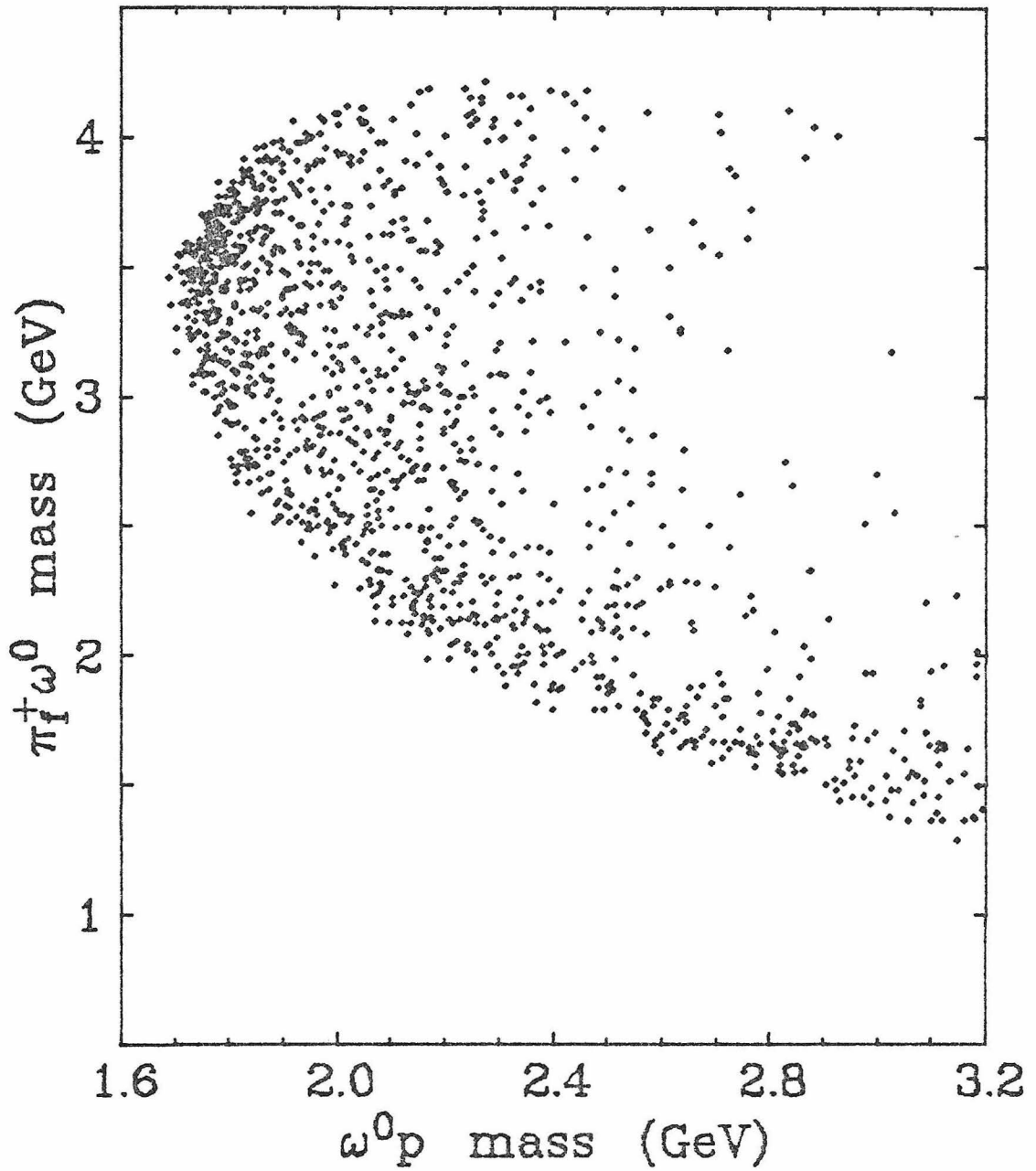
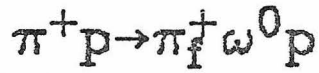


Figure VI.10

Scatterplot of the $\pi^+ \omega^0$ invariant mass versus the $\omega^0 p$ invariant mass for events within the ω^0 peak. The π^- plot is similar to this one.

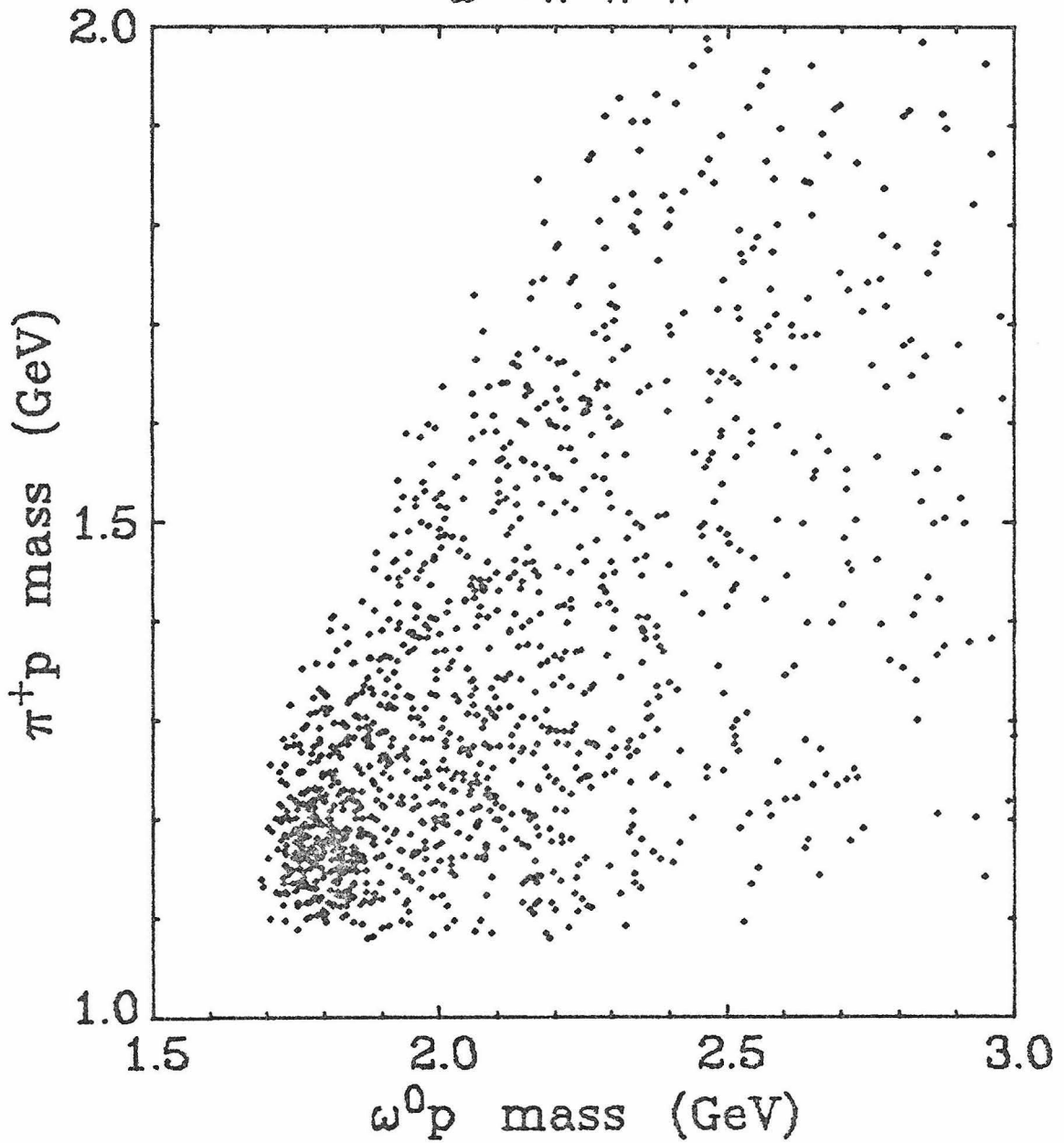
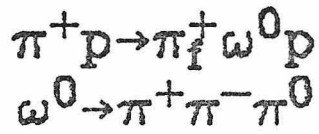


Figure VI.11a

Scatterplot of the $\pi^+ p$ invariant mass versus the $\omega^0 p$ invariant mass for events within the ω^0 peak. The plot for the π^- data is similar to this one.

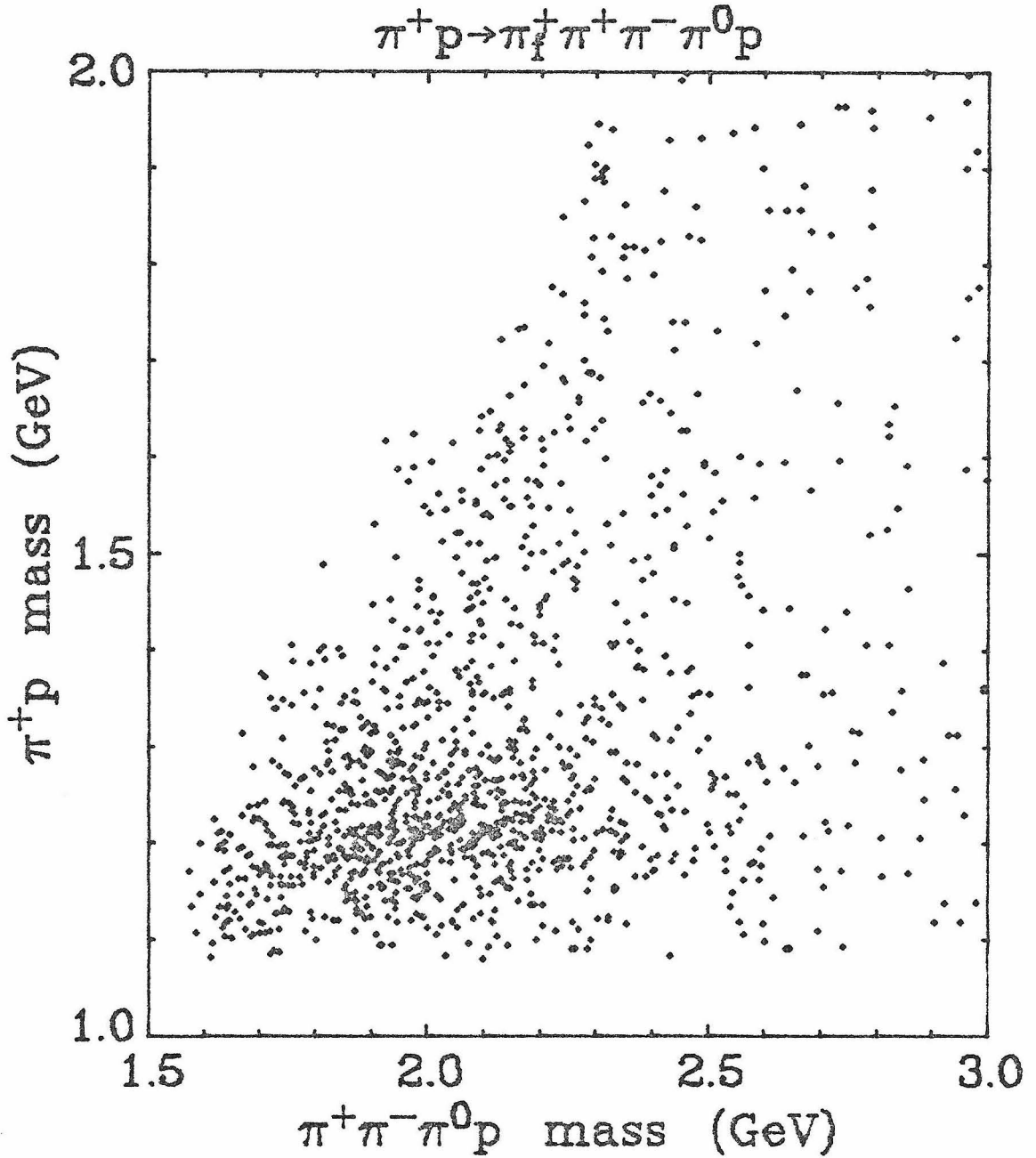


Figure VI.11b

Scatterplot of the $\pi^+ p$ invariant mass versus the $\pi^+ \pi^- \pi^0 p$ invariant mass for events within the ω^0 wings. The π^- plot is once again similar to this one.

for the π^+ cross section and $7.6 \pm 3.5\%$ for the π^- cross section are also included in Table VI.3. These correction values were gotten from the $d\sigma/dt_{\pi\pi}$ distributions for ω^0 p masses below 1.9 GeV (see below) and so are different from those quoted earlier for the total ω^0 production. Finally, the cross sections corrected for the unseen decays of the ω^0 are listed in the table.

Table VI.3

Fitted parameters for the ω^0 p peak

	<u>π^+</u>	<u>π^-</u>
Mass (MeV)	1787.8 \pm 6.4	1786.3 \pm 5.5
Width (FWHM, MeV)	86.3 \pm 12.8	67.7 \pm 10.4
Fitted cross section (μb)	7.16 \pm 0.89	5.13 \pm 0.63
Corrected cross sections (μb):		
For ω^0 peak cut and $t_{\pi\pi}$ loss	9.4 \pm 1.5	7.3 \pm 1.1
And for unseen ω^0 decays	10.5 \pm 1.6	8.1 \pm 1.2

By summing the π^+ and π^- data and fitting as before, we find a mass of 1788.7 ± 4.5 MeV and a width of 80.7 ± 8.6 MeV for the resonance. Refitting the π^+ and π^- data separately with the mass and width fixed at these values gave cross sections in excellent agreement with those given in Table VI.3. Fitting with a mass-dependent width (see Chapter V, $\lambda=0$) changed the cross section values by only a few percent. Likewise, using the low $t_{\pi\pi}$ correction figures for the overall ω^0 production gave a change of only a few percent, well within the quoted errors.

Figures VI.12a-b

Plots of $d\sigma/dt_{\pi\pi}$ for events in the ω^0 peak for different ω^0 p mass regions. The curves are from fits of Ae^{bt} to the distributions.

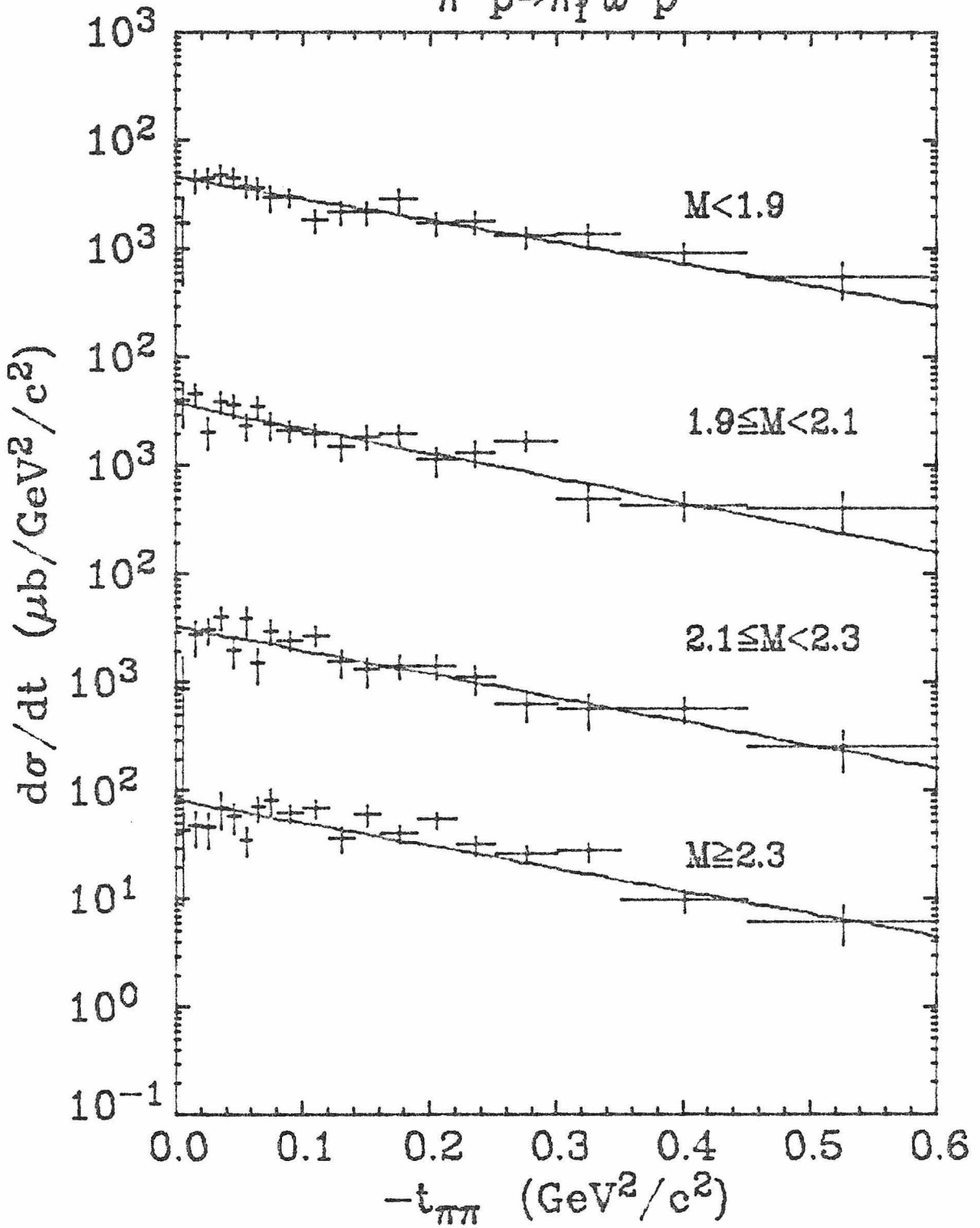
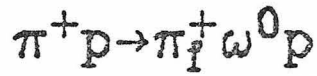


Figure VI.12a

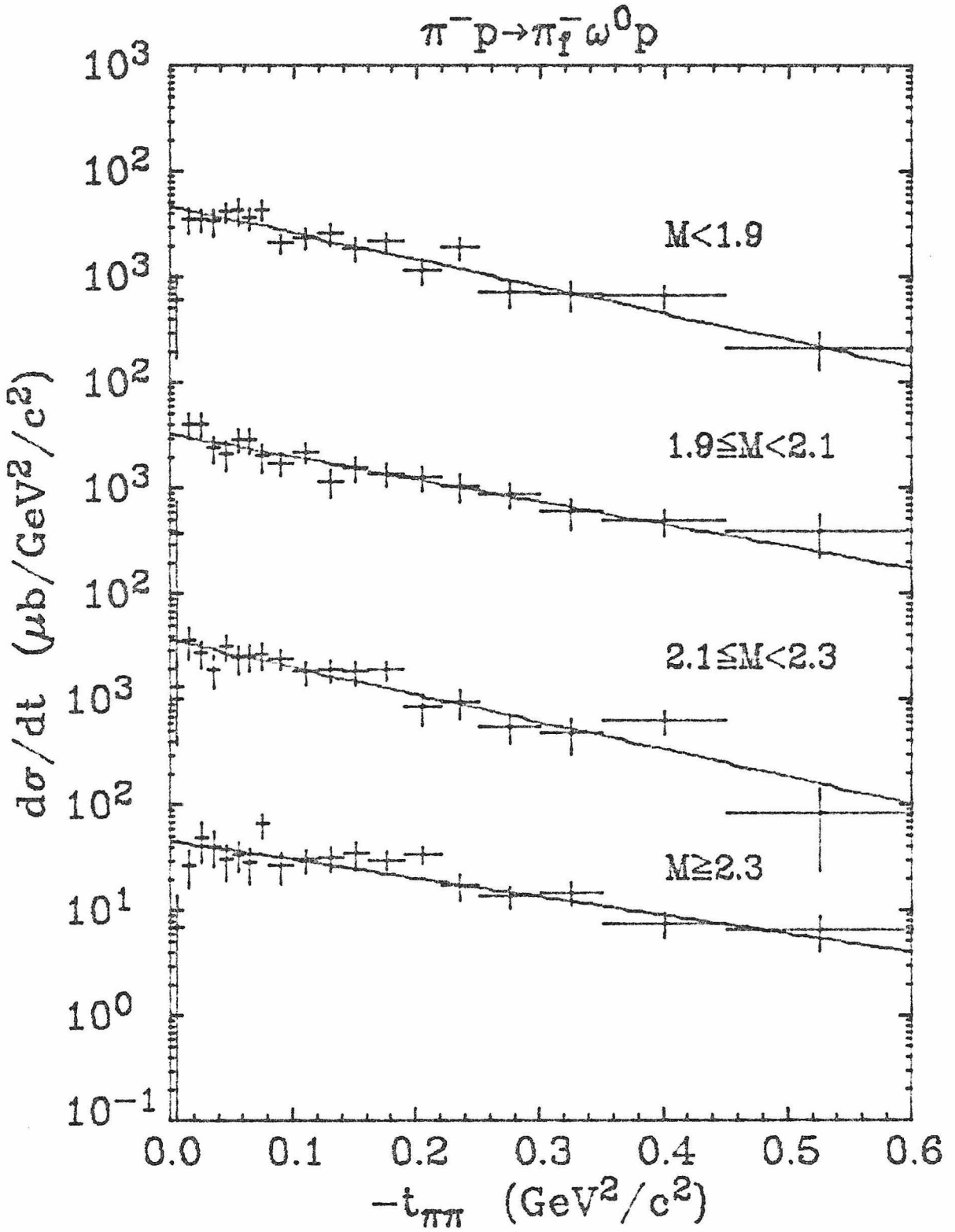


Figure VI.12b

To continue our study of the ω^0 production, we divided the ω^0 p mass distribution into four regions: below 1.9 GeV, 1.9 to 2.1 GeV, 2.1 to 2.3 GeV, and above 2.3 GeV. The first region thus contains the ω^0 p resonance. However, a large fraction of the events in this region are non-resonant background under the ω^0 p peak: $42.1 \pm 4.2\%$ in the π^+ and $45.7 \pm 3.9\%$ in the π^- data. Table VI.4 gives the slopes resulting from fits of exponentials to the $d\sigma/dt_{\pi\pi}$ distributions for the four ω^0 p mass bands. Figs. VI.12 give these $d\sigma/dt_{\pi\pi}$ distributions and the fitted curves. The results are in fair agreement with those of Milgram et al. [1974], though their results have a slightly larger slope (~ 6 (GeV/c) $^{-2}$) the difference between the two experiments is not statistically significant. Note that our results indicate that there is no change in the t-dependence with increasing ω^0 p mass. In particular, there is no change in the t-dependence of events on-resonance and off-resonance.

Table VI.4

<u>ω^0 p mass region (GeV)</u>	<u>$d\sigma/dt_{\pi\pi}$ slopes for ω^0 p mass bands</u>	
	<u>slope ((GeV/c)$^{-2}$)</u>	
	<u>π^+</u>	<u>π^-</u>
<1.9	4.62 ± 0.44	5.82 ± 0.48
1.9-2.1	5.27 ± 0.55	4.90 ± 0.62
2.1-2.3	5.08 ± 0.66	6.00 ± 0.61
≥ 2.3	4.86 ± 0.41	4.05 ± 0.50

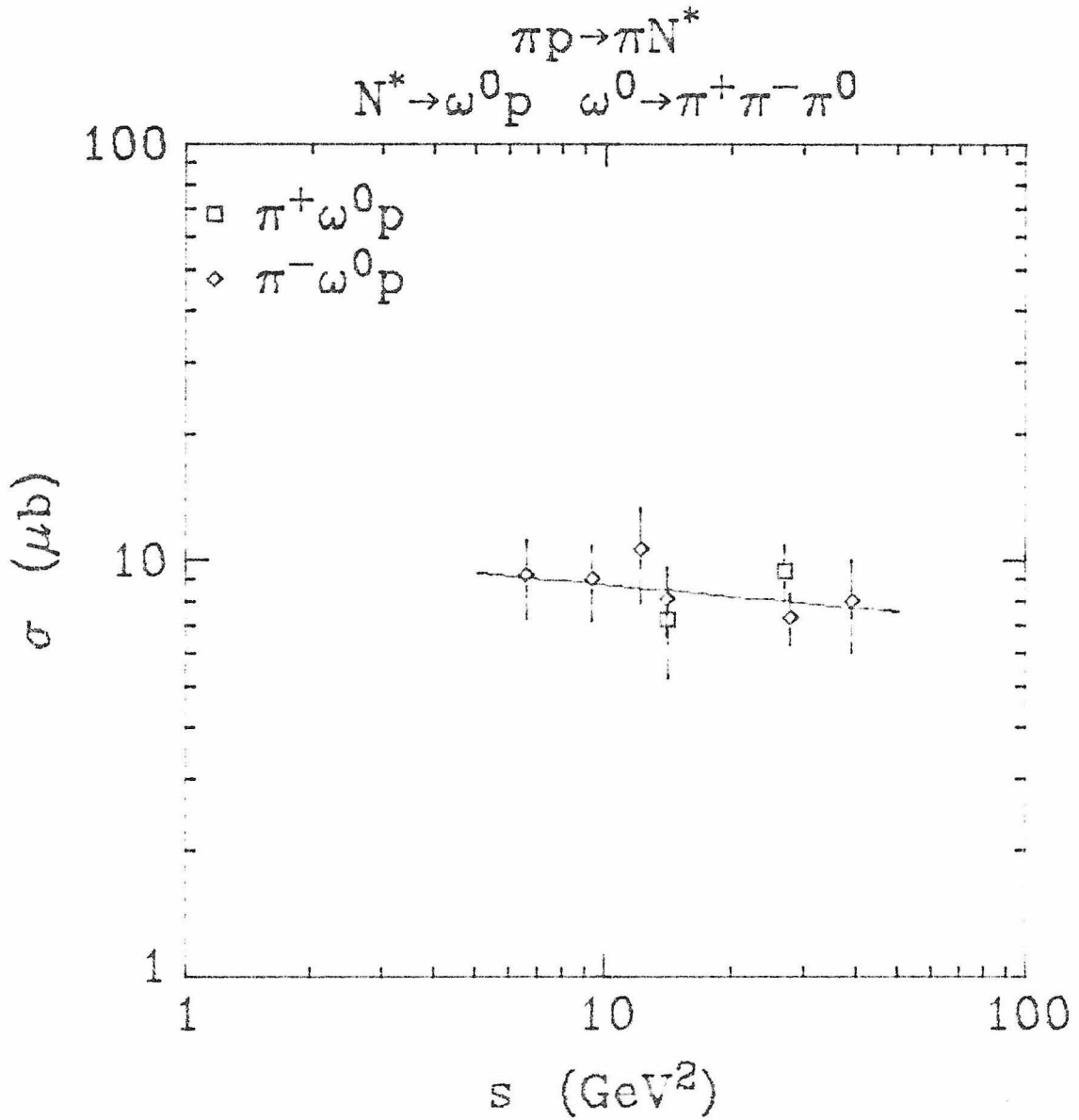


Figure VI.13

Plot of the s dependence of the production cross section for $N^* \rightarrow \omega^0 p$. The data is from several experiments including this one. The curve is a fit to as^{-n} giving $n=0.09 \pm 0.13$. The cross sections are for the $\omega^0 \rightarrow \pi^+ \pi^- \pi^0$ decay mode only.

Fig. VI.13 shows the s dependence of the $\omega^0 p$ resonance production cross section. In addition to the data presented here, lower energy points from our previous papers [Davidson 1974 and Linglin 1974] and the results from other experiments [Milgram 1970 and Sisterson 1970] have been included. The cross section shows little s dependence, and a fit of as^n yields -0.09 ± 0.13 for n . This supersedes our previous result of -0.66 ± 0.06 which was based on only 3 data points [Davidson 1974] and a slightly lower value for the π^- production cross section of the $\omega^0 p$ cross section from our experiment (the earlier paper did not include all the corrections). This rather flat s dependence fits very well with a diffractive excitation picture for the $\omega^0 p$ resonance [Lednicky 1975].

This $\omega^0 p$ threshold enhancement has been seen in several other experiments at various energies and with K and proton beams in addition to pion beams (see Table I.7). The small width of this peak has lead us and several other authors [Atherton 1975 and Milgram 1970 for example] to interpret it as a previously unknown N^* or a new decay mode of a known resonance. There are two known N^* resonances of good standing which have masses near that found for the $\omega^0 p$ resonance: $N(1780)$ and $N(1810)$ [Particle Data Group 1978]. Both have widths (about 160 and 200 MeV respectively) far larger than that observed for the $\omega^0 p$ resonance. Since the $\omega^0 p$ peak is very near threshold, other authors have investigated other models in search of a non-resonant explanation for the peak. Milgram [1970] investigated diffraction models and a Double Regge Pole exchange model and we also tried a

Regge model as reported in our earlier paper [Davidson 1974]. Simple models of this kind fail to reproduce the narrow peak; they produce a broad enhancement usually 200 MeV or more in width much like the A_1 enhancement in π diffraction. Some analyses [Milgram 1970 and Theocharopoulos 1974 for example] obtained better matches to their data with more complex models at the expense of introducing many parameters into the model. However, these experiments had lower statistics than this one and observed a slightly broader peak which made it easier to match a model to the data.

In conclusion, we find a relatively narrow threshold enhancement in the $\omega^0 p$ mass. Both the total ω^0 production cross sections and the $N^* \rightarrow \omega^0 p$ cross sections are independent of the charge of the beam to a good approximation. The N^* cross section is also independent of the beam energy; indicating that it is a diffractively produced state. At this point it is unclear whether this is a new N^* or a new decay mode of a previously observed state. Determination of the spin-parity of this state can shed light on this question.

4. Angular Distributions of the $\omega^0 p$ System

4a) Phenomenology of Angular Distributions

We will now turn to studies of the angular distributions of the $\omega^0 p$ system in an effort to determine the spin-parity of the N^* . Mostly we will present results for the two lowest $\omega^0 p$ mass bins. Events in the 1.9 to 2.1 GeV mass band are taken to illustrate the angular distributions of the background events under the N^* peak in the lowest mass band ($\omega^0 p$ masses below 1.9 GeV). Likewise, angular distributions for events in the ω^0 wings serve to illustrate the effects of the background events under the ω^0 peak. Note that two separate background sources are involved; one is for all the events in the ω^0 cut and the other for events in the $\omega^0 p$ resonance region.

The decay of the $\omega^0 p$ system itself was studied using the angles θ_{pp} and ϕ_{pp} described in Fig. VI.14. The coordinate system described by the figure is the standard Gottfried-Jackson [Gottfried 1964] system in the $\omega^0 p$ rest frame. The angles, θ_{pp} and ϕ_{pp} , are of the outgoing proton (\vec{p}) relative to the z-axis defined by the direction of the target proton (\vec{p}_1) in the $\omega^0 p$ rest frame. The y-axis is given by the normal to the production plane (\hat{n}_{bf}).

We expect that the $\omega^0 p$ resonance will have a small spin value. The ω^0 ($J^P=1^-$) and the proton ($J^P=1/2^+$) spins can combine to give a total spin of 1/2 or 3/2. Since the $\omega^0 p$ resonance is very near threshold, the decay is probably via an S-wave or P-wave (orbital angular momentum, $L=0$ or $L=1$). Coupling the total spin (S) and orbital angular

momentum can give total angular momentum states with J^P 's of $1/2^\pm$, $3/2^\pm$, or $5/2^+$. The decay of a $J^P=1/2^\pm$ state has an isotropic angular distribution. The decay angular distribution of the $J^P=3/2^\pm$ state is given by:

$$W(\theta, \phi) = \frac{3}{4\pi(1+\alpha)} \left\{ \rho_{3/2 \ 3/2} \{ \sin^2\theta + \alpha(\cos^2\theta + 1/3) \} + \right. \quad (6)$$

$$\rho_{1/2 \ 1/2} \{ \cos^2\theta + 1/3 + \alpha\sin^2\theta \} +$$

$$\left. \frac{\alpha-1}{\sqrt{3}} \{ \operatorname{Re}\rho_{3/2 \ 1/2} \sin 2\theta \cos\phi + \operatorname{Re}\rho_{3/2 \ -1/2} \sin^2\theta \cos 2\phi \} \right\}$$

where the angles (θ, ϕ) are the same as (θ_{pp}, ϕ_{pp}) defined above and ρ_{mm} is the density matrix for the ω^0 resonance. In general ρ_{mm} depends on the s and t of the resonance production. This experiment is at a fixed s and ρ_{mm} is integrated over t to yield a constant matrix. For example, Dickey [1978] assumed $\rho_{mm} = 0$ except for $\rho_{1/2 \ 1/2} = \rho_{-1/2 \ -1/2} = 1/2$. The parameter α is the ratio:

$$\alpha = |M_3|^2 / \{ |M_1|^2 + |M_2|^2 \} \quad (7)$$

where M_3 is the helicity $\pm 3/2$ amplitude and M_1 and M_2 are helicity $\pm 1/2$ amplitudes (M_1 is for an ω^0 helicity of ± 1 and M_2 is for an ω^0 helicity of 0).

We can relate the helicity amplitudes to the amplitudes (M_{LS}) for states of definite orbital angular momentum L and total spin (S) [Chung 1971]:

$$M(\lambda_\omega, \lambda_p) = \sum_{LS} \left(\frac{2L+1}{2J+1} \right)^{1/2} \langle LS0\lambda | J\lambda \rangle \langle 1 \frac{1}{2} \lambda_\omega (-\lambda_p) | S\lambda \rangle M_{LS} \quad (8)$$

where J is the total angular momentum and λ_ω and λ_p are the ω^0 and proton helicities ($\lambda = \lambda_\omega - \lambda_p$). The $M(\lambda_\omega, \lambda_p)$ helicity amplitudes are equal to the $M_1, M_2,$ and M_3 amplitudes discussed above [Dickey 1978] and are reduced from 6 amplitudes to 3 by parity conservation. The $\omega^0 p$ system can have $S=1/2$ or $3/2$ and have L 's up to 3 for $J^P=3/2^\pm$ (2 for $J^P=1/2^\pm$). By setting all the M_{LS} amplitudes equal to 0 except M_{0S} for S-wave decay ($J^P=1/2^-$ or $3/2^-$) or M_{1S} for P-wave decay ($J^P=1/2^+$ or $3/2^+$), we can rewrite equation (7). For the S-wave case, it is found that $\alpha=1$ which results in an isotropic decay for a $J^P=3/2^-$ object [Dickey 1978]. For $J^P=3/2^+$ via a P-wave, α can be written as:

$$\alpha = \frac{9}{10\gamma+1} \quad (9)$$

where γ is the ratio $|M_{1\ 1/2}|^2/|M_{1\ 3/2}|^2$. Thus γ is the ratio of the probability of the P-wave decay occurring in a total spin 1/2 state to the probability of total spin 3/2 and is a parameter to be determined from the data or a more fundamental model of the dynamics of this strong decay.

The decay of the ω^0 was studied by using two different sets of angles. The first set, θ_{pn} and ϕ_{pn} , are of the normal to the ω^0 decay plane (\hat{n}_ω) in the ω^0 rest frame. These angles are measured relative to the ω^0 Gottfried-Jackson system which is the same system described above but now transformed to the ω^0 rest frame (see Fig. VI.15a). These distributions can be compared to previously published results [Atherton 1975 and Davis 1972] and as will be seen, show a strong

$\cos \theta_{pn}$ dependence. The other set of angles, $\theta_{n\omega}$ and $\phi_{n\omega}$, are again of the ω^0 decay plane normal but now are defined relative to the ω^0 helicity system (see Fig. VI.15b). In the ω^0 rest frame, the helicity coordinate system z-axis is given by the ω^0 direction which is opposite to the outgoing proton direction in this frame ($\hat{\omega}^0 = -\hat{p}$). The xz-plane is given by the z-axis and the target proton direction [see Jackson 1965]. The ω^0 helicity angles were studied since predictions of their distributions and of the ω^0 density matrix in this frame were made by assuming spin-parities of $1/2^-$ and $3/2^-$ for the $\omega^0 p$ resonance [Dickey 1978].

The ω^0 is a well known particle with a spin-parity of 1^- . The angular distribution of the normal to its decay plane can be calculated given its density matrix elements, ρ_{mm} , [Jackson 1965]:

$$W(\theta, \phi) = \frac{3}{4\pi} \left[\rho_{00} \cos^2\theta + \rho_{11} \sin^2\theta - \rho_{1-1} \sin^2\theta \cos 2\phi - \sqrt{2} \operatorname{Re} \rho_{10} \sin 2\theta \cos \phi \right] \quad (10)$$

where θ and ϕ are either set of angles defined above for the ω^0 . Note that in general the ω^0 density matrix is a function of the decay angles of the $\omega^0 p$ resonance, θ_{pp} and ϕ_{pp} . The density matrix elements determined later are constants, having been integrated over these angles. The one-dimensional distributions (integrated over the other angle) are:

$$W(\phi) = \frac{1}{2\pi} (1 - 2\rho_{1-1} \cos 2\phi) \quad (11)$$

$$W(\theta) = \frac{3}{2} (\rho_{00} \cos^2 \theta + \rho_{11} \sin^2 \theta) \quad (12a)$$

$$= \frac{3(1 - \rho_{00})}{4} \left[1 + \left(\frac{3\rho_{00} - 1}{1 - \rho_{00}} \right) \cos^2 \theta \right] \quad (12b)$$

From equations (12), we see that by fitting the $\cos\theta$ distributions of the ω^0 with the form $a_0(1+a_2\cos^2\theta)$ we can calculate the ρ_{00} density matrix element of the ω^0 :

$$a_2 = \frac{1 - 3\rho_{11}}{\rho_{11}} = \frac{3\rho_{00} - 1}{1 - \rho_{00}} \quad (13)$$

Similarly, by fitting the ϕ distribution with $c_0(1+c_2\cos^2\phi)$ we can calculate the ρ_{1-1} density matrix element:

$$c_2 = -2\rho_{1-1} \quad (14)$$

The real part of the ρ_{10} density matrix element can be determined by fitting the bivariate distribution (in both θ and ϕ) which we have not done.

The density matrix elements of the ω 's from the decay of the $\omega^0 p$ resonance are dependent on the decay angles of the resonance [Jackson 1965]:

$$\rho_{\lambda\lambda'}^{\omega}(\theta_{pp}, \phi_{pp}) = N \frac{M(\lambda, \lambda_p) M^*(\lambda', \lambda'_p)}{W_{\omega p}(\theta_{pp}, \phi_{pp})} \quad (15)$$

$$\sum_{mm'} D_{m\lambda}^{J*}(\phi_{pp}, \theta_{pp}, 0) \rho_{mm'}^{\omega p} D_{m'\lambda'}^J(\phi_{pp}, \theta_{pp}, 0)$$

where the ω^0 and $\omega^0 p$ resonance density matrices are labeled as such.

N is a normalization factor determined from $\text{Tr}\rho^\omega=1$ and $W_{\omega p}(\theta_{pp},\phi_{pp})$ is the decay angular distribution of the $\omega^0 p$ system. The $D_{m\lambda}^J(\phi,\theta,0)$ are the rotation matrices for spin J and $M(\lambda_\omega,\lambda_p)$ is the amplitude for the decay into a state with ω^0 helicity λ_ω and proton helicity λ_p (see Dickey's λ_1 and λ_2 [1978]); also $\lambda=\lambda_\omega-\lambda_p$ and $\lambda'=\lambda'_\omega-\lambda'_p$. Using $\rho_{\lambda\lambda}^\omega$, from equation (15) in the ω^0 decay angular distribution (equation (10)) results in the joint angular distribution $W(\theta_{n\omega},\phi_{n\omega};\theta_{pp},\phi_{pp})$ or, by integrating over the ϕ angles, $W(\theta_{n\omega},\theta_{pp})$. Dickey's predictions for the $W(\theta_{n\omega},\theta_{pp})$ distributions are discussed in the final section of this chapter.

$$\pi^\pm p \rightarrow \pi_f^\pm \omega^0 p \quad \omega^0 \rightarrow \pi^+ \pi^- \pi^0$$

$\omega^0 p$ rest frame

$$\hat{x} = \hat{y} \times \hat{z}$$

$$\hat{y} = \hat{n}_{bf} = \hat{\pi}_b \times \hat{\pi}_f$$

$$\hat{z} = \hat{p}_i$$

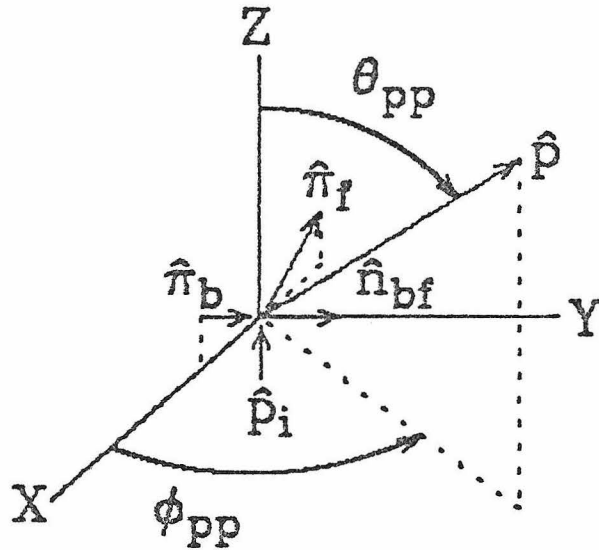


Figure VI.14

Definition of the $\omega^0 p$ Gottfried-Jackson frame angles θ_{pp} and ϕ_{pp} used to study the $\omega^0 p$ system decay angular distributions.

$$\pi^\pm p \rightarrow \pi_f^\pm \omega^0 p \quad \omega^0 \rightarrow \pi^+ \pi^- \pi^0$$

ω^0 rest frame

$$\hat{x} = (\hat{\pi}_b \times \hat{\pi}_f) \times \hat{z}$$

$$\hat{y} = \hat{z} \times \hat{x}$$

$$\hat{z} = \hat{p}_i$$

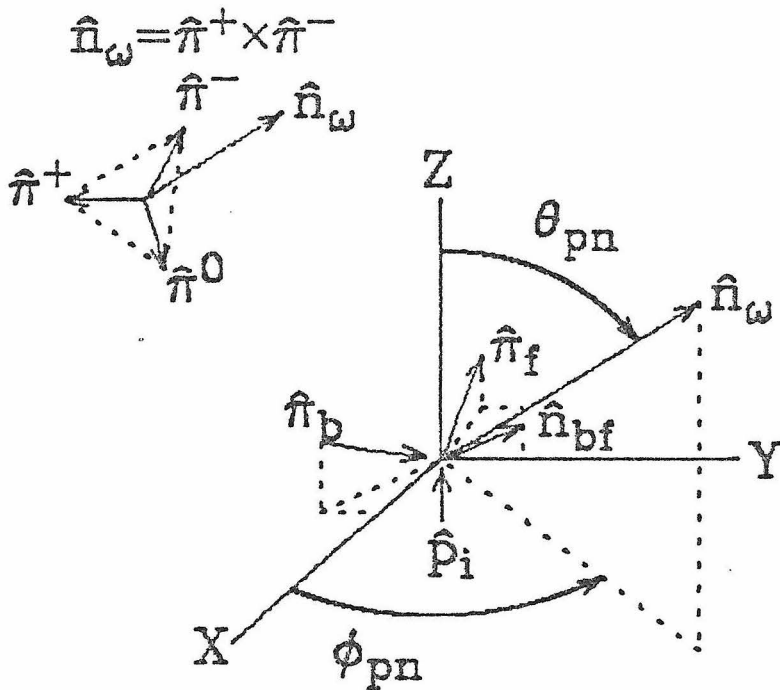
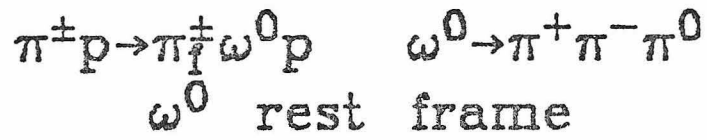


Figure VI.15a

Definition of the ω^0 Gottfried-Jackson frame angles θ_{pn} and ϕ_{pn} used to study the ω^0 decay angular distributions.



$$\begin{aligned} \hat{x} &= \hat{y} \times \hat{z} \\ \hat{y} &= \hat{p}_i \times \hat{\omega}^0 \\ \hat{z} &= \hat{\omega}^0 = -\hat{p} \end{aligned}$$

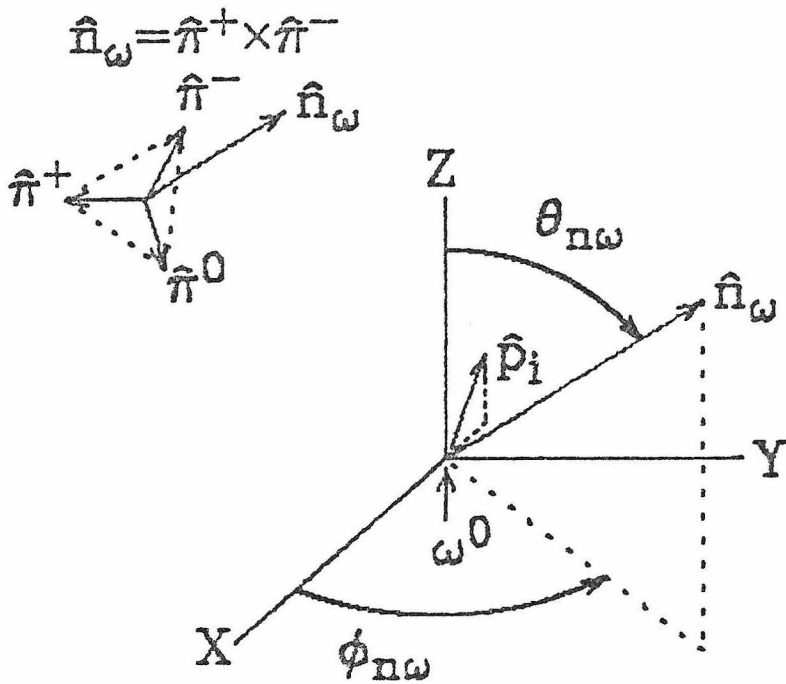


Figure VI.15b

Definition of the ω^0 helicity frame angles $\theta_{n\omega}$ and $\phi_{n\omega}$ used to study the ω^0 decay angular distributions.

4b) Observed Angular Distributions

Fig. VI.16a shows the normalized Y_{ℓ}^0 moments for the data as a function of the ω^0 p mass. These moments are defined by:

$$Y_{\ell}^m = \frac{\sum_i w_i Y_{\ell}^m(\theta_i, \phi_i)}{\sum_i w_i} \quad (16)$$

where the sums (over i) are over the individual events and w_i is the ith event's weight. The angles θ_i and ϕ_i are the values of the θ_{pp} and ϕ_{pp} angles (Fig. VI.14) for the ith event. The differential cross section in terms of $\langle Y_{\ell}^m \rangle$ is just:

$$\frac{d\sigma}{d\Omega} = \sigma_{4\pi} \sum_{\ell, m} \langle Y_{\ell}^m \rangle Y_{\ell}^m(\Omega) \quad (17)$$

where $\sigma_{4\pi}$ is the cross section integrated over the solid angle:

$$\sigma_{4\pi} = \int \frac{d\sigma}{d\Omega} d\Omega \quad (18)$$

As can be seen from the plots, the moments are very small and consistent with zero up to an ω^0 p mass of about 2.1 GeV. Although only the $m=0$ moments are shown, the real and imaginary parts of the $m \neq 0$ moments are also zero below 2.1 GeV. The moments for events in the ω^0 wings are essentially the same as those for events in the ω^0 peak (see Fig. VI.16b).

The moments distributions serve to directly illustrate the change in the angular distributions with the ω^0 p mass. They can also be compared to such distributions presented by other authors [Atherton 1975] and to our earlier preliminary results [Davidson 1974 and Linglin 1974].

However, the moments obscure some of the details of the angular distributions due to their normalizations. For an angular distributions given by $a_0(1+a_1\cos\theta+a_2\cos^2\theta)$, the first two moments are related to the a_j coefficients by:

$$\langle Y_1^0 \rangle = \frac{a_1}{\sqrt{12\pi} (1 + a_2/3)} = \frac{0.163 a_1}{1 + a_2/3} \quad (19a)$$

$$\langle Y_2^0 \rangle = \frac{2a_2}{3\sqrt{20\pi} (1 + a_2/3)} = \frac{0.084 a_2}{1 + a_2/3} \quad (19b)$$

The small normalization constants thus lead to small moments for substantially non-uniform angular distributions. For instance, for $a_1 = -0.5$ and $a_2 = 1.2$, values near those observed (see below), the moments have the values of -0.058 for $\langle Y_1^0 \rangle$ and 0.072 for $\langle Y_2^0 \rangle$. Above about 2.5 GeV, all the moments (up to $\ell=4$) take on large values indicating the the angular distributions are very sharply peaked in this region. Thus we now turn to the $\cos\theta_{pp}$ and ϕ_{pp} distributions for more detailed information.

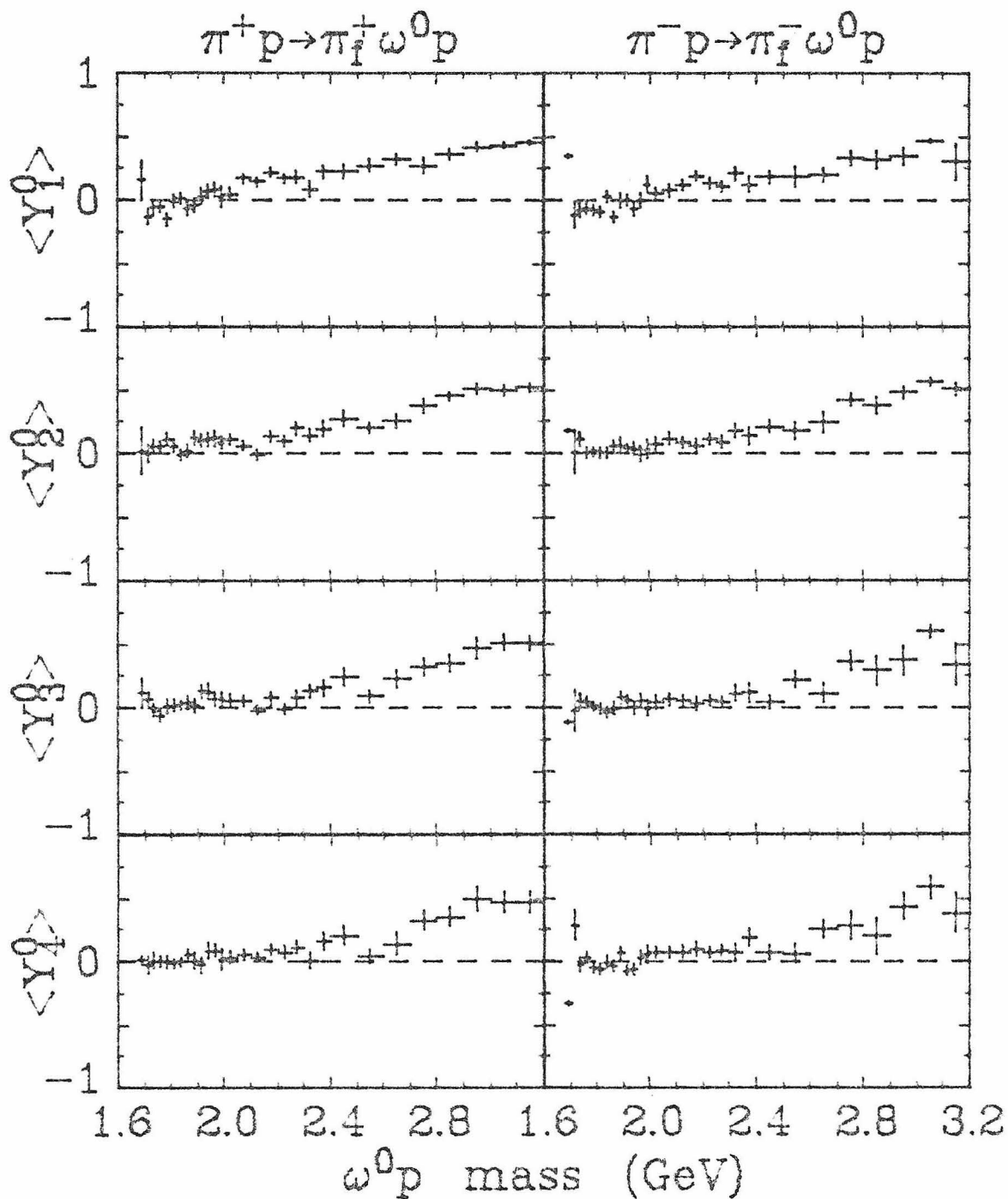


Figure VI.16a

Distributions of the normalized Y_2^0 moments for the π^+ and π^- events in the ω^0 peak versus the $\omega^0 p$ mass.

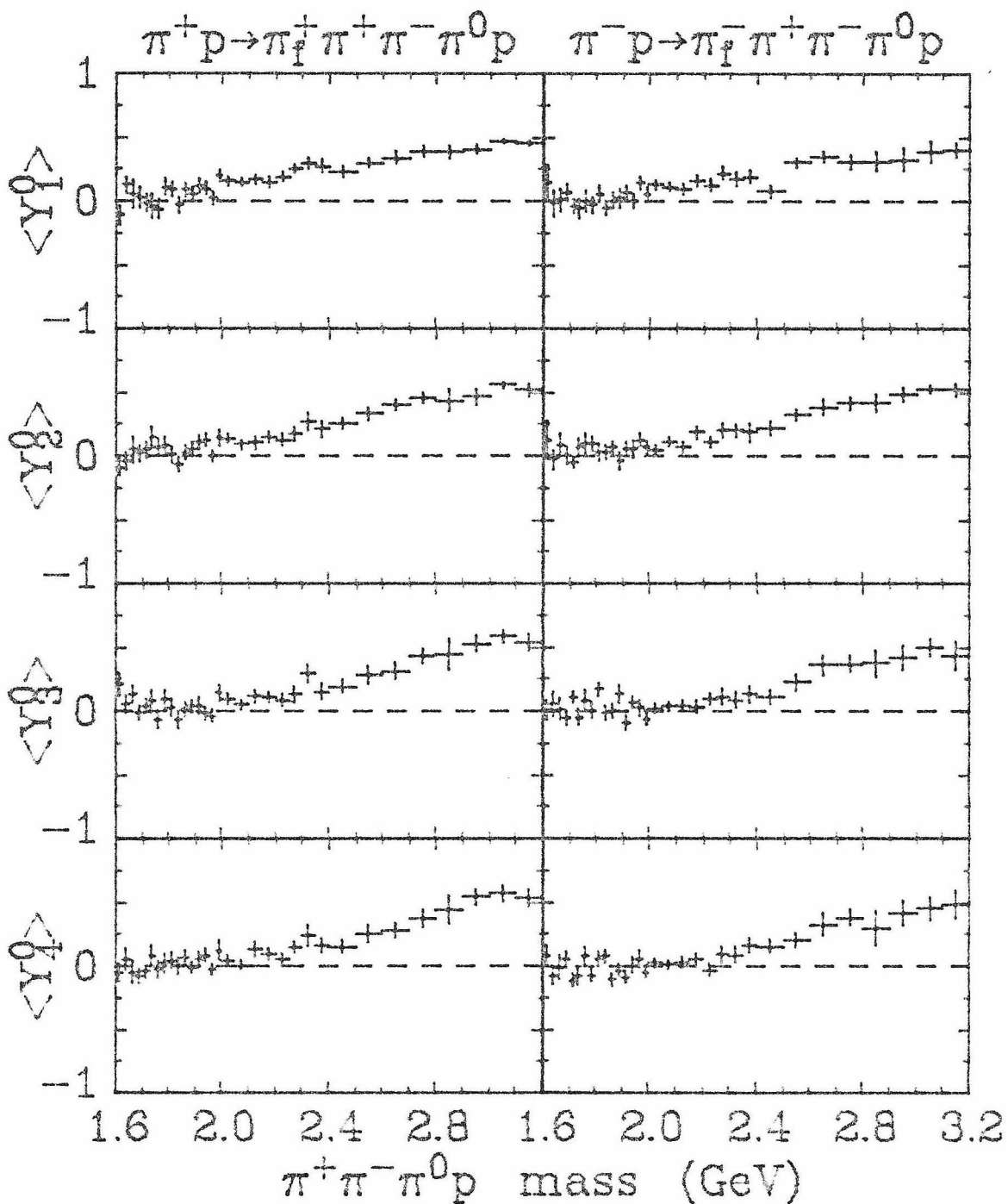


Figure VI.16b

Distributions of the normalized Y_2^0 moments for the π^+ and π^- events in the ω^0 wings versus the $\pi^+ \pi^- \pi^0 p$ mass.

Figs. VI.17 and VI.18 show the $\cos\theta_{pp}$ and ϕ_{pp} angular distributions for ω^0 masses below 2.1 GeV. These distributions are of the same angles used to calculate the moments displayed in Figs. VI.16. The $\cos\theta_{pp}$ distributions for higher masses are given in Figs. VI.19; the corresponding ϕ_{pp} distributions are not shown as they are uniform in ϕ_{pp} (much like those in Figs. VI.18). The curves with the $\cos\theta_{pp}$ distributions are from fits to $a_0(1+a_1\cos\theta_{pp}+a_2\cos^2\theta_{pp})$ and those with the ϕ_{pp} distributions are from fits to $c_0(1+c_1\cos\phi_{pp})$. These functional forms were chosen from examination of the distributions and the expectation that the ω^0 resonance would have an S-wave ($L=0$) or P-wave ($L=1$) decay (equation (6) for example).

The $\cos\theta_{pp}$ distributions for masses above 2.1 GeV (Figs. VI.19) show a forward peak at $\cos\theta_{pp}=+1$ which becomes stronger as the ω^0 mass increases. The higher masses also show large values of the Y_{ℓ}^m moments due to these forward peaks (see Figs. VI.16). For masses above 2.1 GeV, the functional form with which the $\cos\theta_{pp}$ distributions were fit does not reproduce the narrow forward peaks but gives good fits to the $\cos\theta_{pp} < 0.8$ data. This forward peak is more pronounced for the ω^0 wings events as compared to the ω^0 peak events (compare Figs. VI.19b and VI.19a). This forward peak corresponds to forward going protons with a low momentum transfer from the target to the outgoing proton (low $|t_{pp}|$). Since the events have a fairly low $|t_{\pi\pi}|$ (see Figs. VI.8 and VI.12) for the most part, the forward $\cos\theta_{pp}$ peak is due to contributions from events of the form illustrated in Fig. VI.4a with the η^0 replaced by an ω^0 or a $\pi^+\pi^-\pi^0$ system.

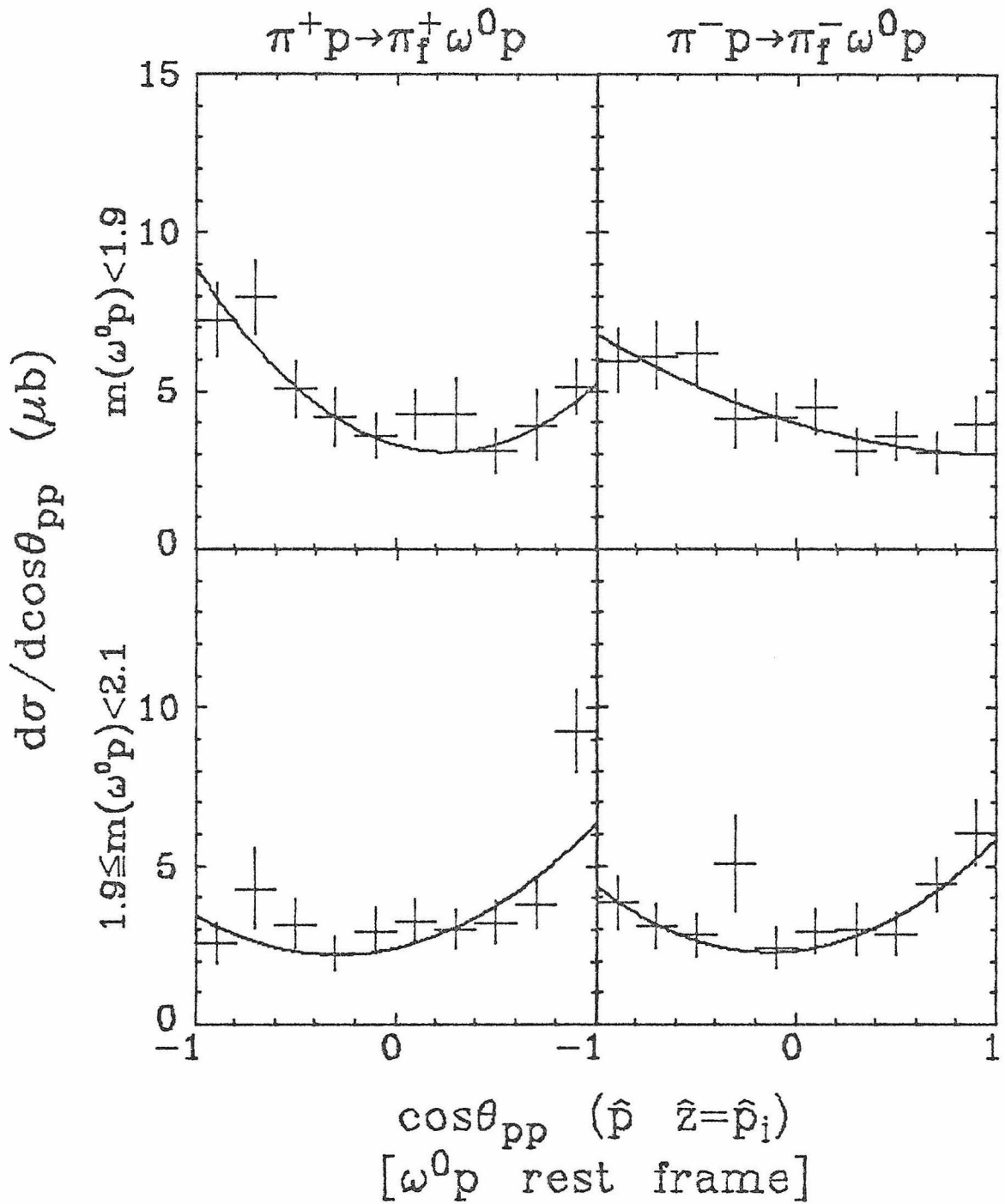


Figure VI.17a

Distributions of $\cos\theta_{pp}$ of the outgoing proton for events in the ω^0 peak with low $\omega^0 p$ masses. The θ_{pp} angle is defined in Fig. VI.14.

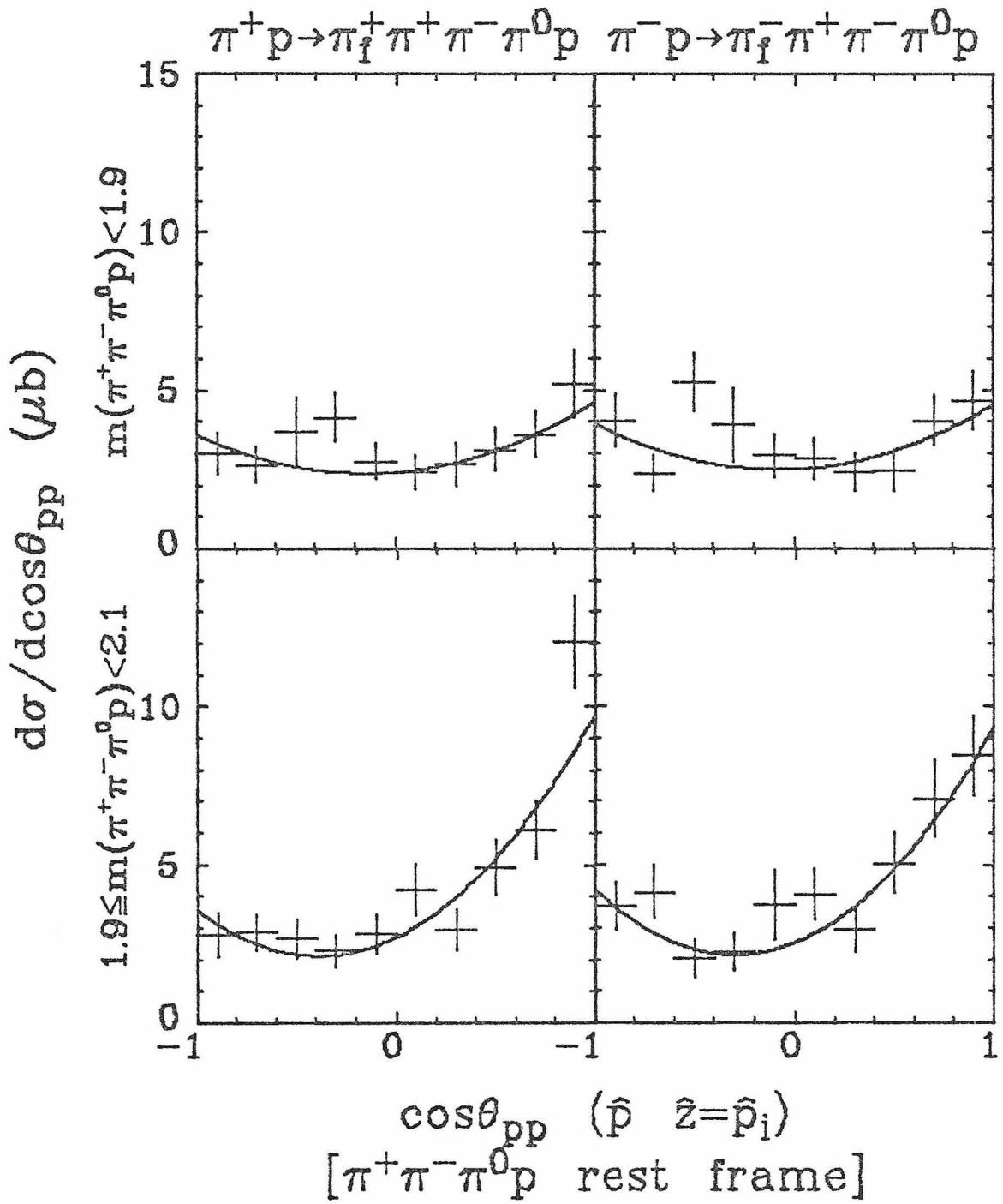


Figure VI.17b

Distributions of $\cos \theta_{pp}$ of the outgoing proton for events in the ω^0 wings with low $\pi^+ \pi^- \pi^0 p$ masses.

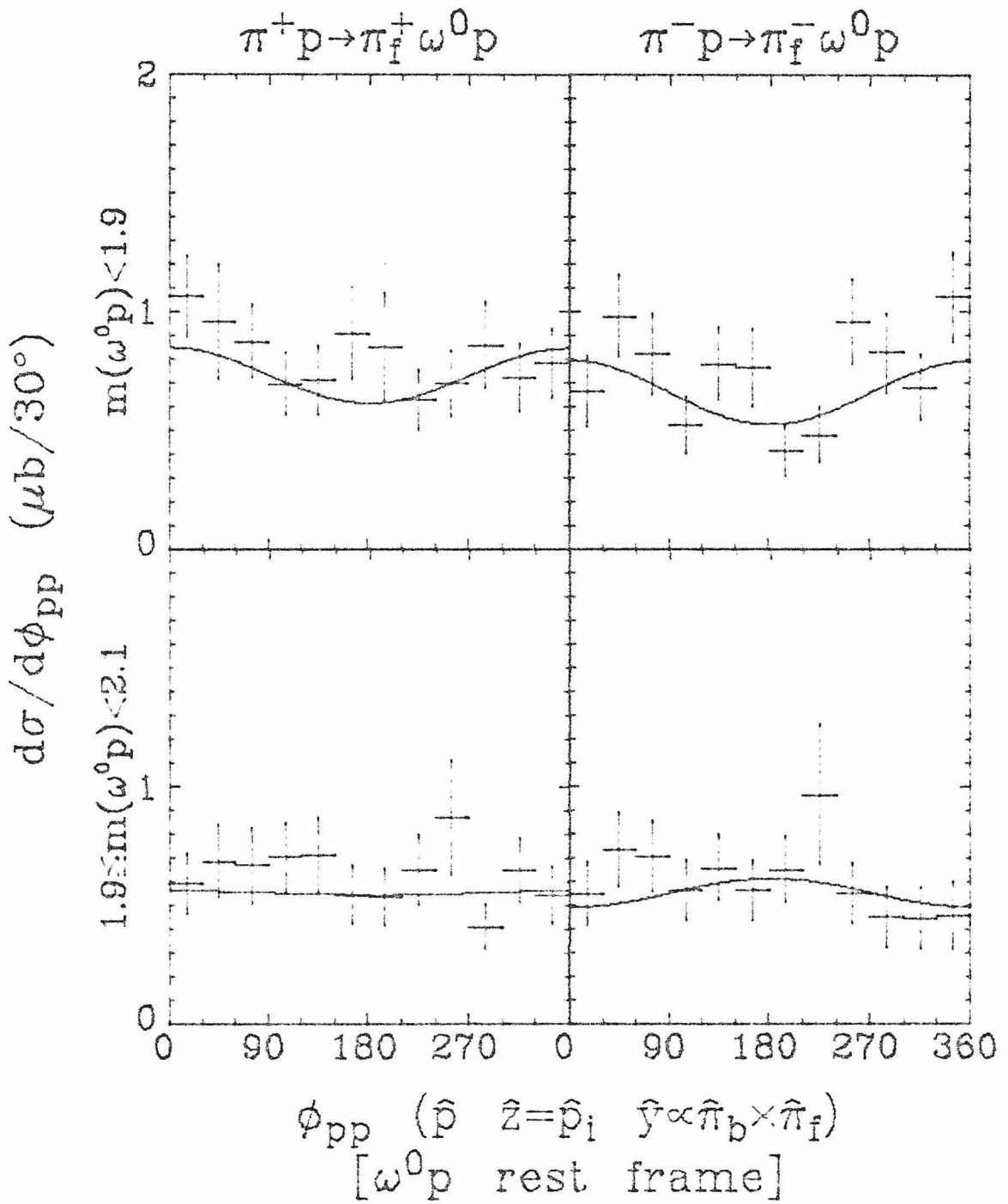


Figure VI.18a

Distributions of the ϕ_{pp} angle of the outgoing proton for events in the ω^0 peak with low $\omega^0 p$ masses. The ϕ_{pp} angle is defined in Fig. VI.14.

VI.14.

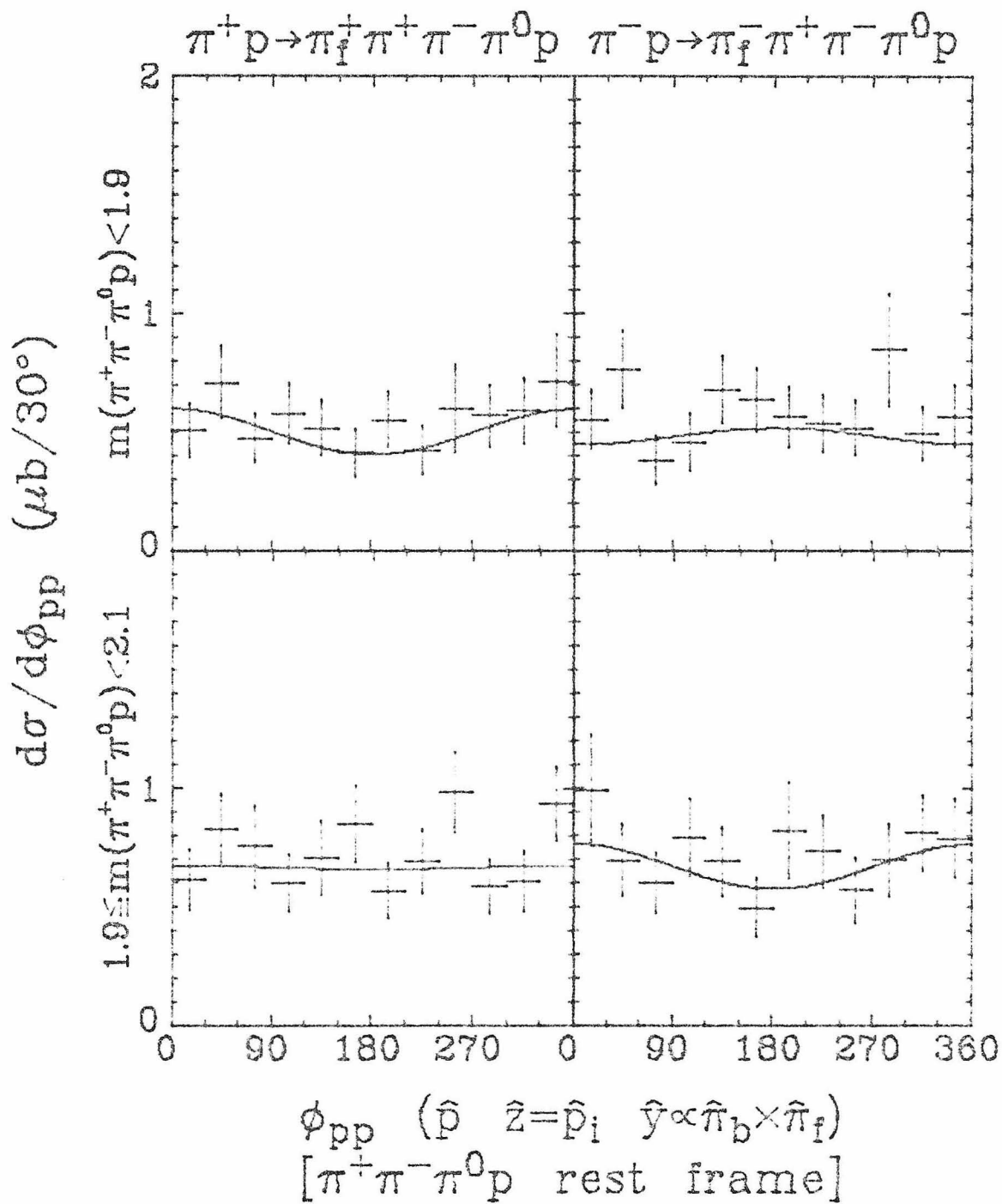


Figure VI.18b

Distributions of the ϕ_{pp} angle of the outgoing proton for events in the ω^0 wings with low $\pi^+ \pi^- \pi^0 p$ masses.

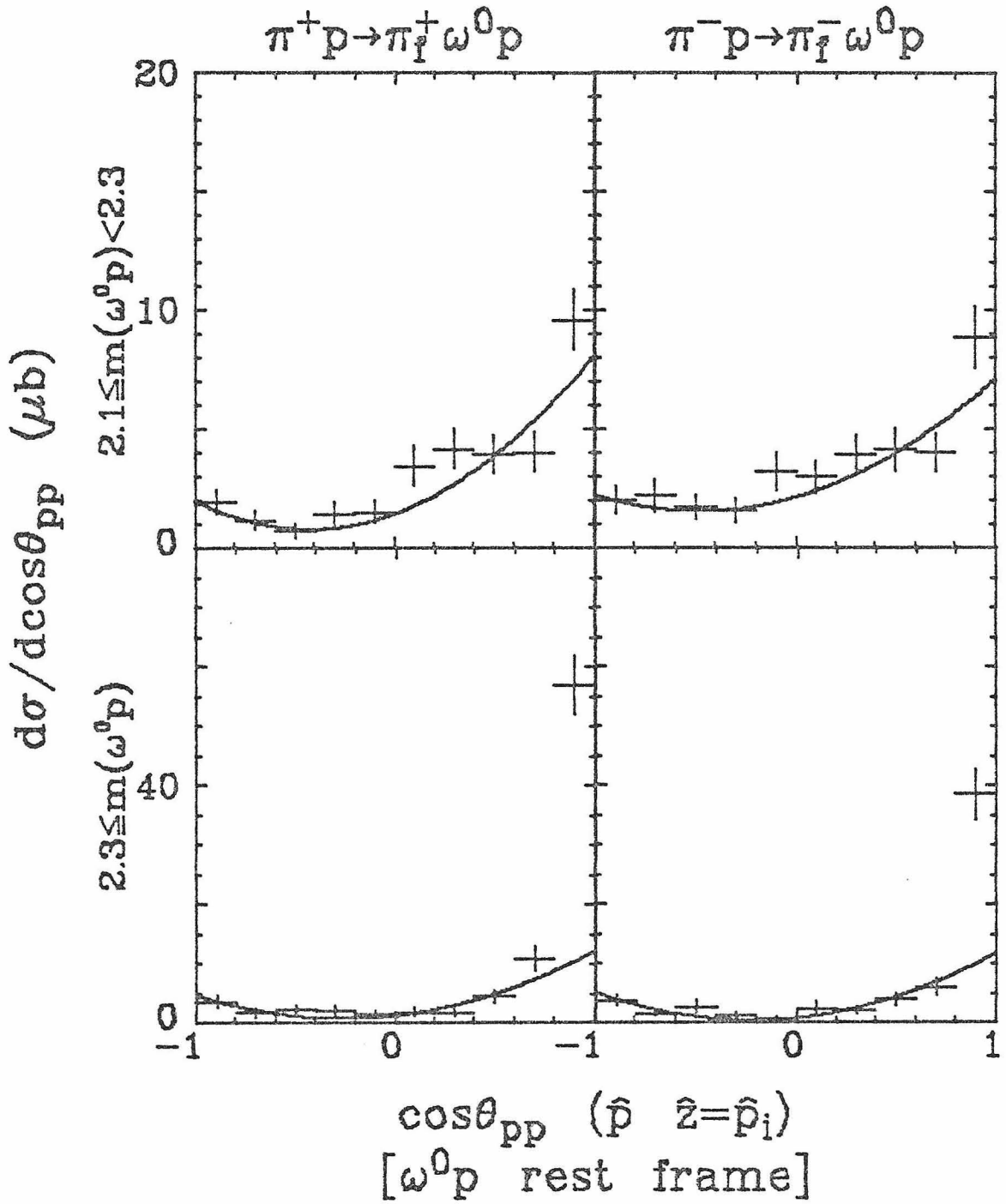


Figure VI.19a

Distributions of $\cos\theta_{pp}$ of the outgoing proton for events in the ω^0 peak with high $\omega^0 p$ masses.

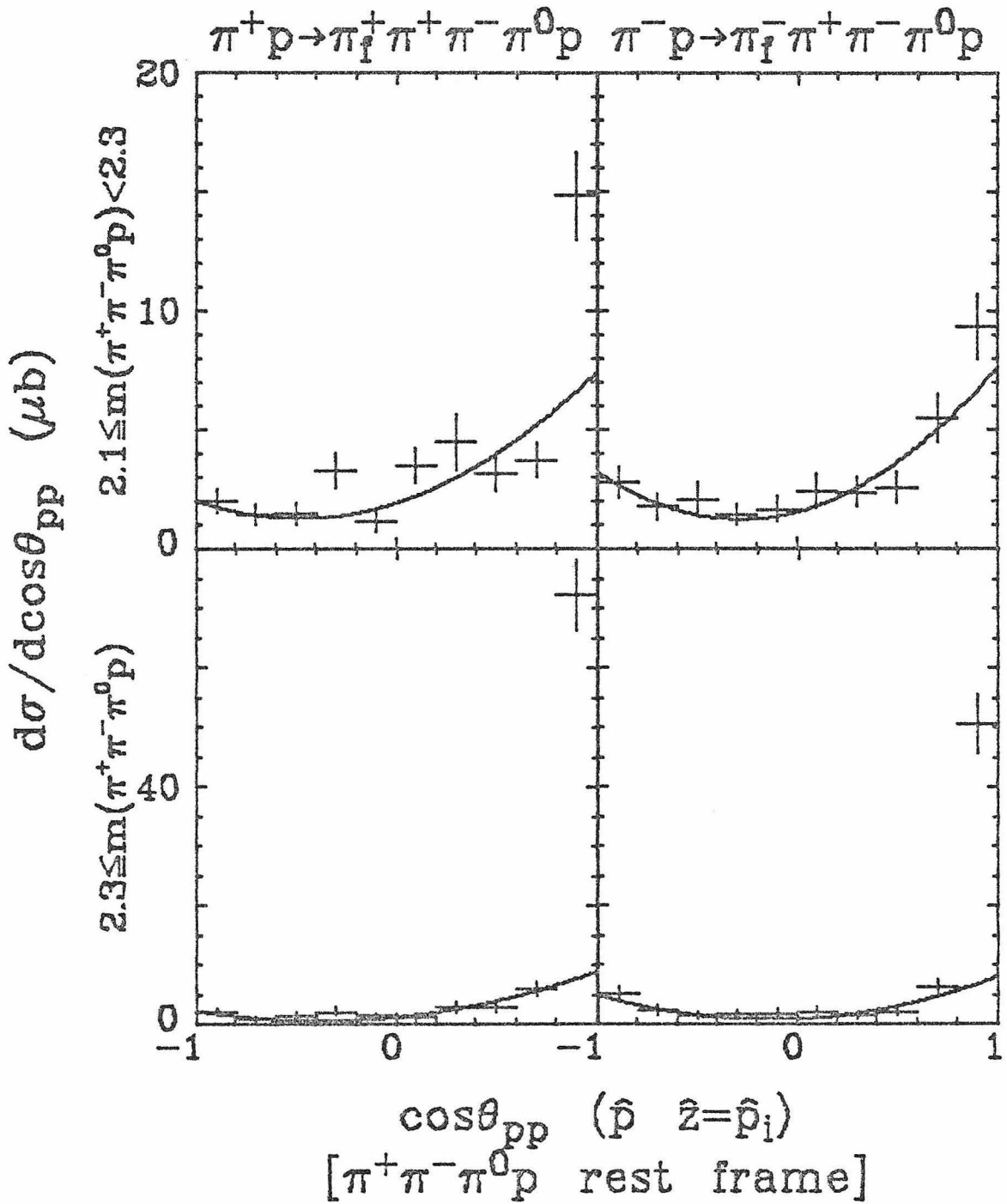


Figure VI.19b

Distributions of $\cos \theta_{pp}$ of the outgoing proton for events in the ω^0 wings with high $\pi^+ \pi^- \pi^0 p$ masses.

The $\cos\theta_{pp}$ distributions for the lowest mass band (<1.9 GeV), which includes the ω^0 p resonance, show a backwards peak at $\cos\theta_{pp} = -1$ (Fig. VI.17a). This backward peak is only evident for the events within the ω^0 peak. The $\cos\theta_{pp}$ distributions for the ω^0 wings events with a $\pi^+\pi^-\pi^0$ p mass below 1.9 GeV are essentially flat with a small forward peak and possibly a small $\cos^2\theta_{pp}$ component (Fig. VI.17b). The next higher mass band (1.9 to 2.1 GeV) $\cos\theta_{pp}$ distributions show forward peaks for both the ω^0 peak events and the ω^0 wings events; though once again the forward $\cos\theta_{pp}$ peak of the ω^0 wings events is stronger than that of the ω^0 peak events (Figs. VI.17b and VI.17a).

The ϕ_{pp} distributions are uniform in ϕ_{pp} for the most part though some of them exhibit a slight $\cos\phi_{pp}$ dependence. The ϕ_{pp} distributions were fit by $c_0(1+c_1\cos\phi_{pp})$; the results are given in Table VI.5. The values found for c_1 are small with nearly half of them being consistent with zero.

Table VI.5

c_1 values from $1+c_1\cos\phi_{pp}$ fits to the
 $d\sigma/d\phi_{pp}$ distributions

ω^0 p mass band (GeV)	ω^0 peak events		ω^0 wings events	
	π^+	π^-	π^+	π^-
<1.9	0.158±0.083	0.203±0.084	0.190±0.092	-0.073±0.104
1.9-2.1	0.016±0.094	-0.110±0.100	0.012±0.082	0.140±0.092

Table VI.6

Results of $1+a_1 \cos\theta_{pp} + a_2 \cos^2\theta_{pp}$ fits to the $\frac{d\sigma/d\cos\theta_{pp}}$ distributions

ω^0 p mass band (GeV)	π^+		π^-	
	a_1	a_2	a_1	a_2
	ω^0 peak events			
<1.9	-0.55±0.16	1.14±0.38	-0.48±0.12	0.23±0.23
1.9-2.1	0.60±0.20	1.03±0.43	0.33±0.19	1.19±0.49
	ω^0 wings events			
<1.9	0.22±0.17	0.70±0.37	0.13±0.16	0.68±0.36
1.9-2.1	1.14±0.21	1.44±0.44	1.01±0.23	1.66±0.53

Table VI.6 gives the results (for masses below 2.1 GeV) of fitting $a_0(1+a_1 \cos\theta_{pp} + a_2 \cos^2\theta_{pp})$ to the $\cos\theta_{pp}$ distributions in Figs. VI.17. The backward $\cos\theta_{pp}$ peak in the lowest mass band for the ω^0 peak data is evident as a negative value for the a_1 coefficient for these distributions. This backward peak in the $\cos\theta_{pp}$ distribution in the ω^0 resonance region has been seen in previous experiments [Milgram 1970, Davis 1972, Chien 1976, and Wohl 1978]. To provide a better comparison between the $\cos\theta_{pp}$ distributions for various mass bands and ω^0 event selections, we have calculated the asymmetry parameter for the $\cos\theta_{pp}$ distributions:

$$A = \frac{W_+ - W_-}{W_+ + W_-} \quad (15)$$

where W_+ is the sum of weights for events with $\cos\theta_{pp} \geq 0$ and W_- is the sum of weights for events with $\cos\theta_{pp} < 0$. The results are given in Table VI.7 and in Fig. VI.20. In this way the relative differences between the mass bands are more obvious. As is seen in Fig. VI.20, masses above 1.9 GeV have greater positive asymmetries (or forward $\cos\theta_{pp}$ peaks) as the ω^0 mass increases. Only for ω^0 peak events below 1.9 GeV is there any appreciable negative asymmetry. We will discuss this asymmetry further when we investigate the spin-parity of the ω^0 resonance later in this chapter.

Table VI.7

Asymmetry of the $d\sigma/d\cos\theta_{pp}$ distributions

ω^0 p mass band(GeV)	ω^0 peak events		ω^0 wings events	
	π^+	π^-	π^+	π^-
<1.9	-0.151±0.059	-0.188±0.058	0.023±0.070	-0.060±0.069
1.9-2.1	0.194±0.067	0.054±0.073	0.385±0.056	0.271±0.063
2.1-2.3	0.575±0.068	0.381±0.068	0.519±0.068	0.394±0.073
≥2.3	0.750±0.056	0.689±0.070	0.837±0.058	0.669±0.064

The $\cos\theta_{pn}$ and ϕ_{pn} angular distributions of the normal to the ω^0 decay plane ($\hat{n}_\omega = \hat{p}_+ \times \hat{p}_-$ where \hat{p}_+ is the direction of the π^+ and \hat{p}_- is that of the π^-) in the ω^0 rest frame are given in Figs. VI.21 thru VI.24. The θ_{pn} and ϕ_{pn} angles are defined in Fig. VI.15a. The distributions for the ω^0 peak events with ω^0 p masses below 1.9 GeV show

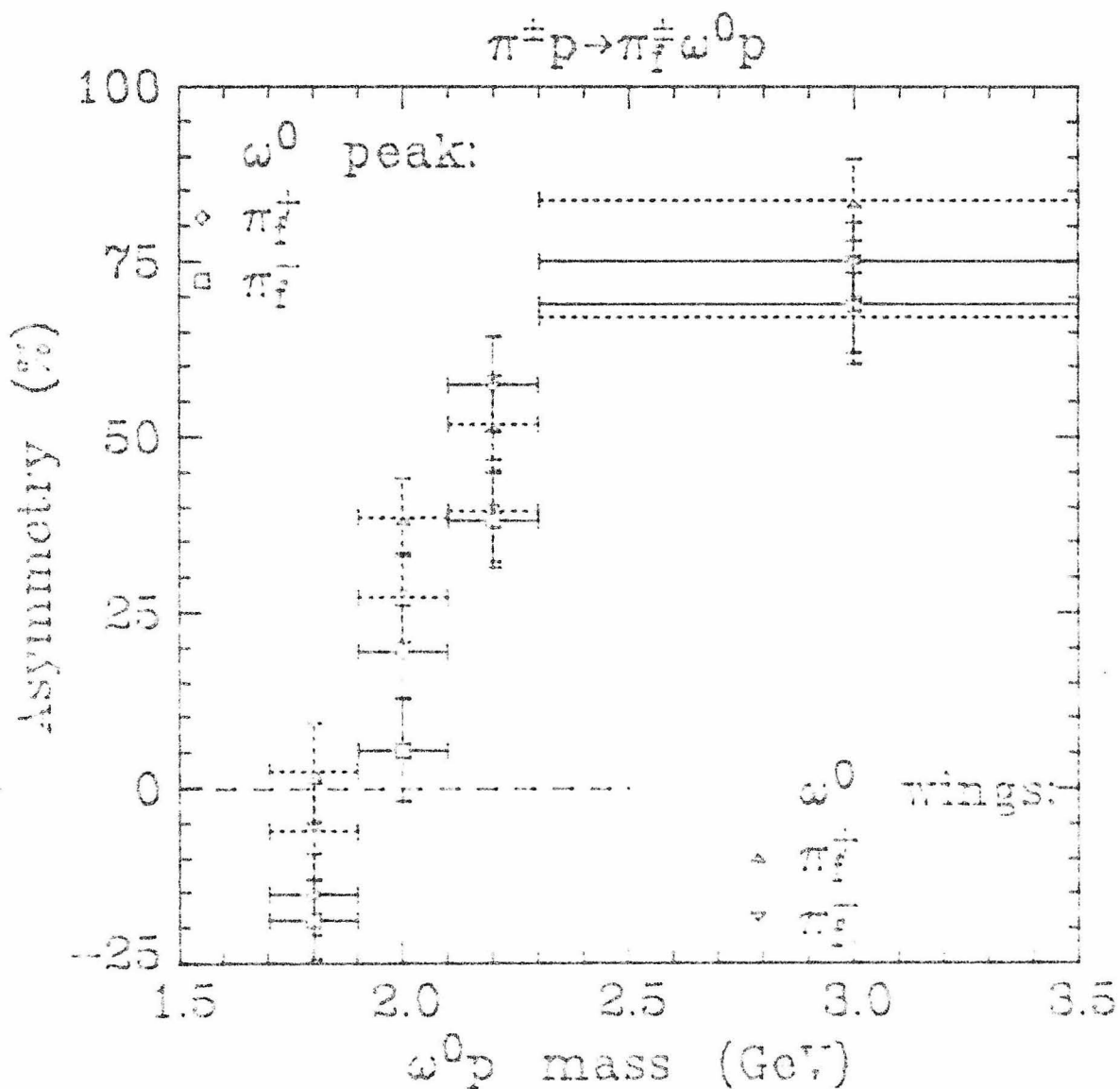


Figure VI.20

Plot of the asymmetry of the $\cos\theta_{pp}$ distributions (as a percent deviation from isotropy) versus the $\omega^0 p$ mass for events in the ω^0 peak and in the ω^0 wings.

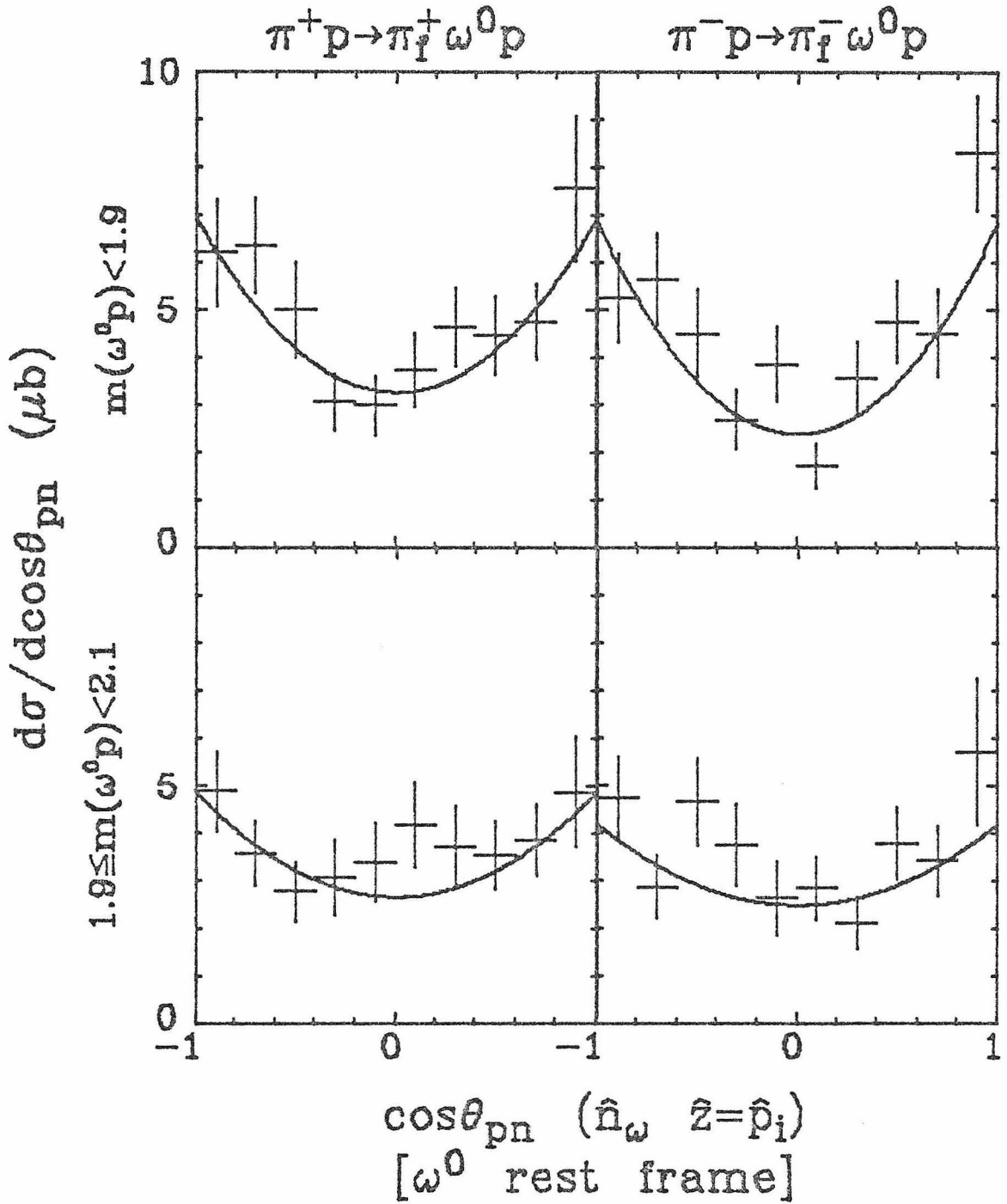


Figure VI.21a

Distributions of $\cos\theta_{pn}$ of the normal to the ω^0 decay plane for events in the ω^0 peak with low $\omega^0 p$ masses. The θ_{pn} angle is defined in Fig. VI.15a.

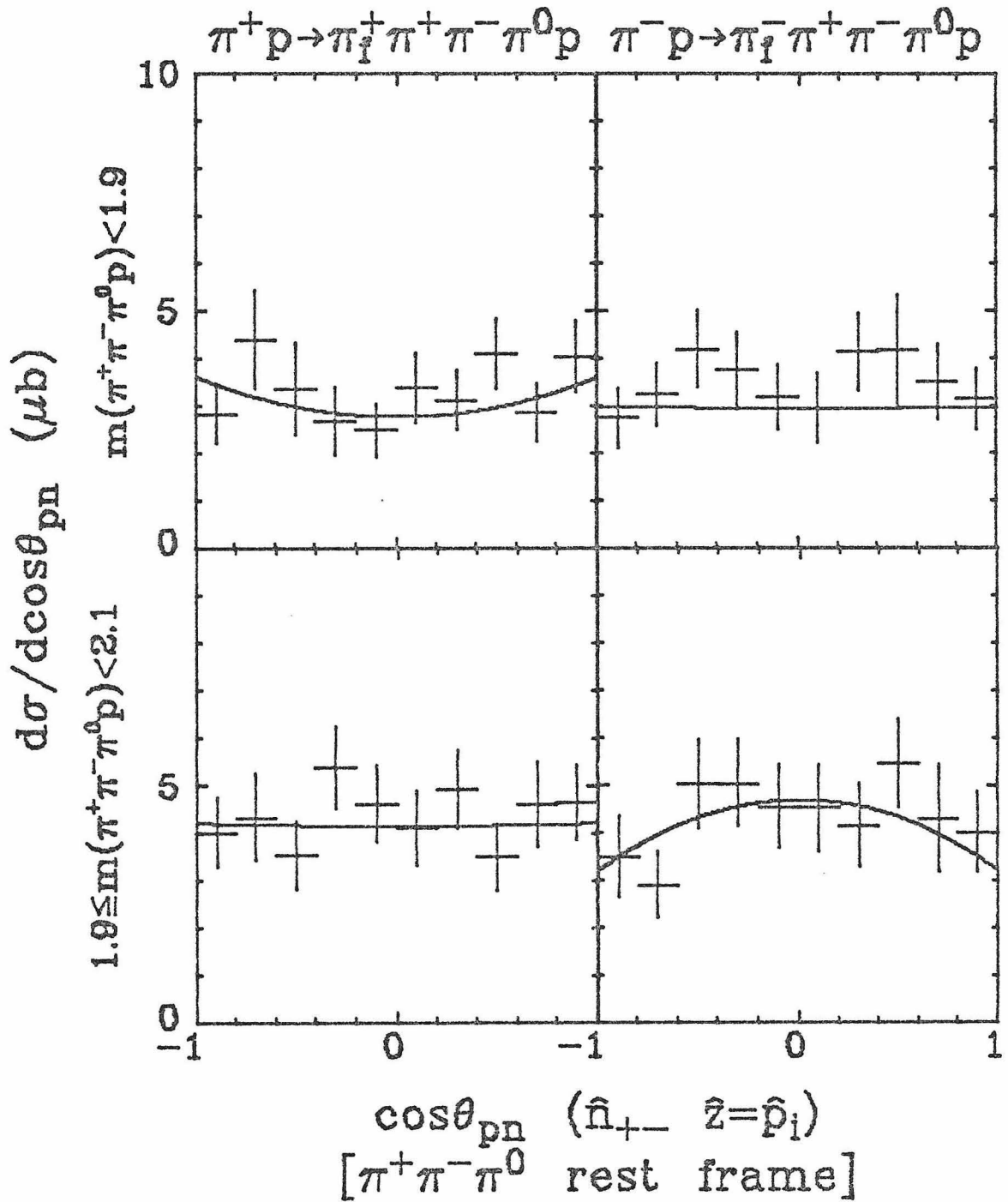


Figure VI.21b

Distributions of $\cos\theta_{pn}$ of the normal to the $\pi^+\pi^-$ plane (\hat{n}_{+-}) for events in the ω^0 wings with low $\pi^+\pi^-\pi^0 p$ masses.

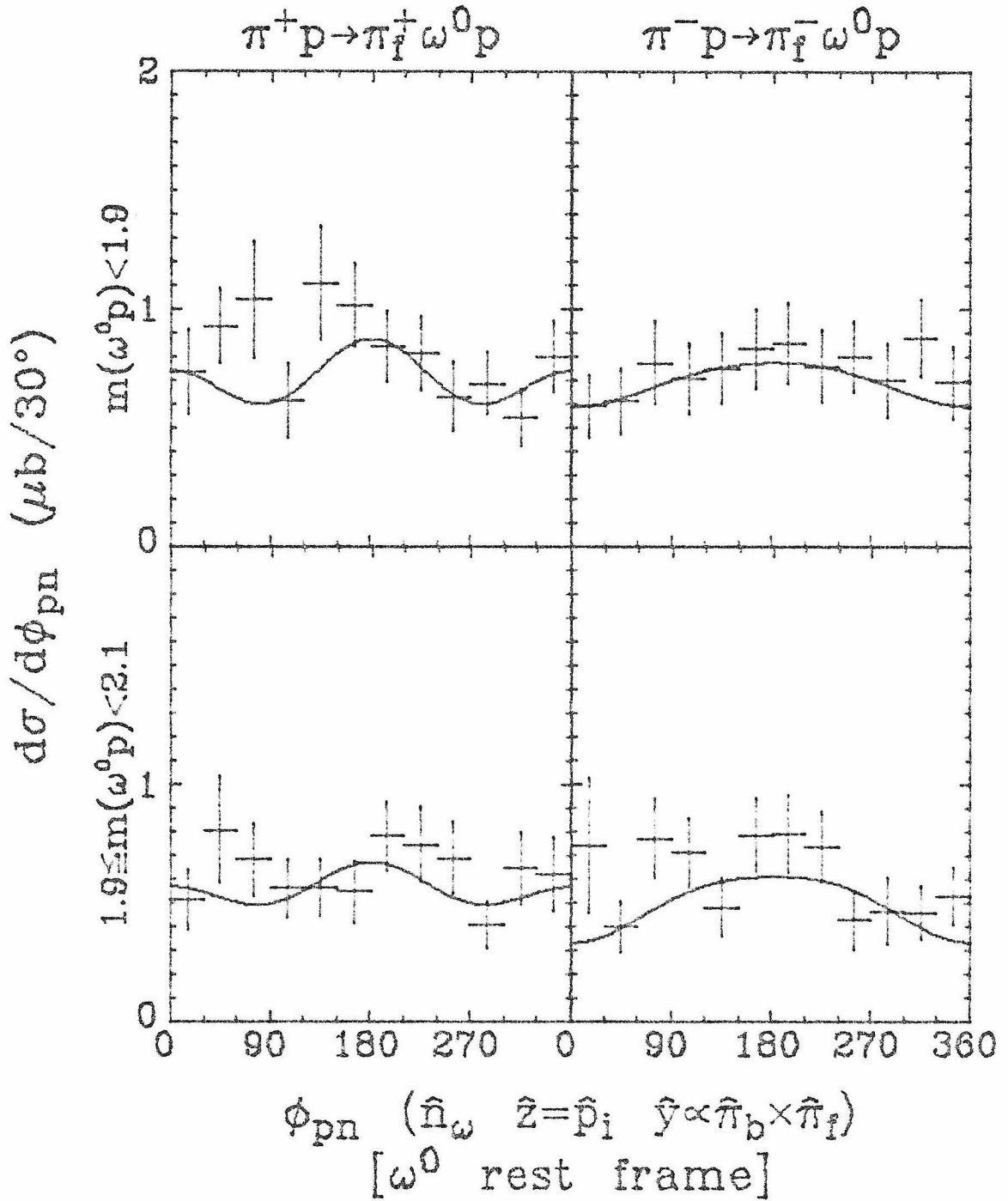


Figure VI.22a

Distributions of the ϕ_{pn} angle of the normal to the ω^0 decay plane for events in the ω^0 peak with low $\omega^0 p$ masses. The ϕ_{pn} angle is defined in Fig. VI.15a.

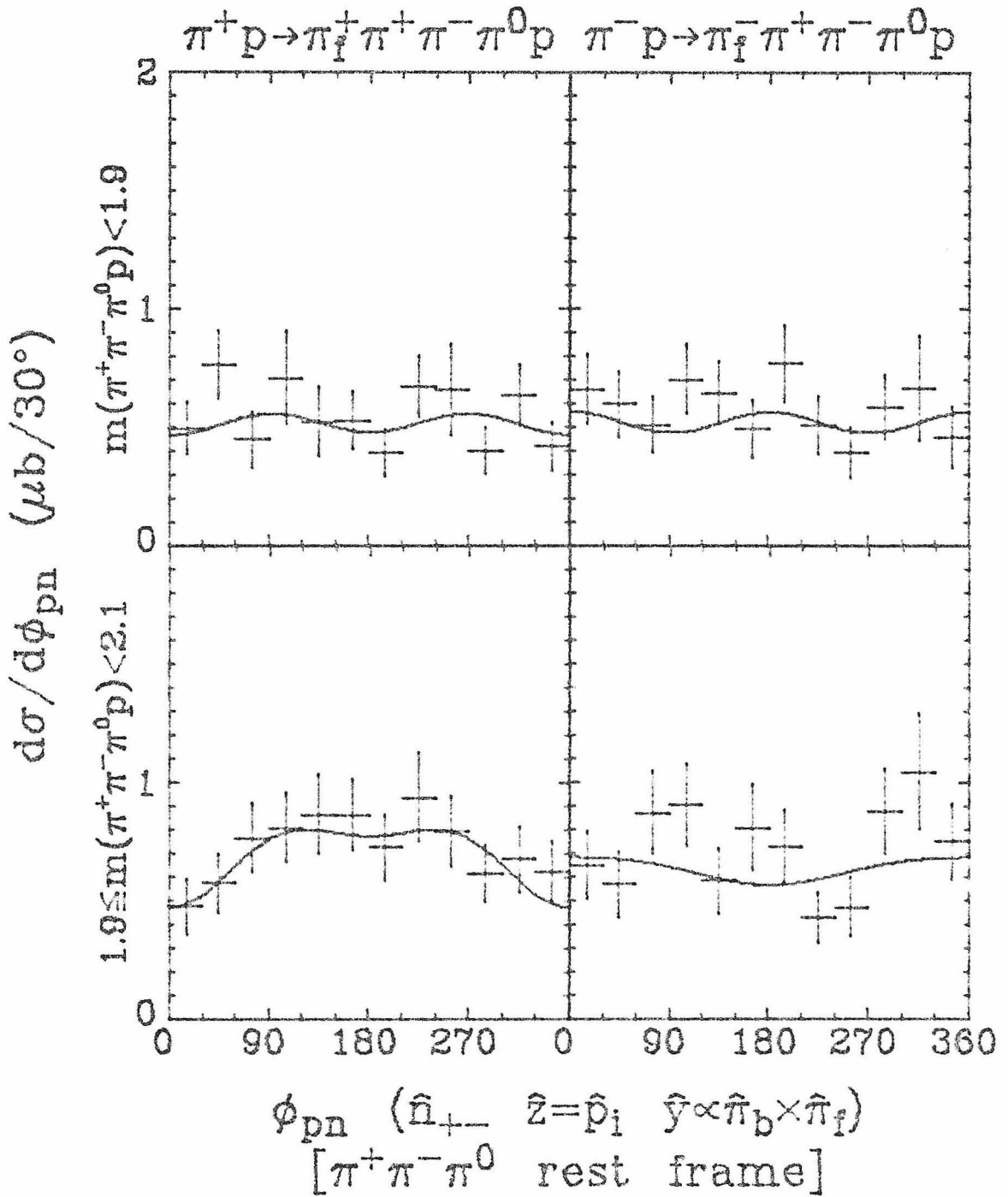


Figure VI.22b

Distributions of the ϕ_{pn} angle of the normal to the $\pi^+ \pi^-$ plane for events in the ω^0 wings with low $\pi^+ \pi^- \pi^0 p$ masses.

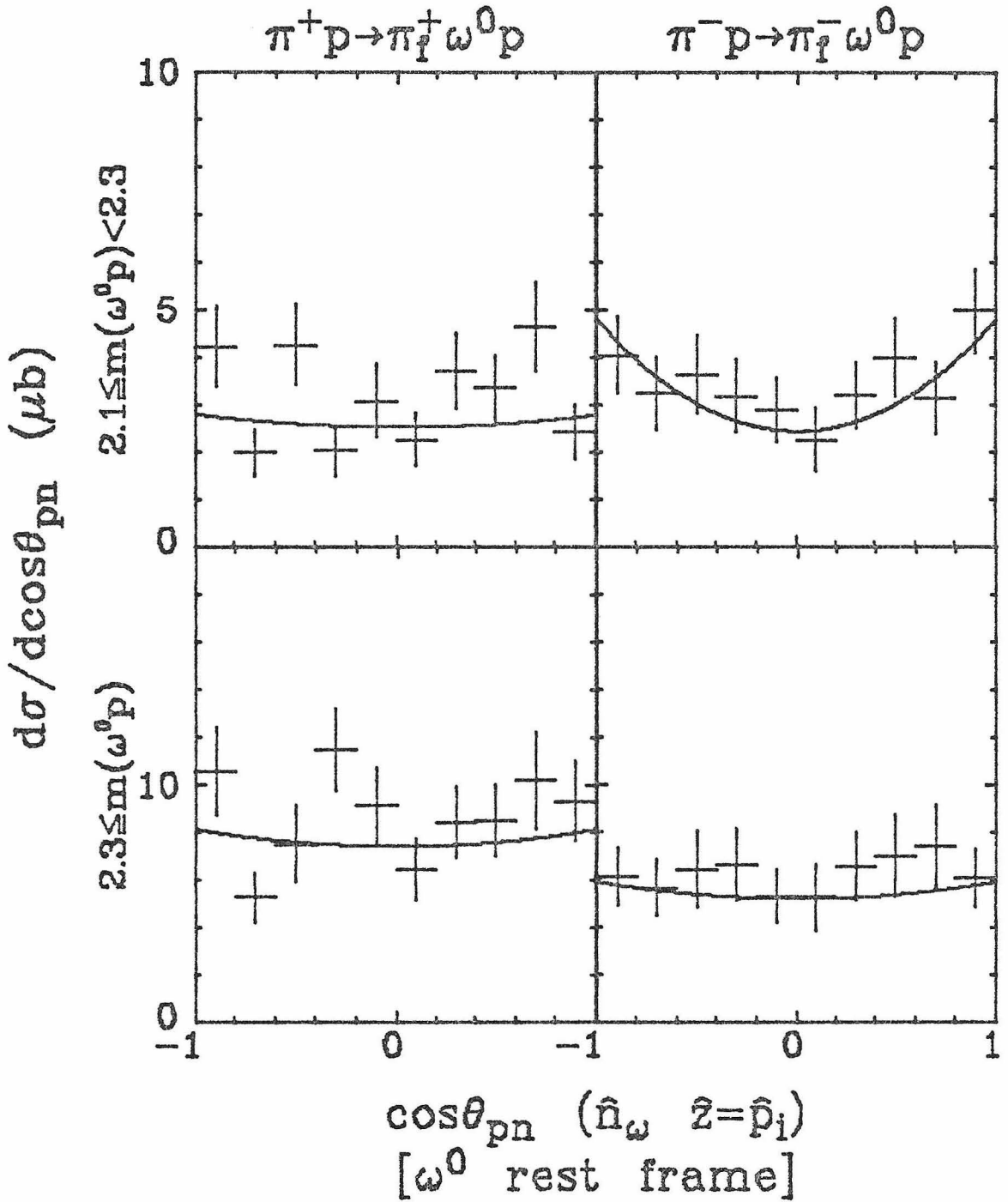


Figure VI.23a

Distributions of $\cos\theta_{pn}$ of the normal to the ω^0 decay plane for events in the ω^0 peak with high $\omega^0 p$ masses.

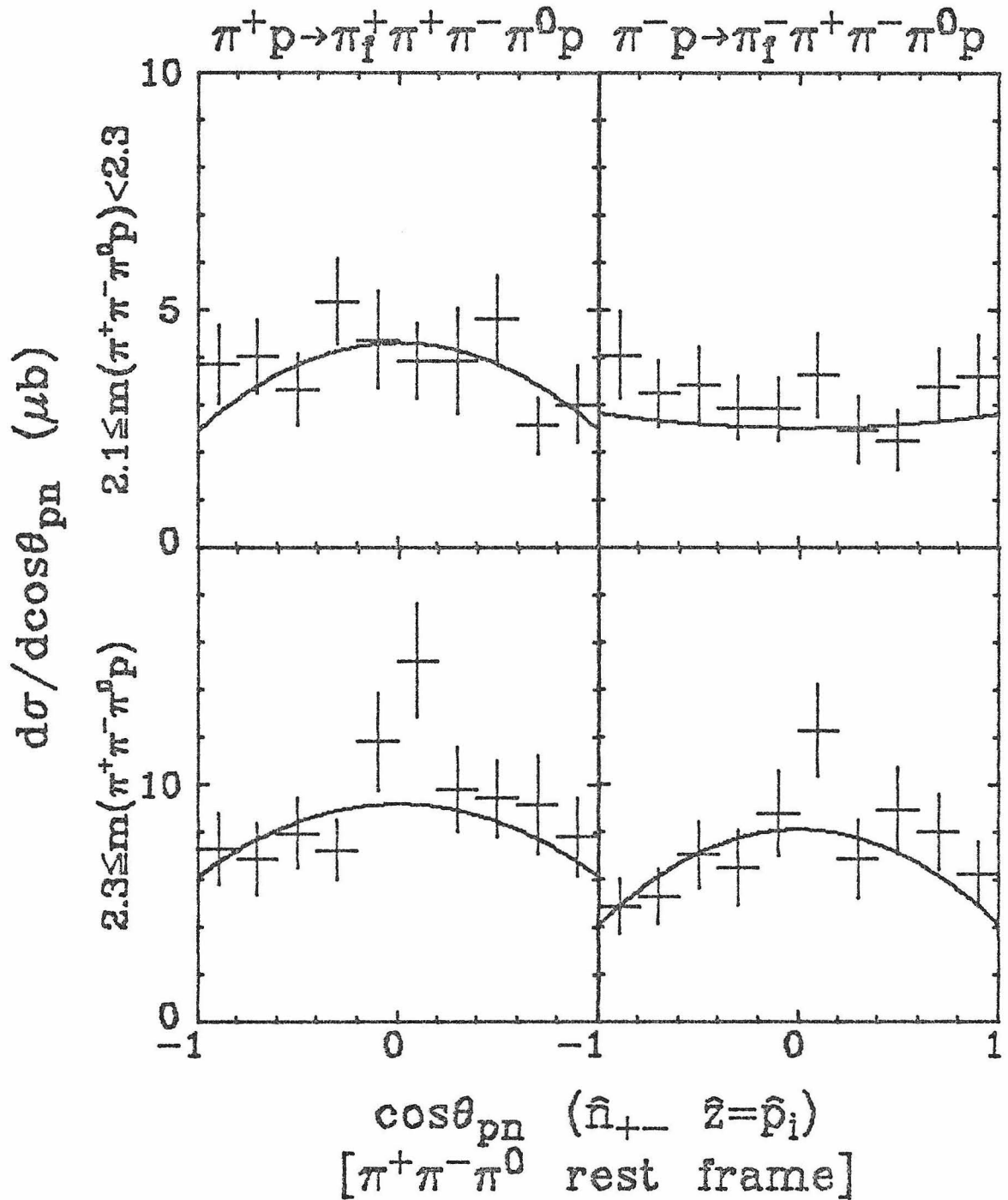


Figure VI.23b

Distributions of $\cos \theta_{pn}$ of the normal to the $\pi^+ \pi^-$ plane for events in the ω^0 wings with high $\pi^+ \pi^- \pi^0 p$ masses.

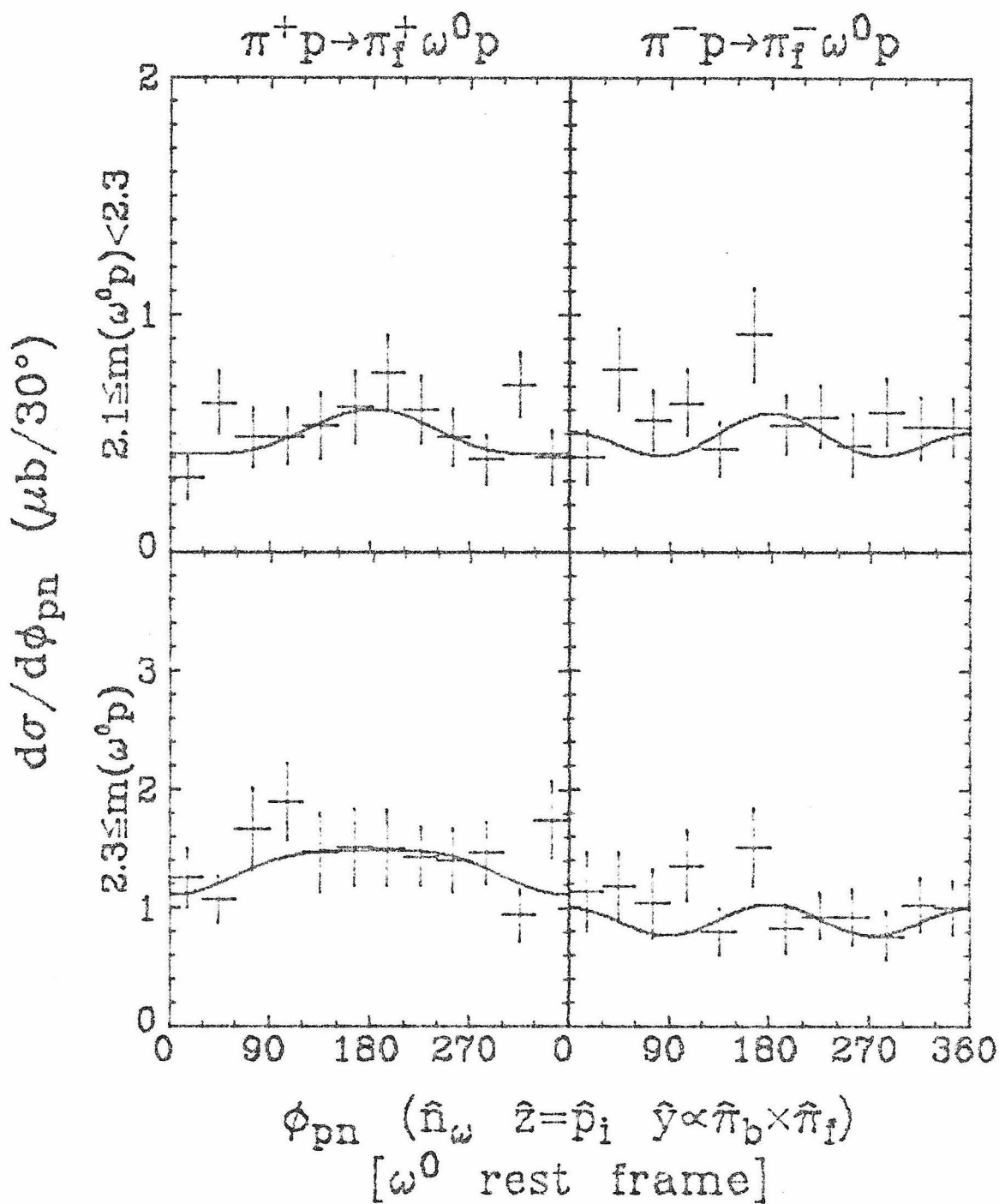


Figure VI.24a

Distributions of the ϕ_{pn} angle of the normal to the ω^0 decay plane for events in the ω^0 peak with high $\omega^0 p$ masses.

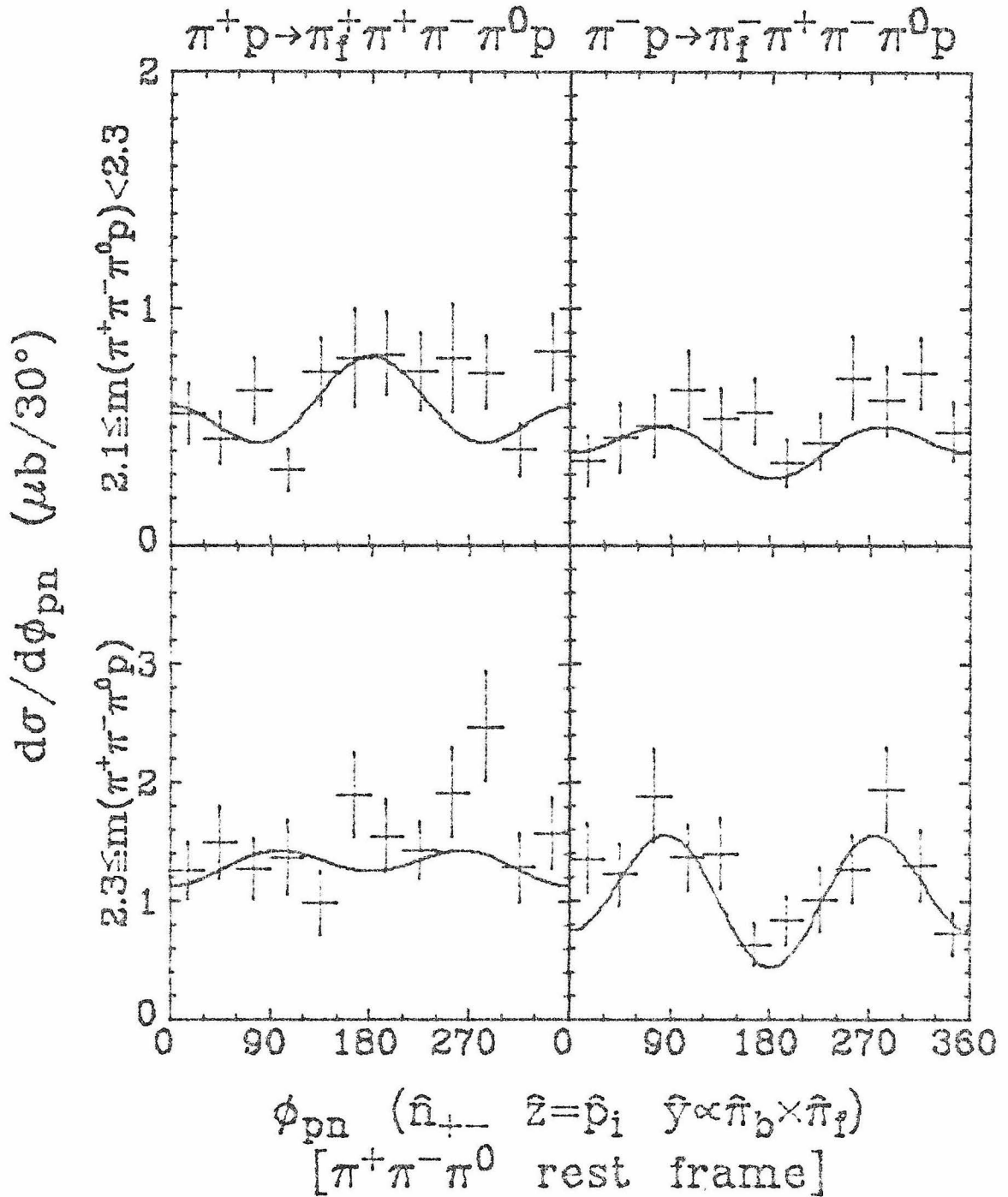


Figure VI.24b

Distributions of the ϕ_{pn} angle of the normal to the $\pi^+ \pi^-$ plane for events in the ω^0 wings with high $\pi^+ \pi^- \pi^0 p$ masses.

a large $\cos^2\theta_{pn}$ anisotropy (Fig. VI.21a). The curves in Figs. VI.21 and VI.23 are the result of fitting $a_0(1+a_2\cos^2\theta_{pn})$ to the data. Fits with a $\cos\theta_{pn}$ term gave small values to this term's coefficient as expected from the ω^0 decay distribution (equation (12a)). The fitted values for a_2 are listed in Table VI.8. Note that only the ω^0 peak events have large a_2 values while the ω^0 wings distributions are nearly isotropic and have small a_2 coefficients (see Figs. VI.21b and VI.23b).

Table VI.8

a_2 values from fits of $1+a_2\cos^2\theta_{pn}$ to the $d\sigma/d\cos\theta_{pn}$ distributions

ω^0 p mass band(GeV)	ω^0 peak events		ω^0 wings events	
	π^+	π^-	π^+	π^-
<1.9	1.12±0.39	1.85±0.54	0.30±0.27	0.01±0.23
1.9-2.1	0.83±0.42	0.69±0.39	0.01±0.20	-0.32±0.17
2.1-2.3	0.11±0.27	0.96±0.42	-0.43±0.16	0.12±0.30
≥2.3	0.10±0.22	0.14±0.25	-0.33±0.16	-0.50±0.14

The ϕ_{pn} distributions in Figs. VI.22 and VI.24 were fit by the form $c_0(1+c_1\cos\phi_{pn}+c_2\cos2\phi_{pn})$; the results are listed in Table VI.9 for the low masses. The choice of this functional form was based on the ω^0 decay distribution (equation (11)) and the lack of any strong non-isotropy in the ϕ_{pn} distributions.

Table VI.9

Results of $1+c_1 \cos\phi_{pn} + c_2 \cos 2\phi_{pn}$ fits to the

$\frac{d\sigma}{d\phi_{pn}}$ distributions

ω^0 p mass band (GeV)	π^+		π^-	
	c_1	c_2	c_1	c_2
	<u>ω^0 peak events</u>			
<1.9	-0.095±0.085	0.143±0.085	-0.135±0.084	-0.013±0.086
1.9-2.1	-0.094±0.098	0.110±0.089	-0.285±0.100	-0.044±0.113
	<u>ω^0 wings events</u>			
<1.9	-0.012±0.092	-0.082±0.093	0.002±0.102	0.086±0.101
1.9-2.1	-0.219±0.078	-0.101±0.080	0.092±0.094	-0.014±0.100

Using the fitted values for a_2 from Table VI.8, we have calculated the ω^0 Gottfried-Jackson frame ρ_{00} density matrix element for the ω^0 by use of equation (13). The values for ρ_{00} are given in Table VI.10 and plotted versus the ω^0 p mass in Fig. VI.25. The high mass ω^0 peak data and the ω^0 wings data have ρ_{00} values near 0.33, the expected value for non-aligned ω^0 production. For the lowest mass band (ω^0 p masses below 1.9 GeV), we find that the ω 's are produced with their spins aligned along the target proton. Atherton et al. [1975] have reported a similar alignment of the ω 's produced in $\bar{p}p\omega^0$ where they find ρ_{00} has a value of 0.57 ± 0.03 .

Similarly, the c_2 coefficient of $\cos 2\phi_{pn}$ (from Table VI.9) will give a value for the ρ_{1-1} density matrix element by using equation (14). The c_2 coefficients in Table VI.9 are essentially zero. From

Table VI.10

ω^0 Gottfried-Jackson frame ρ_{00} density matrix element

ω^0 p mass band(GeV)	ω^0 peak events		ω^0 wings events	
	π^+	π^-	π^+	π^-
<1.9	0.515±0.046	0.588±0.046	0.394±0.050	0.336±0.051
1.9-2.1	0.478±0.057	0.458±0.057	0.336±0.044	0.254±0.047
2.1-2.3	0.356±0.056	0.494±0.054	0.223±0.048	0.359±0.061
≥2.3	0.354±0.045	0.363±0.050	0.250±0.046	0.202±0.045

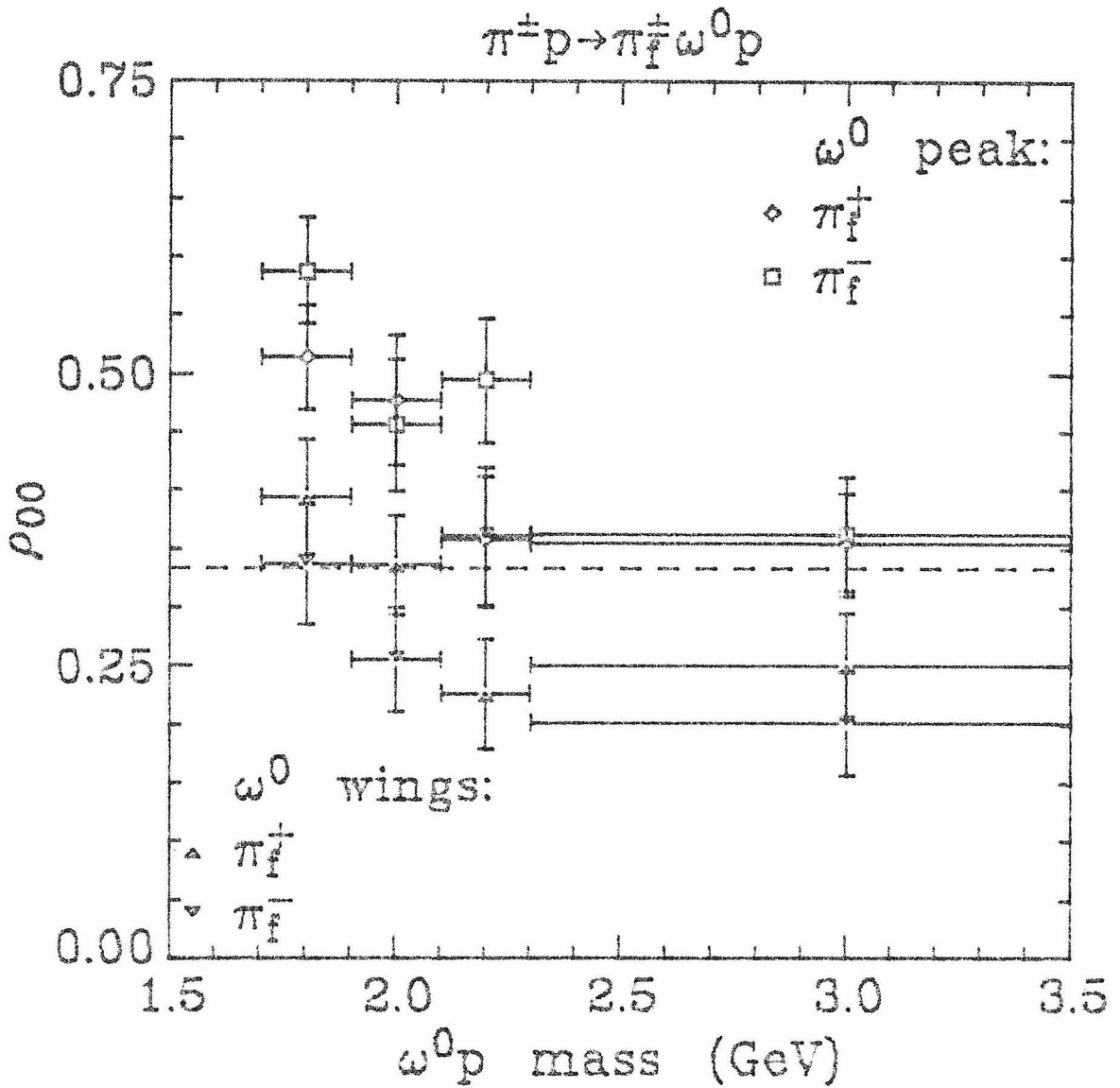


Figure VI.25

Plot of the ω^0 Gottfried-Jackson frame ρ_{00} density matrix element of the ω^0 versus the $\omega^0 p$ mass for events in the ω^0 peak and in the ω^0 wings.

looking at Figs. VI.22 it appears that even for those data sets with a non-zero value of c_2 (not within a standard deviation of 0), the distributions have no obvious $\cos 2\phi_{pn}$ dependence. Thus we conclude that ρ_{1-1} in the ω^0 Gottfried-Jackson frame is zero.

Figs. VI.26 and VI.28 show the $\cos\theta_{n\omega}$ distributions for the normal to the ω^0 decay plane in the ω^0 helicity frame. The ω^0 helicity frame and the angles $\theta_{n\omega}$ and $\phi_{n\omega}$ are defined in Fig. VI.15b. In contrast to $\cos\theta_{pn}$ from Figs. VI.21, the helicity angle distributions are flat, showing no alignment of the ω^0 along its direction of motion. Table VI.11 gives the a_2 values from fitting $a_0(1+a_2\cos^2\theta_{n\omega})$ to these distributions (see also the curves in Figs. VI.26 and VI.28). The ω^0 helicity frame ρ_{00} values derived from the fitted a_2 values are given in Table VI.12 and are in good agreement with the value of 0.33 for an unaligned state.

Table VI.11

a_2 values from $1+a_2\cos^2\theta_{n\omega}$ fits to the

$d\sigma/d\cos\theta_{n\omega}$ distributions

ω^0 p mass band (GeV)	ω^0 peak events		ω^0 wings events	
	π^+	π^-	π^+	π^-
	π^+	π^-	π^+	π^-
<1.9	-0.11±0.20	-0.00±0.20	0.21±0.26	0.38±0.29
1.9-2.1	0.06±0.22	-0.40±0.17	-0.02±0.19	0.23±0.25
2.1-2.3	-0.07±0.23	-0.32±0.19	-0.04±0.22	-0.11±0.24
≥2.3	-0.37±0.14	-0.17±0.22	-0.61±0.12	-0.70±0.11

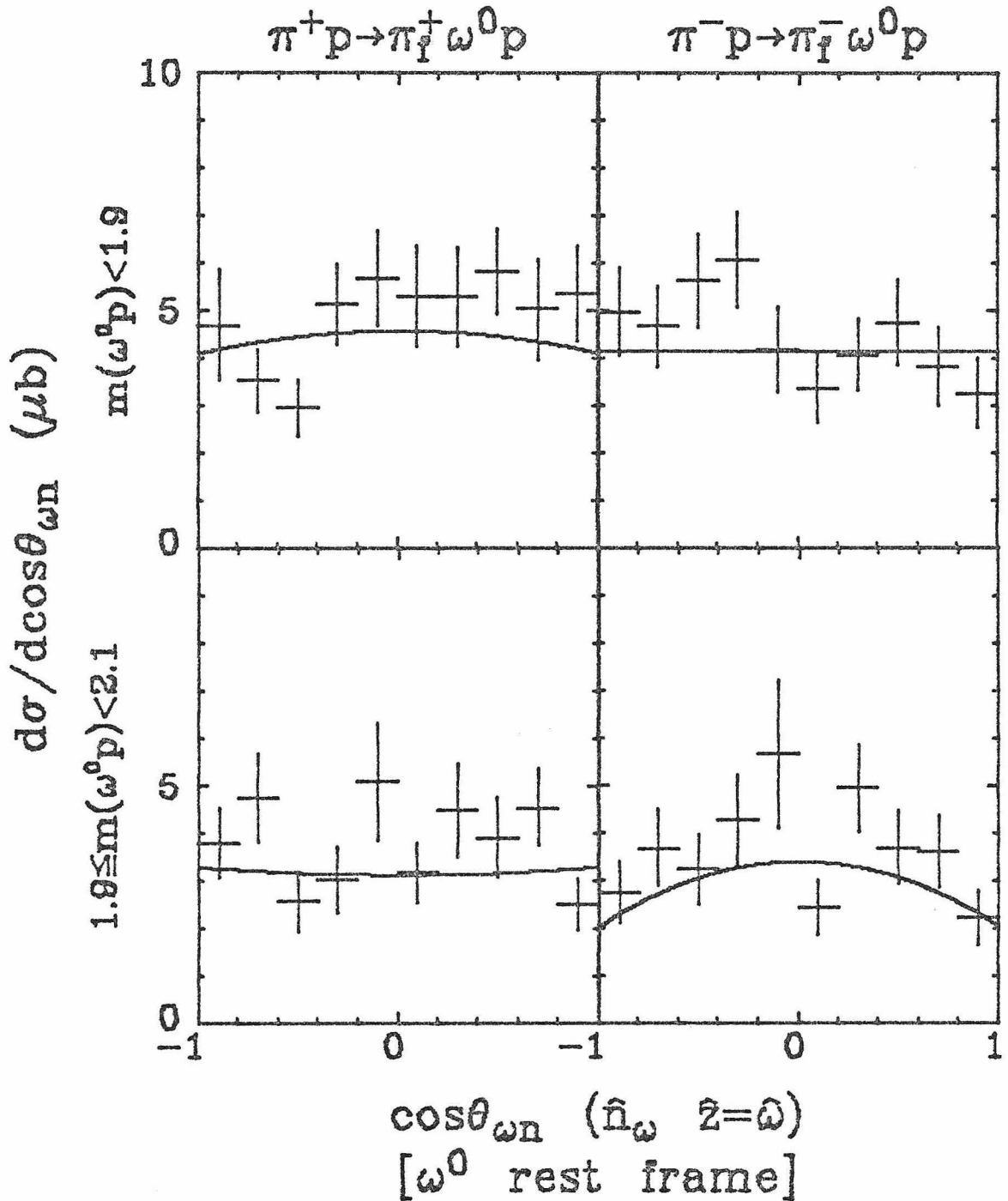


Figure VI.26a

Distributions of $\cos\theta_{\omega n}$ of the normal to the ω^0 decay plane for events in the ω^0 peak with low $\omega^0 p$ masses. The $\theta_{\omega n}$ angle is defined in Fig. VI.15b.

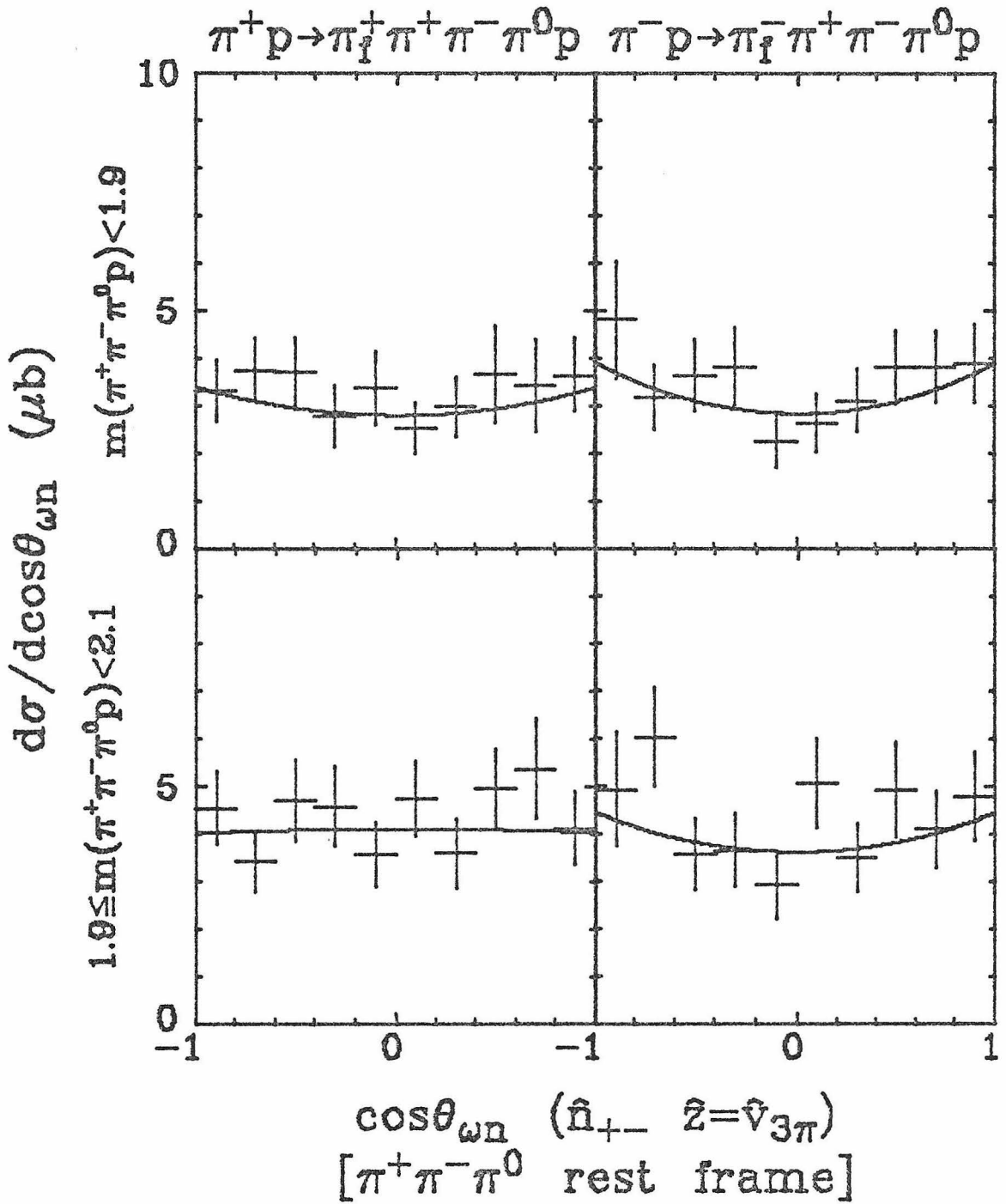


Figure VI.26b

Distributions of $\cos\theta_{n\omega}$ of the normal to the $\pi^+ \pi^-$ plane for events in the ω^0 wings with low $\pi^+ \pi^- \pi^0 p$ masses.

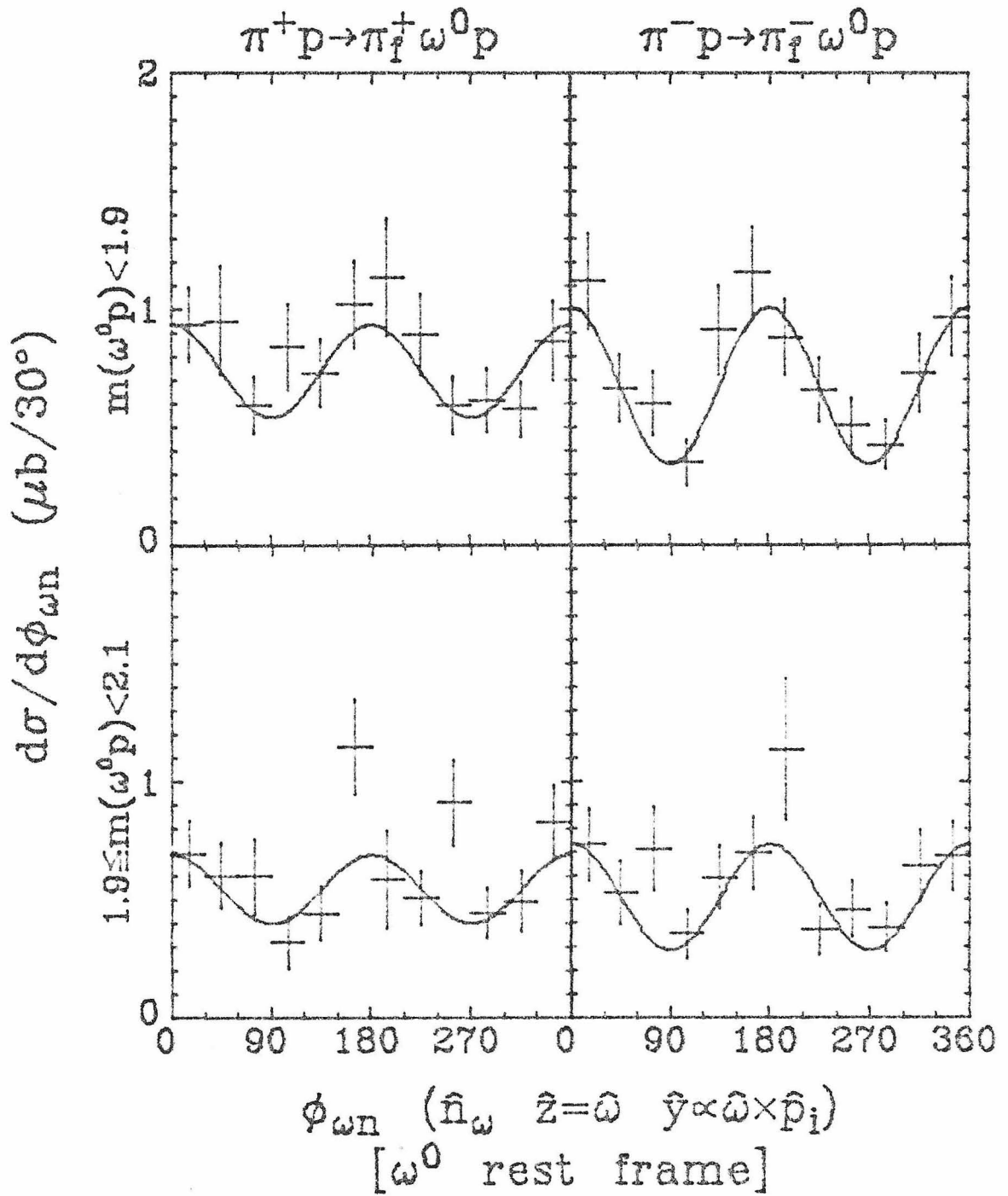


Figure VI.27a

Distributions of the $\phi_{\omega n}$ angle of the normal to the ω^0 decay plane for events in the ω^0 peak with low $\omega^0 p$ masses. The $\phi_{\omega n}$ angle is defined in Fig. VI.15b.

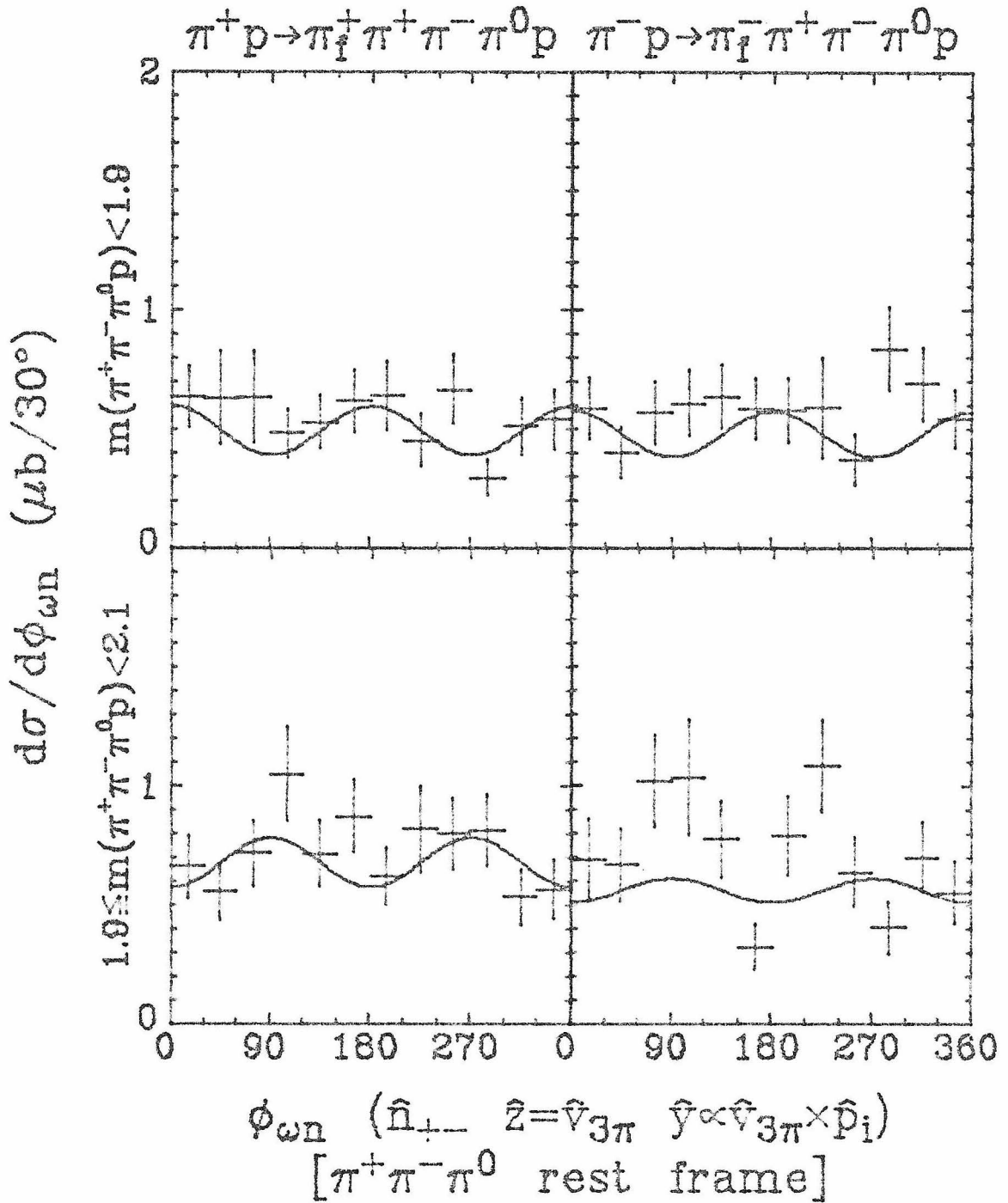


Figure VI.27b

Distributions of the $\phi_{\omega n}$ angle of the normal to the $\pi^+ \pi^-$ plane for events in the ω^0 wings with low $\pi^+ \pi^- \pi^0 p$ masses.

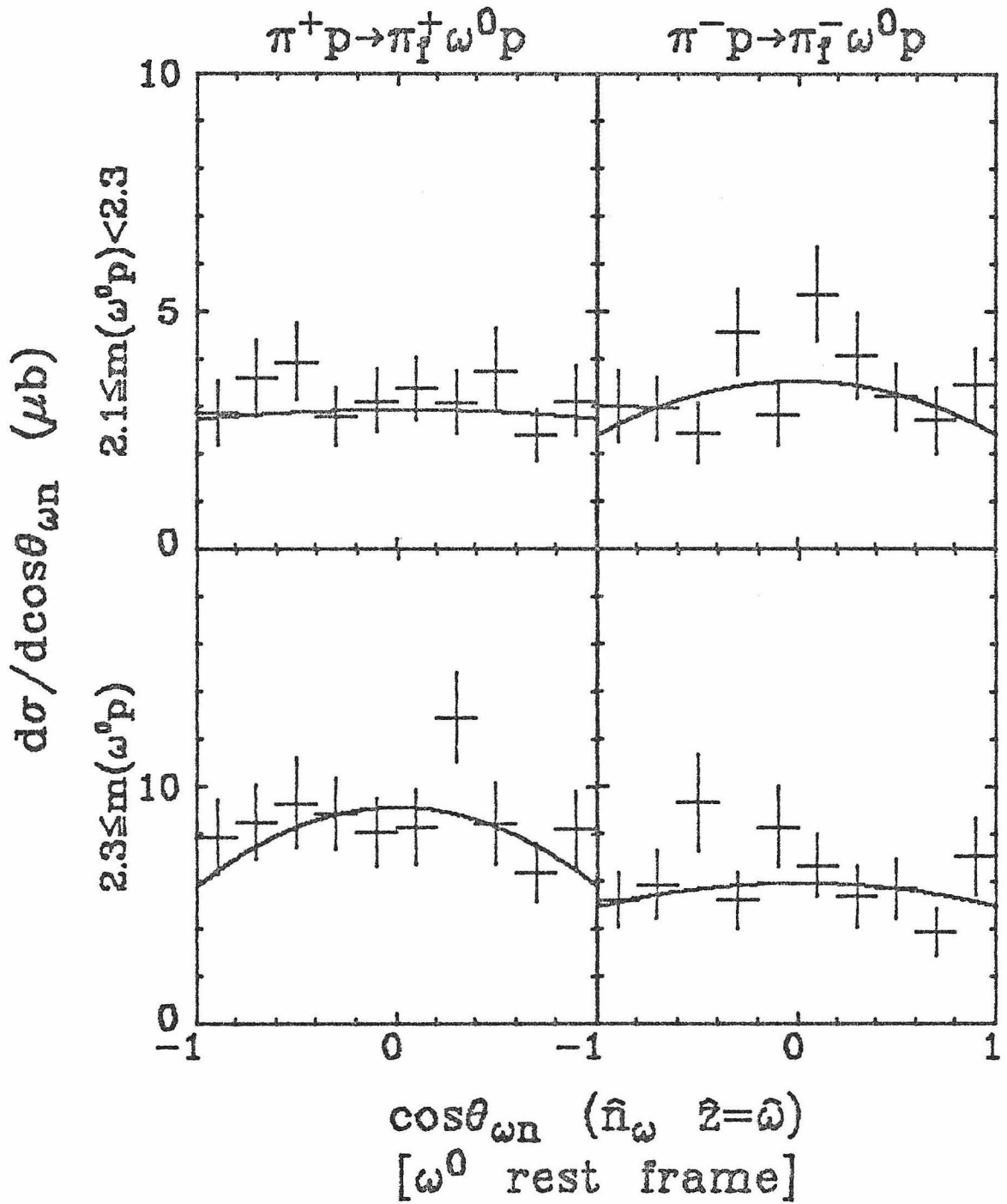


Figure VI.28a

Distributions of $\cos\theta_{\omega n}$ of the normal to the ω^0 decay plane for events in the ω^0 peak with high $\omega^0 p$ masses.

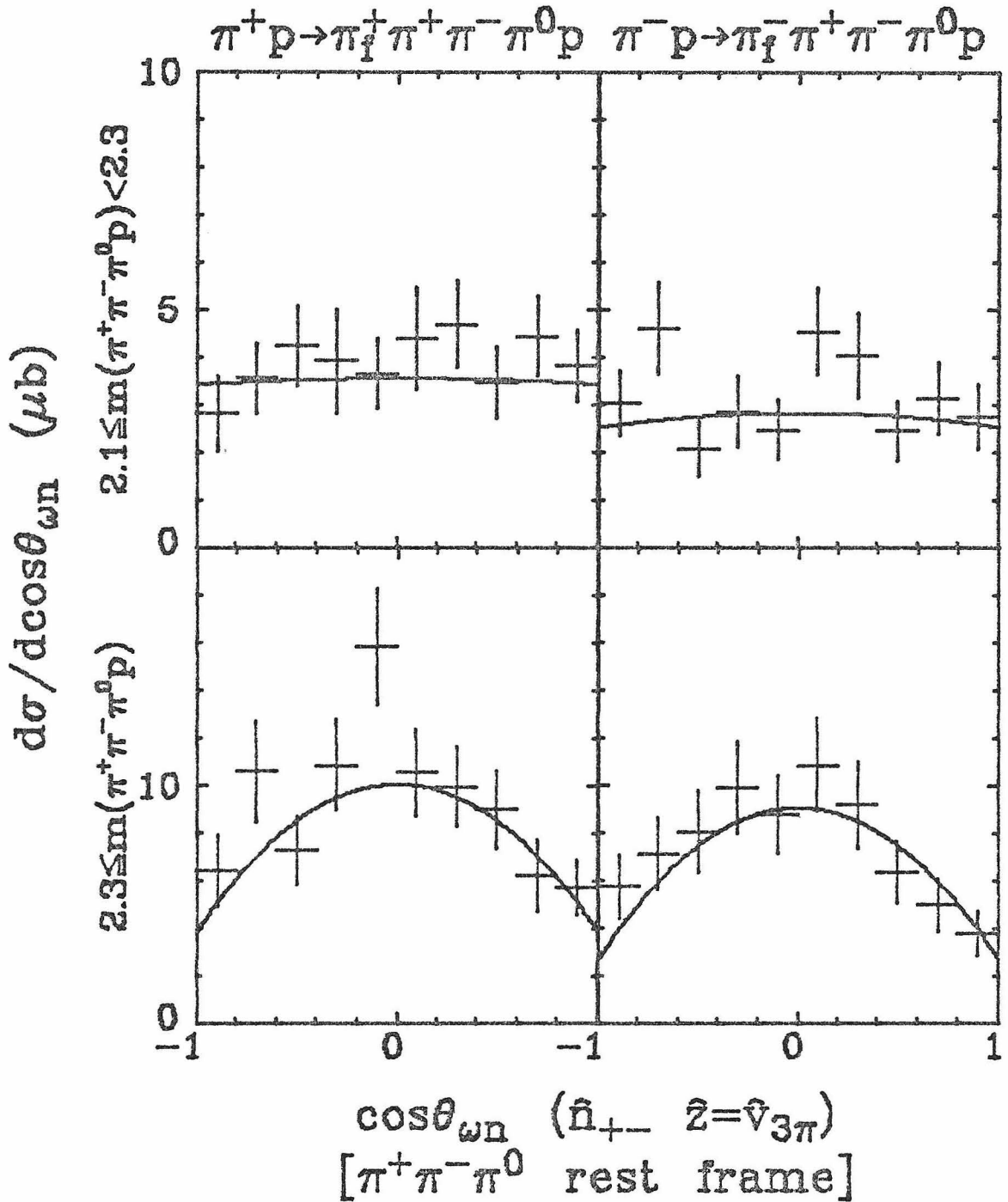


Figure VI.28b

Distributions of $\cos \theta_{\omega n}$ of the normal to the $\pi^+ \pi^-$ plane for events in the ω^0 wings with high $\pi^+ \pi^- \pi^0 p$ masses.

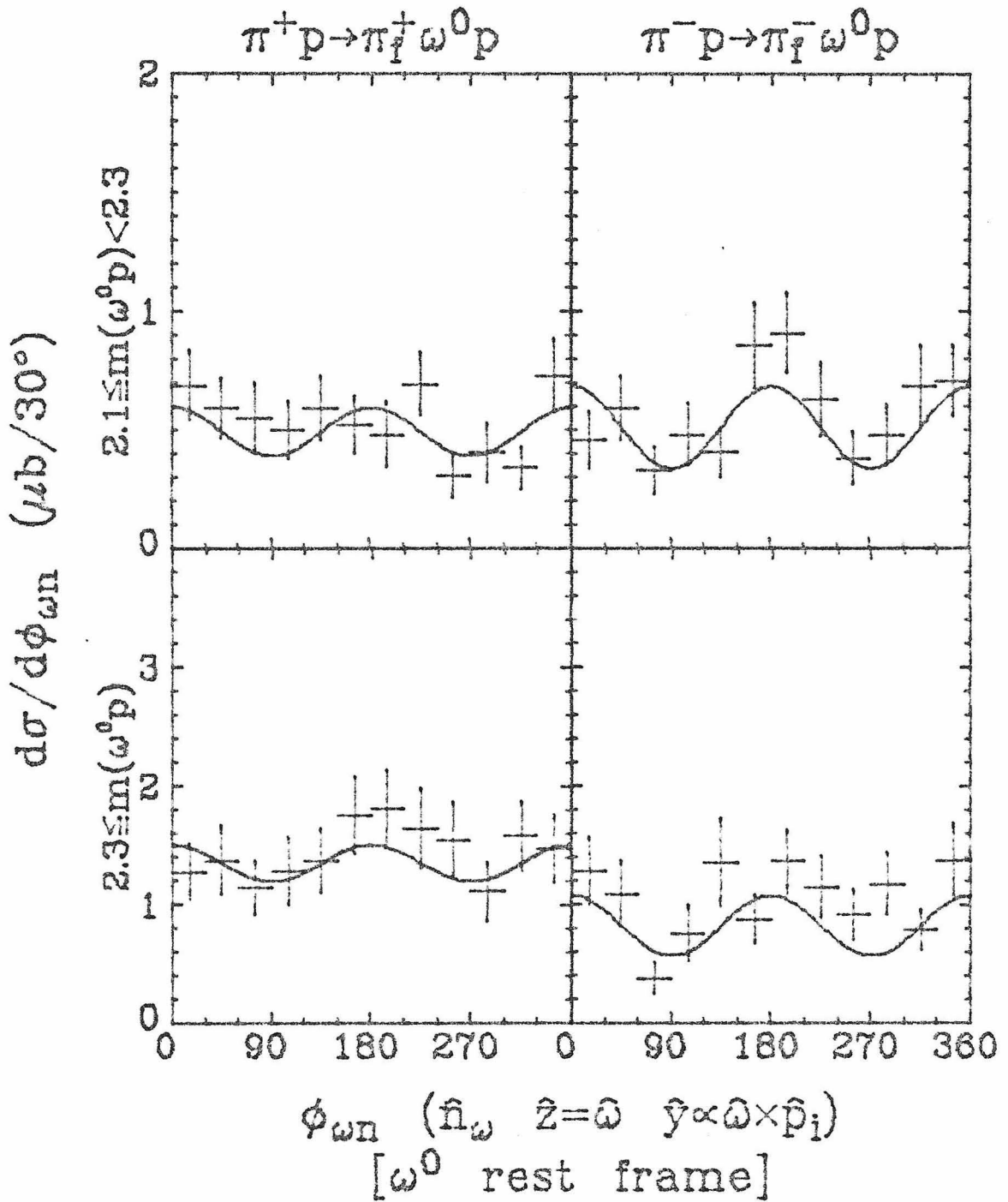


Figure VI.29a

Distributions of the $\phi_{\omega n}$ angle of the normal to the ω^0 decay plane for events in the ω^0 peak with high $\omega^0 p$ masses.

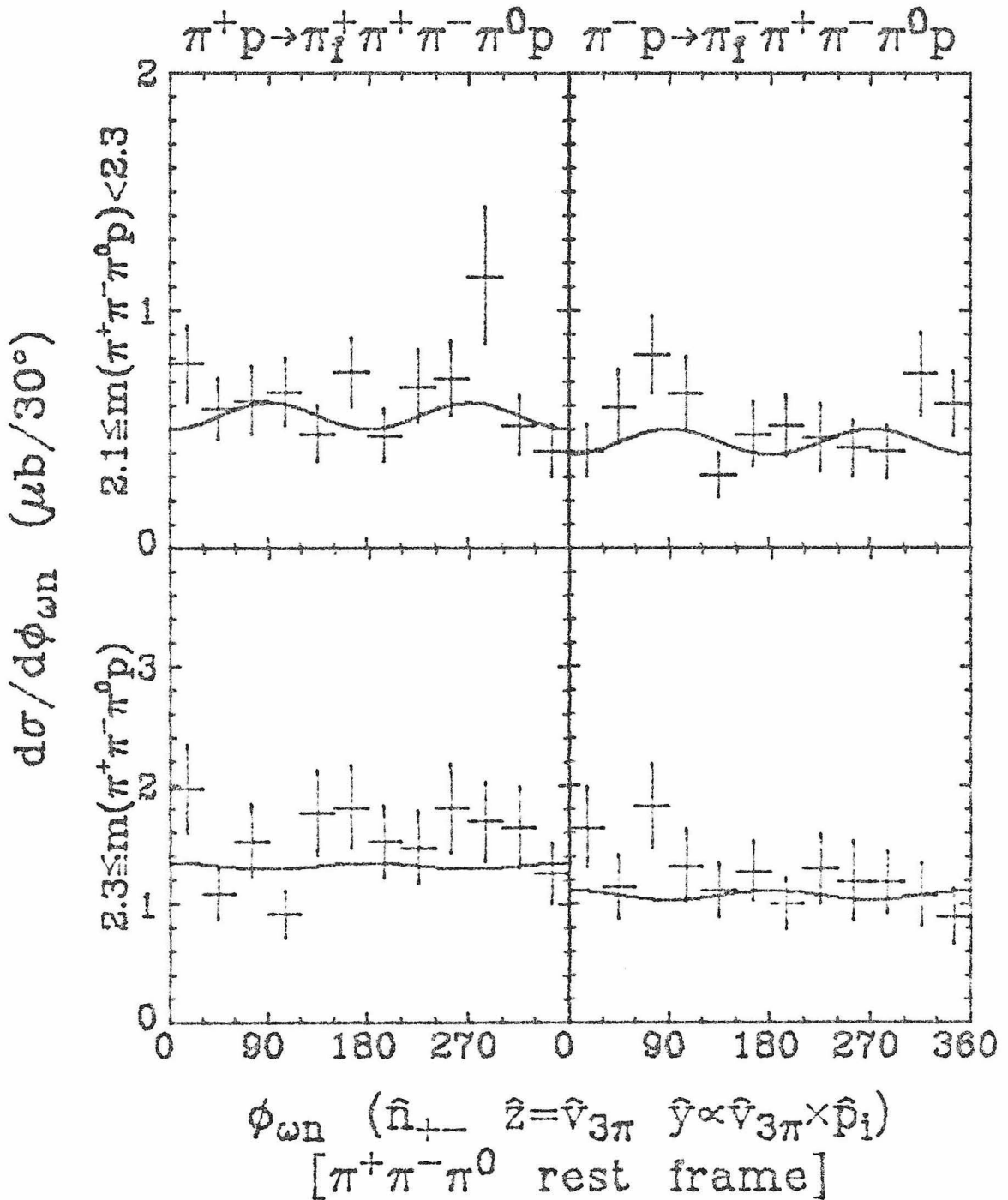


Figure VI.29b

Distributions of the $\phi_{\omega n}$ angle of the normal to the $\pi^+ \pi^-$ plane for events in the ω^0 wings with high $\pi^+ \pi^- \pi^0 p$ masses.

Table VI.12

ω^0 p mass band (GeV)	ω^0 helicity frame ρ_{00} density matrix element			
	ω^0 peak events		ω^0 wings events	
	π^+	π^-	π^+	π^-
<1.9	0.309±0.047	0.333±0.045	0.377±0.050	0.407±0.050
1.9-2.1	0.345±0.047	0.230±0.051	0.328±0.042	0.380±0.049
2.1-2.3	0.317±0.054	0.254±0.053	0.324±0.050	0.308±0.057
≥2.3	0.240±0.040	0.293±0.055	0.163±0.042	0.130±0.042

The distributions of the $\phi_{n\omega}$ angle are given in Figs. VI.27 and VI.29. As is evident from the plots, these distributions (especially for low ω^0 p masses) show a marked $\cos 2\phi_{n\omega}$ dependence. The distributions have been fit by $c_0(1+c_2\cos 2\phi_{n\omega})$ (see equation (11)) with the results being given in Table VI.13. The ρ_{1-1} density matrix elements derived from the c_2 coefficients are given in Table VI.14. As can be seen from these results, the ω^0 density matrix defined in the ω^0 helicity frame has equal diagonal elements (values consistent with 1/3) and a significantly non-zero non-diagonal element (ρ_{1-1}).

Table VI.13

c_2 values from $1+c_2\cos 2\phi_{n\omega}$ fits to the

$d\sigma/d\phi_{n\omega}$ distributions

<u>ω^0 p mass band (GeV)</u>	<u>ω^0 peak events</u>		<u>ω^0 wings events</u>	
	<u>π^+</u>	<u>π^-</u>	<u>π^+</u>	<u>π^-</u>
<1.9	0.267±0.080	0.492±0.078	0.209±0.092	0.200±0.096
1.9-2.1	0.268±0.101	0.442±0.093	-0.154±0.082	-0.089±0.096
2.1-2.3	0.208±0.104	0.339±0.100	-0.102±0.101	-0.120±0.115
≥2.3	0.116±0.081	0.312±0.103	0.021±0.087	0.040±0.100

Table VI.14

ω^0 helicity frame ρ_{1-1} density matrix element

<u>ω^0 p mass band (GeV)</u>	<u>ω^0 peak events</u>		<u>ω^0 wings events</u>	
	<u>π^+</u>	<u>π^-</u>	<u>π^+</u>	<u>π^-</u>
<1.9	-0.134±0.040	-0.246±0.039	-0.105±0.046	-0.100±0.048
1.9-2.1	-0.134±0.051	-0.221±0.047	0.077±0.041	0.045±0.048
2.1-2.3	-0.104±0.052	-0.170±0.050	0.051±0.051	0.060±0.058
≥2.3	-0.058±0.041	-0.156±0.052	-0.011±0.044	-0.020±0.050

As discussed earlier, the ω^0 and N^* decay angular distributions are correlated though the dependence of the ω^0 density matrix on the θ_{pp} and ϕ_{pp} angles (see equation (15)). We present these correlations as fractions of events in each of 9 regions of a $\cos\theta_{n\omega}$ (or $\cos\theta_{pn}$) versus $\cos\theta_{pp}$ plot. The correlations between the θ_{pp} and $\theta_{n\omega}$ angles are given in Tables VI.15 and VI.16 as the region fractions from the $(\cos\theta_{pp}, \cos\theta_{n\omega})$ plots. The region fractions from the $(\cos\theta_{pp}, \cos\theta_{pn})$ plot are given in Table VI.17. Note that an uncorrelated distribution would have 1/9 (or 0.111) of its events in each region of the plot if the individual $\cos\theta$ distributions are fairly uniform.

Table VI.15

$\cos\theta_{pp}$ versus $\cos\theta_{n\omega}$ correlation
results for ω^0 peak events

<u>$\cos\theta_{n\omega}$ range</u>	<u>$\cos\theta_{pp}$ range</u>		
	<u>-1 to -1/3</u>	<u>-1/3 to +1/3</u>	<u>+1/3 to +1</u>
<u>π^+ (ω^0 p mass < 1.9 GeV)</u>			
+1/3 to +1	0.150±0.022	0.119±0.018	0.094±0.020
-1/3 to +1/3	0.199±0.028	0.066±0.013	0.104±0.021
-1 to -1/3	0.097±0.015	0.103±0.024	0.067±0.013
<u>π^+ (ω^0 p mass: 1.9-2.1 GeV)</u>			
+1/3 to +1	0.089±0.020	0.064±0.015	0.154±0.023
-1/3 to +1/3	0.109±0.031	0.109±0.020	0.149±0.027
-1 to -1/3	0.089±0.021	0.072±0.017	0.165±0.023
<u>π^- (ω^0 p mass < 1.9 GeV)</u>			
+1/3 to +1	0.132±0.021	0.092±0.017	0.074±0.017
-1/3 to +1/3	0.152±0.023	0.087±0.017	0.078±0.015
-1 to -1/3	0.161±0.023	0.107±0.019	0.117±0.020
<u>π^- (ω^0 p mass: 1.9-2.1 GeV)</u>			
+1/3 to +1	0.109±0.022	0.054±0.014	0.146±0.024
-1/3 to +1/3	0.106±0.021	0.165±0.044	0.135±0.023
-1 to -1/3	0.087±0.019	0.086±0.018	0.112±0.022

Table VI.16

cos θ_{pp} versus cos $\theta_{n\omega}$ correlation
results for ω^0 wings events

<u>cos$\theta_{n\omega}$ range</u>	<u>cosθ_{pp} range</u>		
	<u>-1 to -1/3</u>	<u>-1/3 to +1/3</u>	<u>+1/3 to +1</u>
<u>π^+ (ω^0 p mass <1.9 GeV)</u>			
+1/3 to +1	0.130±0.032	0.089±0.018	0.136±0.032
-1/3 to +1/3	0.082±0.018	0.085±0.018	0.114±0.024
-1 to -1/3	0.097±0.019	0.115±0.020	0.151±0.023
<u>π^+ (ω^0 p mass: 1.9-2.1 GeV)</u>			
+1/3 to +1	0.049±0.014	0.106±0.018	0.213±0.027
-1/3 to +1/3	0.094±0.017	0.061±0.014	0.149±0.021
-1 to -1/3	0.072±0.014	0.072±0.015	0.184±0.024
<u>π^- (ω^0 p mass <1.9 GeV)</u>			
+1/3 to +1	0.120±0.022	0.120±0.023	0.125±0.022
-1/3 to +1/3	0.129±0.022	0.047±0.013	0.106±0.022
-1 to -1/3	0.144±0.035	0.087±0.019	0.122±0.023
<u>π^- (ω^0 p mass: 1.9-2.1 GeV)</u>			
+1/3 to +1	0.081±0.017	0.092±0.019	0.171±0.027
-1/3 to +1/3	0.071±0.016	0.071±0.015	0.140±0.023
-1 to -1/3	0.087±0.017	0.106±0.026	0.182±0.027

Table VI.17

$\cos\theta_{pp}$ versus $\cos\theta_{pn}$ correlation
results for ω^0 peak events

<u>$\cos\theta_{pn}$ range</u>	<u>$\cos\theta_{pp}$ range</u>		
	<u>-1 to -1/3</u>	<u>-1/3 to +1/3</u>	<u>+1/3 to +1</u>
<u>π^+ (ω^0 p mass <1.9 GeV)</u>			
+1/3 to +1	0.213±0.028	0.096±0.023	0.063±0.013
-1/3 to +1/3	0.067±0.014	0.077±0.014	0.107±0.017
-1 to -1/3	0.166±0.021	0.116±0.017	0.094±0.024
<u>π^+ (ω^0 p mass: 1.9-2.1 GeV)</u>			
+1/3 to +1	0.122±0.031	0.070±0.015	0.160±0.023
-1/3 to +1/3	0.078±0.022	0.094±0.021	0.142±0.026
-1 to -1/3	0.086±0.020	0.082±0.016	0.166±0.024
<u>π^- (ω^0 p mass <1.9 GeV)</u>			
+1/3 to +1	0.214±0.028	0.102±0.018	0.102±0.018
-1/3 to +1/3	0.041±0.012	0.086±0.016	0.085±0.016
-1 to -1/3	0.189±0.025	0.098±0.018	0.083±0.018
<u>π^- (ω^0 p mass: 1.9-2.1 GeV)</u>			
+1/3 to +1	0.132±0.023	0.120±0.038	0.131±0.023
-1/3 to +1/3	0.037±0.012	0.102±0.025	0.119±0.022
-1 to -1/3	0.134±0.024	0.083±0.019	0.142±0.024

5. Discussion of the ω^0 p Resonance Spin-parity Analyses

The information contained in the angular distributions of the ω^0 p and ω^0 decays has been used in an effort to determine the spin-parity of the ω^0 p resonance [Lednicky 1975]. The lack of any significantly non-zero Y_{ℓ}^m moments below an ω^0 p mass of 2.1 GeV has been taken to indicate that the ω^0 p system is in an S-wave state. This then established the possible spin-parities of the N^* as $1/2^-$ or $3/2^-$. Lednicky used the results of several experiments with results similar to those reported in the previous section to conclude that the ω^0 p resonance had a J^P of $3/2^-$. The observations that bear directly on this conclusion are a "nearly" isotropic N^* decay with moments nearly zero in the N^* region and the large ρ_{00} value for the ω^0 found by Atherton et al. [1974] in the ω^0 Gottfried-Jackson frame. However, as we pointed out earlier, the N^* decay distribution contains a significant non-isotropic piece which is not apparent in the moments due to their normalization.

Dickey [1978] has further shown that either the $1/2^-$ or $3/2^-$ spin-parity choice results in an isotropic distribution for the N^* decay. Dickey has also calculated the ω^0 density matrix (in the ω^0 helicity frame) from the N^* decay and has found that either spin-parity choice results in a diagonal matrix for the ω^0 . If the spin-parity is $1/2^-$, then one obtains equal elements (all $1/3$) in the ω^0 density matrix while those from the $3/2^-$ choice contain $\cos\theta_{pp}$ terms. The ω^0 density matrix for the $3/2^-$ choice is:

$$\rho_{mm'}^{\omega} = \begin{bmatrix} (5-3\cos^2\theta_{pp})/12 & 0 & 0 \\ 0 & (1+3\cos^2\theta_{pp})/6 & 0 \\ 0 & 0 & (5-3\cos^2\theta_{pp})/12 \end{bmatrix} \quad (20)$$

When integrated over $\cos\theta_{pp}$, the ω^0 density matrix for either J^P predicts the flat distribution in $\cos\theta_{n\omega}$ which we observe (Fig. VI.25a). The prediction of a flat $\phi_{n\omega}$ distribution is obviously wrong (Fig. VI.26a), but the reason for this failure is currently unclear.

With the ω^0 decay angular distribution from equation (11a), we get the following joint distribution in the angles θ_{pp} and $\theta_{n\omega}$ by using $\rho_{mm'}^{\omega}$, for $J^P=3/2^-$:

$$W(\theta_{pp}, \theta_{n\omega}) = \frac{3}{2} [(1+3\cos^2\theta_{pp})\cos^2\theta_{n\omega} + (5-3\cos^2\theta_{pp})(1-\cos^2\theta_{n\omega})/2] \quad (21)$$

This distribution gives the pattern shown in Table IV.18 (as a fraction of events in each region) and can be compared to the results of this experiment shown in Tables VI.15 and VI.16. As can be seen, the predicted pattern is not evident in any of the distributions. However, the data distributions suffer from low statistics and have errors larger than the deviation of the $3/2^-$ prediction from an uncorrelated distribution (the $1/2^-$ prediction).

Table VI.18

Predicted $\cos\theta_{pp}$ versus $\cos\theta_{n\omega}$ correlation pattern for $J^P=3/2^-$

<u>$\cos\theta_{n\omega}$ range</u>	<u>$\cos\theta_{pp}$ range</u>		
	<u>-1 to -1/3</u>	<u>-1/3 to +1/3</u>	<u>+1/3 to +1</u>
+1/3 to +1	0.117	0.100	0.117
-1/3 to +1/3	0.100	0.133	0.100
-1 to -1/3	0.117	0.100	0.117

We can partially overcome the limited statistics by combining the 9 numbers into just 2. These two numbers are the fractions of events in the regions of the plot that are enhanced or reduced relative to the uncorrelated distribution (0.111 per region). The enhanced regions are the center (0.133) and the four corners (0.117) in Table VI.18. The reduced regions are the remaining four with values of 0.100 each. The predicted enhanced values are 0.556 for $J^P=1/2^-$ and 0.600 for $J^P=3/2^-$; the reduced values are 0.444 for $J^P=1/2^-$ and 0.400 for $J^P=3/2^-$. Table VI.19 summarizes the data results. As can be seen, the results are inconclusive. The N^* region data does not match either prediction. The off-resonance and the ω^0 wings data match the $J^P=3/2^-$ prediction very well for an unknown reason.

Table VI.19

Combined $\cos\theta_{pp}$ versus $\cos\theta_{n\omega}$ correlation fractions					
ω^0 data	ω^0 mass	π^+		π^-	
		Enhanced	Reduced	Enhanced	Reduced
peak	<1.9	0.474±0.038	0.525±0.046	0.571±0.044	0.429±0.037
peak	1.9-2.1	0.606±0.048	0.394±0.047	0.619±0.062	0.381±0.039
wings	<1.9	0.599±0.057	0.400±0.040	0.528±0.054	0.442±0.043
wings	1.9-2.1	0.579±0.044	0.421±0.036	0.592±0.048	0.409±0.043

Both the Lednicky and Dickey analyses and our earlier paper [Davison 1974] argue that the $\omega^0 p$ system is in an S-wave state due to the lack of any significantly non-zero moments in the region of the N^* . However, as we pointed out earlier (equations (19)), the normalizations of the moments can result in small values even if the angular distributions are significantly non-isotropic. In fact the $\cos\theta_{pp}$ distribution in the N^* region (Fig. VI.17a) was found to have a significant backward peak even though the moments have very small values. The higher masses have $\cos\theta_{pp}$ distributions with very strong forward peaks and do show large non-zero moments.

The backward peak in the N^* $\cos\theta_{pp}$ distribution may be the result of non-zero off-diagonal terms in the N^* density matrix or of interference with the background amplitude. The lack of any significant ϕ_{pp} dependence seems to rule out the existence of any non-zero off-diagonal

density matrix elements. On the other hand, the fits to the ω^0 p mass distribution showed that nearly 50% of the cross section in the N^* region is due to background. If the resonance had a P-wave decay ($L=1$) and the background was an S-wave state, then interference between their amplitudes could generate a $\cos\theta_{pp}$ term in the angular distribution. Since there are approximately equal amounts of the resonance and background cross sections for ω^0 p masses below 1.9 GeV, it is likely that the resonance and background amplitudes are of comparable strength. Thus the $\cos\theta_{pp}$ interference term could hide the $\cos^2\theta_{pp}$ dependence from the resonance's P-wave decay.

The choice of a P-wave resonance in the above example was made since the S-wave assumption seems to be invalid. Dickey's predictions based on this assumption are also not completely supported by our data. The lack of the predicted isotropy in the ω^0 p decay has been discussed; the prediction of an isotropic decay distribution for the ω^0 in its helicity frame comes from Dickey's calculation of a diagonal ω^0 density matrix whose terms are all 1/3 after integrating over the N^* decay angles. Our results support the values of 1/3 for the diagonal elements of the ω^0 density matrix but we find a significantly non-zero value for ρ_{1-1} based on the observed strong $\cos 2\phi_{n\omega}$ dependence (Fig. VI.27a). However, the observation of a $\cos 2\phi_{n\omega}$ dependence of similar strength in the mass band above the N^* (Fig. VI.27a) indicates that the background may be the source for the non-zero ρ_{1-1} element. Finally, the pattern predicted by Dickey for the $(\cos\theta_{pp}, \cos\theta_{n\omega})$ plot in Table VI.18 is not seen in our results (Table VI.15). However, there is

some evidence (Table VI.19) that the background under the N^* is in an S-wave state with $J^P=3/2^-$.

We thus find that it is quite likely that Lednicky's result of $3/2^-$ for the spin-parity of the ω_p^0 resonance is in error. The basic assumption of an S-wave decay seems to be unsupported in light of our data. In fact, as discussed above, a P-wave decay for the N^* with an S-wave background may be needed to explain the ω_p^0 angular distribution and in particular the peak at $\cos\theta_{pp}=-1$. If the resonance is in fact a P-wave state, then there are two known resonances whose masses are good matches to that found for the ω_p^0 resonance. These are the N(1780) with a J^P of $1/2^+$ and the N(1810) with a J^P of $3/2^+$ [Particle Data Group 1978]. This match is due to the P-wave ω_p^0 state having possible J^P 's of $1/2^+$, $3/2^+$, and $5/2^+$. An S-wave ω_p^0 state can only have a J^P of $1/2^-$ or $3/2^-$ and will not match any of the known resonances. At this time we can make no definite conclusion except that further work is needed to resolve the question of the spin-parity of the ω_p^0 resonance.

Appendix A

FAST Algorithm

The software trigger algorithm was designed to calculate approximately the mass (m_x) of the products in the bubble chamber recoiling against the fast forward pion. This recoil mass is then compared against preset limits (i.e., $m_l < m_x < m_u$) to suppress the taking of pictures of elastic scatter and pion diffraction events. To reduce the time needed for this calculation, only the horizontal (spectrometer magnet bend plane) projection of the fast track was used.

We begin the analysis of the trigger algorithm with m_x in terms of the four vectors of the beam, target and fast forward particles:

$$m_x^2 = (p_f - p_b - p_t)^2 \quad (1)$$

or, in the laboratory frame with t being the invariant momentum transfer from the beam to the fast pion:

$$m_x^2 = t + m_p^2 + 2m_p(E_b - E_f). \quad (2)$$

The laboratory energies of the beam (E_b) and fast pions (E_f) are very large compared to the pion mass, thus by using the approximation $E \approx p$ (where $p^2 = E^2 + m^2$ is the magnitude of the 3-vector momentum) and rewriting eq. (2), we have:

$$p_f \approx p_b - \frac{m_x^2 - m_p^2}{2m_p} + \frac{t}{2m_p}. \quad (3)$$

Using eq. (3) and the limits to be imposed on m_x , we can set coarse limits on the fast track momentum:

$$p_f \geq p_{\min} = p_b - \frac{m_u^2 - m_p^2}{2m_p} \quad (4a)$$

$$p_f \leq p_{\max} = p_b - \frac{m_l^2 - m_p^2}{2m_p}. \quad (4b)$$

Note that the term with t is left out of both limits because it is always less than zero (thus p_{\max} is at $t = 0$) or it is negligible compared to the energy difference ($E_b - E_f$) term (which dominates at low momenta).

Before continuing with the derivation of a better test for the low mass cut ($m_x \geq m_l$), let us study the momentum tests (eqs. (4a) and (4b)) using the measured quantities. Basically, the trigger program uses the spark positions x_1, x_2, x_3 and x_4 measured in the stations at z_1, z_2, z_3 and z_4 , respectively (see Table A.1). As can be seen from Fig. A.1, the scattering angle (θ) is simply gotten by:

$$\theta \approx \frac{x_2 - x_1}{z_2 - z_1} \quad (5)$$

where the small angle approximation ($\sin\theta \approx \tan\theta \approx \theta$) has been used. A particle of momentum p is bent through an angle $\beta + \beta_0$ in the magnet, but since stations 3 and 4 are positioned such that a particle of momentum p_0 appears to have zero bend angle, only the differential bend β is measured directly. Thus we have:

$$p(\beta+\beta_0) = e \int B dl = p_0 \beta_0 \quad (6a)$$

or, rewriting as:

$$\beta = \frac{\beta_0 p_0}{p} - \beta_0 = \beta_0 p_0 \left(\frac{1}{p} - \frac{1}{p_0} \right). \quad (6b)$$

Thus we have the maximum and minimum bend angles given from the minimum and maximum momenta:

$$\beta_{\max} = \beta_0 p_0 \left(\frac{1}{p_{\min}} - \frac{1}{p_0} \right) \quad (7a)$$

$$\beta_{\min} = \beta_0 p_0 \left(\frac{1}{p_{\max}} - \frac{1}{p_0} \right). \quad (7b)$$

The trigger uses the quantity d_3 (the sagitta at station 3) defined as:

$$d_3 = \left(\frac{x_4 - x_1}{z_4 - z_1} \right) (z_3 - z_1) + x_1 - x_3 \quad (8)$$

to perform the tests required by the cuts. Using Fig. A.1, we can relate d_3 to β by observing that for a particle with scattering angle θ and differential bend β we have:

$$x_3 = x_1 + \theta(z_3 - z_1) + \beta(z_3 - z_m) \quad (9a)$$

$$x_4 = x_1 + \theta(z_4 - z_1) + \beta(z_4 - z_m). \quad (9b)$$

Using eqs. (9a) and (9b) with the definition of d_3 , we find:

$$d_3 = \frac{(z_4 - z_3)(z_m - z_1)}{(z_4 - z_1)} \beta. \quad (10)$$

The test then made on this quantity is:

$$d_{3\min} < d_3 < d_{3\max} \quad (11a)$$

which corresponds to the requirement:

$$\beta_{\min} < \beta < \beta_{\max} \quad (11b)$$

since $d_{3\min}$ and $d_{3\max}$ are gotten from β_{\min} and β_{\max} by using the constant given in eq. (10). This test is used to place some limits on the fast track momentum:

$$p_{\min} < p_f < p_{\max}. \quad (11c)$$

However, near p_{\max} (or equivalently, near $m_x \approx m_\lambda$) a better test is needed which takes into account the scattering angle (i.e., non-zero t).

To produce a better approximation for high momentum, non-zero t events, we return to eq. (2) and now use the approximation:

$$E \approx p + \frac{m^2}{2p} \quad (12)$$

which yields:

$$\frac{m_x^2 - m_p^2}{2m_p} \approx \frac{t}{2m_p} + (p_b - p_f) + \frac{m_\pi^2}{2} \left(\frac{1}{p_b} - \frac{1}{p_f} \right). \quad (13)$$

Now we can write t in terms of laboratory quantities:

$$t = 2m_\pi^2 - 2E_b E_f + 2p_b p_f \cos\theta \quad (14a)$$

and then using the above approximation for E_b and E_f and the small angle approximation, we have:

$$t \approx 2m_\pi^2 - m_\pi^2 \left(\frac{p_f}{p_b} + \frac{p_b}{p_f} \right) - p_b p_f \theta^2. \quad (14b)$$

We now introduce the notation:

$$p_f = (1-\delta)p_b \quad (15)$$

so that (14b) becomes:

$$t \approx 2m_\pi^2 - m_\pi^2 \left(1-\delta + \frac{1}{1-\delta} \right) - p_b^2 \theta^2 (1-\delta) \quad (16)$$

since the approximation will be used for large momenta, $p_f \approx p_b$, so $\delta \ll 1$, we can simplify (16) by neglecting terms in δ^2 to get:

$$t \approx -p_b^2 \theta^2 (1-\delta) = -p_b p_f \theta^2. \quad (17)$$

Combining with eq. (13b) and using (15), we have:

$$\frac{m_x^2 - m_p^2}{2m_p} \approx -\frac{p_b^2}{2m_p} \theta^2 (1-\delta) + p_b \delta - \frac{m_\pi^2}{2p_b} \delta \quad (18)$$

or, by neglecting the third term (p_b is large compared to m_π), we have:

$$\frac{m_x^2 - m_p^2}{2m_p} \approx p_b \delta - \frac{p_b^2}{2m_p} \theta^2 (1-\delta). \quad (19)$$

Now we return to eq. (6a) and include the sextupole correction to the magnetic field (about a 3% effect) so we have:

$$p_f = \frac{p_0 \beta_0 (1+bx^2)}{(\beta_0 + \beta_f)} \quad (20a)$$

and:

$$p_b = \frac{p_0 \beta_0}{\beta_0 + \beta_b} \quad (20b)$$

where x is the horizontal displacement of the particle from the magnet's center:

$$x \approx (z_3 + z_0)\theta \approx z_3\theta. \quad (21)$$

Thus we have:

$$1 - \delta = \frac{p_f}{p_b} \approx (1 + bz_3^2\theta^2) \left(\frac{\beta_0 + \beta_b}{\beta_0 + \beta_f} \right). \quad (22)$$

Now, using eq. (19), we can write, by neglecting terms in θ^4 and using $p_0\beta_0 = p_b(\beta_0 + \beta_b)$:

$$p_b - \frac{m_x^2 - m_p^2}{2m_p} \approx \frac{p_0\beta_0}{\beta_0 + \beta_f} (1 + \theta^2 \left(\frac{p_b}{2m_p} + bz_3^2 \right)). \quad (23)$$

Now, we can use $p_b \approx p_0$ and (since $\beta_f \ll \beta_0$):

$$\frac{1}{\beta_0 + \beta_f} \approx \frac{1}{\beta_0} \left(1 - \frac{\beta_f}{\beta_0} \right) = \frac{1}{\beta_0} - \frac{\beta_f}{\beta_0^2} \quad (24)$$

in the right-hand side of eq. (23) to get (neglecting terms in $\theta^2\beta_f$):

$$\beta_0 \left(1 - \frac{1}{p_0} \left(p_b - \frac{m_x^2 - m_p^2}{2m_p} \right) \right) \approx \beta_f - \theta^2 \beta_0 \left(\frac{p_0}{2m_p} + bz_3^2 \right). \quad (25)$$

This equation can then be translated into a test to require $m_x > m_\ell$ as:

$$\beta_0 \left(1 - \frac{1}{p_0} \left(p_b - \frac{m_\ell^2 - m_p^2}{2m_p} \right) \right) < \beta_f - \theta^2 \beta_0 \left(\frac{p_0}{2m_p} + bz_3^2 \right). \quad (26)$$

Note that the left size is (from eq. (4b)):

$$\beta_0 \left(1 - \frac{1}{p_0} \left(p_b - \frac{m_l^2 - m_p^2}{2m_p} \right) \right) = \beta_0 \left(1 - \frac{p_{\max}}{p_0} \right) = -\beta_{\min}. \quad (27)$$

Finally, in terms of the measured quantities d_3 and $x_2 - x_1$, we have the test made in FAST to eliminate triggers on elastic events:

$$d'_{\min} < d_3 - (x_2 - x_1)^2 C_t \quad (28)$$

where the constants are given by:

$$d'_{\min} = \frac{(z_4 - z_3)(z_m - z_1)}{(z_4 - z_1)} \beta_0 \left(1 - \frac{p_b}{p_0} + \frac{m_l^2 - m_p^2}{2m_p p_0} \right) \quad (29a)$$

$$C_t = \frac{(z_4 - z_3)(z_m - z_1)}{(z_4 - z_1)(z_2 - z_1)^2} \beta_0 \left(\frac{p_0}{2m_p} + bz_3^2 \right). \quad (29b)$$

Before the above tests (eq. (11a) and (28)) can be made, the raw spark chamber spark data as read into the computer memory must be processed. This processing converts from time to position units, giving the spark positions in the overall spectrometer coordinate system. In addition, the two sets of sparks from each of the two X wands in each station are merged to yield a single set of sparks for each station (treating station 4 as two substations 4R and 4L then concatenating their spark sets into a single list). This spark setup process is described in more detail with the description of the spark chamber analysis program TORTIS in Chapters II and III and in Appendix

B. FAST begins searching for tracks by trying sparks from stations 1, 3 and 4 until a set (x_1, x_3, x_4) is found such that the value of d_3 calculated from the set satisfies the conditions given in eq. (11a). To locate a spark in station 2 to complete the track, the sagitta at station 3 (d_3) is geometrically projected to station 2:

$$d_2 = \left(\frac{z_2 - z_1}{z_m - z_1}\right) d_m = \left(\frac{z_2 - z_1}{z_m - z_1}\right) \left(\frac{z_4 - z_m}{z_4 - z_3}\right) d_3. \quad (30)$$

Using this and the line connecting x_1 and x_4 (also used to calculate d_3), a predicted position for the x_2 spark is calculated. The difference between the actual and predicted x_2 spark positions is:

$$r = x_2 - \left(\frac{x_4 - x_1}{z_4 - z_1}\right) (z_2 - z_1) - x_1 + d_2. \quad (31)$$

FAST required r to be within a preset limit for the track (now with four spark coordinates) to be a trigger candidate:

$$|r| < w_r. \quad (32)$$

This candidate track was checked for an interaction vertex outside the bubble chamber by calculating the X positions of the track at the front and rear bubble chamber windows:

$$x_f = x_1 - (z_1 - z_f) \left(\frac{x_2 - x_1}{z_2 - z_1}\right) \quad (33a)$$

$$x_r = x_1 - (z_1 - z_r) \left(\frac{x_2 - x_1}{z_2 - z_1} \right) \quad (33b)$$

and requiring these to be within a preset range of the beam centroid:

$$|x_f - x_0| < w_b \text{ and } |x_r - x_0| < w_b \quad (34)$$

where the constants x_0 (beam center position), w_b (beam width) and w_r (r window) were determined empirically. If the track satisfied all these conditions, the quantity MMF (the right side of eq. (28)) was calculated and the final trigger test (eq. (28)) was made. If the trigger condition was satisfied, a bubble chamber picture was taken for the event.

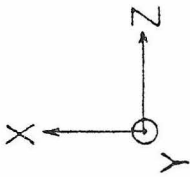
Table A.1

Definition of quantities in Appendix A

Positions along Z-axis of:

z_i	spark chamber station i (i runs from 1 to 4)
z_f	front of bubble chamber
z_r	rear of bubble chamber
z_0	interaction vertex
z_m	spectrometer magnet center
x_i	measured spark positions in each station
θ	scattering angle
β	differential bend angle in spectrometer magnet of particle with momentum p
p_0	design momentum of the spectrometer (14 GeV/c)
β_0	bend angle of particle with momentum p_0 (61.2 mrad)

Spectrometer
Coordinate System



See Table A.1 for definitions

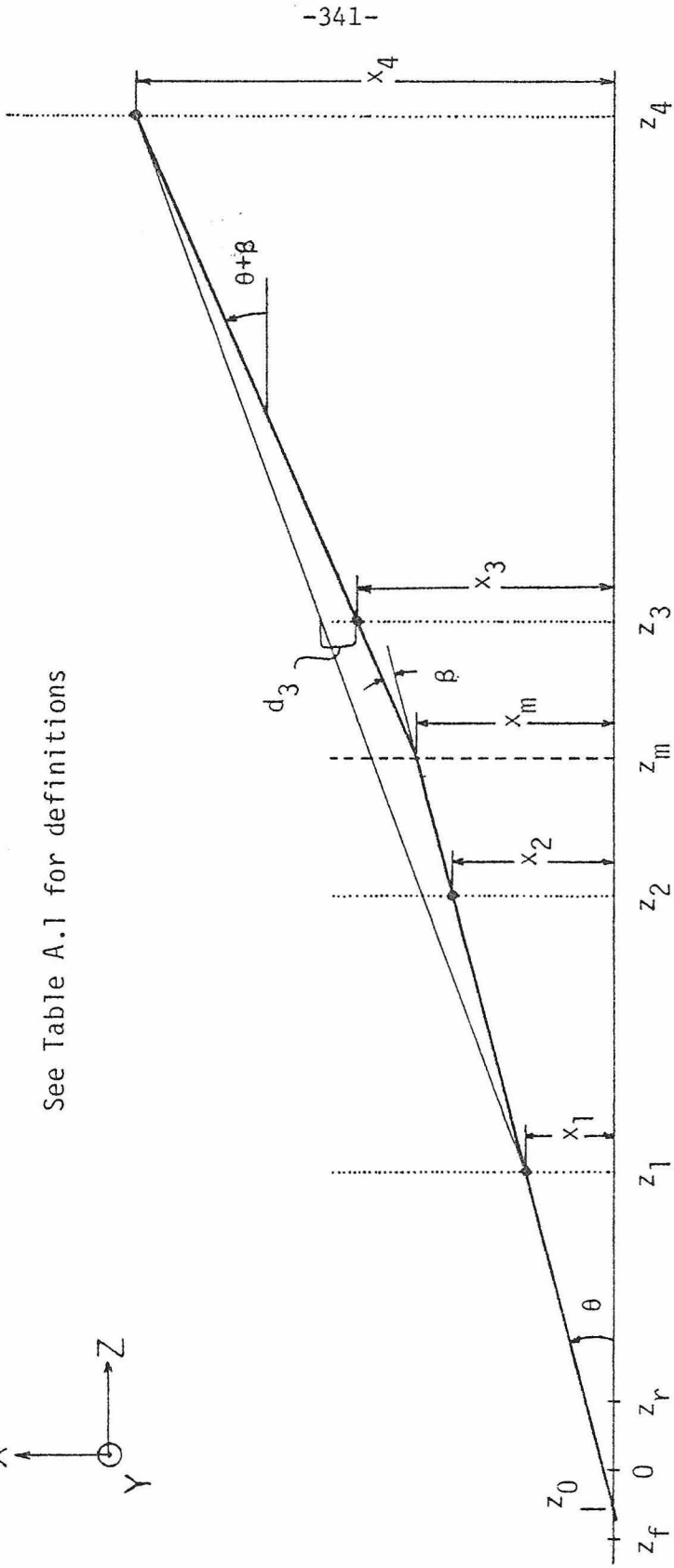


Figure A.1

Schematic illustrating FAST track analysis algorithm (not to scale). The spectrometer design angle has been suppressed by having the Z-axis lie along the beam.

Appendix B

TORTIS Track Finding and Spark Chamber Calibration

1. Track Finding

The raw spark chamber data consisted of the separations between the first fiducial pulse and any sparks (and the second fiducial pulse) in time as counts of a 20 MHz crystal-controlled clock. TORTIS first recognized and removed from the spark lists the second fiducial pulses. A running average was kept for each wand of the time (in clock counts) between the two fiducial pulses. From the known separation between the fiducial wires, the current speed of sound ($\Delta x_{\text{fid}}/\Delta t_{\text{fid}}$) was calculated for each wand and used by TORTIS to convert the spark positions from time to a space position:

$$x = x_0 + (\Delta x_{\text{fid}}/\Delta t_{\text{fid}}) \cdot t \quad (1)$$

where the x_0 constants (one per wand) gave the location of the first fiducial wires in the spectrometer coordinate system. These constants also included a correction for the width of the first fiducial pulse since all the sparks and the second fiducial had their pulse center position recorded by the center-finding circuitry. The x_0 constants were subject to change from electronic drifts and physical movement of the spark chambers. Thus they were initially set by survey measurements and then fine-tuned and tracked by our calibration procedures (see sections 2 through 4 of this Appendix).

Each measuring station of the spectrometer consisted of two pairs of similar spark chambers (for instance, station 1 had 2 XY and 2 UV chambers). Since each chamber had better than a 90% probability of

making a spark for a track, the probability of each station having at least one spark for a track was better than 99%. After the spark measurements were converted to positions, the spark sets from these two chambers were merged into a single set (OR'ed). Thus each station had only one set of X and one set of Y (also a U set and V set if station 1 or 3) measurements of the sparks in that station. The merging was done separately in X and Y (or U and V). As the lists of sparks were merged, a check was made for sparks from the same track which occurred in both chambers of a pair by looking for spark pairs whose difference was less than a prechosen window (± 0.1 inches). These two sparks were then replaced by their average to give a single spark at the station instead of two sparks from the same track. The distributions of the differences between the positions of sparks in the chamber pairs were used to adjust the relative alignment (of the x_0 constants) of these chambers and to determine the spark chamber setting errors.

Once TORTIS had a list of sparks at each station, track finding was done independently in the X and Y-views with the resulting X and Y-tracks then being matched together by use of the sparks in the UV chambers. The X-view track finding algorithm used by TORTIS was similar in some ways to that used by FAST and described in Appendix A. A pair of sparks in stations 3 and 4 (after the magnet) were used to calculate the track position (in X) at the center of the magnet as shown (x_i is the spark position and z_i is the longitudinal position along the beam of station i , with the subscript m representing the magnet center):

$$x_m = x_3 - (z_3 - z_m) \left(\frac{x_4 - x_3}{z_4 - z_3} \right) \quad (2)$$

By assuming the event's vertex was in the center of the bubble chamber (the origin of the spectrometer coordinate system), an approximate spark position in station 1 was calculated using the calculated magnet center intercept (x_m) for the track candidate (x_{BCO} is the transverse location of the beam center at the origin):

$$x_{1T} = (x_m - x_{BCO}) \frac{z_1}{z_m} \quad (3)$$

TORTIS then searched the station 1 spark list for a spark near x_{1T} using a very wide window which was twice the full width of the beam (in X) at the bubble chamber (about 1.5 inches). If no such spark was found, TORTIS selected a new pair of stations 3 and 4 sparks and began the process again, continuing until all the stations 3 and 4 spark pairs (all combinations of sparks from the stations 3 and 4 spark lists) were tried. If a station 1 spark was found within the search window about x_{1T} , it was used along with x_m to calculate a predicted spark position at station 2:

$$x_{2T} = x_1 + (z_m - z_2) \left(\frac{x_m - x_1}{z_m - z_1} \right) \quad (4)$$

The station 2 spark list was then searched for a spark near the x_{2T} position using a window of about 0.4 inches full width. If such a spark was found, the candidate X-track then had a spark at each of the four spark chamber stations. The X-track was accepted and added to the X-track list if the intercepts of the extrapolated track with the front and read bubble chamber positions (at z_{BCF} and z_{BCR}):

$$s_{12} = (x_2 - x_1) / (z_2 - z_1) \quad (5a)$$

$$x_{BCF} = x_1 - (z_1 - z_{BCF}) \cdot s_{12} \quad (5b)$$

$$x_{BCR} = x_1 - (z_1 - z_{BCR}) \cdot s_{12} \quad (5c)$$

were within a window about the beam center (a similar cut was used in FAST, see Appendix A).

The search for Y-tracks was simpler than that used for X since the spectrometer magnet bent the particles in the X-plane. TORTIS began by using sparks from stations 1 and 4 to calculate a predicted position at station 3:

$$y_{3T} = y_4 - (z_4 - z_3) \left(\frac{y_4 - y_1}{z_4 - z_1} \right) \quad (6)$$

Then the station 3 spark list was searched for a spark near y_{3T} . The search window (± 0.25 inches) was large to allow for a small bend in Y due to fringe field focusing in the magnet. If a spark was found in station 3, it was used to calculate the intercept of the track with the magnet center:

$$y_m = y_3 - (z_3 - z_m) \left(\frac{y_4 - y_3}{z_4 - z_3} \right) \quad (7)$$

which was then used with the station 1 spark to calculate a predicted spark position at station 2:

$$y_{2T} = y_1 + (z_2 - z_1) \left(\frac{y_m - y_1}{z_m - z_1} \right) \quad (8)$$

The window used in searching the station 2 spark list was smaller (± 0.15 inches) than that used in the station 1 search since the Y-bend

was explicitly taken into account by calculating y_m . A good Y-track was then one which had sparks at all four stations after the above procedure. As with X, TORTIS tried all pairs of stations 1 and 4 sparks to find all the possible Y-tracks.

After finding X and Y-tracks independently, TORTIS then matched the two track projections to yield the final track representing the trajectory of the fast particle. All pairs of X and Y-tracks were tested as matched tracks. Since station 4 consisted of two sets of XY chambers (each set being two separate spark chambers) mounted side-by-side with the beam passing between them, the first requirement for a matched track was thus that both the X and Y-track have their sparks in the same module (or half) of station 4. The spark positions at stations 1 and 3 of the matched track were then used to calculate predicted spark positions in the UV chambers:

$$u_{iT} = (x_i + y_i) / \sqrt{2} \quad (9a)$$

$$v_{iT} = (y_i - x_i) / \sqrt{2} \quad (9b)$$

where i is 1 or 3. The UV spark lists at the two stations were then searched for sparks within a window (± 0.2 inches) of these predicted values. The track was accepted as a good matched track if a good UV spark was found at either station 1 or station 3 or at both stations (for the spark to be good, both u_i and v_i must have been within the window around u_{iT} and v_{iT}). Some extra tracks were picked up by allowing a matched track to be made up of the single X and Y-tracks (if only 1 of each was found) provided they came from the same station 4 module. Ambiguous and wrongly matched tracks were resolved or

removed outside of TORTIS (for instance, HYBRID used the track match χ^2 and the SC-BC match χ^2 to select the best track).

2. Calibration Test Quantities

Although the spark chamber positions were initially set by the survey, an internal calibration was made using tracks found by TORTIS to fine tune the constants and correct for any run-to-run electronic or mechanical drifts. We did this by using the constraints that tracks were continuous so the magnet center intercepts as extrapolated from the front and back halves of the spectrometer (i.e., using stations 1 and 2 or 3 and 4 sparks to give two separate extrapolations to the magnet center) were the same. Similarly we had the weaker constraints that the average bend angle in the Y-projection was zero and that the elastic peak (in the missing mass) had to fall at the proton mass. Thus we defined a series of test quantities calculated by TORTIS for each track whose average values were used to correct the spark chamber alignment constants for each data run. Before calculating these quantities, TORTIS corrected the stations 3 and 4 spark coordinates by a small amount to remove a small effect introduced by the geometry of the spectrometer. The effect was due to the z-axis being defined as the beam center which was bent at the magnet (through the survey angle, θ_0 , or 61.2 milliradians). This meant that the magnet center intercept extrapolations from the front and rear halves of the spectrometer were not being calculated for the same plane (perpendicular to the z-axis) in space. These corrections were small and dependent on x_{m12} , the magnet intercept in X as extrapolated from stations

1 and 2:

$$x_{m12} = x_2 + (z_m - z_2) \left(\frac{x_2 - x_1}{z_2 - z_1} \right) \quad (10)$$

The correction terms added to the X and Y spark coordinates were then:

$$x_{\text{coor}} = 0.5 \theta_0 x_{m12} \left(\frac{x_2 - x_1}{z_2 - z_1} + \frac{x_4 - x_3}{z_4 - z_3} \right) \quad (11a)$$

$$y_{\text{coor}} = \theta_0 x_{m12} \left(\frac{y_4 - y_3}{z_4 - z_3} \right) \quad (11b)$$

The constraint that the two magnet center intercepts extrapolated from both sides of the spectrometer agree (on the average) leads to the first test quantities:

$$y_{m34} = y_3 - (z_3 - z_m) \left(\frac{y_4 - y_3}{z_4 - z_3} \right) \quad (12a)$$

$$y_{\text{TST}} = y_1 + (z_m - z_2) \left(\frac{y_m - y_1}{z_m - z_1} \right) - y_2 \quad (12b)$$

and similarly for x_{TST} . These quantities were the same as those used to search for station 2 sparks when track finding. If we consider the Y-track as a straight line with position y_0 at the origin and slope α so that the spark position at station i is given by:

$$y_i = y_0 + \alpha z_i + \epsilon_i \quad (13)$$

where ϵ_i ($i > 1$) is the amount station i is misaligned. From this form, y_{TST} can be found to be:

$$y_{\text{TST}} = \epsilon_2 - D_{23} \epsilon_3 + D_{23} \left(\frac{z_3 - z_m}{z_4 - z_m} \right) \epsilon_4 \quad (14a)$$

$$D_{23} = \frac{(z_4 - z_m)(z_2 - z_1)}{(z_4 - z_3)(z_m - z_1)} \quad (14b)$$

which just depends on the misalignment factors. It can also be shown that y_{TST} and x_{TST} are directly proportional to the difference between the magnet center intercepts extrapolated from the two halves of the spectrometer. The other Y-projection test quantity was the the bend angle of the track's Y-projection which was calculated as the difference of the track's slope before and after the magnet:

$$\beta_y = \left(\frac{y_4 - y_3}{z_4 - z_3} \right) - \left(\frac{y_2 - y_1}{z_2 - z_1} \right) \quad (15)$$

Here again we can express β_y in terms of the explicit misalignments only:

$$\beta_y = -(\epsilon_3/C_3) + (\epsilon_4/C_4) \quad (16a)$$

$$C_3 = (z_4 - z_3)(z_m - z_1)/(z_4 - z_1) \quad (16b)$$

$$C_4 = (z_4 - z_3)(z_m - z_1)/(z_3 - z_1) \quad (16c)$$

For the X-projection, the final test quantity was m_{TST} which related the missing mass (m_x) to the proton mass:

$$m_{TST} = m_x^2 - m_p^2 \quad (17)$$

where m_x was calculated using the measured track parameters which gave the momentum (p_f) and the scattering angle (θ_{sc}):

$$m_x^2 = p_b^2 + p_f^2 + 2p_b p_f \cos \theta_{sc} + 2m_p (E_b - E_f) + m_p^2 \quad (18)$$

where p_b is the beam momentum and E_b and E_f are the beam and fast energies. This can be related to an angular test quantity much like

β_y :

$$\beta_x = \left(\frac{p_0 \theta_0}{2m_p p_b} \right) m_{TST} \quad (19)$$

where p_0 and θ_0 are the design momentum and bend angle of the spectrometer. This quantity differs from β_y in that it does not measure a deviation from zero, but from the bend angle associated with an elastic event with $m_x = m_p$.

3. Initial Calibration

Using the survey values as a starting point, a series of three special runs were made to calibrate the spectrometer. In these runs, a low intensity beam was steered to the right or left of its normal center by using the D3.1 steering magnet (see Chapter II) so the beam would miss the dead spots in the spark chambers. In addition, the first run type (with beam steered right) had the spectrometer magnet turned off so the beam was undeflected. By measuring the apparent bend angle in X, the misalignments in X of station 2 and 3 were corrected (relative to stations 1 and 4). The corrections were given by:

$$\delta x_3 = C_3 \langle \beta_x \rangle \quad (20a)$$

$$\delta x_2 = D_{23} \delta x_3 \quad (20b)$$

where $\langle \beta_x \rangle$ was the observed average X-bend angle. After correcting the appropriate constants and with the beam still steered right, the

spectrometer magnet was once again turned on. The measurement of $\langle \beta_x \rangle$ then yielded the beam momentum:

$$P_b = \frac{p_0 \theta_0}{\langle \beta_x \rangle + \theta_0} \quad (21)$$

Finally, by steering the beam to the left and measuring $\langle \beta_x \rangle$ yet again, the correction to the alignment constants of the left half of station 4 (relative to the right half) was gotten from comparison with $\langle \beta_x \rangle$ measured for the beam steered right (with the magnet on):

$$\delta x_{4L} = C_4 (\langle \beta_x \rangle_L - \langle \beta_x \rangle_R) \quad (22)$$

In addition, these runs yielded the beam center position at the origin (x_{BC0}) and the measurement of the width of the beam in X. The Y-constants were handled in the normal manner as discussed below.

4. Tracking the Calibration with Data Runs

Since all the beam pulses for which the spark chambers were fired were recorded on magnetic tape, the data runs were used to track the shifts in the spark chamber constants. This resulted in a set of spark chamber location constants for each run. These constants then effectively welded the entire spectrometer into a single rigid unit which other constants (used in HYBRID) connected as a whole to the bubble chamber. The test quantities discussed in section 2 of this Appendix were used to calculate the corrections to the constants. Some of these quantities were averaged separately for tracks in the two modules of station 4, thus treating station 4 as two separate stations in a sense. Before being added to the sums used to calculate the averages, the test quantities were required to be within a window

about zero that served to make the average more sensitive to the position of the centroid of the distribution.

The y_{TST} and x_{TST} quantities were averaged over all the tracks (in both station 4 modules) and the misalignments of the station 4 modules were taken to be relative to one another, absorbing any overall misalignment of station 4 into those of stations 2 and 3. For instance, in terms of the explicit misalignment formalism used earlier, we have (under the assumption $\epsilon_{4L} + \epsilon_{4R} = 0$):

$$\langle y_{TST} \rangle = \epsilon_2 - D_{23} \epsilon_3 \quad (23)$$

Similarly, β_y and m_{TST} were averaged over all the tracks to eliminate the station 4 misalignments. In addition, both of these were also separately averaged over tracks in the left and right station 4 modules. Once again, using the explicit misalignment formalism and taking $\epsilon_{4L} = \epsilon_4$ and $\epsilon_{4R} = -\epsilon_4$, we have:

$$\langle \beta_y \rangle = -\epsilon_3 / C_3 \quad (24a)$$

$$\frac{1}{2} (\langle \beta_y \rangle_L - \langle \beta_y \rangle_R) = \epsilon_4 / C_4 \quad (24b)$$

where the L and R subscripts indicate quantities averaged over the left or right station 4 modules. Similar formulae apply for X but in that case, β_y is replaced by $C_m m_{TST}$, where:

$$C_m = \frac{p_0^\theta \theta}{2m_p p_b^2} \quad (25)$$

Given these averages, the spark chamber alignment constants were corrected according to the formulae in Table B.1. In the table, those

averaged quantities with the L or R subscripts were averaged over tracks in only one half (left or right) of station 4 while all other averages were over all tracks. Also, the station 3 UV constants were adjusted along with the XY constants:

$$u_{\text{corr}} = C_3(C_m \langle m_{\text{TST}} \rangle + \langle \beta_y \rangle) / \sqrt{2} \quad (26a)$$

$$v_{\text{corr}} = C_3(\langle \beta_y \rangle - C_m \langle m_{\text{TST}} \rangle) / \sqrt{2} \quad (26b)$$

Finally, in addition to these corrections to all the chambers at a station, the constants of the individual spark chambers in a pair were adjusted relative to one another so the residuals from the OR'ing (of the redundant chamber pairs) were centered on zero.

Table B.1

Constants correction formulae

<u>station</u>	<u>X</u>	<u>Y</u>
2	$-\langle x_{\text{TST}} \rangle + C_3 D_{23} C_m \langle m_{\text{TST}} \rangle$	$-\langle y_{\text{TST}} \rangle + C_3 D_{23} \langle \beta_y \rangle$
3	$C_3 C_m \langle m_{\text{TST}} \rangle$	$C_3 \langle \beta_y \rangle$
4 right	$0.5 C_4 C_m (\langle m_{\text{TST}} \rangle_R - \langle m_{\text{TST}} \rangle_L)$	$0.5 C_4 (\langle \beta_y \rangle_R - \langle \beta_y \rangle_L)$
4 left	$0.5 C_4 C_m (\langle m_{\text{TST}} \rangle_L - \langle m_{\text{TST}} \rangle_R)$	$0.5 C_4 (\langle \beta_y \rangle_L - \langle \beta_y \rangle_R)$

These corrections had only small effects on the constants, particularly when compared to the setting (measurement) error of a single spark chamber (which was about 0.018 inches). The numbers given in Table B.2 were gotten by histogramming the differences between the constants used in adjacent runs. Table B.2 lists the sigmas of the resulting distributions as all the average values were considerably

less than 0.001 inches.

Table B.2

R.M.S. run-to-run changes in the
spark chamber constants (in inches)

<u>station</u>	<u>X</u>	<u>Y</u>
1	0.003	0.002
2	0.011	0.007
3	0.007	0.008
4 right	0.011	0.011
4 left	0.012	0.013

Appendix C

Computer Trigger Efficiency Determination

The calculation of the computer trigger efficiency was discussed in Section 5 of Chapter IV. This efficiency is the product of the RESID, DEL3, and MMF cut efficiencies which were calculated by the use of equations (IV.13a-c). This procedure required that we have the means and variances for RESID (\bar{r} and σ_R), DEL3 (\bar{d} and σ_D), and MMF (\bar{m} and σ_M) parameterized as functions of the fast particle's momentum vector (\vec{p}). These functions were determined from Monte Carlo studies using the ray tracing program developed for the geometrical acceptance calculations (see Section 4 of Chapter IV). The test quantities were calculated from the generated spark positions using the same formulas and parameters used in the computer trigger program. For these Monte Carlo studies, the effects of the spark chamber resolutions and multiple scattering of the fast particle were included in the model of the apparatus. The Monte Carlo studies also showed that the online computer program's bubble chamber fiducial volume tests (see Appendix A) were so conservative that no correction was needed for the very few events lost due to these cuts.

The Monte Carlo studies allowed us to construct a table of the means and variances of RESID and DEL3 for selected values of the fast momentum (p) and the scattering angle (θ). We then fit these values to the empirical formula:

$$q(p, \theta) = a_0 + \frac{a_1}{p} + a_2 \theta + \frac{a_3}{p^2} + \frac{a_4 \theta}{p} + a_5 \theta^2 \quad (1)$$

where q stands for a mean (\bar{r} or \bar{d}) or variance (σ_R^2 or σ_D^2). These fits gave acceptable results in describing the variations of the means and variances as functions of p and θ . Though this formula gave the mean of RESID (\bar{r}) as a function of p and θ , the actual value of $\bar{r}(p,\theta)$ was dependent on the spark chamber location parameters.

We examined the model for RESID gotten from the Monte Carlo studies by using the actual online computer trigger RESID's from samples of the data. We compared the actual RESID distributions to those gotten from the integral:

$$g(r) = \int_{p,\theta} f(p, \theta) \frac{1}{\sqrt{2\pi} \sigma_R(p,\theta)} \exp\{- (r - \bar{r}(p,\theta))^2 / 2\sigma_R^2(p,\theta)\} dpd\theta \quad (2)$$

where $g(r)$ is now the calculated distribution of RESID ($\equiv r$) as gotten from the Monte Carlo $\bar{r}(p,\theta)$ and $\sigma_R(p,\theta)$ functions. The integral is over the (p,θ) region occupied by the data with $f(p,\theta)$ being the experimentally observed distribution of events in p and θ . The integral was numerically evaluated by generating ideograms based on $\bar{r}(p,\theta)$ and $\sigma_R(p,\theta)$. The resulting means and variances of these ideograms were then compared to the means and variances of histograms of the actual RESID values. The comparison showed that $\bar{r}(p,\theta)$ and $\sigma_R(p,\theta)$ were adequate for modeling the data except for an empirical additive correction to $\bar{r}(p,\theta)$ by a constant value (-1.6 units for the π^+ experiment and -2.3 for the π^- experiment) so that the model RESID's were distributed about a centroid near zero.

The MMF test quantity was evaluated using the formula:

$$\bar{m}(\vec{p}) = A + Bp + Cd^2 + Dp^2 \quad (3)$$

where ρ and d were gotten from \vec{p} by:

$$\rho = \frac{1}{\sqrt{p_x^2 + p_z^2}} \quad (4a)$$

$$d = \frac{p_z}{p_x} \quad (4b)$$

where p_x is the component of \vec{p} along the beam direction and p_z is the horizontal component of \vec{p} transverse to the beam (i.e., the x and z components of \vec{p} in the general coordinate system). The values of the coefficients A, B, C, and D were gotten by doing a least squares fit of $\bar{m}(\vec{p})$ to the values of MMF from the data. Table C.1 shows an example of the results of the fit as compared to the a priori values calculated from the experimental geometry parameters and the computer trigger program algorithms.

Table C.1

$\bar{m}(\vec{p})$ coefficients

	<u>fitted</u>	<u>a priori</u>
A	-533.5±1.5	-537.3
B	7555±29	7521.7
C	-3737±40	(not evaluated)
D	-100±140	0

The A term is very dependent on the precise values of the spark chamber location parameters which are subject to slight drifts with time. In particular, by studying the variation in the average of:

$$DM = MMF - (A + B\rho) \quad (5)$$

(using the a priori values for A and B) with roll number, we were able to define groups of rolls in which we then did the fits to $\bar{m}(\vec{p})$ to obtain values of the coefficients for each group of rolls. The resulting sets of coefficients were used to calculate $\bar{m}(\vec{p})$ in finding the average of:

$$DM' = MMF - \bar{m}(\vec{p}) \quad (6)$$

which showed no dependence on roll number, recoil mass, or fast momentum. Thus we found that $\bar{m}(\vec{p})$ with a roll-group dependent parameterization was a good model for the average value of MMF.

The dispersion of MMF about its mean was gotten from the dispersion of DM' from equation (6) for each roll group. This observed DM' dispersion was found to be larger than the value obtained from the Monte Carlo studies. The Monte Carlo value, however, did not take into account the residual fluctuations due to secular drifts of the apparatus. An additional check that was made was to calculate the fraction of elastic roll elastic events which would have been accepted as inelastic events by the trigger program. The results of these calculations and the fraction actually observed (calculated from the MMF's actually used by the trigger program) are given in Table C.2. The fraction calculated from the observed events is overestimated because about 5-10% of all the events are events that occur while the spark chambers are still live after being fired by an earlier event (in the same beam pulse). The bottom line of Table C.2 gives the observed fraction corrected for these extra events. From Table C.2, it can be seen that the larger DM' dispersion (than the Monte Carlo dispersion)

gives very nearly the correct mis-trigger fraction. Thus the roll-group dependent DM' dispersions were used in equation (IV.13) to calculate ϵ_{MMF} .

Table C.2

Elastic roll elastic mis-trigger fraction

<u>Value from</u>	<u>Value</u>
Monte Carlo dispersion calculation	8%
DM' dispersion calculation	15%
Observed (from data MMF's)	25%
Corrected observed (for second events)	15-20%

List of References

- Aderholz, M., et al. 1966. Phys. Rev. 138, B897-B912.
- Aderholz, M., et al. 1968. Nucl. Phys. B8, 45-64.
- Albrecht, H. C., et al. 1968. The COBWEB data reduction system.
Lawrence Berkeley Laboratory report UCRL-18528 Rev.
- Allison, W. W. M., F. Beck, and J. G. Loken 1969. POLLY II: A complete system incorporating facilities for measuring bubble chamber film without prescanning. Argonne National Laboratory report ANL/HEP-6916.
- Armenise, N., et al. 1973. Nuovo Cimento 17A, 707-720.
- Atherton, H. W., et al. 1975. Nuovo Cimento 30A, 505-509.
- Ballam, J., et al. 1967. Study of $\pi^{\pm}p$ 4-prong interactions at 16 GeV/c.
SLAC-PUB-334.
- Ballam, J., et al. 1971. Phys. Rev. D3, 2606-2609.
- Baltay, C., et al. 1978. Phys. Rev. D17, 62-82.
- Bartke, J., et al. 1977. Nucl. Phys. B120, 1-13.
- Biswas, N. N., et al. 1964. Phys. Rev. 134, B901-B911.
- Bondar, L., et al. 1964. Nuovo Cimento 31, 485-519.
- Boyarski, A. M., et al. 1968. "Yields of secondary particles from 18 GeV electrons" in SLAC Users Handbook, sec. C2.
- Brandenburg, G. W., et al. 1970. Nucl Phys. B22, 157-178.
- Caso, C., et al. 1967. Nuovo Cimento 47A, 675-679.
- Cason, N. M., et al. 1970. Phys. Rev. D1, 771-789.
- Cason, N. M., et al. Nucl. Phys. B64, 14-28.
- Chadwick, G. B., et al. 1978. Phys. Rev. D17, 1713-1730.
- Chien, C.-Y., et al. 1976. Nucl. Phys. B104, 189-218.
- Chung, S. U., et al. 1968. Phys. Rev. 165, 1491-1532.
- Chung, S. U. 1971. Spin Formalisms. CERN 71-8.

- Colton, E. and E. Gellert 1970. Phys. Rev. D1, 1979-1983.
- Dahl, O. I., et al. 1968. SQUAW kinematic fitting program. Lawrence Berkeley Laboratory Group A Programming Note P-126.
- Davidson, V., et al. 1974. Phys. Rev. Lett. 32, 855-858.
- Davidson, V. 1976. BC25 Internal Note. California Institute of Technology unpublished.
- Davis, P. J., et al. 1972. Nucl. Phys. B44, 344-354.
- Deck, R. T. 1964. Phys. Rev. Lett. 13, 169-173.
- Deutschmann, M., et al. 1964. Phys. Lett. 12, 356-360.
- Dickey, J. O. 1978. Internal Note. California Institute of Technology unpublished.
- Drell, S. D. and K. Hiida 1961. Phys. Rev. Lett. 7, 199-202.
- Foley, K. J., et al. 1967. Phys. Rev. Lett. 11, 425-429.
- Foley, K. J., et al. 1969. Phys. Rev. 181, 1775-1793.
- Good, M. L. and W. D. Walker 1960. Phys. Rev. 120, 1857-1860.
- Gordon, H. A., et al. 1975. Phys. Rev. Lett. 34, 284-287.
- Gottfried, K. and J. D. Jackson 1964. Nuovo Cimento 33, 309-330.
- Grassler, H., et al. 1974. Nucl. Phys. B75, 1-19.
- Guyader, J. le, et al. 1971. Nucl. Phys. B35, 573-591.
- Hones, M. J., et al. 1970. Phys. Rev. D2, 827-838.
- Jackson, J. D. 1964. Nuovo Cimento 34, 1644-1666.
- Jackson, J. D. 1965. High Energy Physics - Les Houches Lectures, ed. C. DeWitt and M. Jacob (Gordon and Breach, New York), p. 325-365.
- Johnson, D., et al. 1976. Nucl. Phys. B115, 195-207.
- Juhala, R. E., et al. 1969. Phys. Rev. 184, 1461-1486.
- Kennedy, C. N., et al. 1978. Phys. Rev. D17, 2888-2900.
- Kittel, W., et al. 1971. Nucl. Phys. B30, 333-373.

- Kung, H. H. 1969. $\pi^+ p$ interactions at 8.5 GeV/c. Columbia University thesis NEVIS-171.
- Lednický, R. 1975. Phys. Lett. 58B, 89-92.
- Leith, D. W. G. S. 1975. Diffractive Processes. SLAC-PUB-1526.
- Leith, D. W. G. S. 1975. Recent developments in diffractive studies. SLAC-PUB-1646.
- Linglin, D., et al. 1974. "A study of the $(p\omega)_{1800}$ enhancement in the reaction $\pi^+ p \rightarrow \pi^+ p \pi^+ \pi^- \pi^0$ at 14 GeV/c in a hybrid bubble chamber experiment" submitted to the XVII International Conference on High Energy Physics in London (paper 978).
- Milgram, M. S., et al. 1970. Nucl. Phys. B18, 1-16.
- Miyashita, S., et al. 1970. Phys. Rev. D1, 771-789.
- Otter, G., et al. 1975. Nucl. Phys. B87, 189-206.
- Particle Data Group 1978. Review of Particle Properties. Lawrence Berkeley Laboratory report LBL-100.
- Prentice, J. et al. 1971. 4-prong $\pi^+ p$ interactions at 5.5 GeV/c. University of Toronto unpublished.
- Pols, C. L., et al. 1971. Nucl. Phys. B25, 109-140.
- Rosenfeld, L. C. 1977. The diffractive dissociation process $\pi^- p \rightarrow \pi^- (\pi^- \pi^+ p)$ at 14 GeV/c. California Institute of Technology thesis.
- Solmitz, F. T., A. D. Johnson, and T. B. Day 1966. Three view geometry program. Lawrence Berkeley Laboratory Group A Programming Note P-117.
- Sisterson, L. K., et al. 1972. Nucl. Phys. B48, 493-518.
- Slattery, P., et al. 1967. Nuovo Cimento 50A, 377-392.
- Theocharopoulos, P., et al. 1974. Nucl. Phys. B83, 1-24.
- Wagner, F., et al. 1975. Phys. Lett. 58B, 377-392.
- White, H. S., et al. 1968. DAPR: Digital pattern recognition approaches production. Lawrence Berkeley Laboratory report UCRL-18543.
- Wohl, C. G., et al. 1978. Nucl. Phys. B132, 401-428.